UNIVERSITAT POLITÈCNICA DE CATALUNYA
BARCELONATECH

Simulation, Detection, And Classification Of Vessels In Maritime SAR Images

Author
Luis Eduardo Yam Ontiveros

Thesis Advisor
Prof. Jordi J. Mallorquí Franquet

This dissertation is submitted for the degree of
DOCTOR OF PHILOSOPHY

Department of Signal Theory and Communications
Remote Sensing Laboratory (RSLAB) Group
Universitat Politècnica de Catalunya (UPC)

Barcelona, June 2016

A mi madre Rosa, mi padre Hilario, y mi hermano Beto,
por todo su apoyo incondicional.
A Katherine, por su amor y paciencia.

Acknowledgements

I would like to acknowledge the following institutions for their support during the development of this research:

- **UPC** (Universitat Politècnica de Catalunya) for providing the pre-doctoral FPI-UPC 2011 fellowship during the first months of this doctoral activity.
- **EC** (European Commission) for providing financial support in the frame of this research, under the FP7-SPACE-NEREIDS Project(Ref. 263468); and for providing the RADARSAT-2 and Cosmo-SkyMed data from the NEREIDS acquisition campaigns carried out in 2013 and 2014.
- **AGAUR** (Agència de Gestió d'Ajuts Universitaris i de Recerca) for providing the pre-doctoral FI-DGR-2012 fellowship (Ref. LY080095) during the development of this doctoral activity.
- **MICINN** (Ministerio de Ciencia e Innovación) for providing financial support to part of the research performed in the frame of this thesis, under the projects TEC2011-28201-C02-01 and TIN2014-55413-C2-1-P.

Abstract

Over the last decades, environmental and socio-economic factors have generated interest on the observation of the ocean. Thus, the monitoring of maritime human activity has become crucial for the protection of the marine environment, the sustainability of the industrial sector, and security of navigation. Spaceborne remote sensing technologies can be used to improve existing marine monitoring systems at a global level. In particular, the Synthetic Aperture Radar (SAR) spaceborne sensors offer significant advantages for global monitoring. These types of sensors acquire high-resolution radar images suitable for the identification of man-made objects such as artificial structures and vehicles. In addition, these images can be obtained from any part of the planet's surface with no need for natural illumination, and practically regardless of the weather conditions over the area of interest. The current spaceborne SAR sensors have the potential to complement traditional maritime monitoring systems by acting as an independent source of information for the detection and identification of presumed vessels.

This research focuses on the analysis of the characteristics of maritime SAR images from spaceborne sensors, the improvement of simulation tools, and the development and evaluation of algorithms for extracting information of interest which can be applied to vessel monitoring. In particular, it takes the case of stripmap SAR single-look complex (SLC) images since this is the most basic SAR product that all of the current spaceborne sensors are capable of providing. Theoretical analysis and evaluation of simulations establish, firstly, the relation between the motions of the vessels and phase errors in their received SAR signals, and secondly, how these phase errors impact on the position and focus quality of the vessels' SAR signatures in the image.

The defocus of the targets is identified as one of the factors that hinders the proper extraction of the characteristics of vessels from the shape of their SAR signature. Thus, this thesis proposes local application of classical autofocus techniques adapted to the case of stripmap SLC images, and evaluates their performance using simulated data and real images of vessels from spaceborne SAR sensors. Moreover, by analysing the SAR signal of the vessels in both the image and Doppler domain, techniques for automatic extraction of features of the SAR signatures such as size, direction, range velocity component, and basic identification of the type of vessel are proposed. Finally, all these techniques are merged into a single

post-processing sequence, which this thesis proposes as an algorithm for automatic refocusing and feature extraction of detected vessels in stripmap SLC SAR images. The evaluation and analysis of the performance of this algorithm with RADARSAT-2 and Cosmo-SkyMed images suggest its potential use in operational applications, although as in the case of other vessel identification algorithms, its performance is dependent on the complexity of the SAR signatures of the vessels.

Table of contents

List of figures

List of tables

Chapter 1

Introduction

The ocean is fundamental to life on Earth. It covers a little more than 70% of the surface of our planet, and is home to array of living species and a provider of a huge amount of resources. Since ancient times, humanity has been deeply linked to it. Our civilization depends directly on the ocean for food, raw materials, and as a means of transport and distribution of goods; and indirectly, it has fundamental influence in our existence due to its crucial role in the regulation of the global climate and weather.

Nowadays, the activities related to the maritime sector have a great impact on the global economy. According the report by the World Wide Fund (WWF) on ocean economy from 2015 [1], the hundreds of millions of jobs generated around the ocean (e.g. fishing, shipping, tourism, biotechnology) placed the annual "gross marine product" (the equivalent to a country's annual gross domestic product (GDP)), as the 7th largest economy in the world when is compared to national GDPs. The fishing-related industry is still a major source of economic value for many countries, especially for developing nations where the fish trade may account for more than half of the total value of traded commodities. It has been fostered by the increase in the world average fish consumption per capita, which has doubled in the past 50 years. In fact, the Food and Agriculture Organization (FAO) reported that in 2010 fish accounted for 16.7% of the global population's consumption of animal protein, with the ocean being accountable for two-thirds of fisheries and aquaculture production (estimated to reach 158 million tonnes by 2012) [2].

Another major contributor to the ocean economy is the sector of seaborne transport of passengers and goods. On the one hand, although passenger transport is mainly reduced to domestic routes or routes to international ports of neighbouring countries, it is still an active industry. In 2013 alone, the number of passengers passing through ports in the European Union (EU) was estimated at around 400 million people, Italy and Greece being the leaders in seaborne passenger transport [3]. On the other hand, the transport of all kinds of goods and merchandise has fostered the global economy through international trade. It is an industry that has been grown steadily. The United Nations Conference on Trade And Development

(UNCTAD) reported a growth of 3.4% in the volume of the world's seaborne shipments in 2015, reaching around 9.84 billion tons or 80% of the world's total merchandise trade [4]. Under these circumstances, global trade has fomented interdependencies and connections between countries up to the point that almost no nation today can be considered fully self-sufficient. It is expected that seaborne shipping will maintain its dominant role in the world merchandise trade as it is still the most efficient way to transport large volumes of goods across the globe [5].

Looking at the big picture, all economic benefits are eclipsed by what the ocean represents in the sustainability of life on earth. It is home to around 2.2 million species, of which 90% still wait description [6]. Some of the most biologically rich ecosystems are the areas of coral reefs, where over 25% of all marine species are concentrated. For terrestrial ecosystems, the ocean is also crucial since it produces of over 50% of the planet's oxygen (from marine plants) and absorbs around 30% of the CO_2 from the atmosphere. Moreover, its currents support the distribution of heat, regulating the global climate and driving the weather [7, 8].

The health of the ocean is crucial for the equilibrium of the ecosystems, the well-being of millions of people, and the industrial sectors dependent upon it. Today, it can no longer be considered an endless provider of resources. The cumulative impact of human activity has started to show through an evident deterioration of marine ecosystems: around 50% of the world's coral reefs have been destroyed, 21% of global fish stocks are over-exploited and 61% fully-exploited, the ocean has become more acidic, and the average sea temperature has increased by 0.31°C to 0.65°C over the past 50 years. This deterioration is linked to actions like overfishing, coastal pollution, oil spills, and the volume of greenhouse-gas emissions; and with the current deterioration rates, marine ecosystems are likely to be exhausted up to the point of no return [1, 8].

The surveillance of the ocean has become an imperative action motivated by both environmental and socio-economical factors. In the past decade, several initiatives from international organizations and governments have promoted the global observation of environmental parameters and, in particular, the monitoring of human activity in the ocean. They seek to safeguard the marine environment, the sustainability of the industrial sector, and the security of navigation. Today, the regulation of fishing has become a necessity to avoid overexploitation of resources. In addition, due the quadrupling of global ship traffic in the past two decades [9], improvements in the robustness of traffic monitoring systems are required to maintain the rate of accidents low and enhance security against illegal activities such as piracy, trafficking of arms and narcotics, and smuggling of goods and people.

Currently, human activities in the ocean are mainly monitored by cooperative systems which use transponders on the ships and vessels. The most common ones are the Automatic Identification System (AIS) from the International Maritime Organization(IMO) [10],and the Vessel Monitoring System (VMS) fostered by the European Commission and adopted mainly for fishing vessels [11]. They are able to provide real-time information about the vessels' type,

position, speed, and heading, while relying on the cooperation of these vessels. Nevertheless, the self-identification approach represents the main constraint of these monitoring systems. Failures, intentional disablement, or hacking of the transponders may produce unreliable data or shadowing of the ongoing activity of the vessel. In this sense, other technologies like spaceborne sensors can be used as a support for the robustness in vessel monitoring systems.

The evolution of the Earth observation from spaceborne sensors has provided the technology for monitoring a wide variety of phenomena, including human activity, on a global scale. In general, spaceborne sensors measure the scattered electromagnetic (EM) radiation from the surface of the Earth. They are typically divided into *passive* and *active* sensors depending on the source of the radiation used for the measurements. Optical and radiometric sensors belongs to the passive category since they detect the radiation from natural sources like reflected sunlight or thermal radiation from the Earth's surface; examples of these sensors are the GeoEye-1, WordView constellation, and Sentinel-2 [12, 13]. In contrast, active sensors provide their own source of illumination, emitting EM radiation and sensing the backscattered signal. These sensors are commonly based on lidar (Light Detection And Ranging) systems as in the case of the CALIPSO [14], or radar (Radio Detection And Ranging) systems as in the RADARSAT constellation, TerraSAR-X, or Sentinel-1 sensors [15–17]. All of these have provided data for several applications, such as environmental protection, agriculture, forestry, fishing, climate change analysis, sustainable development, and civil protection. But in the case of monitoring human activity in the sea, the synthetic aperture radar (SAR) sensors appear to be one of the technologies that can provide most benefits.

The spaceborne SAR sensors have been actively used in Earth observation for the past 60 years, providing 2D reflectivity maps (i.e. radar images) of wide areas of the Earth's surface. Since the seaSat [18], the first civilian spaceborne SAR sensor launched in 1978 by NASA, several missions carried out by Canada, Japan, Europe, and Russia have successfully placed in orbit and managed SAR satellites. Nowadays, spaceborne SAR sensing is a mature technology, and its level of sophistication allows the acquisition of high-resolution images suitable for the identification of man-made objects on a global scale. Being a radar-based technique, it operates independently from natural illumination, and the acquisitions can be done under almost any weather condition due to the little or zero deterioration of the EM signals within the frequency bands that are commonly employed. All of these characteristics have made the analysis of the SAR images an active area of research for its application in target detection and recognition.

SAR imaging from spaceborne sensors represents a support for the traditional vessel monitoring systems. The capabilities of the spaceborne SAR technology can be exploited to provide information of interest for the surveillance of wide areas of the ocean. Contrary to the transponder-based systems like AIS or VMS, employing SAR images is a non-cooperative approach. Thus, the detection and feature extraction of the presumed vessels are perfomed using the SAR images, without the knowledge of the targets. In the EU, an example of

initiatives that encourage the research and application of space-based solutions to vessel monitoring is the FP7 NEREIDS project [19, 20]. NEREIDS aimed to integrate different remote sensing technologies to enhance the capabilities of automatic vessel monitoring systems; and in particular, it promoted the use of spaceborne SAR sensors for real-life operational application in this field.

In practice, detection and classification algorithms are required for the application of the SAR images in the maritime surveillance. Typical SAR acquisitions may result in images of several thousands of pixels, covering large areas of the ocean with a huge amount of vessels, especially in areas near the coasts. In these conditions, it is impractical and time-consuming to manually search for and select likely vessel candidates, so algorithms for the post-processing of the image are commonly applied. Whereas the vessel detection techniques have achieved a high level of refinement and present low false alarm rates [21], the classification and feature extraction algorithms still face great challenges related to the complex behaviour of the SAR signatures of the vessels. Moreover, aberrations such as the defocus introduced by the motion of the vessel may affect the quality of the image [22], undermining the classification process.

In general, the algorithms developed for vessel monitoring with SAR images aim to obtain estimations of useful information, such as the position, speed, dimensions, or heading of the detected vessel. Each technique requires specific configurations or capabilities of the SAR sensor in order to provide a certain type of data. For instance, some techniques work directly with single-channel SAR acquisitions; others may employ *multidimensional* data for the analysis of the backscattered EM radiation with different polarization, or multichannel configurations (with a single or more antennas) for interferometric processing. In this sense, the applicability of some algorithms could be limited to acquisitions from only few SAR sensors with the expected capabilities.

1.1 Objectives and Structure of the Thesis

Today, only a few civilian spaceborne SAR sensors are able to offer specific types of multidimensional data. Therefore, single-channel acquisitions are still the most available data as they can be provided by any current spaceborne SAR sensor. Of particular interest is the usage of the single-look complex (SLC) format as it is the closest product to the SAR raw data. Thus, it preserves resolution and allows the implementation of advanced post-processing techniques. Motivated by these conditions, this research work aims to assess the exploitation of SLC SAR data from single-channel acquisitions in their application for vessel monitoring. In order to do this, the five main objectives of this thesis are:

- The development of basic simulation tools and the improvement of the existing tools in order to provide realistic SAR data which can support the analysis of the reflectivity phenomena of vessels in maritime environments.

- The analysis of the effects on the SAR signal of slow-moving targets in the case of spaceborne SAR acquisitions. For the image formation, the SAR processor assumes complete knowledge of the relative motion of the satellite with respect to the targets. In this sense, the unknown motion of the vessels likely introduces singular phase errors in their SAR signal.

- The analysis, implementation and evaluation of autofocus techniques applied to refocus the SAR signatures of the vessels. Blurring effects are commonly observable in the SAR signatures of the vessels, limiting the potential extraction of features from their shape.

- The analysis of the characteristics of the SAR signal and the SLC images of vessels to extract features of interest for the vessel monitoring systems.

- The development of a methodology for automatic feature extraction of the imaged vessels and the assessment of its performance with real SLC data.

This dissertation is structured in six chapters. Chapter 2 is dedicated to providing the theoretical framework for spaceborne SAR systems and their application in the field of vessel monitoring. The chapter begins with a brief overview of the basic principles of SAR imaging. The signal of an ideal static point target is obtained to define resolutions achieved in the SAR images based on the basic parameters of the sensor. Moreover, the inherent geometrical distortions of the SAR signals are discussed as the 3D objects are projected in the image plane (i.e. the *slant-range* plane). Similar to the static case, the description of the SAR signal of a moving point target is obtained, this being the base model used in later chapters for the typical motion of the vessels. The last part of this chapter is devoted to discussing on the state-of-the-art techniques for the detection and classification of vessels using SAR data, paying particular attention to the techniques that employ single-channel data.

Chapter 3 provides an overview of the simulation and vessel detection tools employed in this research work. The first section introduces GRECOSAR, a SAR simulator of complex targets developed at the Universitat Politècnica de Catalunya (UPC), highlighting its support in the study of vessels in maritime environments. Then, the improvements implemented in GRECOSAR throughout the development of this research work are discussed. This section covers the improvements in the interpolation process to reduce the computational burden, the addition of a new multi-harmonic model of the sea surface for a more realistic simulation of maritime scenarios, and the modification of the antenna "sweep" for a more realistic simulation of the effects of the motion of the scatterers in the Doppler signal. The next part of the chapter introduces the main tool employed in this research work for the detection of the vessels in actual spaceborne SAR acquisitions. It is based on the exploitation of persistent features in the different sub-bands of the wavelet-transform (WT) of the SAR image, inspired by the multiscale operation of human vision in the perception of features. The technique

is reported to be a robust algorithm in vessel detection and landmasking, which makes it suitable for application in this research work.

In Chapter 4, the principles of the autofocus techniques are analysed along with the description of their implementation in the case of refocusing the SAR signature of vessels. First, three widely used autofocus algorithms are described, namely: the Gradient Autofocus (PGA) algorithm, the Multiple Aperture Mapdrift (MAM), and the Image Contrast-based Autofocus (ICBA). Comments on their implementation are provided as guidance for their practical application to the processng of SAR signatures of vessels. Next, the results of their validation are discussed in the case of a controlled scenario from the simulation of a test target (a corner reflector) with different phase error functions. In the final part of the chapter, the algorithms are applied and assessed using SLC chips from RADARSAT-2 and Cosmo-SkyMed stripmap acquisitions, and the application of the autofocus in an *independent range-bin* mode is discussed as a possible way to improve variable defocus along range direction.

Chapter 5 is devoted to the study and analysis of the extraction of features of interest from the SLC data. It describes the approaches taken for the extraction of the physical dimensions of the vessel, its heading, and the estimation of the ground-range velocity. All these techniques use the SAR signatures of the vessels from stripmap data of single-channel spaceborne SAR sensors. First, the methodology for the statistical modelling of the sea clutter to extract, in an unsupervised manner, the vessel's contour is described. Then, the process of calculating box to fit the obtained contour and the use of this box in computing the dimensions of the vessel's SAR signature is presented. Next, a proposed method for the estimation of the heading is presented. It employs the main orientation of the computed fitted box, resolving the 180° ambiguity with the direction of the ground-range velocity component of the vessel. The rest of the chapter is focused on discussing the techniques for the estimation of this ground-range velocity from the spectral information of the SAR signal, analysing the effects of using range-compressed data and SLC data, and discussing the encountered complications of the methodologies in the cases of complex targets like the vessels.

Chapter 6 proposes a novel feature extraction algorithm and shows the experimental results for the automatic estimation of the vessel's dimensions and heading, along with a rough classification of the type of vessel. In the first part of the chapter, the description of the steps of the algorithm is given along with comments on the assumptions made for the whole processing chain. The next part is focused on the presentation and discussion of the results of the application of the feature extraction algorithm with real SAR data. The assessments were done based on the available ground-truth data of the SLC chips of vessels' SAR signatures from RADARSAT-2 and Cosmo-SkyMed stripmap images. These images are part of the extensive database of acquisition campaigns carried out during the NEREIDS project. The analysis of the results highlights typical cases faced during the experimental tests and the limitations observed in the algorithm.

Finally, Chapter 7 summarizes the main results, the main conclusion drawn from this research, and proposes potential future lines of research related to this work.

Chapter 2

Preliminaries

2.1 Introduction

Synthetic aperture radar (SAR) systems belong to the group of technologies developed for Earth observation. SAR has been actively evolving during the past 60 years in the remote sensing community, achieving the level of sophistication and maturity that can be seen today in radar imaging sensors. It provides unique capabilities in the acquisition of high-resolution images as a radar-based technology: it can operate independently from sunlight because it carries its own illumination source (EM radiation); additionally, the acquisitions can be done under any weather conditions due to the little or zero deterioration of the EM waves in the frequency bands used [23–25]. Moreover, in the case of spaceborne systems, SAR images can be acquired from any area of the surface of the Earth, resulting in a system capable of continuous observation on a global scale. Thanks to these characteristics, SAR images have recently been the focus of active research which looks at their applicability in the field of vessel monitoring and surveillance. In this sense, SAR systems are considered a potential source of information which would complement current vessel surveillance systems.

This chapter is devoted to providing a framework for spaceborne SAR systems and their application in the field of vessel monitoring. First, Section 2.2 provides a brief overview of the theoretical background of the SAR technique. Then, Section 2.3 analyses the effects of the motion of a target on its SAR signal; in particular, the case of a slow-moving target is considered in order to analyse the SAR signal of typical vessels, given the difference in the relative speed of the vessel and the satellite. Finally, Section 2.4 reviews the latest methods that have appeared in the literature on the detection and classification of vessels using SAR data.

2.2 SAR Basics

2.2.1 Imaging radar

An imaging radar system basically consists of a platform that carries the radar and moves along a flight path. In this way, the 2D reflectivity map is obtained by transmitting EM pulses and receiving the echoes from the illuminated area as the radar moves. The side-looking real aperture radar can be considered as the precursor of SAR technology and the simplest system that provides a 2-D reflectivity map of the imaged area [26]. As its name suggests, it consists of a platform moving in a straight line and illuminating perpendicularly to the flight path. Figure 2.1 shows a basic diagram of the geometry of this configuration, known as the *stripmap* mode, which assumes a flat-earth model. There, the direction aligned with the platform velocity vector is known as the *azimuth* direction, while the radar-to-surface direction is known as the *range*, its projection over the ground being the *ground-range* direction.

The dimensions of the image in range mainly depend on the extension of the illuminated area [23, 27]. The footprint of the antenna is defined by the vertical and horizontal beamwidth of the antenna, θ_V and θ_H respectively, and the range to the surface. In addition, these beamwidths are commonly associated with the width (W_A) and length (L_A) of antenna, and wavelength (λ) of the transmitted signal such that $\theta_V = \lambda/W_A$ and $\theta_H = \lambda/L_A$ [23, 24]. Then, the extension of the image in ground-range direction, i.e. the *swath* width (w_g), can be approximated to

$$w_g = \frac{\theta_V R_m}{\cos\theta_{inc}} = \frac{\lambda R_m}{\cos\theta_{inc}} \tag{2.1}$$

where R_m and θ_{inc} are the range and the incidence angle (i.e. angle between the radar beam and the normal to the surface) to the midswath, respectively. In azimuth direction, the image does not have a fixed length because it is normally limited by the storage and processing capabilities of the sensor [28].

Range resolution

The resolution of the image can be defined as the minimum separation of the two points that can be distinguished as individual targets by the system[23]. In this sense, and base on the diagram of Figure 2.1b, the range resolution is given by

$$\delta_r = \frac{c\tau_p}{2} \tag{2.2}$$

where τ_p is the length of the transmitted pulse, c is the speed of light, and the factor of two in the denominator is introduced due to the two-way path taken by the radar signal. Notice that the equation (2.2) suggests that the range resolution improves as the pulse is shortened. However, by reducing the length of the pulse, the transmitting power needs to

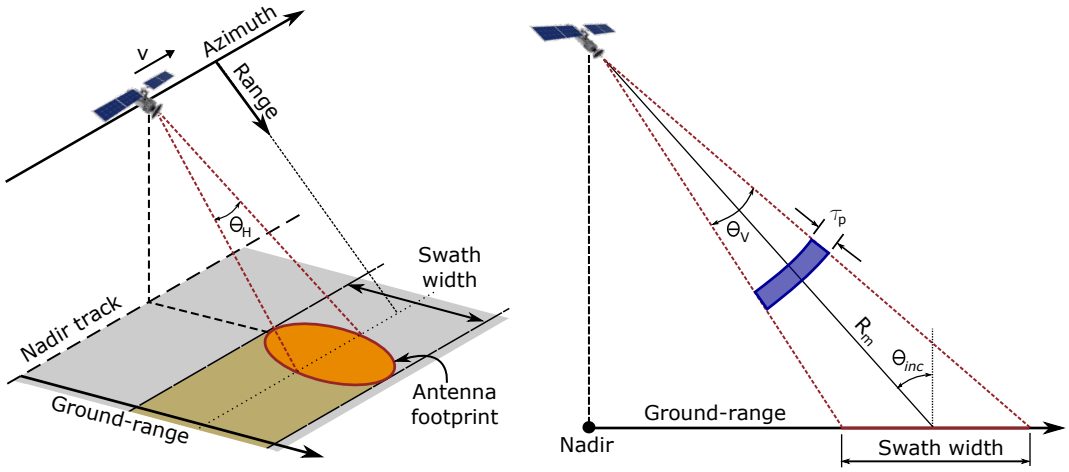

(a) (b)

Fig. 2.1 (a) Diagram of the basic geometry of a side-looking imaging radar (stripmap configuration); (b) diagram of range resolution for a side-looking imaging radar.

increase in order to have a pulse with enough energy to produce an echo signal that fulfills the signal-to-noise ratio (SNR) required for a reliable detection. In practice, there are physical limitations that constrain the peak power of the pulses, and the most common solution is to employ a *pulse compression* technique.

In the pulse compression technique, the radar transmits an "expanded" pulse that can be later shortened in a post-processing stage. In this way, the use of longer pulses raises the average transmitted power, which translates into an increase in the SNR, and their compression ensures the required range resolution. The pulse compression is commonly achieved by using a linear frequency modulated (LFM) signal or *chirp*. This type of signal increases (or decreases) its instantaneous frequency linearly as a function of time, and it can be described in baseband as:

$$s_{chirp}(\tau) = \text{rect}\left[\frac{\tau}{\tau_p}\right] e^{j\pi\kappa\tau^2} \tag{2.3}$$

where τ represents the time (in seconds), τ_p the duration of the pulse, rect$[\cdot]$ the rectangular function, and κ the *chirp rate*. The sign of κ determines if the pulse is an "up-chirp" ($\kappa > 0$) or a "down chirp" ($\kappa < 0$). The chirp rate is a parameter which must be known in order to perform the pulse compression correctly, but the use of an up- or a down-chirp does not have further implications.

By using the matched filtering technique [29] to compress the pulse, the range resolution is decoupled from the pulse length τ_p. Then, it becomes dependent only on the bandwidth of the pulse, rewriting equation (2.2) as [23, 24]:

$$\delta_r = \frac{c}{2B_r} \tag{2.4}$$

where B_r is the frequency bandwidth of the transmitted pulse, and it can be derived from the equation (2.2) for a chirp pulse of duration τ_p as:

$$B_r = \frac{1}{2\pi}\left|\frac{\mathrm{d}\phi_{chirp}(\tau)}{\mathrm{d}\tau}\right|_{\tau=-\frac{\tau_p}{2}}^{\tau=\frac{\tau_p}{2}} = \frac{1}{2\pi}\left|\frac{\mathrm{d}\pi\kappa\tau}{\mathrm{d}\tau}\right|_{\tau=-\frac{\tau_p}{2}}^{\tau=\frac{\tau_p}{2}} = |\kappa|\,\tau_p \tag{2.5}$$

Azimuth resolution

In real aperture radar systems, the azimuth resolution (δ_a) is constrained to the footprint along this direction. Thus, for a given range R_i, it results in [23]:

$$\delta_a = \theta_H R_i = \frac{\lambda R_i}{L_A} \tag{2.6}$$

where θ_H and L_A are the beamwidth and length of the antenna in the azimuth direction, respectively; and λ is the wavelength of the transmitted signal. It can be seen from equation (2.6) that, in this type of systems, the azimuth resolution depends on both the length of the antenna (in azimuth) and the range point over the swath. Then, for a given range and wavelength, the resolution can only be improved by increasing the antenna length L_A. This creates problems for high-resolution imaging systems (e.g. δ below 10 meters) as the radar gets further from the area of interest; for instance, a spaceborne system with the carrier frequency in the X-Band ($\lambda \approx 3.5$ cm) would require an antenna of hundreds of meters. In practice, it is difficult to overcome all of the technical problems in the construction and deployment of systems with antennas of this size. So the feasible alternative to improve the azimuth resolution came with the development of the *synthetic aperture radar* concept.

2.2.2 Synthetic Aperture Radar concept

In the Synthetic Aperture Radar (SAR) technique, the echo data from the different positions are coherently processed to synthesize a larger antenna length (Figure 2.2). This approach is similar to how a phased array works, but SAR uses the different positions of the antenna in the flightpath as the individual elements in the phased array. The coherent processing of the echoes is based on the analysis of the Doppler of the signal in the azimuth direction. In this way, the beamwidth of the final synthetic array is narrowed, achieving a much better resolution than the real aperture system [23, 24].

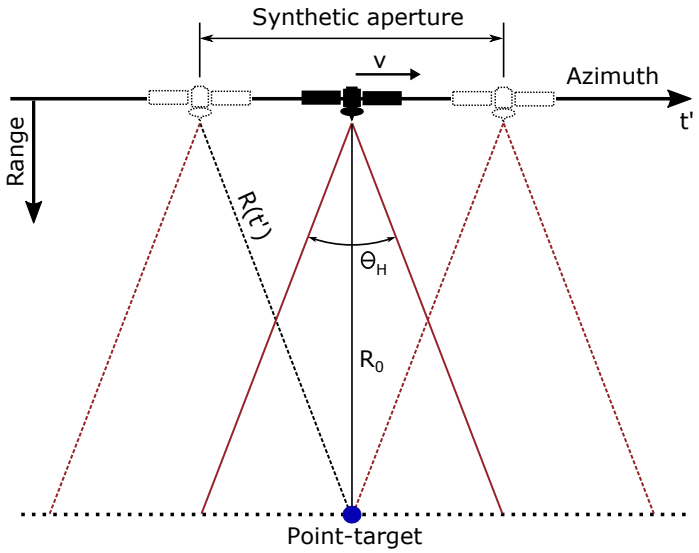

Fig. 2.2 Azimuth geometry of a SAR system (stripmap mode) in the slant-range plane.

Azimuth resolution of SAR systems

The SAR technique involves coherent signal processing of the phase history during the *observation time* (or aperture time). For a static point target, and assuming the basic stripmap configuration of Figure 2.2, a simplified model of the baseband SAR signal in the azimuth direction can be expressed as

$$s_a(t' - t'_c) = A_0 \text{rect}\left[\frac{t' - t'_c}{T_a}\right] e^{-j\frac{4\pi}{\lambda}R(t'-t'_c)} \tag{2.7}$$

with A_0 as a complex constant related to the amplitude and phase of the backscattered signal due to the target; t' and t'_c as the azimuth-time reference and the beam centre crossing time, respectively; and T_a representing the observation time. The variation of the range, R, during the synthetic aperture can be approximated to a quadratic function as [23, 24]:

$$R(t' - t'_c) \approx R_0 + \frac{v^2(t' - t'_c)^2}{2R_0} \tag{2.8}$$

where R_0 is the range of closest approach (assumed at $t' = t'_c$) and v the speed of the sensor's platform. By using this quadratic function of the range in equation (2.7), and defining $t = t' - t'_c$ to simplify the notation, the basic model of the azimuth signal turns in

$$s_a(t) = A_0 \text{rect}\left[\frac{t}{T_a}\right] e^{-j\frac{4\pi}{\lambda}R_0} e^{-j\frac{2\pi v^2}{\lambda R_0}t^2} \tag{2.9}$$

In essence, the signal $s_a(t)$ in equation (2.9) is a down chirp signal with phase $\phi_{az}(t) = -\frac{2\pi v^2}{\lambda R_0}t^2$ and chirp rate (known as the *Doppler rate* in this context) of $K_a = -\frac{2v^2}{\lambda R_0}$. In this sense, the theoretical achievable azimuth resolution can be obtained in a similar way to the

range direction, using the linear chirp pulse compression approach (Section 2.2.1). Through matched filtering, the azimuth resolution of a SAR system becomes proportional to the inverse of the bandwidth of the azimuth chirp B_{az}, which is given by

$$B_{az} = \frac{1}{2\pi}\left|\frac{\mathrm{d}\phi_{az}(\tau)}{\mathrm{d}\tau}\right|_{t=-\frac{T_a}{2}}^{t=\frac{T_a}{2}} = \frac{2v}{L_a} \tag{2.10}$$

with the observation time T_a defined as $T_a = R_0\theta_H/v = R_0\lambda/(L_a v)$. Thus, the azimuth resolution of the SAR system can be expressed as

$$\delta_{az} = \frac{v}{B_{az}} = \frac{L_a}{2} \tag{2.11}$$

The SAR azimuth resolution δ_{az} comes out as half of the real antenna length L_a and independent from the range and wavelength. As suggested in equation (2.11), shorter antennas yield to finer azimuth resolution because the aperture time increases, and consequently, the bandwidth is larger. This implies that the system would only have to send pulses at a *pulse repetition interval* (PRI) that ensures the Nyquist condition. However, in practice the minimum length (in azimuth) of the antenna is limited in order to achieve the design specifications of the whole SAR system, such as the required SNR or the PRI constraints for a given swath width [23–25]. To overcome these limitations, modifications of the simple stripmap SAR configuration are used to increase further the resolution in azimuth via the *spotlight* mode [30], or the swath width via the *scanSAR* mode [31, 32]. In the spotlight mode (Figure 2.3a), the beam is steered so as to keep the area of interest in the beam for a longer time, i.e. a longer synthetic antenna; a higher resolution is achieved, but the covered area in azimuth is limited to the footprint of the antenna. In the scanSAR mode (Figure 2.3b), subswaths are taken in a stepwise manner by sweeping the antenna into different positions in range; thus, the final swathwidth of the image increases, but the azimuth resolution decreases as the targets are not illuminated by the whole synthetic aperture.

2.2.3 Basic SAR signal processing

In the case of SAR systems with antenna beam almost perpendicular to the flightpath (the so-called *low-squint* case), the corresponding baseband signal received from a static point target can be approximated by [24]

$$s(\tau, t) = A_0 w_r\left(\tau - \frac{2R(t)}{c}\right) e^{j\pi\kappa_r\left[\tau-\frac{2R(t)}{c}\right]^2} w_a(t) e^{-j\frac{4\pi}{\lambda}R_0} e^{j\pi K_a t^2} \tag{2.12}$$

where τ represents the time in range or *fast-time*, t is the azimuth time[1] or *slow-time*; and $w_r(\cdot)$ and $w_a(\cdot)$ represent the envelops of the range pulse and the received signal in the azimuth

[1] The change of variable $t = t' - t'_c$ has been assumed to simplify the notation

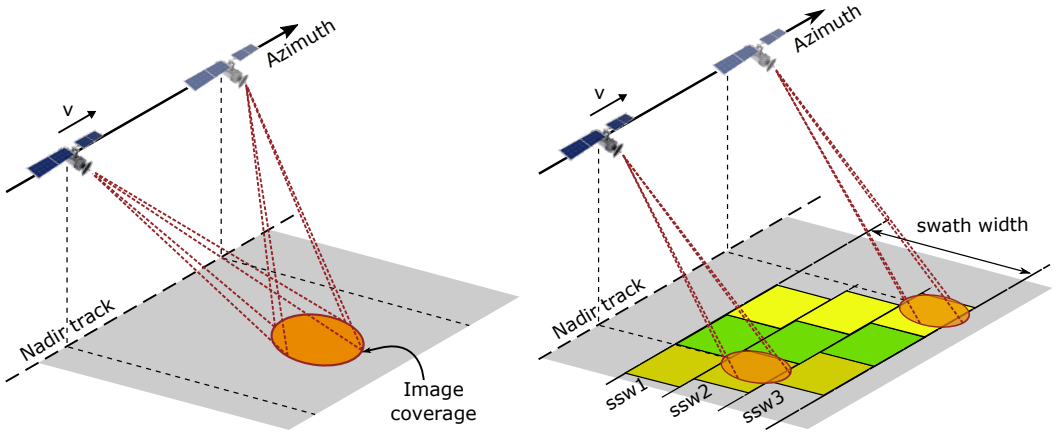

Fig. 2.3 Diagrams of other common SAR acquisition modes: (a) spotlight mode; (b) scanSAR mode.

direction, respectively. From equation (2.12), it can be seen that the echo of the pulses would be detected at different ranges due to the variation of the distance to the target, $R(t)$, during the synthetic aperture time. As a consequence, the signal of a single target migrates through range cells in the raw data. This phenomenon is known as the *range cell migration* (RCM) and is inherent to the SAR technique. If it is not corrected, the range resolution could deteriorate, with smearing effects appearing. In addition, it complicates the focusing process of high-resolution images since the RCM is range-variant, i.e. targets at different ranges present different migrations. As a result, it makes SAR focusing a two-dimensional space-variant problem. The different techniques developed to efficiently compensate the RCM have in turn fostered the development of different SAR image processing algorithms such as the $\omega - k$, Range-Doppler, or Chirp scaling [26].

Intuitively, from the discussion of Section 2.2.1 and Section 2.2.2, the basic compression of the SAR signal of equation (2.12) should include the matched filtering of chirps in range and azimuth directions, along with a RCM compensation (RCMC) step. In general, the most common algorithms starts with: 1) the range compression, then 2) the RCMC, and finally, 3) the azimuth compression. The main difference in each approach lies in how the RCMC is implemented. The thorough analysis and description of the focusing algorithms are out of the scope of this thesis, but further details and discussion can be found in [23, 24, 30].

2.2.4 Geometrical effects in SAR images

SAR images are 2D maps of the reflectivity of the targets in a given area. Whereas their azimuth positions are mainly related to their corresponding Doppler frequency variation(equation (2.9)), their range positions in the image are functions of the pulse transit time between the sensor and the target; in other words, these range positions are proportional to

the radar-to-target distances along their corresponding line-of-sight. This causes a non-linear compression of the ground-range position of the targets into the SAR image.

Depending on the local incidence angle of the illumination of the targets, geometrical effects in the slant-range plane (i.e. the image plane) can be observed, namely: *foreshortening*, *layover*, and *shadowing* [23, 27]. Figure 2.4 illustrates the basic diagram of the distortion of a pyramidal structure. In this figure, the foreshortening appears as a reduction of the ground-range distances of the scatterers due to their difference in height. Layover is similar to the foreshortening, but in this case the position of the scatterers would appear inverted in the SAR image; for example, in figure 2.4b, point B would appear before point A in the slant-range direction plane. Finally, shadowing occurs in areas that are not in line-of-sight from the radar to the scatterers due to their occlusion (figure 2.4c).

The presence of these geometrical effects in the SAR images is a key point in the understanding of SAR imagery. The structure of the targets will be distorted, and as a consequence, their SAR signature will likely present layover effects and inner shadowing [33], giving different results to what is usually expected in the common optical image. To illustrate this, Figure 2.5 shows examples of the comparison of the optical image of a vessel (in free space) as seen from the radar and the projection of its visible parts into the slant-range plane. Nevertheless, SAR signatures are more complex to predict than the simple projection; EM interaction and the multiple bounces of the radiation off the structure of the target are factors that also have to be considered [34].

2.3 The SAR signal of a slow-moving target

The SAR technique assumes that the relative motion of the platform and the targets are known in order to model the range variation along the construction of the synthetic aperture. This constitutes a problem in the case of targets in motion such as sailing vessels because they produce unexpected variations in the radar-to-target distance. As a consequence, phase errors are induced, and aberrations such as defocus and azimuth displacements of the scatterers may be present in the SAR image of the moving target [22].

For spaceborne SAR systems, typical vessels can be considered to be slow-moving targets because the satellite travels at a much higher speed. Under these circumstances, it can be assumed that the target stays in the same range resolution cell during the synthetic aperture time. Thus, the main deterioration of the image would be associated to the azimuth direction.

In order to analyse the effects of the motion of a slow-moving target in the azimuth direction, an uniformly accelerated point-target is considered. For a basic low-squint stripmap SAR configuration, Figure 2.6 shows a diagram of a moving point target in the slant-range plane; its motion is decomposed into the range and along-track components. Then, the

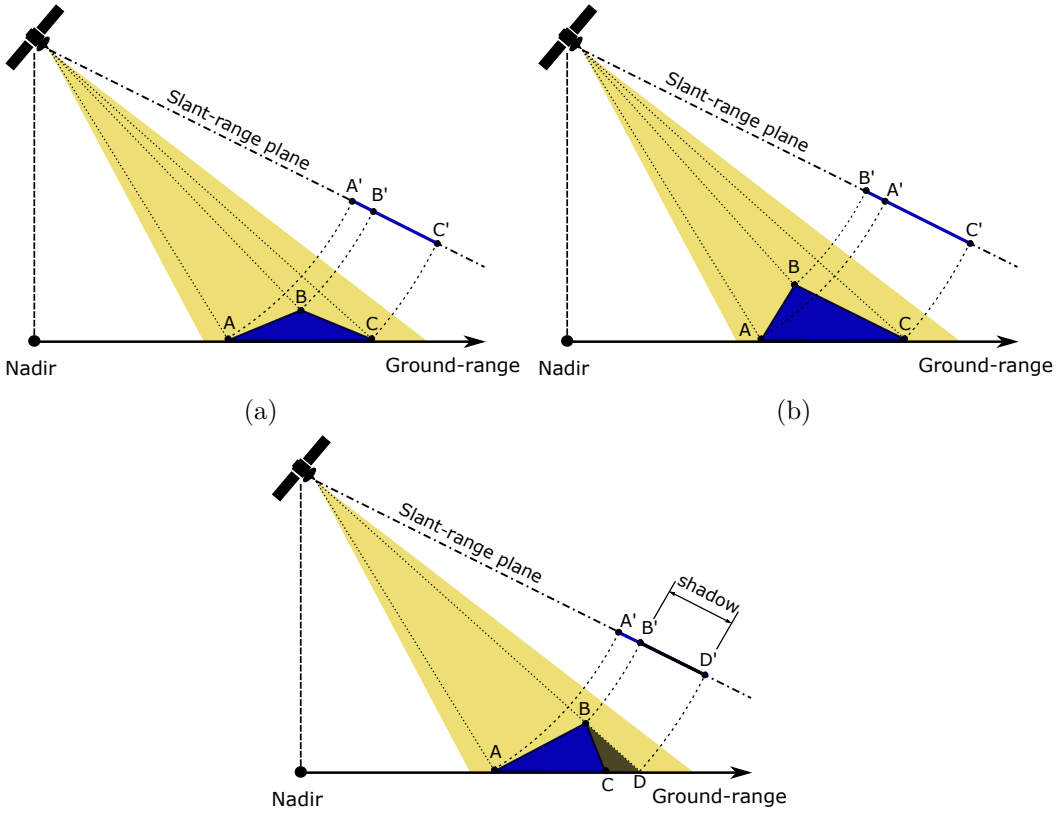

Fig. 2.4 Diagram of geometrical effects in SAR images: (a) foreshortening; (b) layover; (c) shadowing. (Based on [35])

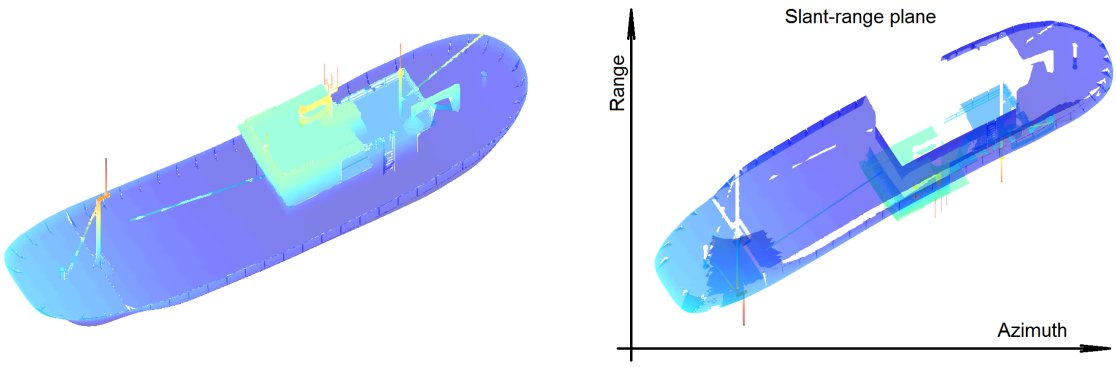

Fig. 2.5 Comparison of the (a) optical image of a vessel (in free space) as seen from the radar and (b) the respective slant-range projection of the visible parts.

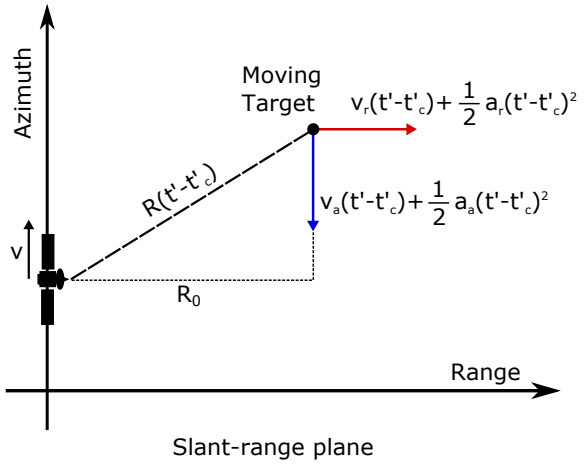

Fig. 2.6 Slant-range projection of an accelerated moving target for a basic stripmap configuration

baseband model of the range-compressed signal after range cell migration correction (RCMC)[2] (hereinafter referred to simply as the range-compressed signal), can be expressed as [24]:

$$s(\tau, t'-t'_c) \approx A_0 p_r\left(\frac{\tau - 2R_0}{c}\right) w_a\left(t'-t'_c\right) e^{-j\frac{4\pi}{\lambda}R(t'-t'_c)} \tag{2.13}$$

which is similar to equation (2.12), only that $p_r(\cdot)$ represents the compressed pulse in range. The complex exponential in equation (2.13) is related to the processing of the signal in the azimuth direction. In particular, the instantaneous range $R(t'-t'_c)$ for the moving target in Figure 2.6 is described as:

$$R(t'-t'_c) = R(t) = \sqrt{\left[R_0 + v_r t + \frac{1}{2}a_r t^2\right]^2 + \left[(v+v_a)t + \frac{1}{2}a_a t^2\right]^2} \tag{2.14}$$

with $t = t' - t'_c$ as the change of variable to simplify the notation; R_0 is the reference distance at $t' = t'_c \Rightarrow t = 0$; v_r and v_a represent the magnitude of the range and along-track velocity components of the moving target, respectively; in the same way, a_r and a_a are the magnitude of the range and along-track acceleration components of the respective directions; and v represents the nominal speed of the sensor's platform. By doing a second-order Taylor approximation around $t = 0$, $R(t)$ can be expressed as:

$$R(t) \approx R_0 + v_r t + \left[v_r^2 - \frac{v_r}{2R_0} + (v+v_a)^2 + R_0 a_r\right]\frac{t^2}{2R_0} \tag{2.15}$$

[2] Recall that it is assumed slow-moving targets which stay within the same range resolution cell during the most part of the observation time, so residual RCM errors from applying the RCMC for stationary targets can be negligible.

A further simplification can be made to the quadratic term in equation (2.15) for the case of spaceborne SAR sensors and slow-moving targets. It can be expected that the magnitudes of the terms that contain the v_r components are a lot smaller than the others since $R_0 >> v_r$, so they do not have a significant impact on the whole quadratic term. Then, equation (2.15) can be rewritten as:

$$R(t) \approx R_0 + v_r t + \left[(v + v_a)^2 + R_0 a_r\right] \frac{t^2}{2R_0} \tag{2.16}$$

This final expression of the range variation shows that the v_r component introduces a linear term in $R(t)$, inducing a shift in the azimuth position of the target in the image; a further analysis of the effects of this linear term will be done in Chapter 5 (Section 5.4). Both components v_a and a_r modify the quadratic term, and their individual effects cannot be separated as they are merged into the quadratic coefficient; but for spaceborne SAR sensors and sailing vessels (assumed to be slow-moving targets), the $R_0 a_r$ factor may tend to have more weight in modifying the coefficient of the quadratic term. Expanding the products of equation (2.16) and using equation (2.13), the model of the range-compressed signal is

$$s(\tau, t) = A_0 p_r \left(\frac{\tau - 2R_0}{c}\right) w_a(t)\, e^{-j\frac{4\pi}{\lambda}R_0} e^{-j\frac{4\pi}{\lambda}v_r t} e^{j\pi K_a t^2} e^{-j\frac{4\pi}{\lambda}\left(\frac{2vv_a + v_a^2 + a_r R_0}{2R_0}\right)t^2} \tag{2.17}$$

where $K_a = -\frac{2v^2}{\lambda R_0}$ is the frequency Doppler Rate used in the azimuth compression of the stripmap signal. Notice that if $v_r = v_a = 0$ and $a_r = 0$, equation (2.17) would turn into the obtained model of the static target of equation (2.12).

2.4 Vessel detection and classification in SAR imaging

The SAR technique is widely used in the microwave remote sensing community for analysis and observation of the phenomena on the Earth's surface. In the case of marine applications, SAR imaging has been exploited to analyse different parameters of the ocean's surface, like swell directions, surface wind, and oil-polluted areas [36]. Moreover, the improvement of civilian spaceborne SAR sensors such as RADARSAT-2 or TerraSAR-X has provided high-resolution images that make the detection of man-made objects possible.

In recent years, high-resolution spaceborne SAR sensors have been considered an interesting source of information for vessel surveillance systems due to their imaging capabilities, namely: 1) acquisition of images of any area of interest on the sea's surface on a global scale; 2) lack of dependence on the presence of natural illumination to obtain the images since they have their own source of radiation (i.e. the radar); and 3) the frequency bands of the common radar systems have little or practically no sensitivity to the presence of rain or clouds, so the radar signal sees practically no deterioration and the acquisitions can be done regardless of the weather conditions over the area of interest [24]. In addition, the spaceborne SAR sensors

can complement traditional cooperative monitoring systems based on transponders such as the Automatic Identification System (AIS) [10] or the Vessel Monitoring System (VMS) [11]. With the use of SAR images, the identification of vessels follows a non-cooperative approach. In contrast to the AIS or VMS, the detection is performed without knowledge of the targets, so the extracted information can be cross-checked to highlight suspicious activity. All these characteristics have made the application of SAR imaging to vessel monitoring an intensive research area with initiatives such as the Copernicus Programme[3] [37, 38], supported by the European Space Agency (ESA), and the RADARSAT Constellation [15], supported by the Canadian Space Agency.

Algorithms that use SAR images for vessel monitoring have appeared in recent literature. For example, Brusch *et al.* [39] use single channel TerraSAR-X for the detection and velocity estimation of the vessels; Saur *et al.* [40] also employ TerraSAR-X data, but explore the use of optical images for additional detection and finer extraction of the dimensions of the vessels; Martorella *et al.* [41] employ Cosmo-SkyMed images and refocus the SAR signature to enhance their quality for a better estimation of the dimensions. In general, the processing chain of all these kinds of algorithms have three fundamental steps: 1) *land masking* to process only the section of the sea surface in the image, 2) *detection* of the likely vessels, and 3) *feature extraction (and classification)* of the targets previously detected.

Current algorithms that perform the whole processing chain, such as those previously mentioned, have reported good results that encourage the use of SAR images in vessel monitoring. Nevertheless, there are ongoing efforts which aim to improve the performance of the individual processing steps, in particular to ensure the robustness of the Detection and Feature Extraction in the variety of cases that may appear in the maritime SAR images.

2.4.1 Vessel Detection techniques

The most common approach adopted by the vessel detection algorithms using single-channel data is based on the expected highly reflectivity of the targets. They search for clusters of pixels whose reflectivity is particularly distinctive with respect to those surrounding them, labelling them as target candidates by using constant false alarm rate (CFAR) detectors [21]. In this process, the pixel being tested is surrounded by a guard area to avoid a pixel of the target being considered part of the background (Figure 2.7). Then, the statistics of this local background is employed to separate the pixels of the potential targets by keeping a constant false alarm rate.

Working directly with the histogram of the background leads to high computational burden because of the large amount of samples required to accurately estimate the threshold for low false alarms rates [21]. Instead, models of the probability density function (p.d.f.) are usually applied, estimating their parameters from the background samples. Thus, a threshold,

[3] Previously known as GMES (Global Monitoring for Environment and Security) programme

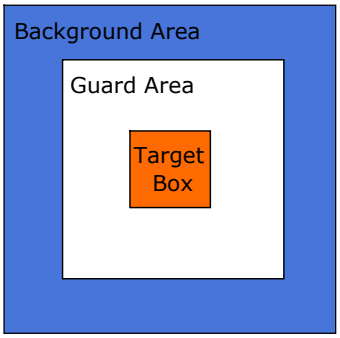

Fig. 2.7 Typical window used in adaptive threshold algorithms

T, can be obtained for a specified probability of false alarm (PFA) by solving analytically or numerically the equation:

$$PFA = \int_{T}^{\infty} f(x)\,\mathrm{d}x \tag{2.18}$$

with $f(x)$ being the model of the p.d.f. of the local background. Statistical distributions such as K, Weibull, and Log-normal are well-known for modelling reflectivity of the sea clutter for high-resolution SAR images [21, 42]. The performance of CFAR detection relies on the accuracy of the background model selected and the estimation of its parameters. However, a more complex approach could be done for a finer estimation of the p.d.f. of the clutter; for example, Gao [43] proposes a non-parametric method based on the iterative sum of weighted basic functions (or kernels). In this case, no analytical p.d.f. model of the clutter is assumed at the expenses of increasing computational burden.

Instead of working on the original SAR image, the performance of the CFAR detectors can be improved by preprocessing the image to emphasise the difference between the reflectivity of the targets and the background. For instance, Gambardella *et al.* [44, 45] obtain the coherent-to-incoherent received power ratio of the backscattered signal by evaluating the Rice factor with a sliding window over the whole SAR image; as a result, the pixels of the coherent targets (i.e. the vessels) are highlighted, aiding their differentiation from the clutter; they applied the CFAR approach by considering a log-normal distribution as the model of the clutter in the preprocessed image. Tello *et al.* [46, 47] exploit the preservation of irregularities (i.e. the edges) at multiple scales in each sub-band of the stationary wavelet transform (SWT) of the SAR image. These sub-bands are spatially multiplied, which increases the dynamic range between the pixels of the vessels and the sea clutter, making it easier to establish a single decision threshold for all the potential vessels in the whole image.

Besides the single-channel approach, other algorithms try to enhance the vessel detection by considering other sources of information such as polarimetric data or along-track multichannels. For instance, Ferrara *et al.* [48] compute the Rice factor over the cross-polar channel to improve the detection of metallic objects; Touzi *et al.* [49] use the Degree of Polarization (DoP) as a sensible indicator of the presence of vessels in the ocean in order to enhance the detection procedure; and Liu *et al.* [50] employ the likelihood ratio test and a multivariate Gaussian distribution for the quad-pol data of each pixel to approximate a decision variable by using mainly the covariance of the ocean samples. Moreover, Suchandt *et al.* [51] employ the along-track multichannel data to apply the Displace Phase Center Antenna (DPCA) technique in maritime images of TerraSAR-X, and obtain the coherent difference for the detection of moving targets. Notice that these techniques are not applicable to all the SAR sensors since they rely on specific configuration and capabilities of the SAR systems to provide the required data.

2.4.2 Vessel Classification techniques

The classification segment based on SAR images can be still considered an emerging technology, and it has not yet achieved the robustness of its detection counterpart. In fact, many works on this matter are focused mainly on the research and understanding of the best characteristics of the vessel signatures that could be exploited for their classification in different scenarios [34, 52]. In practice, this task presents several challenges. Vessels are complex targets from the scattering perspective, and their signatures are expected to change as a function of the angle of observation [34]. In addition, the dynamics of the vessels commonly introduce aberrations that may distort their SAR signature [22], complicating even further their analysis for real case scenarios.

The two most common features for the classification of vessels in radar imaging are: 1) the characteristic reflectivity of the targets, i.e. the *radar cross section selection* (RCS), and 2) the shape and dimensions of the SAR signatures associated with them [33]. A quick classification approach may take into account only the dimensions of the SAR signature to discriminate between general sizes of vessels [39, 40]; but methods that look for a more refined or robust classification may consider a feature vector containing the dimensions and sectional information of the distribution of the scatterers. For example, Margarit and Tabasco [53] employ the dimensions of the SAR signature along with the RCS of the bow, middle, and stern sections to form a feature vector; a similar approach is taken by Zhang *et al.* [54] using the dimensions of the vessels, but they analyses the expected distribution and densities of the scatterers to discriminate among larger vessels such as bulk carriers, oil tankers, and containers.

Similar to the detection process, the use of the polarimetric data aims to improve of the classification step by analysing the suitable feature parameters for the different SAR

signatures of the vessels. In recent publications, the trend is to focus on the application of the theory of target decomposition (either coherent or incoherent) and the analysis of permanent scatterers to define the features in the vessel classification [52, 55–57]. In this way, these methods aim to lessen the problem of the variation of the backscattering as a function of the observation angle.

The classification stage presents an additional problem: available ground-truth databases. Despite the complexity of the feature vector used for the classification, its construction has to be based on the analysed features of known targets. This is a major problem from the practical point of view for SAR imaging. The construction of a database with ground-truth data from acquisition campaigns with different types of vessels, positions, sea conditions, etcetera, is a challenge in itself. In this sense, the use of SAR simulators based on CAD models are a more convenient option [34, 58], being constrained only by the computational burden and the availability of the detailed CAD models for several entries in the data-base.

2.5 Summary

SAR is a mature and widespread technology employed in Earth observation. It provides unique capabilities in the acquisition of high-resolution images in any weather conditions and without the constraints of natural illumination; and in the case of spaceborne systems, their acquisition can be extended on a global scale.

The SAR images are obtained by side-looking radars that transmit and receive echoes of the EM pulses from the illuminated areas as the radar moves. The pulse compression technique is used in the range direction to achieve high resolution, which is inversely proportional to the bandwidth of the transmitted signal (usually a chirp). In azimuth, the high resolution is obtained by synthesizing a large antenna aperture from the coherent processing of the received echoes. In the case of the traditional stripmap mode, the azimuth resolution is independent from the range and proportional to one-half of the length (in azimuth) of the antenna.

Geometrical distortions in the slant-range plane are inherent to SAR imaging. Since the system is based on radar, the range position of the target in the 2D reflectivity map represents the distance radar-to-target in the line of sight. As a consequence, effects of foreshortening, layover, and shadowing occur in SAR images. In addition, other effects may be observable in azimuth direction for unexpected motions of the target. The dynamics of the target may introduce azimuth shifts and blurring artefacts, the latter being critical in the deterioration of the quality of the target's image.

Due to the advantages of the spaceborne SAR technique and the high-resolution imaging capabilities of current systems, their application to vessel monitoring has been an intensive area of research in the recent years. SAR imaging is intended to be used as a complementary technique for traditional vessel monitoring systems such as the AIS or the VMS. The analysis

of the images can potentially act as an additional source of information for data correlation, providing support in highlighting abnormal activity.

The extraction of relevant information about the vessels from the images involves steps of detection and classification of the candidates. In the former detection, state-of-the-art techniques have reported a great refinement and robustness, which translates to low false-alarm rates. However, in the classification step, the complexity of the SAR signatures of the vessels, and their large variety, make the classification analysis an intricate task. Few techniques in recent literature have addressed the classification of vessels; and although the reported results are encouraging, they are still far from the achieved robustness of the detection counterpart.

Chapter 3

Simulation and Vessel Detection tools

3.1 Introduction

Assessing the performance of new SAR processing algorithms requires SAR data from a diverse range of testing cases. Even though it is always desirable to use real data, it is common to have constraints such as the period of the acquisitions, the available content and control of the ground truth, or budget. In this sense, SAR simulators may assist in generating SAR raw data in a controllable framework.

It is advantageous that SAR simulators be accurate and allow flexibility in setting up the characteristics of the sensor and the scene. Current SAR simulation techniques are focused on different aspects of the SAR system other than its accuracy. For instance, the techniques in [59] and [60] are focused on the efficiency of the simulation, but they have the constraint of using known reflectivity maps of the targets known *a priori*. Other techniques give more flexibility in the control of the scene by allowing 3D models of simple targets [61] and complex ones [34],[62]. For the current project, a SAR simulator with this flexibility is used: GRECOSAR, developed and used in previous research on vessel SAR signatures [34, 53, 55]. By using 3D CAD models and the electromagnetic solver GRECO® , it is able to generate SAR raw data of virtually any spaceborne SAR sensor, and in this way, a realistic SAR signature of the target can be obtained.

When using real stripmap data of maritime scenes, the vessels have to first be detected on the SAR image in order to extract or analyse its signature. The SAR images may cover several kilometres of sea surface and the usage of vessel detection algorithms is a common practice to facilitate the task of spotting the most likely vessel candidates. Most of them employ adaptive threshold techniques with Constant False Alarm Rate (CFAR) to detect objects that present reflectivity with different statistical properties than the sea clutter [21]. In our case, the vessel detection tool employed in the current project follows the CFAR

approach but it is based on wavelet transform (WT) theory to improve the robustness of the detection [46].

In the following sections, an overview of the GRECOSAR simulator is presented, focusing mainly on the updates implemented whilst carrying out the current research work. Then, a description of the WT-based vessel detection algorithm and tool are provided.

3.2 GRECOSAR: a SAR simulation tool

The GRECOSAR simulator was developed in 2006 in the frame of the European Project IMPAST [34]. It was conceived as a tool to simulate the raw data of complex targets such as vessels, making it a suitable option to provide ground-truth that is hardly ever possible to get in maritime scenes. In this section, a brief description of the simulation process is presented, followed by the description of the target modelling, the updates made to GRECOSAR throughout this thesis, and finally some examples of SAR signatures using simulated raw data.

3.2.1 An overview of the GRECOSAR simulator

The Graphical Electromagnetic Computation SAR (GRECOSAR) simulator is a numerical tool developed at the Remote Sensing Laboratory of the Universitat Politècnica de Catalunya (UPC). It is able to generate polarimetric and interferometric stripmap raw data (e.g. POLSAR, POLinSAR), and images of complex targets for a wide range of scenarios with, virtually, any SAR sensor.

GRECOSAR was mainly conceived as a tool for the study of individual SAR signatures of vessels in typical conditions on the sea surface [28]. In this sense, it has features that can be used to simulate this type of environment in a reduced area. Translational and rotational movements can be considered for the simulation of a given target, and the use of a modulated plane as the sea surface aims at emulating a more realistic scenario. Thanks to these characteristics, GRECOSAR has been used as the test-bed for the analysis of the scattering phenomenon of SAR vessel signatures [34, 53, 55].

The processes of the GRECOSAR tool can be summarized in five modules [28]:

- **Scenario characterization**: The set-up parameters of the simulation (e.g. radar, satellite, and target model parameters) are used to compute the chirp signal, the orbital positions, and the observation time of the SAR sensor. Here, the motion of the target is taken into account in order to modify the perspective of the sensor and emulate the target's rotations.

- **Electromagnetic Simulation**: GRECO® software computes in real time the mono-static radar cross section (RCS) of the three-dimensional CAD model of the target.

GRECO® employs high-frequency approximations such as physical optics (PO), the method of equivalent currents (MEC), the physical theory of diffraction (PTD), and the impedance boundary condition (IBC) technique [63]. The electromagnetic simulations take into account the radar parameters for the emulation of the chirp signal, while the defined view angles are used to obtain correct perspective of the sensor in relation to the target.

- **Raw data generation**: The propagation phase term and the range cell migration (RCM) time shift are included in the azimuth direction of the magnitude-normalized output data of the EM solver GRECO®. Here, the antenna footprint is simulated by multiplying the final raw data by a *sinc* function in the azimuth direction.
- **SAR processing**: a SAR processor based on the Extended Chirp Scaling Algorithm (ECSA) [64], developed at the UPC, is used as the embedded application to obtain the SAR image.
- **Post-processing**: In-built tools allows the use of image interferometry and coherent target decomposition (CTD) analysis.

Figure 3.1 shows a block diagram of the simulation process. The blue boxes indicate the input parameters when setting up the simulation and that are used to calculate the orbital position of the platform, the antenna pointing and synthetic aperture length ("satellite parameters"), the chirp parameters ("radar parameters"), the geometrical structure of the target in a GRECO-compatible format ("target model file"), and environment-related information ("target environment") such as the target's movements, its position within the swath and the sea state. The outputs of the GRECOSAR simulation are the green boxes in the diagram. For further details about GRECOSAR, reference [28] gives the complete description of the simulation processes and implementation.

3.2.2 Target Modelling

One advantage that the GRECOSAR simulator offers is that allows the use of targets with complex structures. In theory, the SAR signature of any target can be simulated because GRECO® employs 3D Computer-Aided Design (CAD) model as the input for the EM simulation [63]. These CAD models can be defined based on facets or parametric surfaces and different formats are compatible with GRECO® such as Initial Graphics Exchange Specification (IGES), I-DEAS from UGS corporation, FAM, MicroStation packages, and GiD® from the International Center for Numerical Methods in Engineering (CIMNE) at the UPC. However, it has been observed that for the simulation of vessels, the latter format is preferable due to the assumptions made in GRECOSAR's implementation when considering the addition of sea surface plane. Figure 3.2 shows examples of 3D models of different vessels obtained via GiD®.

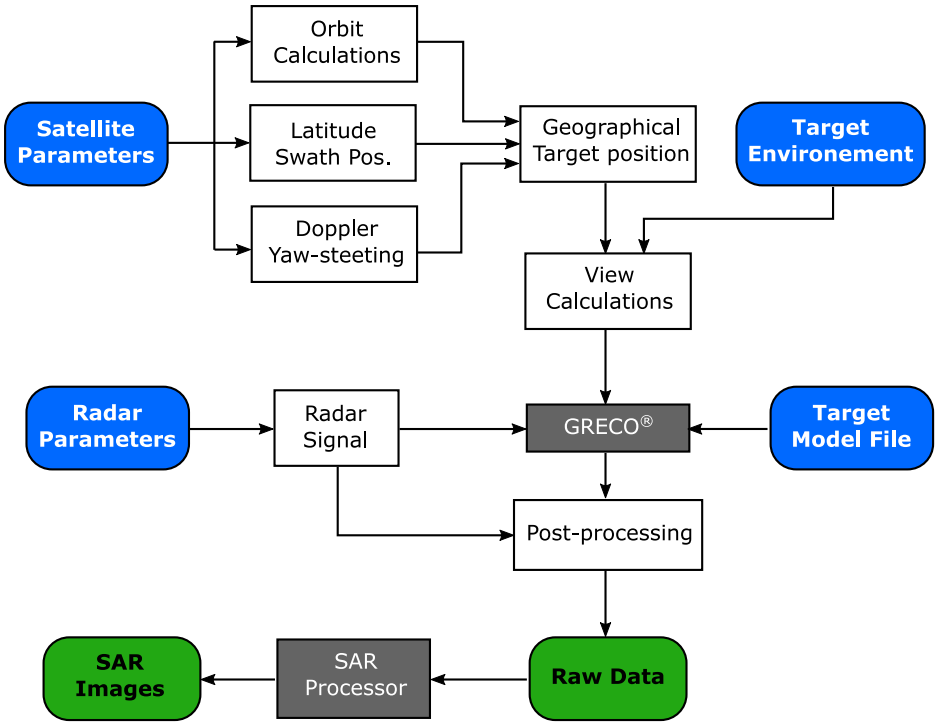

Fig. 3.1 Block diagram of SAR simulation in GRECOSAR. The blue blocks indicate the inputs, while the green ones highlight the outputs. Source [28]

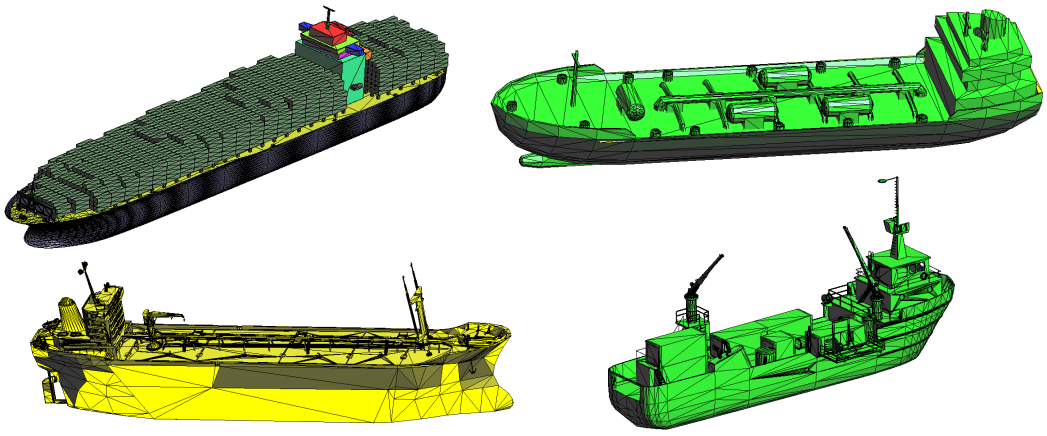

Fig. 3.2 Examples of 3D CAD models of different vessels obtained via GiD®.

The target modelling input has a direct impact on the quality of SAR images in GRECOSAR. The more details in the CAD model, the closer the simulated data is to the real raw data. Additionally, the model parameters for the rendering process (e.g. pixel size considered) of the EM solver may influence the RCS computations if they are loosely set up. GRECO renders the visible surfaces of the CAD model into a bitmap to boost the speed of the EM calculations. Thus, the rendering errors have less influence if the selected pixel size is small. For instance, reference [28] recommends a pixel size of 0.01[m] to make the rending error negligible. However, all of these conditions regarding the details in the CAD model and the rendering parameters increase the computational burden for the simulation, imposing a trade-off between the accuracy of the approximation of the computed RCS and the time required to do it.

3.2.3 Improvements in the SAR simulator

Its flexibility to simulate different spacebone SAR sensors and virtually any target makes GRECOSAR a suitable tool in the study of algorithms related to the processing of vessel signatures. Nevertheless, this numerical tool can still be enhanced in order to get a better performance. Throughout this thesis, improvements to the original version of GRECOSAR have been made. They mainly aimed to reduce the computational burden and improve of the modelling of maritime scenarios so that they are closer to the real cases. In the following sections, the three main improvements are discussed: improving the azimuth interpolation process, the implementation of a multi-harmonic model of the sea surface, and the modification of the antenna pointing for stripmap simulations.

The azimuth interpolation process

In SAR systems, the selection of the PRF of the sensor is based on the length of the swath required and the bandwidth of the azimuth signal in order to fulfil the Nyquist condition for a given resolution [24]. If a real SAR system is emulated in GRECOSAR, this PRF determines the number of the platform's positions that are required for the simulation of the synthetic aperture. In theory, GRECOSAR would need to perform the EM computation of the RCS of the model at each point of the synthetic aperture to obtain the raw data, which implies a considerable computational burden when using detailed and complex targets. However, in practice, the synthesis of the raw data usually employs interpolation from only some of the simulated positions. In fact, a down sampling factor of 16 for the number of positions is suggested in [28] as the results of testing canonical and complex targets. In this way, a fewer number of simulated positions reduces greatly the computational load and the simulation time. For stripmap mode, an arbitrary reduction of the simulated positions may lead to the aliasing of the azimuth signal for large targets. In this sense, it is necessary to establish a limit for the minimum number of simulated positions.

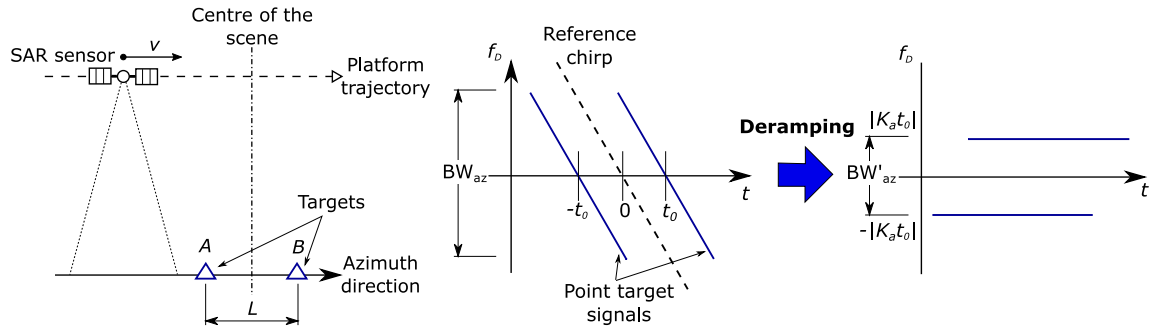

Fig. 3.3 (a) Example of the deramping process: Frequency-time azimuth signal of two centred point targets before and after deramping. (b) Basic diagram of a SAR acquisition of a scene of length L in azimuth direction.

The minimum number of azimuth positions during the aperture time for the simulation of stripmap mode is calculated based on the length of the target/scene in the azimuth direction and the ideal point-target conditions. First, a closer look at the process of synthesizing the raw data in the azimuth direction reveals that the set of EM computations from GRECO forms a de-ramped signal in azimuth. This makes the Doppler bandwidth lower than the PRF used for the stripmap set-up. For illustration, Figure 3.3b depicts a diagram of the differences in bandwidth between the azimuth signal with and without de-ramping. Now, the Doppler bandwidth of a deramped signal of a target of length L can be used to define the minimum number of positions. Considering a scene of two ideal point targets placed symmetrically with respect to the centre (Figure 3.3a), the azimuth signal of the target A, $s(t)_A$, and the centred reference signal, $s(t)_{ref}$, can be expressed as:

$$s(t)_A = e^{j\pi K_a (t+t_0)^2} \tag{3.1}$$

$$s(t)_{ref} = e^{j\pi K_a t^2} \tag{3.2}$$

where K_a represents the Doppler rate. Then, the deramped azimuth signal, $s(t)_{deramp}$, results in:

$$s(t)_{deramp} = e^{j\phi_A(t)} = s(t)_A \cdot s^*(t)_{ref} = e^{j\pi K_a \left[(t+t_0)^2 - t^2\right]} \tag{3.3}$$

and the instant Doppler frequency as

$$f_{D,A} = \frac{1}{2\pi}\frac{\mathrm{d}\phi_A(t)}{\mathrm{d}t} = K_a t_0 \tag{3.4}$$

Following a similar process for target B, its instant Doppler frequency results in:

$$f_{D,B} = \frac{1}{2\pi}\frac{\mathrm{d}\phi_B(t)}{\mathrm{d}t} = -K_a t_0 \tag{3.5}$$

Then, the bandwidth of the deramped signal is reduced to:

$$\Delta f_{deramp} = |K_a \cdot 2t_0| = |K_a t_{length}| = \left|K_a \frac{L}{v}\right| \tag{3.6}$$

with L as the distance between the point scatterers A and B in the azimuth direction, and v as the speed (on ground) of the platform. To accomplish the Nyquist condition, the deramped signal should be sampled at such a rate, PRF_{deramp}, that $PRF_{deramp} > \Delta f_{deramp}$. The interpolation factor is defined in GRECOSAR as the ratio of the number of positions of the synthetic aperture to the number of simulated positions. Thus, by considering the minimum number of these positions for the simulation (in the ideal case), the interpolation factor comes out as a function of the length of the scene/target :

$$F_{interp} < \frac{PRF}{PRF_{deramp}}, \qquad \text{with} \quad PRF_{deramp} > \left|K_a \frac{L}{v}\right| \tag{3.7}$$

The interpolation condition of equation (3.7) assumes ideal point target scatterers. In practice, the simulated targets may differ from this scattering behaviour, and a lower interpolation factor should be used to obtain a SAR signature of the target closer to that expected in real data. In this way, possible variations in the reflectivity of the targets along the aperture would not be omitted. Thus, equation (3.7) can be seen as an upper limit to be aware of when setting up the interpolation parameters for the simulation of a target of certain length.

An additional improvement to the interpolation process itself was also implemented for the GRECOSAR simulator. Rather than the polynomial interpolation methods that are usually applied, the *sinc* interpolation approach would suit better when the number of simulated positions in the aperture are closer to the theoretical minimum from equation (3.7). Its implementation was motivated by the fact that the signal can be perfectly reconstructed as long as the Nyquist condition is fulfilled. The *sinc* interpolation is commonly implemented as a convolution of the discrete signal $g_d(i)$ with a kernel $h(x)$ [24]:

$$g(x) = \sum_i g_d(i) h(x - i) \tag{3.8}$$

$$h(x) = \mathrm{sinc}(x) = \frac{\sin(\pi x)}{\pi x} \tag{3.9}$$

where x is a continuous independent variable, i is an integer and represents the sample number, and $g(x)$ represents the original signal such that $g_d(i) = g(x)$ when $x = i$. In this way, the interpolation point x is a weighted average of samples of $g_d(i)$ within the kernel. In

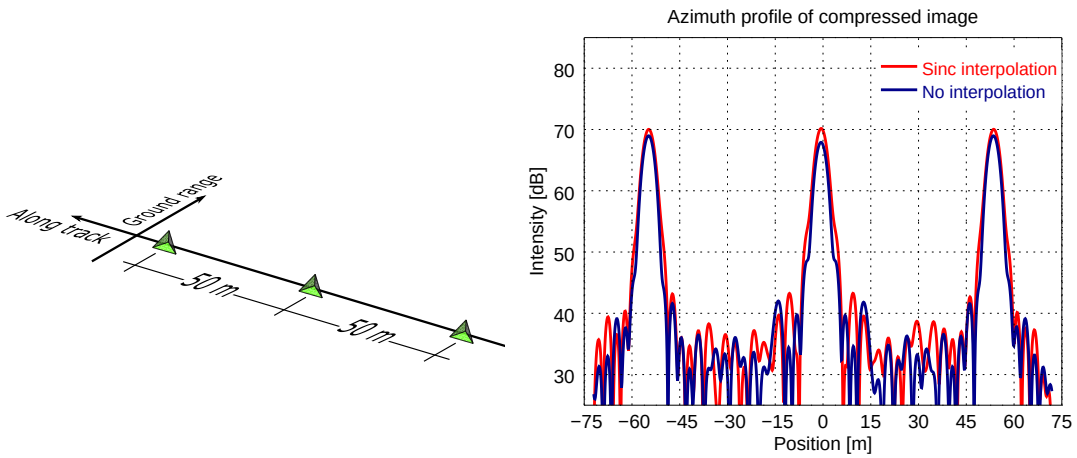

(a) (b)

Fig. 3.4 (a) Diagram of the corner reflectors array. (b) Azimuth profile of SAR image of corner reflector array with and without sinc interpolation

practice, this kernel is normalized to unify its gain and weighted by a tapering window, such as the Kaiser window, to reduce the Gibb's phenomenon ("ringing") [24]. Additionally, it is usually generated at the required subsample intervals and stored in a table, thus avoiding its computation every time at each interpolation point.

For the GRECOSAR simulator, an 8-point sinc kernel was implemented and adapted as an additional option for the current interpolation methods that can be used for the simulations. For previous interpolation methods, GRECOSAR always computes the first, middle and last position of the platform for the synthetic aperture for any interpolation factor. However, the sinc interpolation, as implemented, required regular sampling and extra samples at both ends of the azimuth signal, which imposed modifications to the regular process of selection of the simulated synthetic aperture positions. The extra samples (i.e. extra positions of the set of the original aperture) are only used to ensure that the azimuth signal is reconstructed in the length of the synthetic aperture. After the interpolation is done, these samples are not taken into account for the construction of the raw data.

The implemented sinc interpolation was validated by the simulation of an array of three corner reflectors aligned in azimuth (Figure 3.4a) with a generic X-band SAR sensor. By using twice the amount of the simulated positions as the theoretical minimum for the interpolation, the simulation of 1943 positions of the synthetic aperture was decreased to 129, reducing considerably the computational burden. Figure 3.4b shows the aligned azimuth profiles of the final SAR image of the corner array with and without interpolation. The interpolated profile presented a shift of one sample that was compensated to compare both of the responses in the plot.

Multi-harmonic model of the sea surface

GRECOSAR has already been used in the research of vessel classification techniques using different 3D ship models and a simple two-harmonic modulated surface as the sea [28, 34, 55, 56, 65]. This simplified model of the sea surface provides SAR images with sea clutter whose amplitude statistics follows a Rayleigh distribution [56]. However, literature suggests that, in general, SAR images of the sea present clutter with statistics closer to the K, Weibull or Log-normal distributions [42]. For this reason, the improvement of the sea surface model in order to provide more realistic maritime scenes with clutter statistics closer to what is expected in real SAR images was of particular interest.

The new model implemented for the sea surface elevation is based on the linear wave theory approach followed in ship motion control and suggested for real-time simulation of ocean dynamics [66]. From the hydrodynamic description of a fluid motion, and considering a travelling wave and infinite depth, the elevation of a regular wave (i.e. a harmonic component) is expressed as [67]:

$$\zeta(x, y, t) = \bar{\zeta} \sin\left(\omega t + \phi_0 - k\left(x \cos\chi + y \sin\chi\right)\right) \tag{3.10}$$

where x and y are the Cartesian coordinates on the horizontal plane, $\bar{\zeta}$ is the amplitude of the wave, t is the time, ϕ_0 is an initial phase, k is the wave number, ω is the circular wave frequency (related to the wave period T_1 by $\omega = \frac{2\pi}{T_1}$), and χ is the angle between the wave course and the positive axis x. Due to the random nature of ocean waves, elevation $\zeta(x, y, t)$ at a certain point (x, y) is considered a stochastic process. Moreover, this process is usually assumed to be stationary, homogeneous zero mean Gaussian, and characterized by the Power Spectral Density (PSD) $S_{\zeta\zeta}(\omega)$, describing how the energy of the sea surface is distributed in the frequency domain. For the model implemented in GRECOSAR, the PSD adopted was the International Towing Tank Conference (ITTC) spectrum formulation for fully developed seas with no swell (a.k.a. the modified Pierson-Moskowitz spectrum), which is one of the standard models for the sea spectrum [67]. For a gravity acceleration of $9.81\frac{m}{s^2}$, this spectrum is defined as:

$$S_{\zeta\zeta}(\omega) = \frac{A}{\omega^5} e^{-\frac{B}{\omega^4}} \tag{3.11}$$

$$A = \frac{173 h_s^2}{T_1^4}, \quad B = \frac{691}{T_1^4} \tag{3.12}$$

with h_s as the significant wave height, and T_1 as the average wave period. In general, it can be considered that in the usual case of the sea surface the waves propagate in different directions with one dominant direction. Hence, the PSD is expanded into a function of the

frequency ω and the direction angle χ, and it is usually represented as a product of two functions:

$$S_{\zeta\zeta}(\omega,\chi) = S_{\zeta\zeta}(\omega)M(\chi) \tag{3.13}$$

$$M(\chi) = \begin{cases} \frac{2^{2\alpha-1}\alpha!(\alpha-1)}{\pi(2\alpha-1)!}\cos^{2\alpha}(\chi-\chi_0), & |\chi-\chi_0| < \frac{\pi}{2} \\ 0 & \text{otherwise} \end{cases} \tag{3.14}$$

where χ_0 is the dominant wave propagation direction, $M(\chi)$ is a spreading function, and α a shape parameter with typical values of $\alpha = 1, 2$. Based on the assumption that elevation is a stationary process, the sea surface elevation at a point (x, y) can be represented as a sum of regular waves of different amplitudes for short-crested seas as [67]:

$$\zeta(x,y,t) = \sum_{n=1}^{N}\sum_{m=1}^{M} \bar{\zeta}_{n,m}\sin(\tilde{\omega}t + \phi_{n,m} - k_n(x\cos\chi_m + y\sin\chi_m)) \tag{3.15}$$

$$\bar{\zeta}_{n,m} = \sqrt{2S_{\zeta\zeta}(\tilde{\omega},\tilde{\chi})\,\Delta\omega\Delta\chi} \tag{3.16}$$

where N is the number of harmonics, M is number of directions of propagation, and $\tilde{\omega}$ and $\tilde{\chi}$ are values taken randomly in each of the intervals $\left[\omega_n - \frac{\Delta\omega}{2}, \omega_n + \frac{\Delta\omega}{2}\right]$ and $\left[\chi_n - \frac{\Delta\chi}{2}, \chi_n + \frac{\Delta\chi}{2}\right]$, respectively; $\Delta\chi$ represents the regular angular difference between the consecutive direction of the propagation of the waves, and $\Delta\omega$ is the frequency separation between consecutive harmonics. The derivation of equation (3.16) in reference [67] assumes that both $\Delta\omega$ and $\Delta\chi$ are small in comparison to the range of the significant values of $S_{\zeta\zeta}(\omega,\chi)$. In the case of the implementation of the modulated sea surface in GRECOSAR, it has been observed that values of $N > 20$ and $M > 10$ result in $\Delta\omega$ and $\Delta\chi$ small enough to fulfil the assumptions in [67] and to produce a more realistic sea surface model than the one used in previous versions of GRECOSAR. Figure 3.5 depicts an example of the ITTC spectrum for a moderate sea state and the respective 3D elevation model of the 200×200 [m] surface. Notice that the elevation ζ is also a function of the time t (equation(3.15)). This dependence was considered while the model was implemented in the GRECOSAR simulator. In this way, the sea surface elevation is dynamic and generated according to aperture time in turn.

For simulated sensors in C- and X-band, the multi-harmonic model has shown clutter that is similar to K and Weibull distributions [68], which are typical models used as good descriptors of the statistics of the clutter in real maritime SAR images of high resolution. For an X-band sensor with similar parameters to TerraSAR-X, Figure 3.6 shows an example of the SLC image of a simulated 200×200 [m] multi-harmonic sea surface and the Probability-Probability (PP) plot to compare the amplitude of the clutter against the K and Weibull distributions. In the plot, both distribution models are closer to the straight line (the

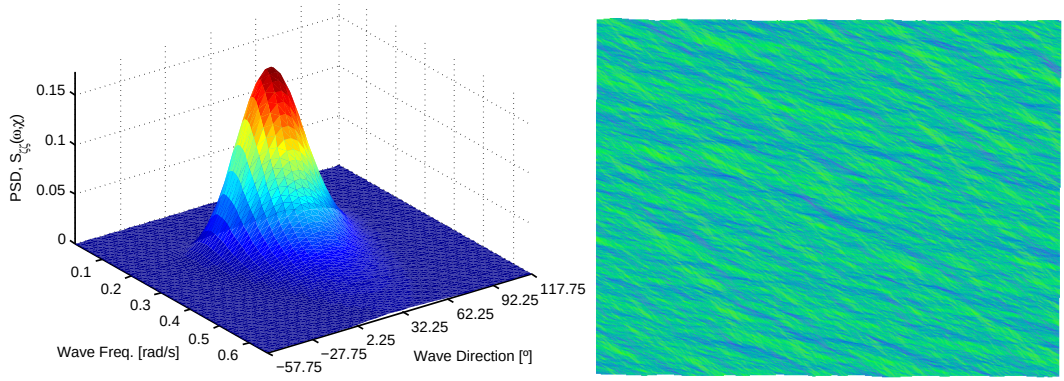

(a) (b)

Fig. 3.5 Example of the multi-harmonic model of a sea surface with moderate sea state: (a) profile of the ITTC spectrum ($h_s = 2.28$ [m] and $T_1 = 4.5$ [s]). (b) image of the 3D model elevation model.

reference), which is a qualitative indicator that the models can be used to described the amplitude of the simulated clutter.

Antenna pointing

A well known characteristic of stripmap raw data is that the envelop of the Doppler spectrum of the signal is directly related to the antenna pattern of the SAR sensor [24]. The original version of GRECOSAR employs this relationship to introduce the antenna pattern into the simulations. While synthesizing the raw data, the same Doppler centroid frequency was assumed for the whole simulated scene, applying the envelop of the antenna pattern to the Doppler spectrum of the signal. This approach implied the omission of modifications in the shape of the spectrum due to scatterers with different Doppler centroid frequencies. In the cases of structures with rotational motion, it is likely that the scatterers present shifts of their Doppler spectrum according to their range motion [22], resulting in a more complex envelop of the Doppler spectrum.

Instead of implementing the antenna pattern in Doppler domain, a different approach can be considered for a more realistic simulation by applying it in time domain for each of the simulated positions of the synthetic aperture. This new approach was implemented in GRECOSAR thanks to latest feature of the recent release of GRECO® v11.2 that allows antenna pointing. In this way, GRECOSAR emulates closely the antenna's beam-sweep in stripmap acquisitions. For the scope of the current project, the new approach of implementing the antenna pattern in time domain required modifications in the processes related only to the single-pass simulation acquisition. Specifically, the sensor orbit computations, the interpolation, and the target's motion process were updated and validated. Figure 3.7 shows an example of the geometry of the antenna pointing in GRECOSAR simulation near to

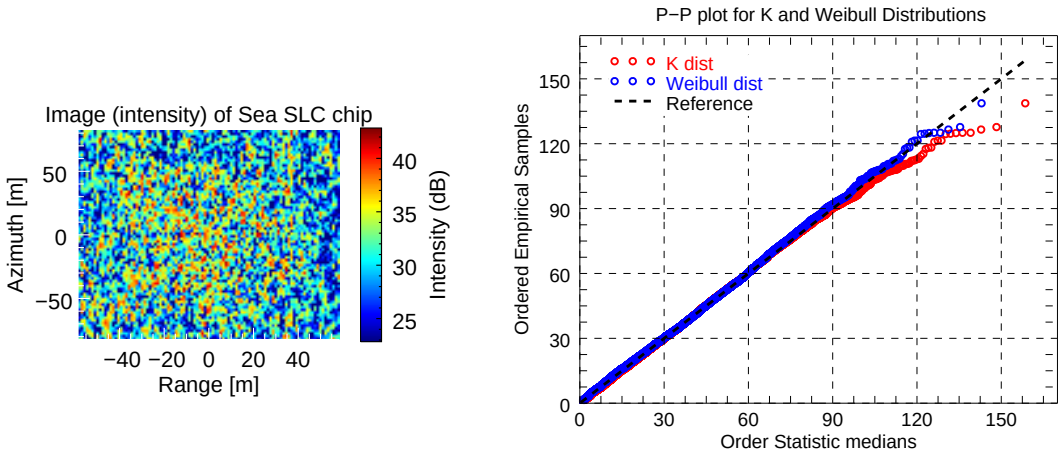

(a) (b)

Fig. 3.6 Example of the simulation of the multi-harmonic model of a sea surface in GRECOSAR for a generic X-band sensor: (a) cropped SAR image of the simulated sea clutter. (b) Probability-Probability plots using K and Weibull distributions

the target; there, the line represents the path of the beam-sweep and the dots mark the location of the centre of the beam for each simulated position of the aperture. Additionally, an example of the behaviour of the signal in the Doppler domain is shown in Figure 3.8 by using the new time-based implementation of the antenna pattern. First, Figure 3.8a shows the Doppler spectrum of a corner reflector whose envelop follows the radiation pattern of the antenna as expected in real SAR data. Figure 3.8b shows the individual Doppler spectra from the simulation of two moving corner reflectors with enough separation in ground-range direction to minimize interferences between their backsignals. They were simulated with rotational motion with respect to a symmetry axis in the middle of the scene to induce opposite direction for their range velocities. As a consequence, their spectra are shifted in opposite directions. The most remarkable feature is that the envelop of each spectrum follows the antenna radiation pattern as one could expect in real SAR data of structures with the same motion.

3.2.4 Examples of simulations with GRECOSAR

A couple of examples of maritime scenarios simulated in GRECOSAR are shown for an X-band sensor with similar parameters to TerraSAR-X (Table 3.1). First, Figure 3.9a depicts the 3D model of a cargo ship with the multi-harmonic sea surface model as seen by the sensor in the middle of the simulated aperture for the stripmap mode. No motion of the vessel was considered; only the elevation of the sea surface was updated in each of the simulated aperture positions according to its model (equation (3.15)). The SAR image from the simulated stripmap raw data (HH-channel) for this scenario is shown in Figure 3.9b.

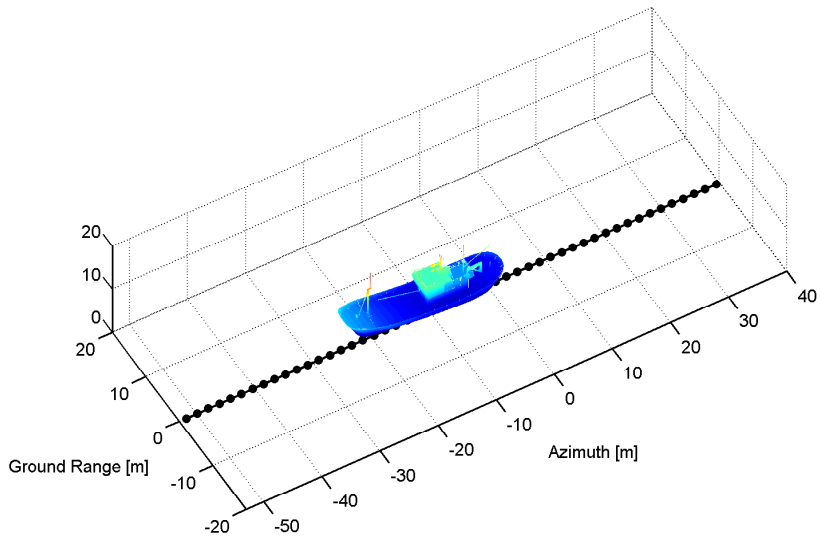

Fig. 3.7 Example of the antenna pointing feature in GRECOSAR simulations near to the target. Each dot represents the location of the centre of the beam for the simulated aperture position

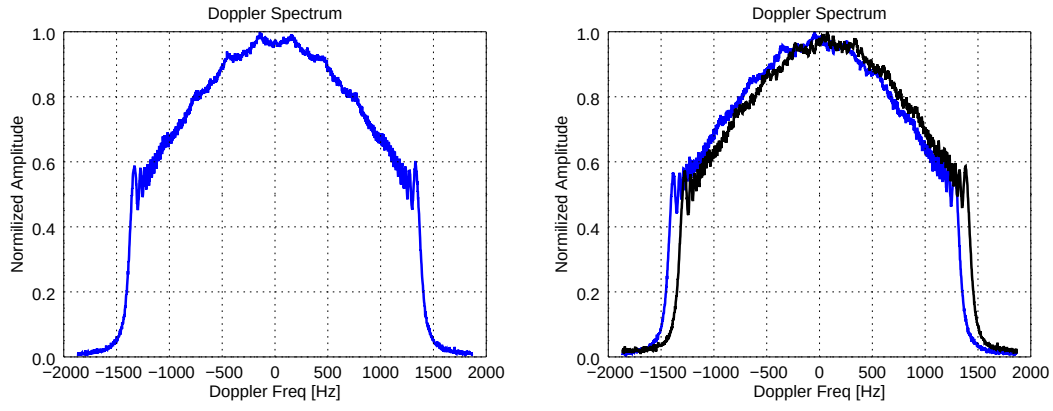

(a) (b)

Fig. 3.8 Doppler spectrum of range-compressed data of two corner reflectors using the antenna pointing feature in GRECOSAR simulation of a generic X-band SAR sensor: (a) Spectrum of the static corner reflector. (b) Isolated spectrum of each of the two corner reflectors simulated with opposite range velocities in the same scene.

Table 3.1 Parameters of the X-band SAR sensor for the GRECOSAR simulation of stripmap raw data of maritime scenes.

SAR Sensor Parameters	**Value**	
Pulse duration (τ)	28×10^{-6}	[s]
Sampling Frequency	128×10^{6}	[Hz]
Chirp bandwidth	116×10^{6}	[Hz]
Carrier frequency	9.65×10^{9}	[Hz]
PRF	3736	[Hz]
Doppler Rate	-5370.18	[Hz/s]
Incidence angle	40	[°]
Reference distance	654174.71	[m]
Antenna length	5.1	[m]
Nominal speed of the platform	7686.12	[m/s]
Range resolution	1.3	[m]
Azimuth resolution	2.55	[m]

Similarly, Figure 3.10 shows another example of the 3D model and the final SAR image of a maritime scene with a smaller vessel. In both examples, the main scatterers that belong to the vessel can be identified; in addition, other artefacts (e.g. high reflectivity pixels around the SAR signature of the vessel) are likely related to the multiple reflections of the EM signal due to the interaction between the vessel's structure and the sea surface.

3.3 Wavelet-transform based detection algorithm and tool

Vessel detection algorithms usually rely on the differences in the statistical reflectivity of man-made objects and the sea clutter. One of the most popular techniques reported in the literature is the Constant False Alarm Rate (CFAR) based detector [21]. By assuming a model of the sea clutter, the idea is to maintain a constant false alarm detection rate by establishing a reflectivity threshold in order to differentiate pixels of possible vessels from those ones of the sea clutter. The best results are obtained when the reflectivity statistics of the clutter and the vessels are clearly separated.

Different preprocessing techniques can be applied to the SAR image to extend the gap between the statistical behaviour of the two categories of pixels (i.e. target/clutter). Examples of this preprocessing of the images are: the combination of available polarimetric information [48, 69], the local evaluation of coherent-to-incoherent intensity pixel ratio [44, 45], along-track interferometry techniques (assuming vessels in motion) [51, 70], and Wavelet Transform analysis [46]. In the current research work, this last technique forms the basis of the detection tool employed to spot the vessels in the real SAR images. The Wavelet Transform (WT) based technique has been successfully applied in vessel and coastline detection on maritime SAR images with a robust performance [46, 47], and in the GMV's ship detection algorithm

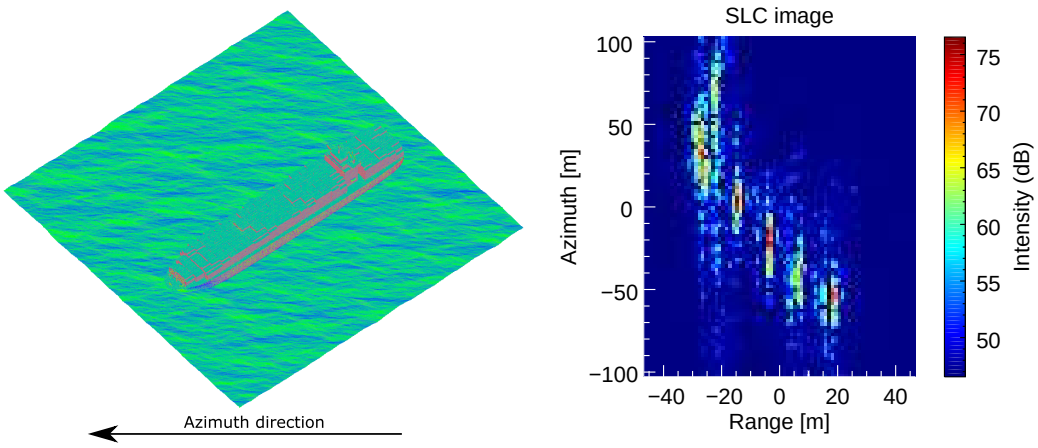

(a) (b)

Fig. 3.9 Example of simulated raw data of a maritime scenario of a cargo ship for an X-band sensor: (a) Orientation of the 3D model of a cargo ship ($\sim 163[m]$ length) with the multi-harmonic sea surface model as view from the sensor. (b) SLC SAR image from the simulated stripmap raw data (HH-channel)

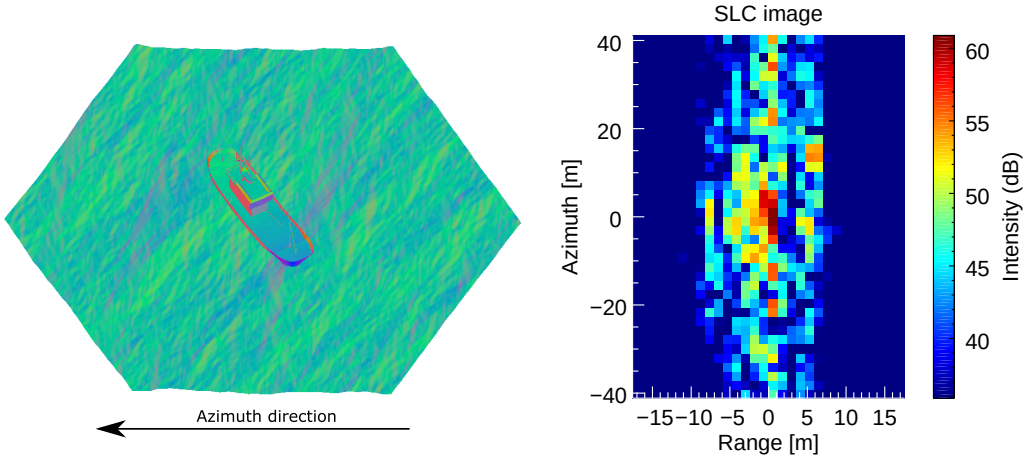

(a) (b)

Fig. 3.10 Example of simulated raw data of a maritime scenario of a fishing ship for an X-band sensor: (a) Orientation of the 3D model of a fishing ship ($\sim 28[m]$ length) with the multi-harmonic sea surface model as view from the sensor. (b) SLC SAR image from the simulated stripmap raw data (HH-channel)

deployed in the operational SIMONS service [53]. In the following section, a brief description of this WT-based detection algorithm is presented.

3.3.1 Brief description of the WT-based detection algorithm

This detection algorithm is inspired by the multiscale operation of human vision in perceiving features in an image. It uses Wavelet Transform as the tool for the multiresolution (i.e. multiscale) analysis of the spatial and frequency characteristics of the SAR images [46].

In the simplest case of a one-dimensional signal, the WT can be seen as a decomposition of a function $f(t)$ in terms of basic functions or atoms, $\psi_{j,k}(t)$, localized in both time and frequency,

$$Wf(j,k) = \int_{-\infty}^{+\infty} f(t)\psi^*_{j,k}(t)\mathrm{d}t \tag{3.17}$$

where $\psi_{j,k}(t)$ comes from dilation and translation of a "mother wavelet" $\psi(t)$:

$$\psi_{j,k}(t) = \alpha^{-j/2}\psi(\alpha^{-j}t - k) \tag{3.18}$$

with α^j as the scale parameter, k as the translation parameter, and $\psi(t)$ a finite energy function that generates an orthogonal basis. Then. In practice, it is commonly used as $\alpha^j = 2^j$ to simplify computational implementations [71]. Now, for a complete representation of the original signal, a *scaling function*, $\phi(t)$, which is an aggregation of wavelets at scales larger than 1, is used for signal approximation. The selection of both functions $\psi(t)$ and $\phi(t)$ is not trivial, and details regarding this task (along with a complete description of the wavelet theory) can be found in [71]. For the scope of the current description of the detection algorithm is enough to concentrate on the final implications from the signal processing perspective once the functions $\psi(t)$ and $\phi(t)$ have been defined.

The multiresolution decomposition of a discrete signal can be assimilated as a filtering process by using quadrature mirror filters. They are obtained by the inner product of $\psi(t)$ and $\phi(t)$ as [72, 73]

$$h[n] = \frac{1}{\sqrt{2}}\left\langle \phi\left(\frac{t}{2}\right), \phi(t-n)\right\rangle \tag{3.19}$$

$$g[n] = \frac{1}{\sqrt{2}}\left\langle \psi\left(\frac{t}{2}\right), \phi(t-n)\right\rangle \tag{3.20}$$

$h[n]$ being a low-pass filter, and $g[n]$ a band-pass filter. Then, the wavelet decomposition can be expressed as [73]

$$A_j[n] = \sum_k h[k-2n]A_{j-1}[k] \tag{3.21}$$

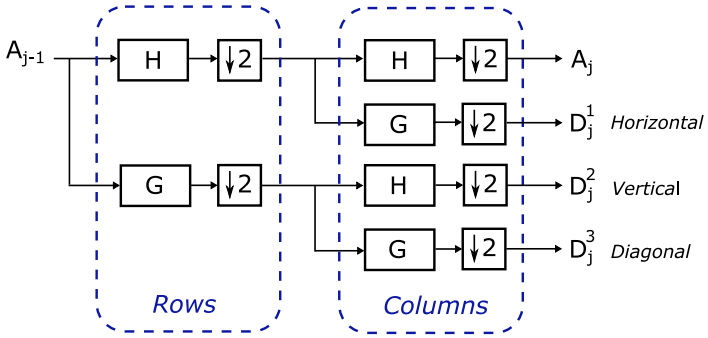

Fig. 3.11 Schematic diagram of separable filter banks for the DWT of a 2D signal

$$D_j[n] = \sum_k g[k-2n] A_{j-1}[k] \tag{3.22}$$

where A_j and D_j are the low and high frequency approximations at resolution j, respectively, of an original signal $A_0[k]$. Thus, the filters can be implemented in a cascade manner to compute the wavelet representation of the signal for a certain resolution level j. For the case of two-dimensional (2D) signals (e.g. images), the wavelet decomposition is usually expanded by applying the filtering process independently to each dimension, first in the vertical direction and then in the horizontal one. The result is a division of the original 2D signal into four sub-bands: Low-Low, Low-High, High-Low, and High-High. The first sub-band is a low resolution version of the input 2D signal, while the others contain the information about the horizontal, vertical, and diagonal details, respectively. Figure 3.11 shows a diagram of this Discrete Wavelet Transfrom (DWT) as it is commonly applied to 2D signals.

The detection algorithms uses, however, a variation of the standard DWT: the Stationary Wavelet Transform (SWT). The basic idea of the SWT is to apply the classical DWT without the subsampling (Figure 3.12). The filters are modified by inserting $2^j - 1$ zeros between each of their original taps at each level j [74]. Thus, the components of the transformation have the same dimensions as the input 2D signal. The SWT transform still preserves the benefits of the multiresolution analysis: irregularities (edges) are sharpened in the direction of each sub-band (i.e. vertical, horizontal, and diagonal), and most local dependences remain for regular spatial structures and patterns[47, 75]. Then, the detection algorithm consists of exploiting the information of the sub-bands by spatially multiplying the absolute value of the three components that result from each iteration of the SWT. As a consequence, there is a significant increase in the contrast of regular structures with respect to the sea clutter, which facilitates the selection of the intensity threshold for the detection of the vessels [47, 75].

The WT-based algorithm, like many other detection techniques based on intensity, assumes that the reflectivity of the vessel is greater than the clutter. In this sense, the presence of even a small section of land in the image is likely to trigger the rise of the number of false

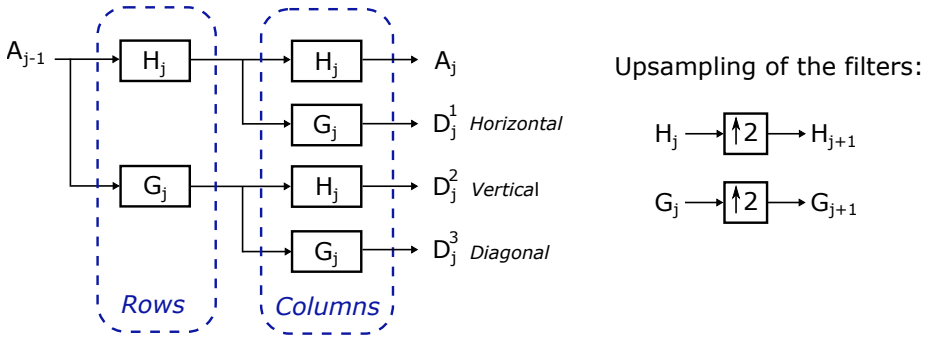

Fig. 3.12 Schematic diagram of separable filter banks for the SWT of a 2D signal

alarms due to the high reflectivity of land structures. Thus, a land masking preprocessing has to be applied before using the vessel detection algorithm in images near the coast. An advantage of using the WT-based algorithm is that the results of edge detection enhancement of the WT decomposition can be further employed to detect the coastline via an additional segmentation processing [76]. In this way, the boundaries of the land areas can be estimated directly from the SAR image, which avoids the errors of mapping external coastline contours and inaccurate land masking.

3.3.2 Vessel detection process and examples using the WT-based detection tool

The WT-based detection tool, developed by the Active Remote Sensing Lab at the UPC, makes it easier to detect possible vessels in maritime SAR images of large extension. The tool is not restrictive regarding the usage of land-free images since a landmasking step is applied if required. Figure 3.13 depicts the block diagram of the general detection processing for a maritime SAR image. First, the preprocessing step for landmasking is done by using a given coastline; then, the thresholding is performed based on the statistic of the sea clutter, followed by the detection step to spot potential vessels.

The landmasking step can be done by using either an external coastlines file (e.g. the ones provided by the Global Self-consistent, Hierarchical, High-resolution Geography Database (GSHHG) [77]), or the computed coastline from the image itself by using the results of the WT decomposition. Although using the former approach may reduce computational burden, high detail coastlines are not always available, and small islands or man-made constructions may not be masked. Moreover, in some cases the geo-positioning of the satellite image may also have limited accuracy, which can lead to distortions of the mapped coastline. On other hand, by using the edge enhancement results from the WT process, it is possible to obtain a contour with a good fit by employing the proper set-up of the parameters for the coastline detection algorithm. For illustration, Figure 3.14 shows a RADARSAT-2 SLC VV-image (1219×649 pixels) of the coast of Nigeria at the Gulf of Guinea from an acquisition campaign

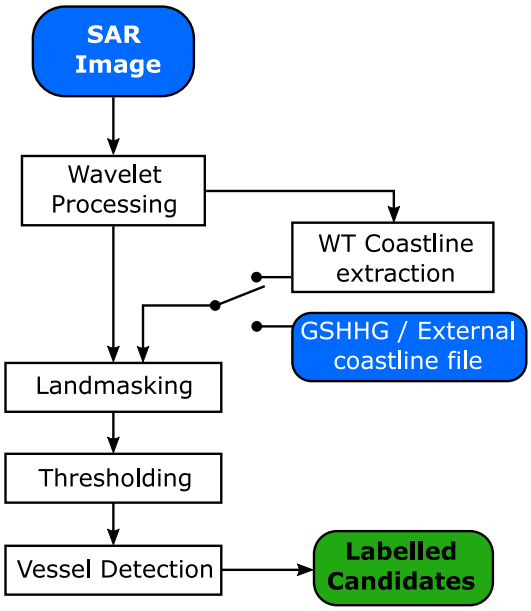

Fig. 3.13 Block diagram of the processing of the WT-based detection tool for a general maritime SAR image

of the NEREIDS Project (09-March-2013, 17:45 hrs, resolution $Az \times Rg$: 4.98 [m] $\times$11.83 [m]). In the image, the red line belongs to the slant-range projection of the coastline geometry from the GSHHG database. The yellow line was obtained from the WT edge computations by using the coast detection process. Notice that this yellow contour fits better to the actual coastline in the image, which allows getting an accurate mask for the land areas.

The detection of the vessels is carried out by applying the WT-based algorithm on the maritime image. At this point, it is assumed that the input image contain only the sea surface area from either a region of interest (ROI) without land or the result of the landmasking. The WT-based detection tool allows the adjustment of parameters such as the threshold, the Probability of False Alarm (PFA), minimum and maximum vessels size, and minimum distance between spotted candidates. Based on these parameters, the potential vessels are labelled and listed, making it easier to visualize them individually for closer inspection by the user. Figure 3.15 shows an example of potential vessels labelled in a RADARSAR-2 SLC HH-image (1261 $\times$ 665 pixels) from the Gulf of Guinea (acquisition campaign of the NEREIDS Project: 18-March-2013, 05:45 hrs, resolution $Az \times Rg$: 5.23 [m] $\times$4.73 [m]).

The capabilities of the WT-based detection tool by itself can be used to cross-check the position of potential vessels with regular monitoring systems of maritime traffic. Moreover, these capabilities can be expanded to offer more details about the spotted target such as their dimensions or motion. The next chapters are devoted to the analysis of the stripmap SLC images of the vessels in order to develop algorithms to improve their quality and/or

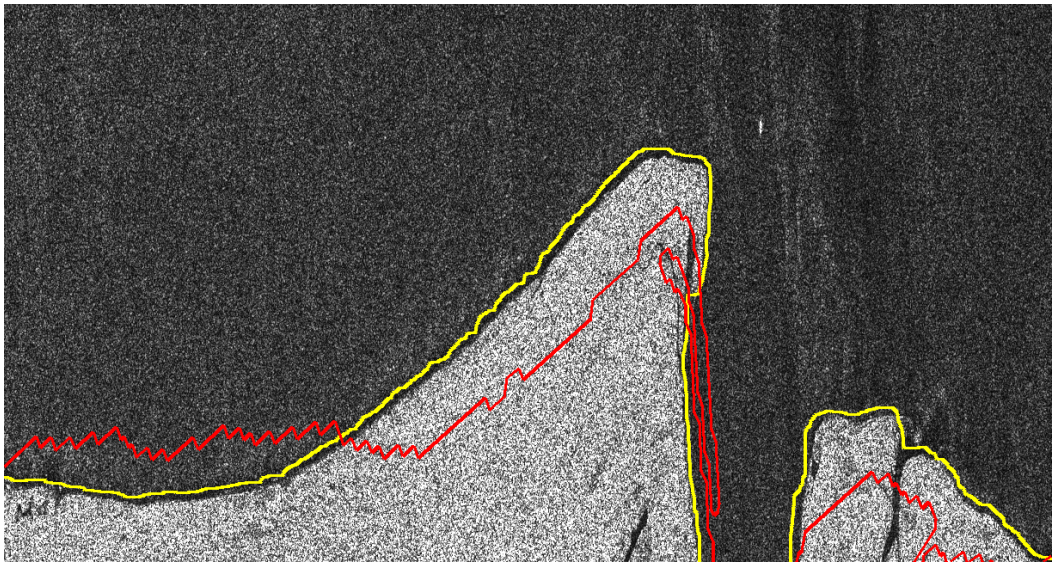

Fig. 3.14 Comparison between the coastline of the projection of external GSHHG database (red) and the one from the processing of the WT edge detection computations (yellow). Coast of Nigeria at the Gulf of Guinea. RADARSAT-2 image from the acquisition campaigns of NEREIDS Project (09-March-2013, 17:45 hrs, resolution $Az \times Rg$: 4.98 [m] $\times$11.83 [m]). Range direction: horizontal.

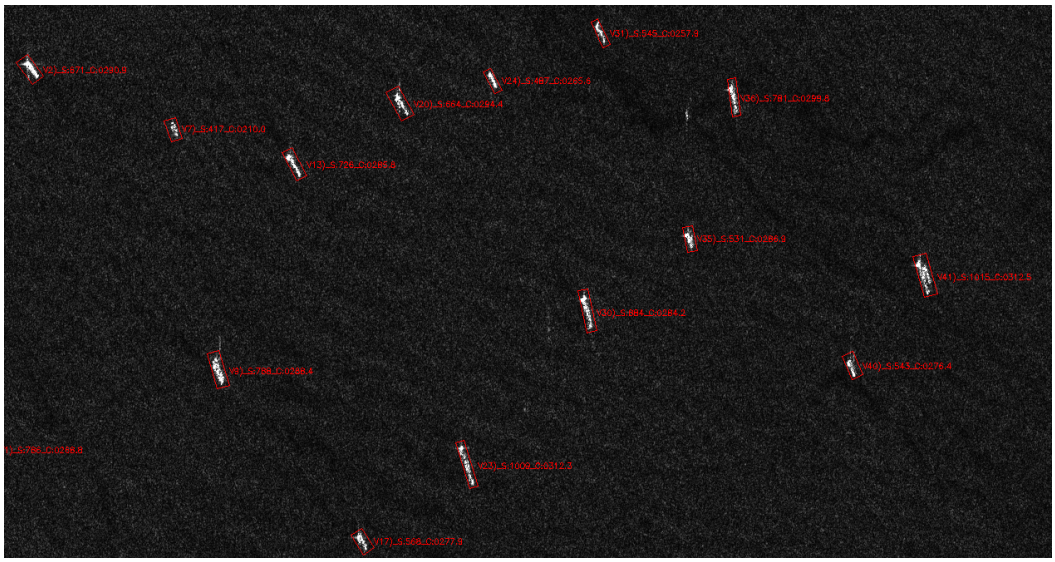

Fig. 3.15 Example of detected and labelled vessels using the WT-based detection tool on a SLC image of the Gulf of Guinea. RADARSAT-2 HH-image from the acquisition campaigns of NEREIDS Project (18-March-2013, 05:45 hrs, resolution $Az \times Rg$: 5.23 [m] $\times$4.73 [m]). Range direction: horizontal.

extract additional information about them. These algorithms can be included as a part of the detection tool to widen the range of information extracted from the SLC SAR images.

3.4 Summary

The use of real SAR data is always preferable when working with processing algorithms to evaluate its performance. However, there could be constraints regarding either the type of data available or their content. In many cases, a suitable alternative is the use of raw data from SAR simulators. They offer the advantage of allowing flexibility in the selection of the SAR sensor, and more importantly, the control of the content in the scene. For applications related to the analysis of the SAR signature of specific targets, this control of the scene makes possible to have the desired ground-truth that in real SAR acquisition would be costly and challenging to deploy.

In this chapter, the raw data simulator GRECOSAR was introduced. This numerical tool generates simulated raw data of complex targets, having already been used in previous research on vessel SAR signatures. Its synthesized raw data is the result of employing 3D CAD models of the target, orbital parameters of the SAR sensor, and computations of the electromagnetic solver GRECO®. Moreover, motion parameters of the target can be included to represent a more realistic behaviour of the vessels. The result is simulated raw data with similar characteristics to actual SAR acquisition of vessels.

Modifications were made to improve the performance of GRECOSAR. In the process of the synthesis of the raw data, the sinc interpolation process in azimuth was implemented. This kind of interpolation is intended to be used when the number of simulated aperture positions are near to the theoretical minimum. Additionally, the antenna pointing was modified to be applied in time domain for a more accurate simulation of moving targets. Now, with regard to the scene simulation, a more realistic multi-harmonic model for sea surface was implemented. Its reflectivity distribution suggests a similar probability behaviour to the reported models in the literature for real acquisitions of the sea clutter.

If real SAR data is available, maritime surveillance applications require a processing of the image in order to extract information about the vessels. Vessel detection algorithms are commonly used to spot likely candidates in an automatic way. The one employed throughout the current research project is based on the edge enhancement of the structures in the image using the intrascalar products of the Stationary Wavelet Transform. The mixing of the information at the different resolution levels increases the contrast of regular structures, which makes the establishment of a threshold to discriminate likely vessels easier. Additionally, the basic idea of the algorithm can also be applied to coastline detection, resulting in a more accurate masking of the land areas in the input SAR image. This WT-based process has been reported as a robust technique for both coastline estimation and vessel detection in maritime SAR images.

Chapter 4

Autofocus of the SAR signatures of the vessels

4.1 Introduction

SAR processing is based on the use of matched filtering in both range and azimuth dimensions to obtain the final image. While in the range dimension this process is straightforward due to the complete knowledge of the generated radar pulse signal, in azimuth dimension it relies on the modelling of the range variation for a static point-target during the whole time in which the synthetic aperture is constructed. Any unexpected discrepancy of this model with respect to the actual evolution of the range will introduce phase errors, whose quadratic and higher order terms produce the most severe deterioration by defocusing the SAR image [30].

A common way to compensate the quadratic and higher order phase errors is by using autofocus techniques. They estimate these phase errors in a computer-automated manner from the SAR data and compensate them. In general, the algorithms follow two approaches: model-based and non-parametric [24]. The model-based ones estimate the coefficients of an *a priori* defined function (usually a polynomial) that models the expected phase error, and they have the advantage of a simple implementation in the case of the quadratic model. Examples of these methods are the well-known Mapdrift and its multiple aperture expansion (MAM) [30], the image contrast based autofocus (ICBA) technique [24, 78]), and the Phase Difference (PD) algorithm[79]. In contrast, the non-parametric approaches do not assume an explicit model of the phase error function, which means that, in theory, they could compensate arbitrary high order phase errors. The most known technique using this type of approach is the phase gradient autofocus (PGA) algorithm [80, 81].

Autofocus techniques are commonly used to sharpen the whole SAR image. In fact, most of the techniques were originally developed to refine the estimation of the precise trajectory of airborne platforms. However, in the case of spaceborne SAR sensors, the platform trajectory is virtually stable, so one can assume that the azimuth phase errors

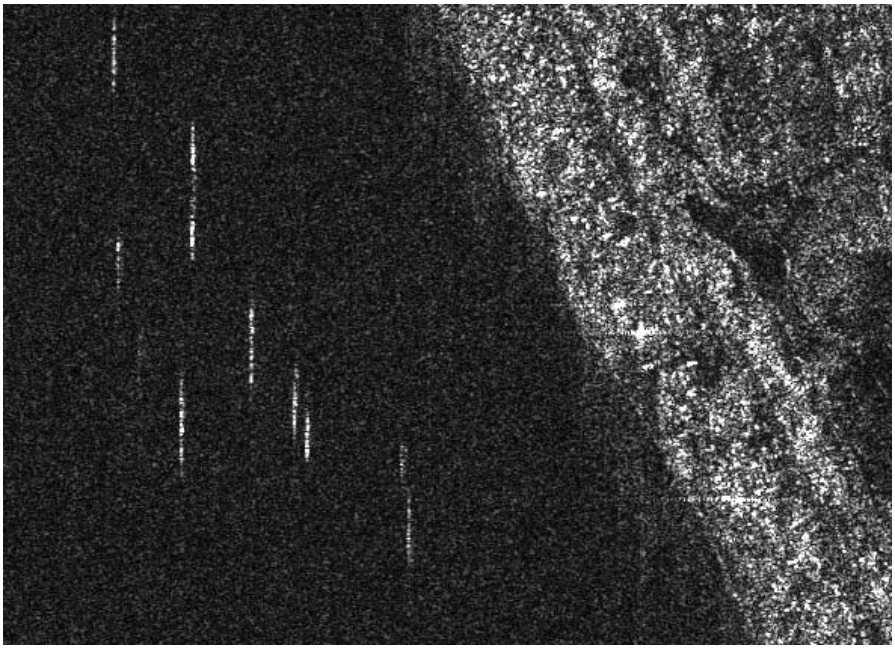

Fig. 4.1 Example of defocus of small vessels in front of the coast in the Gulf of Guinea. COSMO-SkyMed image, 2013.

of the signal are produced mainly by target movements. Figure 4.1 shows an example of a SAR image from COSMO-SkyMed of the Gulf of Guinea; it is possible to note blurring artefacts in the azimuth direction (vertical), likely associated to the motion of the vessels during the exposure time. The autofocus techniques can be applied locally to enhance the SAR signature of a defocused moving target. In our case, the autofocus of vessels would lead to obtaining high-quality SAR signatures, which can be used later to extract a more reliable estimation of features such as the length or breadth of the vessel.

In this chapter, three of the most used autofocus techniques are presented, applied and analysed in relation to focusing SAR signatures of vessels. The principles of the Phase Gradient Autofocus (PGA) algorithm, the Multiple Aperture Mapdrift (MAM), and the Image Contrast-based Autofocus (ICBA) algorithm are described in Section 4.2. In Section 4.3, the algorithms are validated with simulated raw data from a simple point target, and later from GRECOSAR simulations for more realistic targets, to compare their performance. Finally, in Section 4.4 the algorithms are applied to real data from NEREIDS project's acquisition campaigns.

4.1.1 Effects of the motion of the target on its SAR signal

In SAR images, moving targets produce unexpected variations in the radar-to-target distance, which introduce phase errors that may deteriorate the quality of the image [22]. A model of

an uniformly accelerated moving point-target was presented in Section 2.3 to identify the effects of the motion of a slow target on its SAR signal. For the spaceborne SAR case and a slow-moving target, the baseband model obtained for the range-compressed signal (with RCMC) in the slant-range plane was given by

$$s(\tau,t) = A_0 p_r\left(\frac{\tau - 2R_0}{c}\right) w_a\left(t\right) e^{-j\frac{4\pi}{\lambda}R_0} e^{-j\frac{4\pi}{\lambda}v_r t} e^{j\pi K_a t^2} e^{-j\frac{4\pi}{\lambda}\left(\frac{2vv_a + v_a^2 + a_r R_0}{2R_0}\right)t^2} \tag{4.1}$$

There, the v_r component introduces a linear term in the range variation $R(t)$ that shifts the azimuth position of target in the compressed image. The components v_a and a_r modify the quadratic term, changing the expected range variation used for the matched filter. As a consequence, these v_a and a_r components can deteriorate the quality of the image by introducing defocus aberrations. Notice that equation (4.1) can be seen as the SAR signal of the static target multiplied by a complex exponential with phase errors. Then, in general, this model can be written as

$$s(\tau,t) = s_s(\tau,t)e^{j\phi_e(t)} \tag{4.2}$$

with $s_s(\tau,t)$ as the SAR signal for the static case, and $\phi_e(t)$ as

$$\phi_e(t) = -j\frac{4\pi}{\lambda}v_r t - j\frac{4\pi}{\lambda}\left(\frac{2vv_a + v_a^2 + a_r R_0}{2R_0}\right)t^2 \tag{4.3}$$

which is a phase function that represents the errors in the range variation due to the motion of the target. For the autofocus techniques, the linear term in $\phi_e(t)$ is often ignored since the most severe deterioration of the quality of the image comes from higher order terms.

4.2 Autofocus techniques

The aim of the autofocus techniques is to improve the focus of the final image by first estimating automatically the phase errors from the SAR signal, and then, applying the respective error compensation. In this sense, 2^{nd} and higher order phase errors are usually the ones that the autofocus techniques look to compensate since they are responsible for the deterioration of the SAR image through the introduction of the blurring artefacts.

Most of the autofocus techniques were originally developed to compensate phase errors in spotlight SAR systems, and due to the nature of the data acquisition and processing, they cannot be applied directly to the stripmap data. Indeed, in the spotlight mode all targets in the scene have the same phase history because they have all been illuminated within the same exposure time; but in the stripmap mode, the targets are illuminated at different azimuth times. Additionally, classical implementations of these autofocus techniques assume

that the complex image and the phase history are Fourier transform pairs, a consequence of the Polar Format processing of the spotlight data [30, 81], which is not the case in the regular image processing of the stripmap mode. Some autofocus techniques rely on these two characteristics of the SAR data for the implementation of the algorithm, so adaptations have to be considered either in their implementation or in the SAR data for the stripmap mode case.

There are many autofocus techniques in the literature, but three of them that are widely use in practice have been selected [24, 30]: Phase Gradient Autofocus (PGA), Multiple Aperture Mapdrift (MAM), and Image Contrast-based Autofocus (ICBA). In the following sections, an adaptation of the stripmap data that would allow the application of the classical autofocus algorithms is presented; then, each autofocus technique is briefly described and the details of their implementation are given. In the case of PGA and MAM, their description corresponds to the classical approach for spotlight SAR mode data with the polar format processing [30].

4.2.1 Adaptation of Stripmap SAR data

The PGA and MAM techniques were originally meant to be applied to spotlight mode SAR data processed with the polar-format algorithm [30]. They both exploit the fact that, in azimuth, the complex image and the phase history are Fourier transform pairs and have to be adapted to conventional stripmap imaging. However, in the case of small areas such as those of vessel signatures, it is more convenient to adapt the stripmap data to fulfil the conditions expected in the classical implementation of these autofocus techniques. Thus, both the PGA and the MAM algorithms can be implemented in the same efficient way while preserving all of their functionalities.

Since the defocus effects in spaceborne SAR systems are significant only in the azimuth direction, the adaptation can be confined to the azimuth signal. Then, a modification of the signal is sought, so that the complex image and the phase history are turned into Fourier transform pairs in azimuth direction, as expected by PGA and MAM. In the case of small areas such as vessel SAR signatures, this can be achieved through the multiplication of the range-compressed stripmap signal by the conjugate of the azimuth reference chirp at the centre of the image, i.e. a dechirping process [82]. Indeed, assuming two ideal point targets in the same range bin but in different azimuth positions, the range-compressed signal for a given range-time τ_0 can be expressed as in equation (4.2) as the convolution of the azimuth chirp signal $f_{chirp}(t) = e^{-j2\pi\frac{v^2}{\lambda R_0}}$:

$$s(\tau_0, t) = s_0(t) = \left[(A_0\delta(t) + A_1\delta(t - t_1)) * f_{chirp}(t)\mathrm{rect}(t)\right] e^{j\phi_e(t)} \tag{4.4}$$

where A_0 and A_1 are complex constants related to the amplitude and phase of the respective backscattered signal of each target, and $\mathrm{rect}(t)$ is a model of the effective footprint of the

antenna. If equation (4.4) is multiplied by the complex conjugate of the azimuth chirp function f_{chirp} as

$$s_0(t) = \left[(A_0\delta(t) + A_1\delta(t-t_1)) * f_{chirp}(t)\text{rect}(t)\right] e^{j\phi_e(t)} f^*_{chirp}(t) \tag{4.5}$$

then, by doing the convolution and multiplication of the terms, the previous equation reduces to [82] :

$$s_0(t) = \left[A_0\text{rect}(t) + A_1 e^{-j\frac{2\pi v^2 t_1^2}{\lambda R_0}} e^{-j\frac{4\pi v^2 t_1}{\lambda R_0}t}\text{rect}(t-t_1)\right] e^{j\phi_e(t)} \tag{4.6}$$

In equation (4.6), the phase of the second ideal point-target is a linear function of t, which would produce a shift proportional to t_1 in the frequency domain when the Fourier Transforms is applied:

$$\begin{aligned} S_0(\omega) &= \mathscr{F}\left\{\left[A_0\text{rect}(t) + A_1 e^{-j\frac{2\pi v^2 t_1^2}{\lambda R_0}} e^{-j\frac{4\pi v^2 t_1}{\lambda R_0}t}\text{rect}(t-t_1)\right] e^{j\phi_e(t)}\right\} \\ S_0(\omega) &= A_0\text{sinc}(\omega) * e^{j\phi_e(\omega)} + A_1 e^{j\pi K_a t_1^2} e^{j\omega t_1}\text{sinc}(\omega - 2\pi K_a t_1) * e^{j\phi_e(\omega)} \end{aligned} \tag{4.7}$$

with $K_a = -\frac{2v^2}{\lambda R_0}$. Notice that $S_0(\omega)$ can be interpreted as the image formed from the adapted stripmap data. In this way, the condition of the azimuth phase history and the complex image being a Fourier transform pair is obtained. Nevertheless, there is a constraint in the extension of the image in azimuth for which the conversion is valid [82]. To fulfil Nyquist criterion, the maximum allowed bandwidth is limited by the PRF of the SAR sensor. Then, the maximum number of azimuth lines of the image can be computed using the model of the Doppler rate with parameters of the SAR platform. From the model of the range-compressed signal in equation (4.1), the complex exponential with the phase of the azimuth chirp is

$$f_{chirp}(t) = e^{-j\phi_{chirp}(t)} = e^{-j2\pi\frac{v^2}{\lambda R_0}t^2} \tag{4.8}$$

Then, the frequency content in the chirp must be limited by the PRF as

$$\frac{1}{2\pi}\left|\frac{\mathrm{d}\phi_{chirp}(t)}{\mathrm{d}t}\right| = \frac{2v^2\,|t|}{\lambda R_0} \leq PRF \tag{4.9}$$

and since the number of azimuth lines are obtained by $N_{az} = t \times PRF$, the number of azimuth lines is limited by

$$N_{az} \leq \frac{\lambda R_0 PRF^2}{2v^2} \tag{4.10}$$

The dechirping process must be applied to the centre of a section of range-compressed data with a number of azimuth lines within the boundary computed above. This results in SAR data that has similar characteristics in azimuth to those expected by the classical implementation of the PGA and MAM algorithms.

4.2.2 Phase Gradient Autofocus

The phase gradient Autofocus is a non-parametric technique developed for the phase error correction of spotlight mode SAR. It is known as a robust algorithm because of its performance in estimating higher order phase errors in a variety of scene contents with different signal-to-clutter ratio [80, 81]. Typically, the process begins by selecting a subset of range bins containing the greatest energy of the range-compressed signal from the Polar Format algorithm (PFA). Then, the algorithm obtains a phase error correction vector based on the estimation of the gradient of the phase of the signal in the azimuth dimension. The correction vector is applied to the range-compressed input signal and the algorithm iterates on the corrected data to minimize the residual phase error [30].

Description

For the description of the PGA algorithm, the simplest case of a single range-bin at a given value of $\tau = \tau_r$ of the range-compressed signal from the PFA processing is considered. If this bin contains a point scatterer, the slow time-domain SAR signal during the acquisition time T_a can be modelled as [30]:

$$s(\tau_r, t) = s_r(t) = A_0 e^{j[\omega_0 t + \phi_e(t)]} \qquad -\frac{T_a}{2} \leq t \leq \frac{T_a}{2} \tag{4.11}$$

where A_0 is a complex constant related to the amplitude and phase of the backscattered signal, ω_0 the frequency of the target signal history (i.e. a constant proportional to its azimuth position), and $\phi_e(t)$ is the phase error function. First, the algorithm passes to the image domain by performing the Fourier transform of $s_r(t)$ in the azimuth direction, which results in

$$\mathscr{F}\{s_r(t)\} = S_r(\omega) = F(\omega - \omega_0) * E(\omega) \tag{4.12}$$

with $F(\omega - \omega_0) = \mathscr{F}\{A_0 e^{j\omega_0 t}\}$ as the impulse response function, and $E(\omega) = \mathscr{F}\left\{e^{j\phi_e(t)}\right\}$ the transform of the phase error function. Then, the pixel with the highest energy in the azimuth direction is selected and a symmetric window, $W(\omega)$, is applied with respect to the pixel position:

$$S_w(\omega) = W(\omega - \omega_0) F(\omega - \omega_0) * E(\omega) \tag{4.13}$$

and by taking the inverse Fourier transform with respect to $\omega - \omega_0$, the new signal $s_w(t)$ is

$$s_w(t) = A_0 e^{j\phi_e(t)} * w(t) \tag{4.14}$$

being $w(t) = \mathscr{F}^{-1}\{W(\omega)\}$. This process has the effect of removing the frequency offset ω_0 and other scatterers that may influence the estimate, and limiting the highest frequency phase error that the algorithm is able to estimate. Additionally, it is usually assumed that

the effect of $w(t)$ in equation (4.14) is small and can be ignored if $W(\omega)$ is long enough to enclose the significant components of $E(\omega)$ [30]. Then, by taking the derivative of $s_w(t)$ (and assuming negligible effects of $w(t)$), a relationship between $s_w(t)$ and the gradient of $\phi_e(t)$ is obtained:

$$\frac{\mathrm{d}s_w(t)}{\mathrm{d}t} = \dot{s}_w(t) = j\dot{\phi}_e(t)s_w(t) \tag{4.15}$$

For this single range bin case, the estimation of $\dot{\phi}_e(t)$ in equation (4.15) is done in terms of $s_w(t)$ and its gradient $\dot{s}_w(t)$ as

$$\hat{\dot{\phi}}_e(t) = \frac{\Im\left[\dot{s}_w(t)s_w^*(t)\right]}{|s_w(t)|^2} \tag{4.16}$$

The first derivative of $s_w(t)$ can be computed by using the properties of the Fourier transform:

$$\mathscr{F}\left\{\frac{\mathrm{d}s_w(t)}{\mathrm{d}t}\right\} = j\omega S_w(\omega) \tag{4.17}$$

Thus, once $S_w(\omega)$ has been obtained (equation (4.13)), $\dot{s}_w(t)$ can be computed by taking the inverse Fourier transform of $j\omega S_w(\omega)$, simplifying its practical implementation.

In equation (4.13), notice that small errors, ϵ_ω, can be produced while locating the exact position of ω_0 due to the pixel resolution. This makes that equation (4.14) would change to

$$s_w(t) = A_0 e^{j(\phi_e(t)+\epsilon_\omega t)} * w(t) \tag{4.18}$$

consequently, an error term would appear in the estimation of the phase gradient in equation (4.16):

$$\hat{\dot{\phi}}_e(t) = \frac{\Im\left[\dot{s}_w(t)s_w^*(t)\right]}{|s_w(t)|^2} = \dot{\phi}_e(t) + \epsilon_\omega \tag{4.19}$$

The PGA algorithm is usually applied to complex scenes containing several range bins, combining all the available information to estimate the error phase derivative. In this case, for N range bins used in the estimation, the linear unbiased minimum variance (LUMV) estimator is given by [80, 81]

$$\hat{\dot{\phi}}_e(t) = \frac{\sum\limits_N \Im\left[\dot{s}_w(n_\tau,t)s_w^*(n_\tau,t)\right]}{\sum\limits_N |s_w(n_\tau,t)|^2} = \dot{\phi}_e(t) + \frac{\sum\limits_N |s_w(n_\tau,t)|^2 \epsilon_\omega(n_\tau)}{\sum\limits_N |s_w(n_\tau,t)|^2} \tag{4.20}$$

The final step of the algorithm consists of the integration of the derivative of the phase error to obtain $\hat{\phi}_e(t)$. After removing any bias and linear trends induced by the error term, the phase correction is applied by multiplying the range-compressed data by $e^{-j\hat{\phi}_e(t)}$, and the algorithm is repeated iteratively. Figure 4.2 depicts the block diagram of a single iteration of the PGA algorithm.

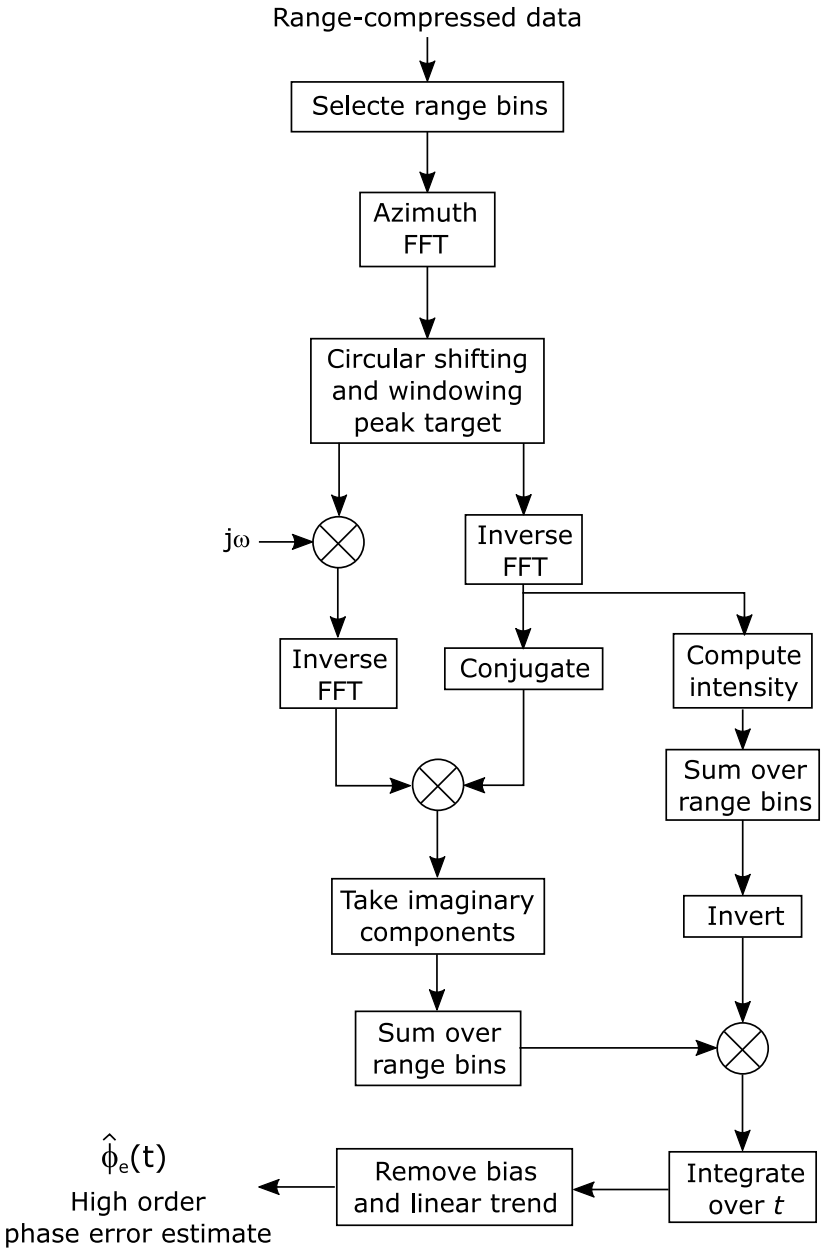

Fig. 4.2 Block diagram of a single iteration of the PGA algorithm. (Based on [30])

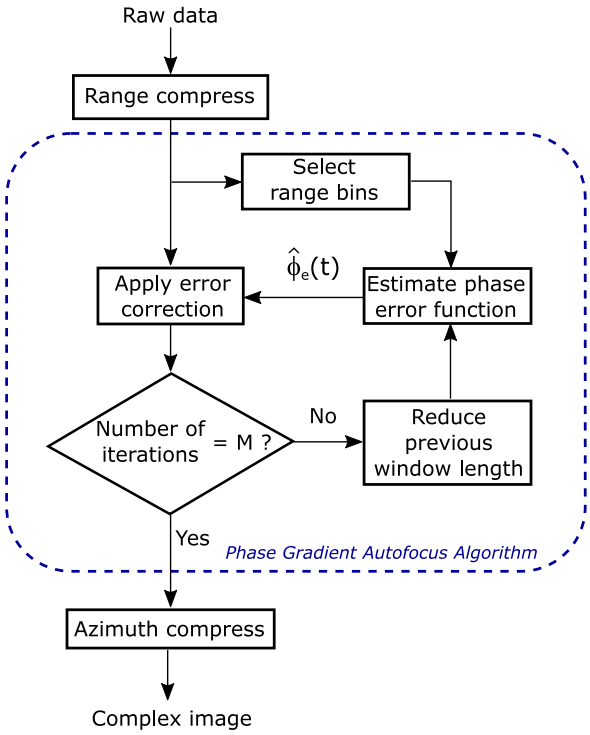

Fig. 4.3 Block diagram of the iterative implementation of the PGA algorithm.

Implementation

In practice, PGA is implemented as an iterative algorithm, using the corrected data to reduce the residual phase error each time. The parameters that have to be taken into account in each iteration are the location and the length of the window $W(\omega)$. For the former, instead of moving the window, the typical implementation uses a circular shift of the highest energy pixel of $S(\omega)$ to the reference origin (i.e. the centre of the image), so the window (and the inverse Fourier transform) is always referenced to the same position. For the length of the window, it is reported that the best strategy is to start the algorithm with a window length much larger than the anticipated phase errors require and reduce the length in subsequent iterations [81]. For instance, the algorithm can start with a length window 50% larger than the threshold of the average range-compressed signal at 10 dB below the peak intensity value. Then, this length is reduced between 20% and 50% with respect to the previous window in subsequent iterations up to a minimum value. Figure 4.3 shows a basic block diagram of this iterative implementation of the PGA algorithm when using the adapted stripmap data.

4.2.3 Multiple Aperture Mapdrift

The Mapdrift (MD) algorithm is one of the classical and widely most used technique in SAR systems to correct defocus aberrations in images that result from to quadratic phase errors

(QPE). It is a model-based autofocus algorithm that exploits the effects of the shift that the images of two sublooks suffer due to QPE. By correlating these looks, the measured shift is associated to an estimate of the phase error [24, 30]. In the case of higher order phase errors, the MD concept is extended by using more sublooks in the so-called Multiple Aperture Mapdrift (MAM). To do this, the permutations of multiple looks are correlated in order to measure the respective shifts, which are used in the estimation of the coefficients of the polynomial phase error. The number of sublooks (or subapertures) used determines the maximum order of the polynomial phase error function [30]. In the next sections, the MAM algorithm is briefly described as it is typically used in data from the spotlight mode after the PFA processing.

Description

The basic idea of the classical Mapdrift algorithm is to use the Fourier frequency shift theorem to estimate the coefficients of a polynomial phase error function based on the different linear terms in the sublooks [30]. Assuming a single range bin case as in equation (4.11), the model of the polynomial phase error function, $\phi_e(t)$, that deteriorates the focus of the image (i.e. 2^{nd} through N^{th} order function) can be modeled as

$$\phi_e(t) = \sum_{k=2}^{N} a_k t^k \qquad -\frac{T_a}{2} \leq t \leq \frac{T_a}{2} \tag{4.21}$$

where t is the azimuth time, a_k represents the coefficients of the polynomial function, and T_a the aperture time. By taking N non-overlapping sublooks (or subapertures), the phase error in each of them is described by [30]

$$\phi_i(t) = \sum_{k=2}^{N} a_k (t + t_i)^k \qquad -\frac{T_a}{2N} \leq t \leq \frac{T_a}{2N} \tag{4.22}$$

with

$$t_i = \left(\frac{i}{N} - \frac{N+1}{2N} \right) T_a \tag{4.23}$$

as the centre of the i^{th} sublook. Based on the binomial theorem, the linear phase in the i^{th} sublook can be obtained from its respective polynomial expansion, resulting in

$$\phi_i^{lin}(t) = \sum_{k=2}^{N} a_k k t_i^{(k-1)} t \qquad -\frac{T_a}{2N} \leq t \leq \frac{T_a}{2N} \tag{4.24}$$

Assuming that the complex image and the phase history of the signal are a Fourier transform pair in the azimuth direction, the linear term of each sublook given in equation (4.24) induces a shift in its respective image of

$$\Delta_i = \sum_{k=2}^{N} a_k k t_i^{(k-1)} \tag{4.25}$$

The MAM algorithm exploits the induced shift of the images to estimate the coefficients of the polynomial phase error function. It takes non-overlapping sublook apertures and cross-correlates each pair of intensity images. Then, it obtains the relative shift between them by measuring the peak location. By using equation (4.25), the relative shift between two sublooks, i and j, is given by

$$\Delta_{i,j} = \sum_{k=2}^{N} a_k k \left[t_j^{(k-1)} - t_i^{(k-1)} \right] \qquad i < j \tag{4.26}$$

In practice, equation (4.26) is written in a matrix form that facilitates implementation [30]

$$\begin{bmatrix} \Delta_{1,2} \\ \Delta_{1,3} \\ \vdots \\ \Delta_{1,N} \\ \Delta_{2,3} \\ \Delta_{2,4} \\ \vdots \\ \Delta_{N-1,N} \end{bmatrix} = \begin{bmatrix} d_2(1,2) & d_3(1,2) & \cdots & d_N(1,2) \\ d_2(1,3) & d_3(1,3) & \cdots & d_N(1,3) \\ \vdots & \vdots & \ddots & \vdots \\ d_2(1,N) & d_3(1,N) & \cdots & d_N(1,N) \\ d_2(2,3) & d_3(2,3) & \cdots & d_N(2,3) \\ d_2(2,4) & d_3(2,4) & \cdots & d_N(2,4) \\ \vdots & \vdots & \ddots & \vdots \\ d_2(N-1,N) & d_3(N-1,N) & \cdots & d_N(N-1,N) \end{bmatrix} \begin{bmatrix} a_2 \\ a_3 \\ \vdots \\ a_N \end{bmatrix} \tag{4.27}$$

or in a compact form

$$\underline{\Delta} = \mathbf{D_N} \underline{a} \tag{4.28}$$

where $\underline{\Delta}$ is the vector with the measured shifts between the pair of images, $\underline{a}$ is the vector with the coefficients of the phase error function, and $\mathbf{D_N}$ is a relation matrix of dimension $N(N-1)/2 \times (N-1)$ whose elements are defined based on equation (4.26) as

$$d_k(i,j) = k \left[t_j^{(k-1)} - t_i^{(k-1)} \right] \qquad i < j \tag{4.29}$$

The MAM algorithm takes advantage of the redundancy of the overdetermined system of linear equations in (4.28) to overcome the effects of noise and target signature variations in the sublooks [30]. Since the matrix $\mathbf{D_N}$ is known *a priori*, the algorithm computes the vector

$\underline{a}$ by a single matrix multiplication of the measured shifts and the pseudo-inverse of the $\mathbf{D_N}$ matrix

$$\underline{a} = \mathbf{D_N^{-1}}\underline{\Delta} \tag{4.30}$$

Figure 4.4 shows a block diagram of that summarized the MAM procedure described so far.

Implementation

Typically, the MAM procedure employs a subset of range bins of the image that contains the most reflective scatterers in order to have high correlation between the sublooks. Then, the algorithm its applied individually to each of the range bins, and the final estimation of the coefficients of the phase error function is obtained by averaging the individual estimates. In theory, a single estimation would give the correct values of the unknown coefficients, but the MAM algorithm is usually applied iteratively to improve its performance [30]. In each iteration, the range bins whose estimates are not within the vicinity (usually one standard deviation) of the average QPE are discarded, reducing the subset for the next iteration. In this way, the procedures lessen the effect of range bins that produce anomalous estimates. Figure 4.5 depicts a diagram of the MAM implemented as an iterative procedure when using the adapted stripmap data.

Another procedure used to improve the MAM performance is to oversample the azimuth signal before the correlation of the sublooks [24]. This oversampling enhances the resolution of the correlation function, minimizing the error in the location of its peak.

Theoretically, the MAM algorithm could estimate a polynomial phase error function of arbitrary order. However, there is a practical limit of the order of the phase error model. As the order N grows, the length of the sub-aperture decreases, deteriorating both the resolution and the signal-to-noise ratio (SNR) of targets. Since the degree of deterioration depends of the scene content, the maximum order of the polynomial phase error model may change from image to image. For instance, it is recommended that the algorithm be applied up to a fifth order phase error function for typical SAR images of land regions [30].

4.2.4 Image Contrast-based Autofocus

The image contrast-based autofocus (ICBA) algorithm uses the contrast of the image as a sharpness function to measure the degree of the focus quality of the image. In the absence of azimuth phase errors in the raw data, the image is compressed flawlessly and one can expect the match-filter to concentrate the energy of a scatterer into one resolution cell. Conversely, unexpected variations in the phase spread the energy of the scatterer along more cells, blurring the image. Therefore, the degree of concentration of the energy with respect to

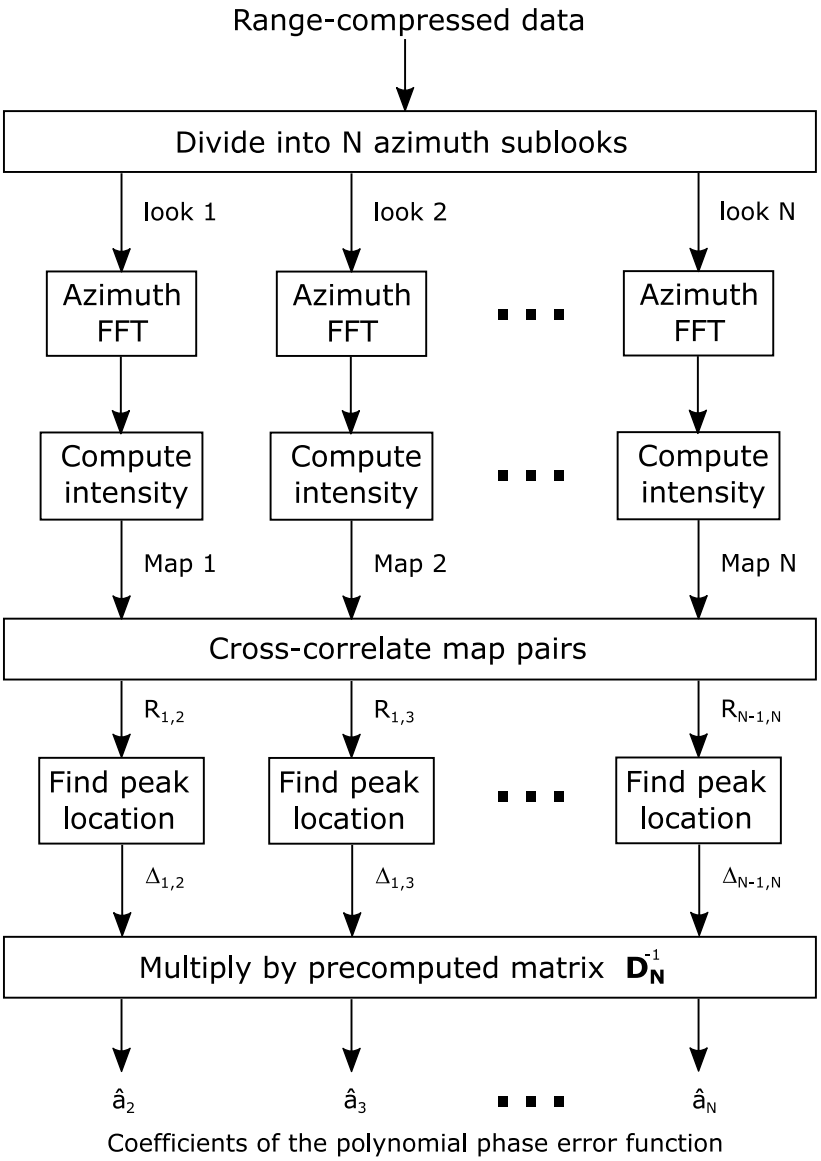

Fig. 4.4 Block diagram of the MAM algorithm. (Based on [30])

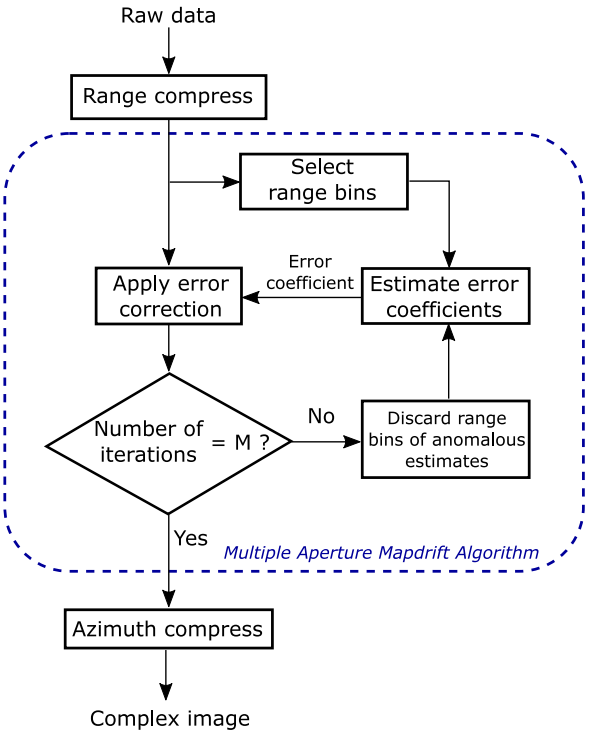

Fig. 4.5 Block diagram of the iterative implementation of the MAM algorithm. (Based on [30])

the mean value would offer information about the image focusing, which is assessed through the contrast of the image [24, 78].

Description

The idea of the ICBA algorithm is to employ the intensity image to compute its respective contrast and maximize it by applying compensating phase function. As mentioned in Section 4.1.1, a range compressed SAR signal, $s(\tau, t)$, with a phase error $\phi_e(t)$ can be modelled as

$$s(\tau, t) = s_{ideal}(\tau, t)e^{j\phi_e(t)} \tag{4.31}$$

with $s_{ideal}(\tau, t)$ as the ideal range compressed SAR signal. The ICBA algorithm assumes a polynomial phase error model to compensate it in the range-compressed data:

$$s_c(\tau, t|a_2, ..., a_N) = s(\tau, t)e^{-j\hat{\phi}_e(t)} \tag{4.32}$$

with

$$\hat{\phi}_e(t) = \sum_{k=2}^{N} a_k t^k \tag{4.33}$$

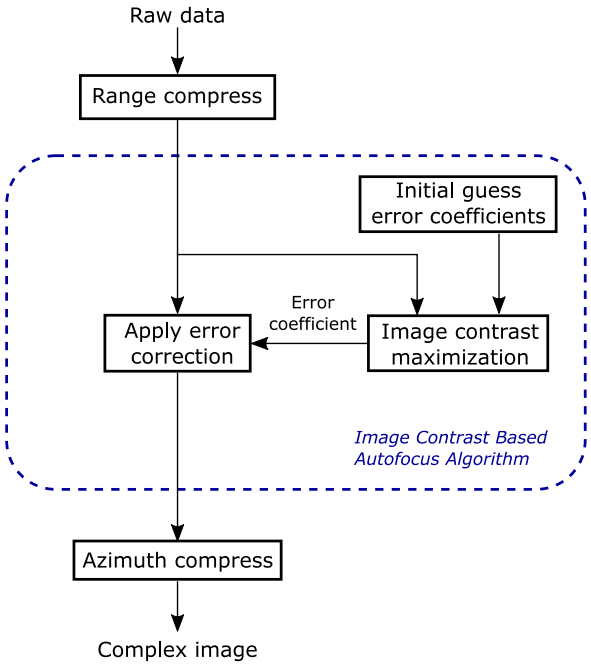

Fig. 4.6 Block diagram of the Image Contrast Based Autofocus (ICBA) algorithm.

a_k being the coefficients of the N^{th} order polynomial model. By performing the azimuth compression of $s_c(\tau, t)$, and adjusting to image coordinates, the corrected image is obtained

$$\tilde{s}_c(x, y|a_2, ..., a_N) = \mathcal{P}_{az}\left\{s_c(\tau, t|a_2, ..., a_N)\right\} \tag{4.34}$$

where $\mathcal{P}_{az}\{\cdot\}$ represents the azimuth compression processor, and x and y are the image coordinates in range and azimuth direction, respectively. Then, the intensity image results in

$$I(x, y|a_2, ..., a_N) = |\tilde{s}_c(x, y|a_2, ..., a_N)|^2 \tag{4.35}$$

and its image contrast is given by [78]

$$IC(a_2, ..., a_N) = \frac{\sqrt{E\{[I(x, y|a_2, ..., a_N) - E\{I(x, y|a_2, ..., a_N)\}]^2\}}}{E\{I(x, y|a_2, ..., a_N)\}} \tag{4.36}$$

where $E\{\cdot\}$ is the expectation operator. Thus, the image would be properly focused by finding the unknown coefficients that maximizes the image contrast function:

$$(\hat{a}_2, ..., \hat{a}_N) = \arg\left(\max_{a_2,...,a_N}\{IC(a_2, ..., a_N)\}\right) \tag{4.37}$$

Figure 4.6 depicts a block diagram that summarizes the ICBA procedure.

Implementation

The ICBA technique, as described above, has the most straight-forward implementation. It requires a defined model of the azimuth phase error that is expected (which is usually a second order polynomial [24]), and iterative testing for the coefficients that maximizes the image contrast. In fact, the algorithm can be seen an optimization process that employs the image contrast as a cost function to focus the image. In this sense, existing optimization routines can be use to compute the coefficients of the phase error function faster. In our case, the implementation of the ICBA algorithm employs the in-built IDL® function *AMOEBA()*, a multi-dimensional minimization method that has been adapted to maximize the image contrast. Additionally, for a given region of interest (ROI) to be refocused, it has been observed that the algorithm presents better results when the image contrast function is evaluated only in the ROI, rather than the whole scene, during the optimization process.

Note that no particular SAR mode is assumed with this implementation of the algorithm. The ICBA employs the intensity of the final image regardless of its compression. Then, its implementation can be applied directly to stripmap SAR data at the expense of an increase in the computational burden due to the match-filtering procedure.

4.3 Validation with simulated data

The PGA, MAM, and ICBA algorithms are applied to range-compressed stripmap data with azimuth phase errors for the simplest case of a point-target in order to analyse their performance. The GRECOSAR simulator is used to obtain the raw data with $SNR = 30$[dB] for an X-band sensor with parameters similar to those of TerraSAR-X (Table 4.1), and a 2[m]-side trihedral (a corner reflector) is employed as the point-target to generate an impulse response. Figure 4.7 shows the SLC SAR image of this corner reflector compressed with the nominal parameters and the plot of the (interpolated) azimuth profile of the range bin that contains the most energy.

To assess the performance of the algorithms, first, azimuth phase errors are added to the SAR data. Once the raw data has been compressed in range, a phase error function is added in the azimuth direction in the time domain to deteriorate the focus of the image; Table 4.2 lists the three phase error functions used for this validation, while Figure 4.8 shows their respective plots. This corrupted range-compressed data will be the input data for the algorithms. After phase compensation, two parameters of the final impulse response will be used to analyse the performance of the autofocus techniques: the peak value of the impulse response, P_{IPR}, and the impulse response width, W_{IPR}, which is related to the resolution of the SAR image. The no-phase error case will work as the reference point with measurements of $P_{IPR}^{ref} = 94.779$ [dB] and $W_{IPR}^{ref} = 3.471 \pm 0.128$[m] (Figure 4.7b).

Table 4.1 Parameters of the X-band SAR sensor for the set-up of GRECOSAR simulations

Sensor Parameter	**Value**	
Pulse duration (τ)	28×10^{-6}	[s]
Sampling Frequency	128×10^{6}	[Hz]
Chirp bandwidth	116×10^{6}	[Hz]
Carrier frequency	9.65×10^{9}	[Hz]
PRF	3736	[Hz]
Doppler Rate	-5370.18	[Hz/s]
Reference distance	654174.71	[m]
Antenna length	5.1	[m]
Nominal speed of the platform	7686.12	[m/s]

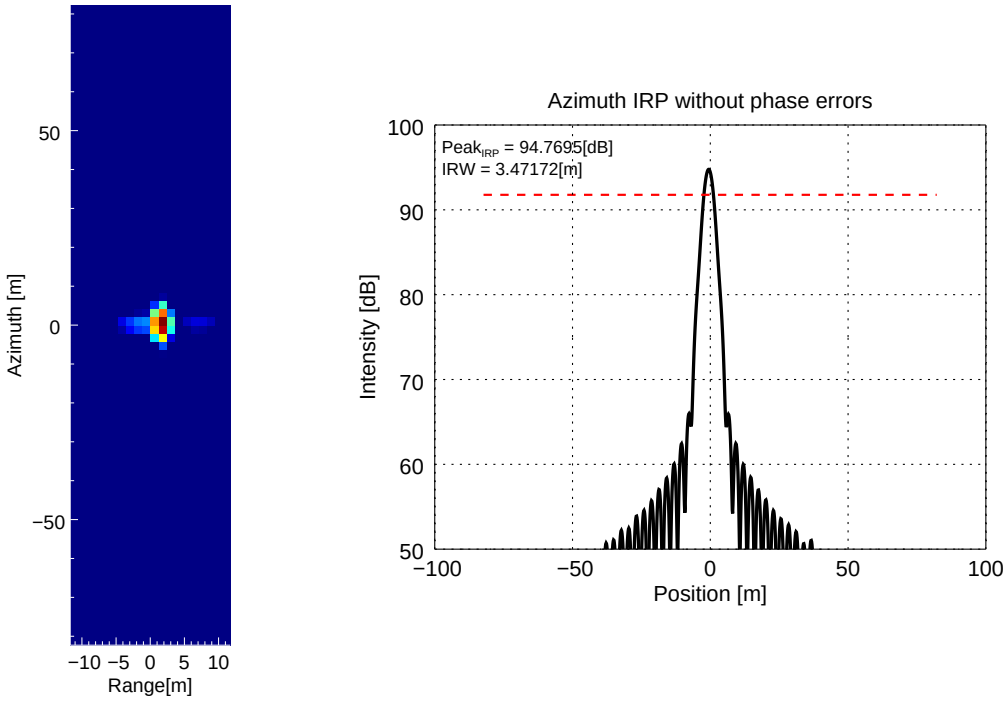

(a) (b)

Fig. 4.7 Static corner reflector from raw data simulated in GRECOSAR: (a) Single-look Complex image; (b) Azimuth profile of the range bin containing the most energy

Table 4.2 Phase error functions applied in azimuth direction in time domain.

Function type	**Function definition**
Quadratic	$\phi_{e1}(t) = 200\pi t^2$
Polynomial	$\phi_{e2}(t) = 50\pi t^2 + 300\pi t^3 + 100\pi t^4$
High-order	$\phi_{e3}(t) = 10\pi cos(20t)$

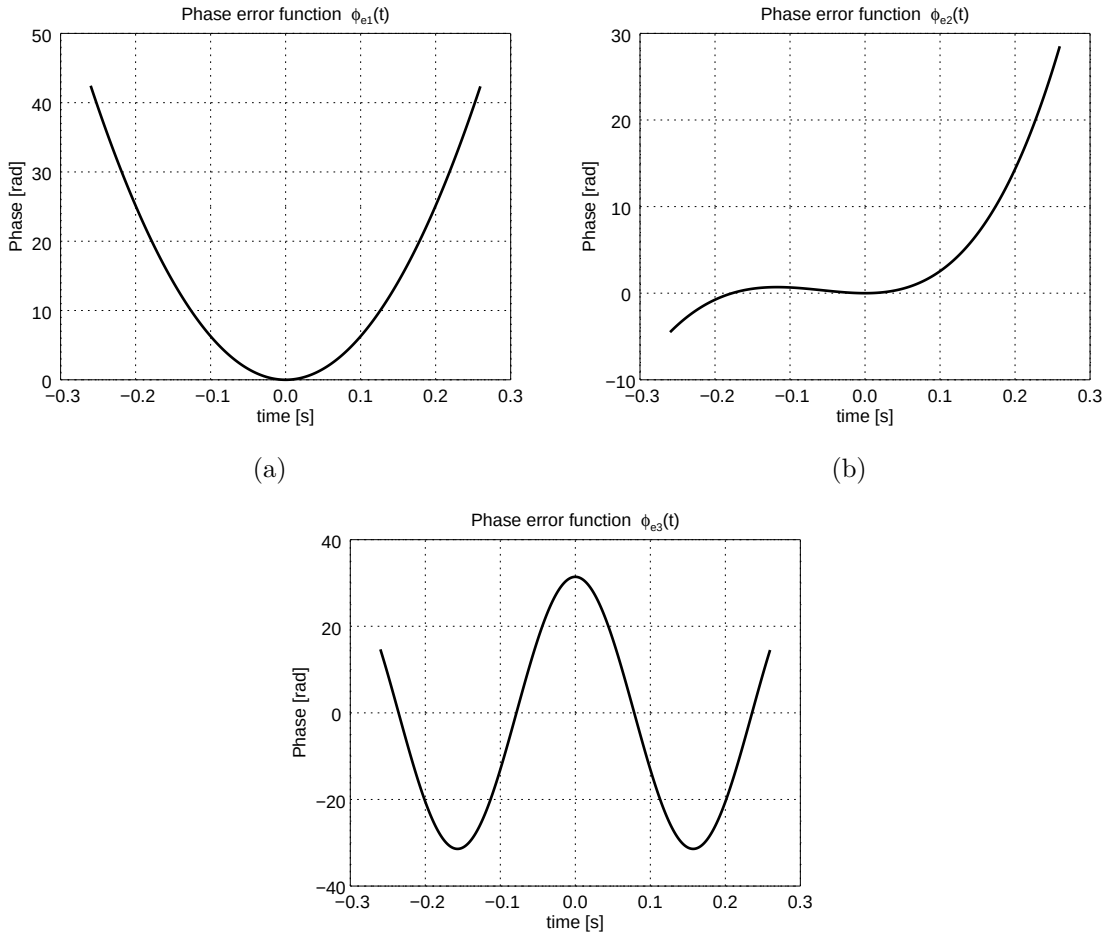

Fig. 4.8 Phase error functions applied in azimuth direction in time domain: (a) $\phi_{e1}(t)$, typical QPE; (b) $\phi_{e2}(t)$, fourth-order polynomial phase error. (c) $\phi_{e3}(t)$, high-order phase error.

In this validation, the iterative techniques (i.e. PGA and MAM) will be set to be applied for 10 cycles, and the model-based techniques, MAM and ICBA, will be set to a fourth order polynomial model for all the tests, as it is the maximum phase error order expected. Additionally, a special plot will be considered only to compare the estimated phase error function with PGA and the actual phase error. PGA estimates may include linear phase components as a consequence of the integration process. Recall that PGA actually estimates the gradient of the azimuth phase error as a function of the time; then, any residual constant value in the gradient function translates, after it is integrated, to a linear trend of the final azimuth phase error function. After the phase error compensation, the final effect of this linear trend is a small shift of the image in the azimuth direction (proportional to the residual constant value of the estimated gradient function). As a consequence, the linear trend of the estimated phase error function is usually subtracted before delivering the final estimated function [81]. In this sense, the linear trend of the actual phase error function and the one estimated by the PGA is subtracted in order to compare easily the higher order terms. In the following sections, the compressed images with different phase errors are shown. Also shown are their respective impulse responses in the azimuth direction, and their estimated phase function obtained using PGA, MAM, and ICBA on the range-compressed data.

Compensation of quadratic phase error with MAM, PGA, and ICBA algorithms

The quadratic phase error, $\phi_{e1}(t)$, is applied to the range-compressed data, and the MAM, PGA, and ICBA algorithms are used to focus the image again. Compressing in azimuth the corrupted data without using any autofocus algorithm results in the impulse response width and the peak value of $W_{IPR} = 68.020 \pm 0.128$[m] and $P_{IPR} = 82.135$ [dB], respectively. After applying the autofocus techniques to the defocused data, each of them estimates a phase error function (Figure 4.9) and uses it to compensate the range-compressed data. Figure 4.10 shows the initial defocused SLC image and the results after phase compensation; their respective azimuth profiles are shown in Figure 4.11. For MAM, the final impulse response width and peak value results in $W_{IPR}^{MAM} = 3.472 \pm 0.128$[m] and $P_{IPR}^{MAM} = 95.168$ [dB], respectively; for PGA, they results in $W_{IPR}^{PGA} = 3.343 \pm 0.128$[m] and $P_{IPR}^{PGA} = 95.273$ [dB]; and for ICBA, $W_{IPR}^{ICBA} = 3.343 \pm 0.128$[m] and $P_{IPR}^{ICBA} = 95.252$ [dB].

Compensation of fourth-order polynomial phase error with MAM, PGA, and ICBA algorithms

Now, the fourth-order polynomial phase error, $\phi_{e2}(t)$, is applied to the range-compressed data. By compressing this corrupted data in azimuth, the impulse response width and peak value of $W_{IPR} = 5.786 \pm 0.128$[m] and $P_{IPR} = 90.974$ [dB], respectively. By applying the autofocus algorithms, their respective phase error functions are estimated and they are depicted in

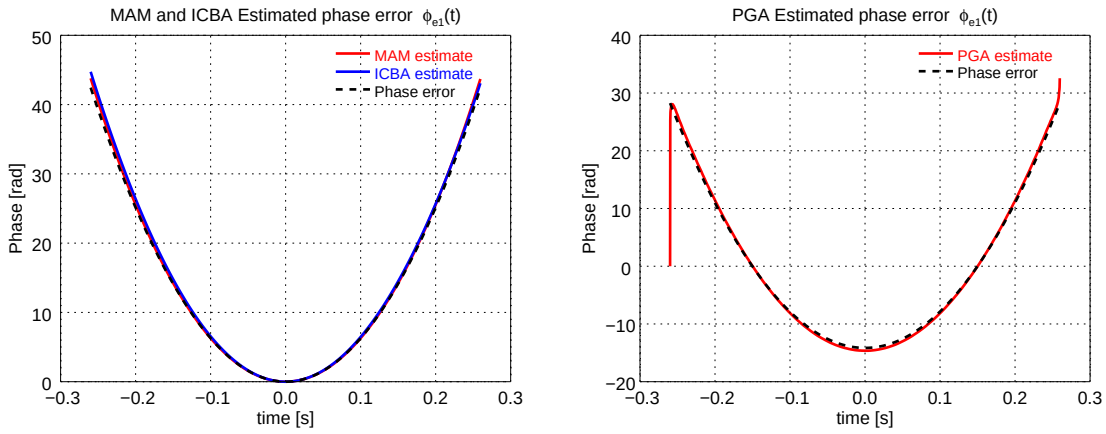

(a) (b)

Fig. 4.9 Estimated phase error by MAM, PGA, and ICBA for the QPE case: (a) Estimated phase error by MAM and ICBA algorithms (b) Estimated phase error by PGA (linear trends removed).

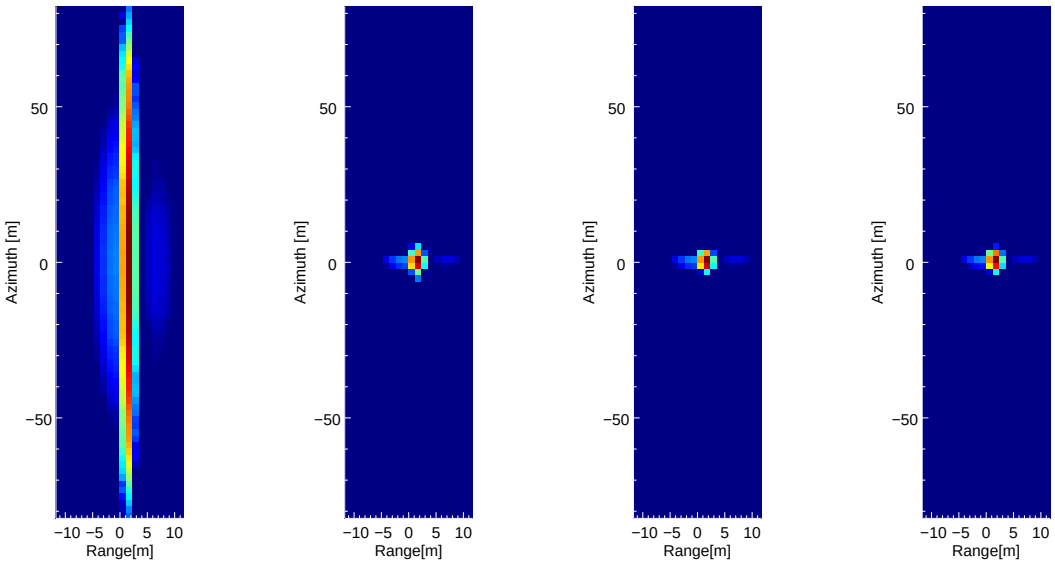

(a) (b) (c) (d)

Fig. 4.10 SLC image before and after applying the autofocus algorithms: (a) Defocused SLC image with QPE. SLC image after phase compensation: (b) MAM, (c) PGA, (d) ICBA.

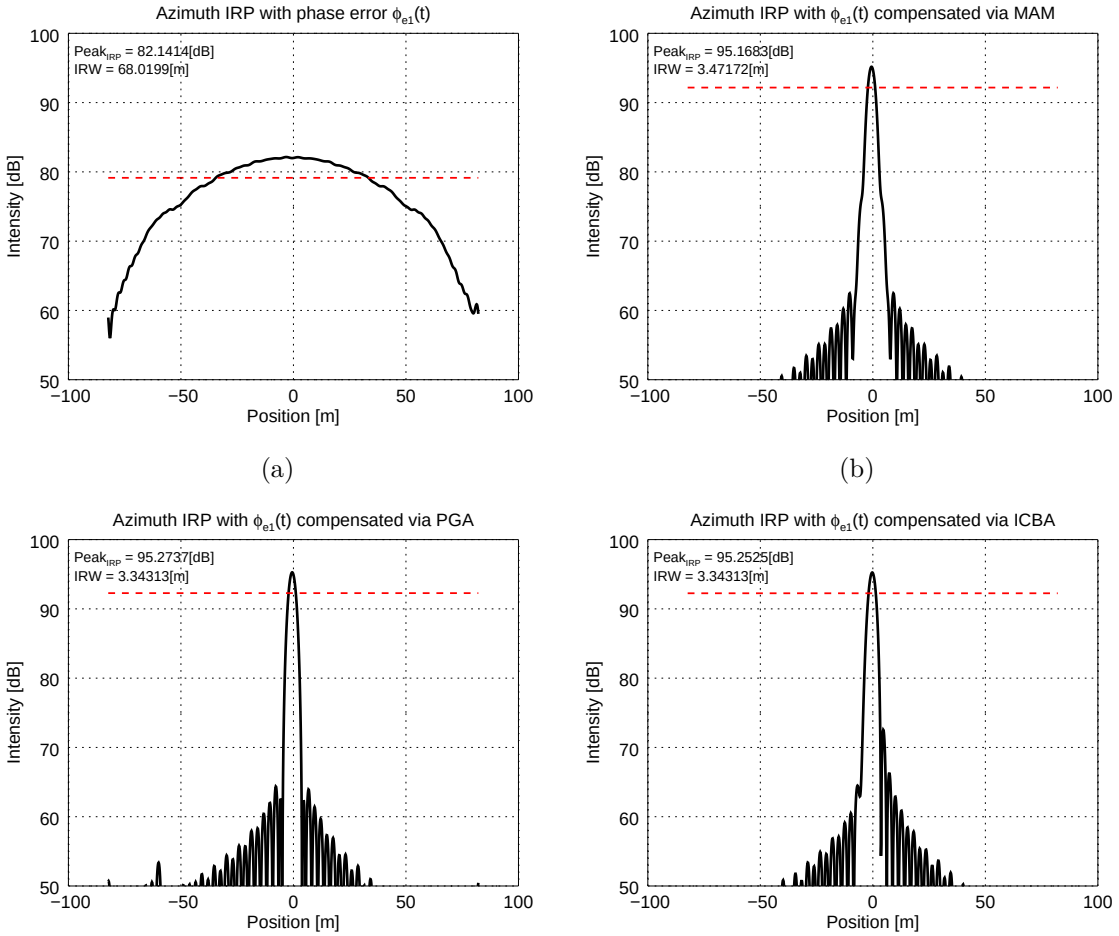

Fig. 4.11 Azimuth profile of the defocused SLC image before and after applying the autofocus algorithms: (a) Initial defocused data with QPE. Profile after phase compensation: (b) MAM, (c) PGA, (d) ICBA.

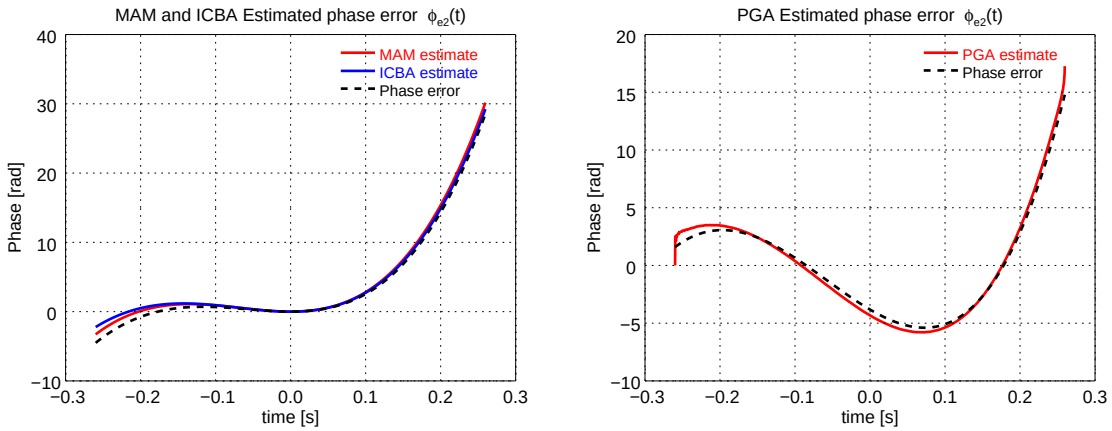

(a) (b)

Fig. 4.12 Estimated phase error by MAM, PGA, and ICBA for the polynomial phase error case: (a) Estimated phase error by MAM and ICBA algorithms (b) Estimated phase error by PGA (linear trends removed).

Figure 4.12. Then, Figure 4.13 shows the result of the refocused images using the estimated phase errors, and Figure 4.14 plots the details of the respective azimuth profiles. For MAM, the final impulse response width and peak value results in $W_{IPR}^{MAM} = 3.343 \pm 0.128$[m] and $P_{IPR}^{MAM} = 95.285$ [dB], respectively; for PGA, they results in $W_{IPR}^{PGA} = 3.343 \pm 0.128$[m] and $P_{IPR}^{PGA} = 95.286$ [dB]; and for ICBA, $W_{IPR}^{ICBA} = 3.343 \pm 0.128$[m] and $P_{IPR}^{ICBA} = 95.254$ [dB].

Compensation of high-order phase error with MAM, PGA, and ICBA algorithms

Finally, the cosine phase error function„$\phi_{e3}(t)$, is applied to the range-compressed data. This high-order phase error spreads the energy in a different way in the SLC image. It affects the width of the main lobe by spreading the energy symmetrically, but it also adds ripples whose peak values exceed the -3[dB] with respect to the maximum intensity value $P_{IPR} = 81.851$ [dB]. The defocused imaged, in this case, results in a vertical line with many peak values(Figure 4.16a). The phase error functions estimated by the autofocus algorithms are shown in Figure 4.15, and the compensated SLC images and azimuth profiles are shown in Figure 4.16 and Figure 4.17, respectively. The final impulse response width and peak value results as follows: for MAM, $W_{IPR}^{MAM} = 9.129 \pm 0.128$[m] and $P_{IPR}^{MAM} = 88.543$ [dB]; for PGA, $W_{IPR}^{PGA} = 3.343 \pm 0.128$[m] and $P_{IPR}^{PGA} = 95.271$ [dB]; and for ICBA, $W_{IPR}^{ICBA} = 10.023 \pm 0.128$[m] and $P_{IPR}^{ICBA} = 86.885$ [dB].

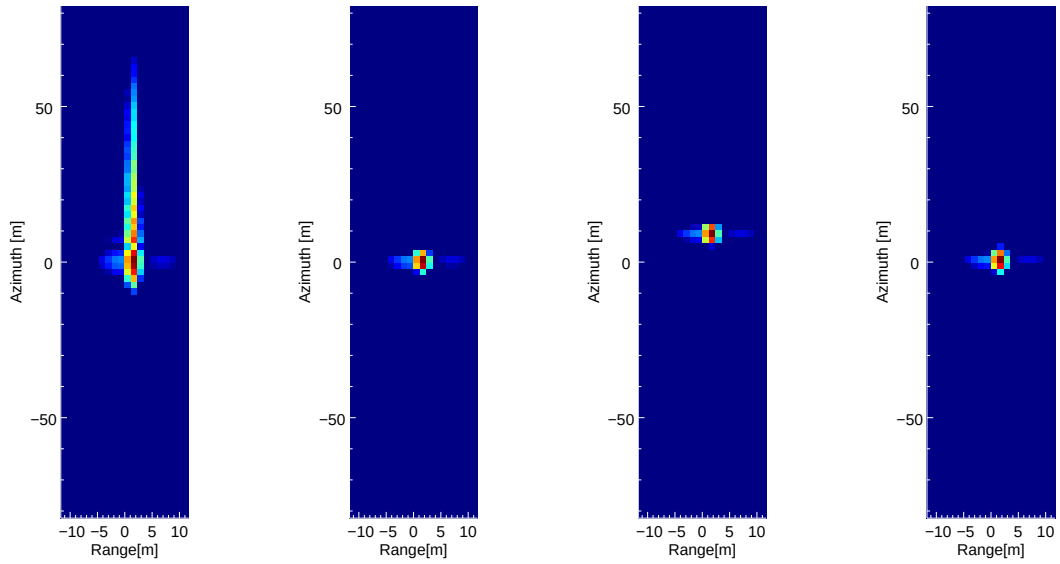

Fig. 4.13 SLC image before and after applying the autofocus algorithms: (a) Defocused SLC image with polynomial phase error. SLC image after phase compensation: (b) MAM, (c) PGA, (d) ICBA.

Table 4.3 Impulse Response width and peak value after applying the PGA, MAM, and ICBA algorithms.

Phase error function	**Defocus**		**MAM**		**PGA**		**ICBA**	
	W^*_{IRP}	P_{IRP}	W^*_{IRP}	P_{IRP}	W^*_{IRP}	P_{IRP}	W^*_{IRP}	P_{IRP}
No phase error	3.471	94.779	–	–	–	–	–	–
$\phi_{e1}(t)$	68.020	82.135	3.472	95.168	3.343	95.273	3.343	95.252
$\phi_{e2}(t)$	5.786	90.974	3.343	95.285	3.343	95.286	3.343	95.254
$\phi_{e3}(t)$	~ 250	81.851	9.129	88.543	3.343	95.271	10.023	86.885

* $W_{IRP} \pm 0.128$ [m]

Summary of the autofocus of a single point target with PGA, MAM, and ICBA algorithms

The three autofocus algorithms were able to improve the focus of the images. In the case of the quadratic and polynomial phase errors, all the algorithms achieve the same impulse response width as in the no phase error case. In fact, some of them even achieve a slightly narrower width that can be attributed to a finer adjustment of the nominal Doppler rate used for the compression of the signal in azimuth. Table 4.3 compiles the impulse response width and peak values of the azimuth profiles with and without the application of the autofocus algorithms. In this table, the compression of a signal without phase error and with the nominal parameters is included as a reference.

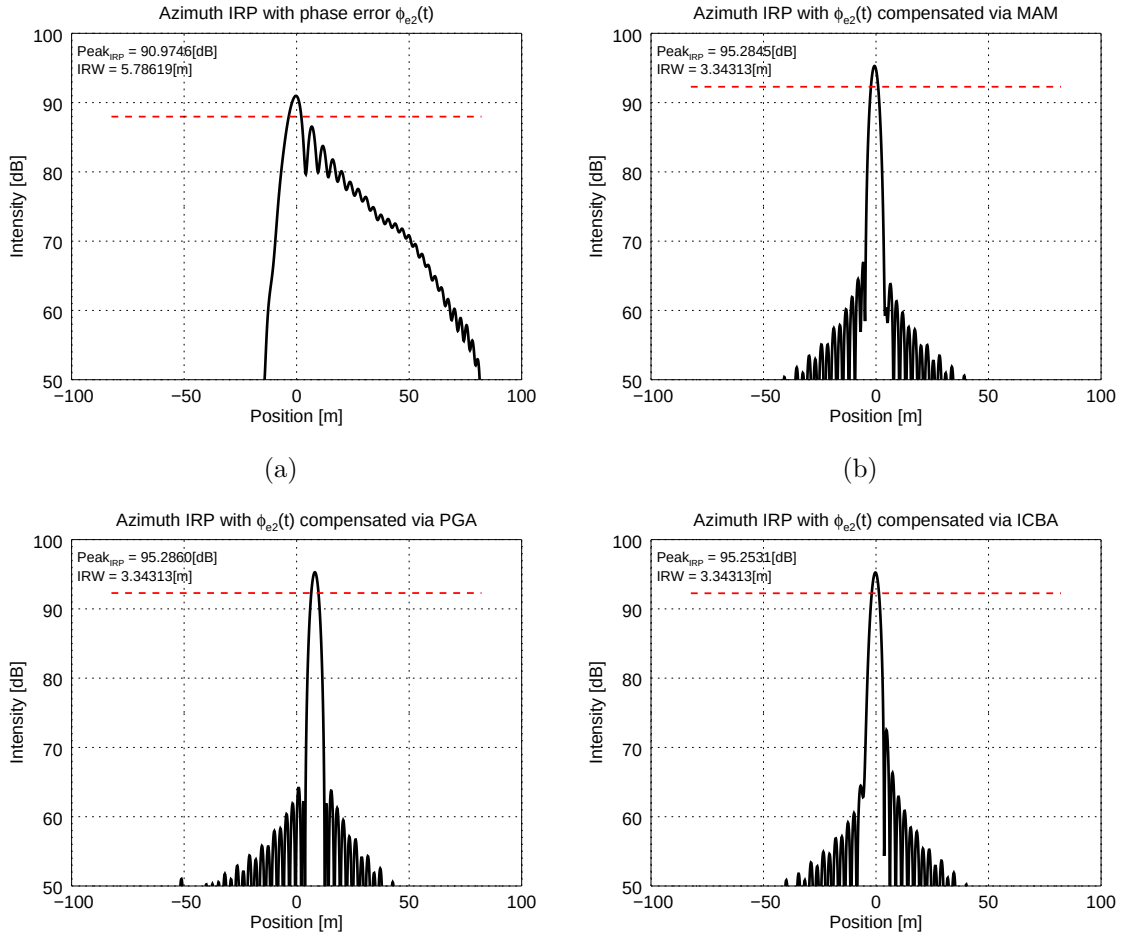

Fig. 4.14 Azimuth profile before and after applying the autofocus algorithms: (a) Initial defocused data with polynomial phase error. Profile after phase compensation: (b) MAM, (c) PGA, (d) ICBA.

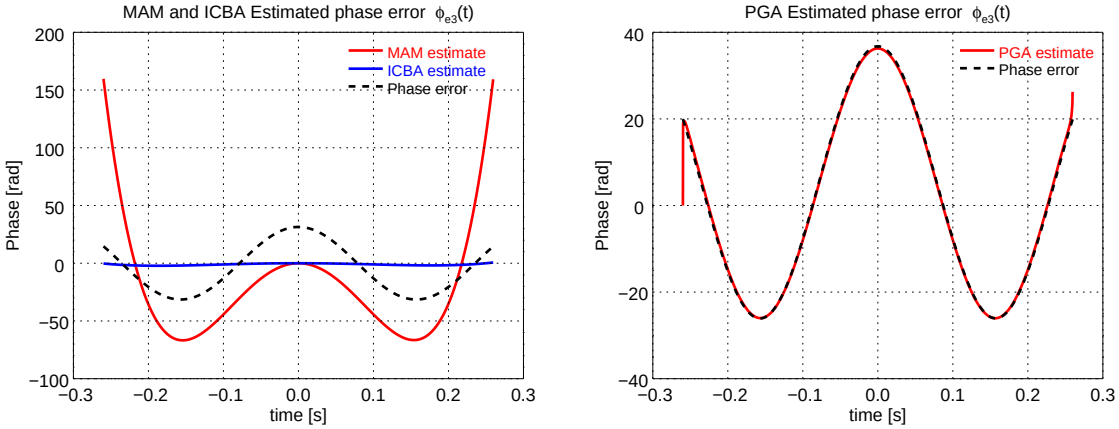

(a) (b)

Fig. 4.15 Estimated phase error by MAM, PGA, and ICBA for the high-order phase error case: (a) Estimated phase error by MAM and ICBA algorithms (b) Estimated phase error by PGA (linear trends removed).

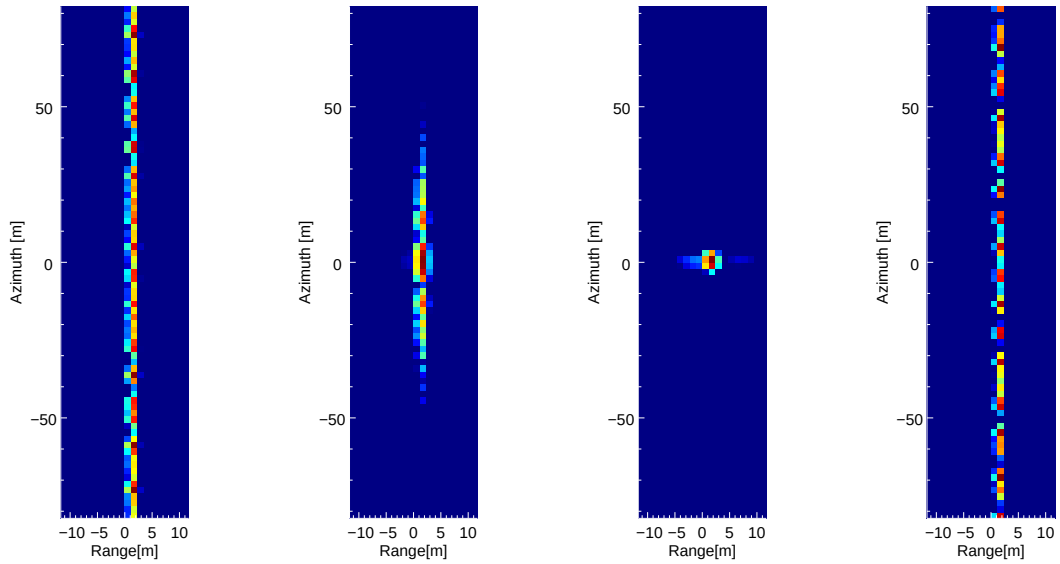

(a) (b) (c) (d)

Fig. 4.16 SLC image before and after applying the autofocus algorithms: (a) Defocused SLC image with QPE. SLC image after phase compensation: (b) MAM, (c) PGA, (d) ICBA.

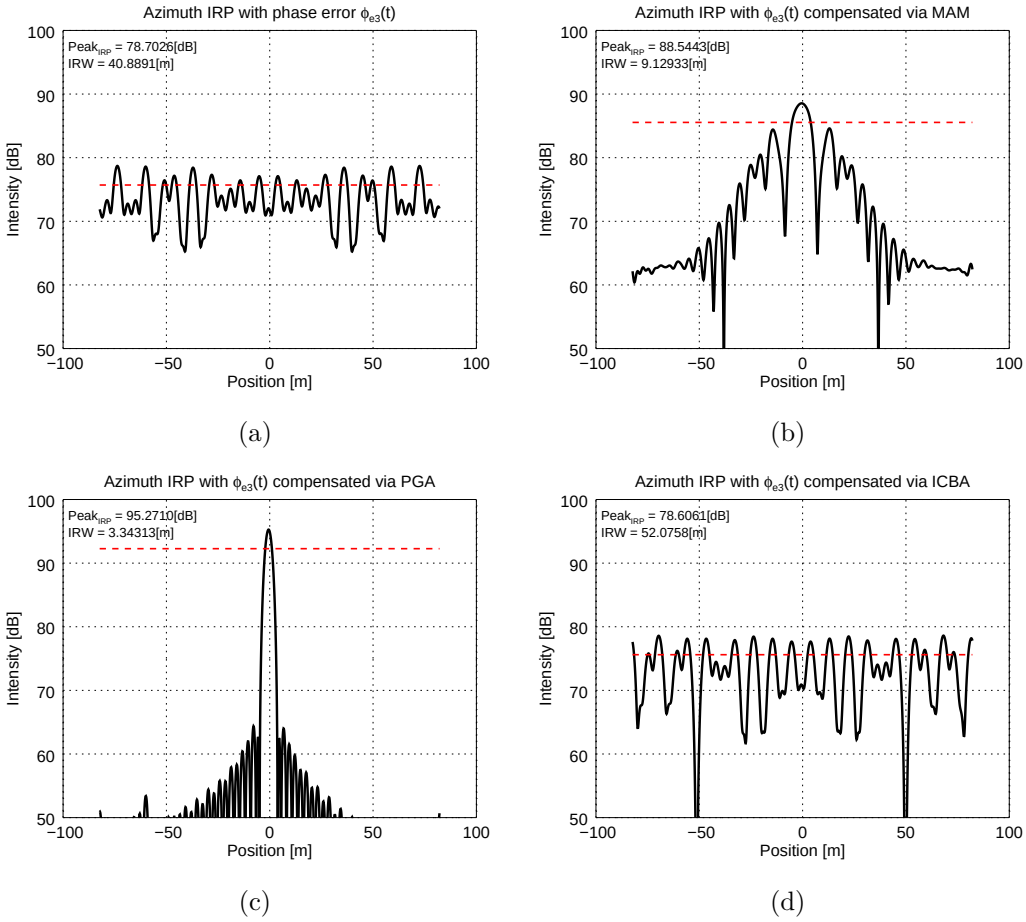

Fig. 4.17 Azimuth profile before and after applying the autofocus algorithms: (a) Initial defocused data with high-order phase error. Profile after phase compensation: (b) MAM, (c) PGA, (d) ICBA.

Note that the PGA technique is the only one that has a similar performance for the three phase error functions. However, this technique may introduce residual linear phase error terms that appear as a small shift that moves the SAR image in the azimuth direction as is illustrated in the Figure 4.14c. In fact, in the current case of using the phase compensation vector in the stripmap range-compressed data, the linear terms induce a shift in the Doppler spectrum of the SAR signal, and as a consequence produces the shift in the compressed SAR image. For typical implementation of PGA, these small shifts are not of interest because a single compensation phase error function is applied on all range bins, i.e. it is considered that all the range bins are affected by the same phase error. Nevertheless, the linear term becomes problematic when the PGA is applied to individual range bins of the same image, for instance, to compensate different defocus aberrations in individual range bins of a SAR signature of a vessel.

4.4 Application of the autofocus algorithms on real vessel SAR signatures

In an ideal case, the autofocus algorithm should be applied using the original raw data. However, when working with spaceborne SAR systems, this is not possible because access to data is often limited to the single-look complex (SLC) format. In fact, this was the case for the data available from the acquisitions during the NEREIDS project. Therefore, to apply the autofocus algorithms using SLC data, a decompression process in the azimuth direction is required. However, this new range-compressed signal would differ from the original one (i.e. before compressing) mainly due to the modifications of the spectrum in azimuth during the initial image formation process. A window is usually applied to the usable Doppler spectrum to reduce the sidelobes, noise, and the appearance of ambiguities in the final image at the expense of deteriorating the resolution [24]. Since the windowing process suppresses the tails of the spectrum, information outside the window will no longer be retrieved when using SLC.

4.4.1 Considerations when using SLC data

Windowing the Doppler spectrum has a more considerable effect on the signal of a non-static target. A shift of its Doppler spectrum may be induced by its motion (Section 5.4.1), and the application of a window centred in the Doppler centroid frequency of the whole scene may lead to a partial suppression of the target's spectrum (Figure 4.18a). This reduces the Doppler bandwidth of the azimuth signal, which may worsen the final resolution and the SNR. Thus, a refocused SAR signature from SLC data may be limited with regard to the resolution it can achieve due to the loss of information during the formation of the image [83].

For slow-moving targets such as vessels, the shift of their spectrum is a fraction of the PRF, so the deterioration of their signature resolution may be up to 20% for typical speeds

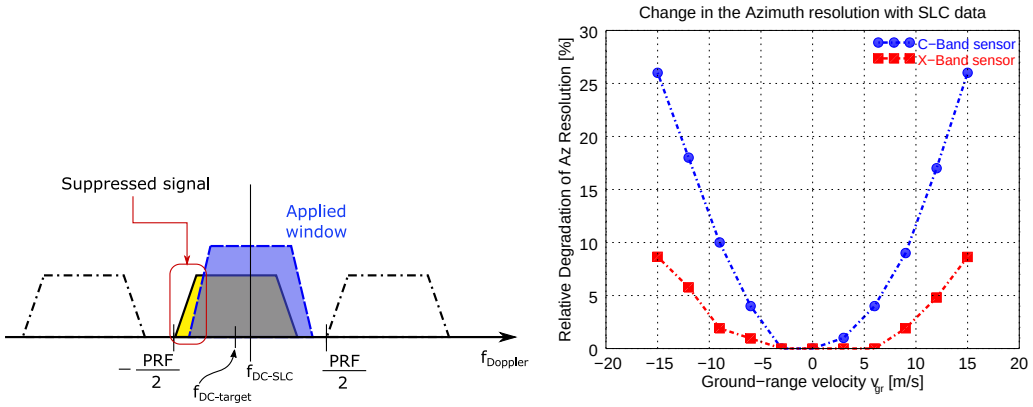

(a) (b)

Fig. 4.18 Effects of the Doppler spectrum windowing with moving targets: (a) Diagram of the windowing effect with a shift of the Doppler spectrum of the target. (b) Relative deterioration of the azimuth resolution for generic C- and X-band sensors due to the ground-range velocity

of the vessels in the ground-range direction. The actual value in each case would depend on the parameters of the acquisition and formation of the image such as the PRF, type of the window applied, and the effective bandwidth considered. For illustration, Figure 4.18b shows the relative deterioration of the azimuth resolution with respect to the static case from simulated raw data. The simulations were carried out with GRECOSAR for C- and X-band sensors with similar parameters to RADARSAR-2 and TerraSAR-X in stripmap mode (impulse response width of $W_{IPR}^{X} = 3.343$ [m] and $W_{IPR}^{C} = 10.531$ [m], respectively). Additionally, a corner reflector was used as a test target. It was simulated at different ground-range velocities in the range of $v_{gr} = \{-15[\frac{m}{s}], 15[\frac{m}{s}]\}$, which contains typical values of ground-range velocities expected for sailing vessels. Then, the plot in Figure 4.18b was obtained by measuring the impulse response width after processing the simulated stripmap raw data. The SAR processor used a Hamming window of length $0.9PRF$ in the Doppler domain for both C- and X-band sensors.

4.4.2 Refocus of SAR signatures from real SLC data

The MAM, PGA, and ICBA algorithms are used on stripmap SLC data of maritime SAR images from the acquisition campaigns of the NEREIDS Project carried out between 2013 and 2014. Small SLC chips cropped from the original image are used as the input images. Each of them encloses a high reflectivity structure (likely a vessel) that has been spotted on the sea surface by the Vessel Detection Tool (Section 3.3.2). Prior to the processing of these SLC chips, an azimuth decompression step is performed.

Every input SLC chip has different characteristics of reflectivity, content, and defocus. Consequently, the improvements in their quality by the autofocus algorithms are not assessed

Table 4.4 Summary of the characteristics of the set of twenty SLC chips

SLC chip #	**Sensor**	**Resolution** [m]	**Incid. angle**[°]	**Zone**
1 - 10	RADARSAT-2	2.66×2.99	$42.75 - 48.15$	Alesund
11 - 15	COSMO-SkyMed	3.00×3.00	$44.42 - 56.21$	Gulf of Guinea
16 - 19	COSMO-SkyMed	3.00×3.00	43.15	Lampedusa
20	RADARSAT-2	1.33×2.09	40.67	Senegal

in the same way as in Section 4.3 due to the more complex signature of the vessels. Instead, similarly to [84], the intensity peak value and the image contrast are used as the parameters to quantify the degree of refocus of the image.

The autofocus algorithms are applied to a set of twenty SLC chips (with different degrees of defocus) that belong to SAR images of RADARSAT-2 and Cosmo-SkyMed constellation acquisitions of the sea surface in different parts of the world (Table 4.4). For every SLC chip, the algorithms employ only one subset of range bins containing the brightest scatterers that belong presumably to the structure of interest. For the current processing procedure, only the range bins that contains scatterers above the threshold of -5 [dB] with respect to the brightest one are selected. Once the phase error has been estimated, the same phase compensation is applied to all the range bins of the SLC chip to focus the image. The MAM and PGA are applied for ten iterations, and for the ICBA and MAM, a 4^{th} order polynomial is considered. Additionally, a special consideration is made when applying the MAM algorithm. It was observed that setting an *a priori* fixed number of sublooks may not lead to the best results for a random image due to the trade-off between the number of sub-looks and the deterioration of the SNR. Then, the MAM was applied for 2, 3, and 4 sublooks in the same image, and the best output was chosen based on the maximum image contrast achieved. Figure 4.19 and Figure 4.20 depict the peak-intensity gain and the image contrast, respectively, after the application of the autofocus algorithms. Additionally, Figures 4.21 to 4.23 show examples of the SLC chips from this test set before and after refocusing. For each example, the original SLC chip is followed by the refocused ones after applying the autofocus algorithms.

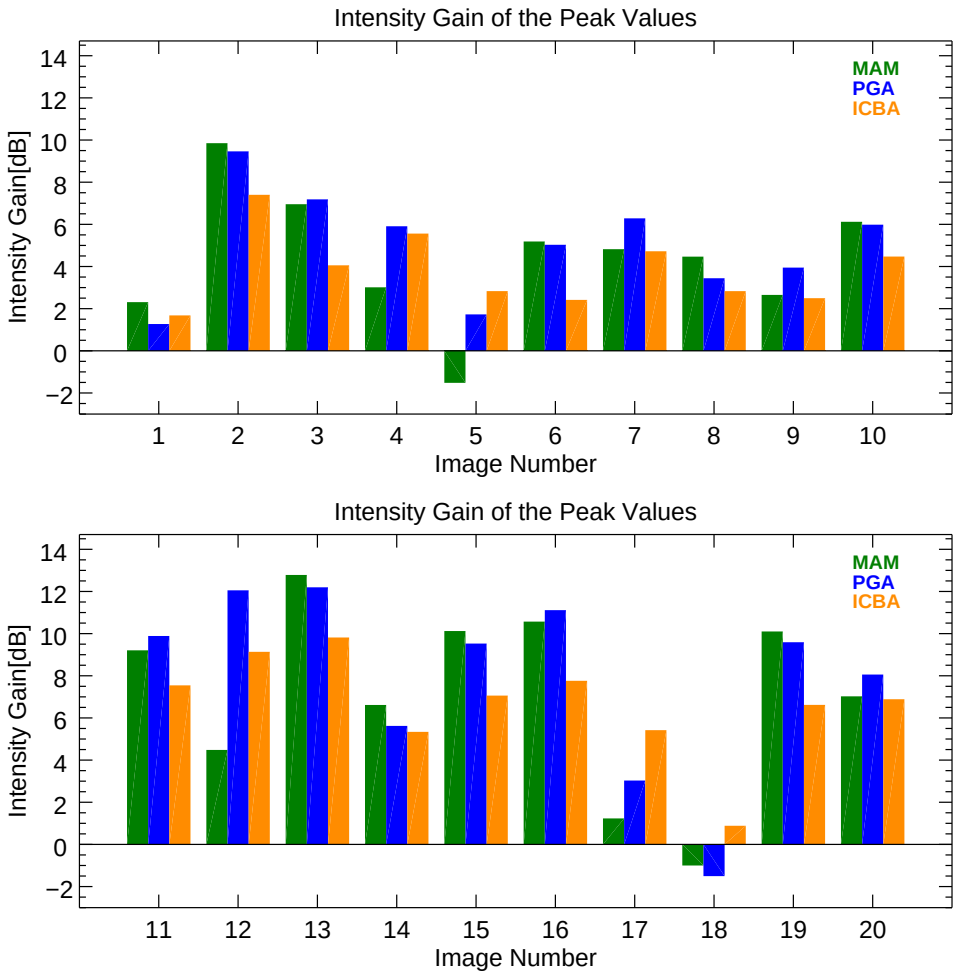

Fig. 4.19 Intensity gain of the peak value after the application of the autofocus algorithms in a test set of 20 SLC chips

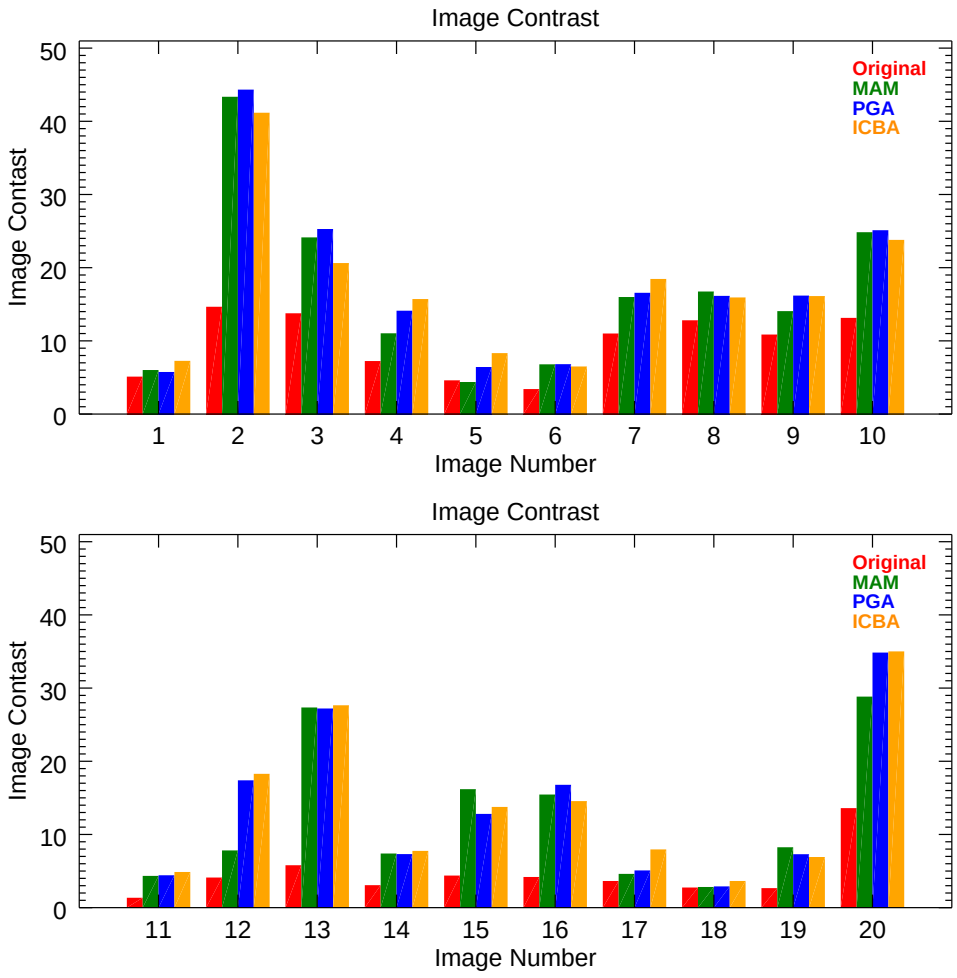

Fig. 4.20 Image contrast after the application of the autofocus algorithms in the image test set

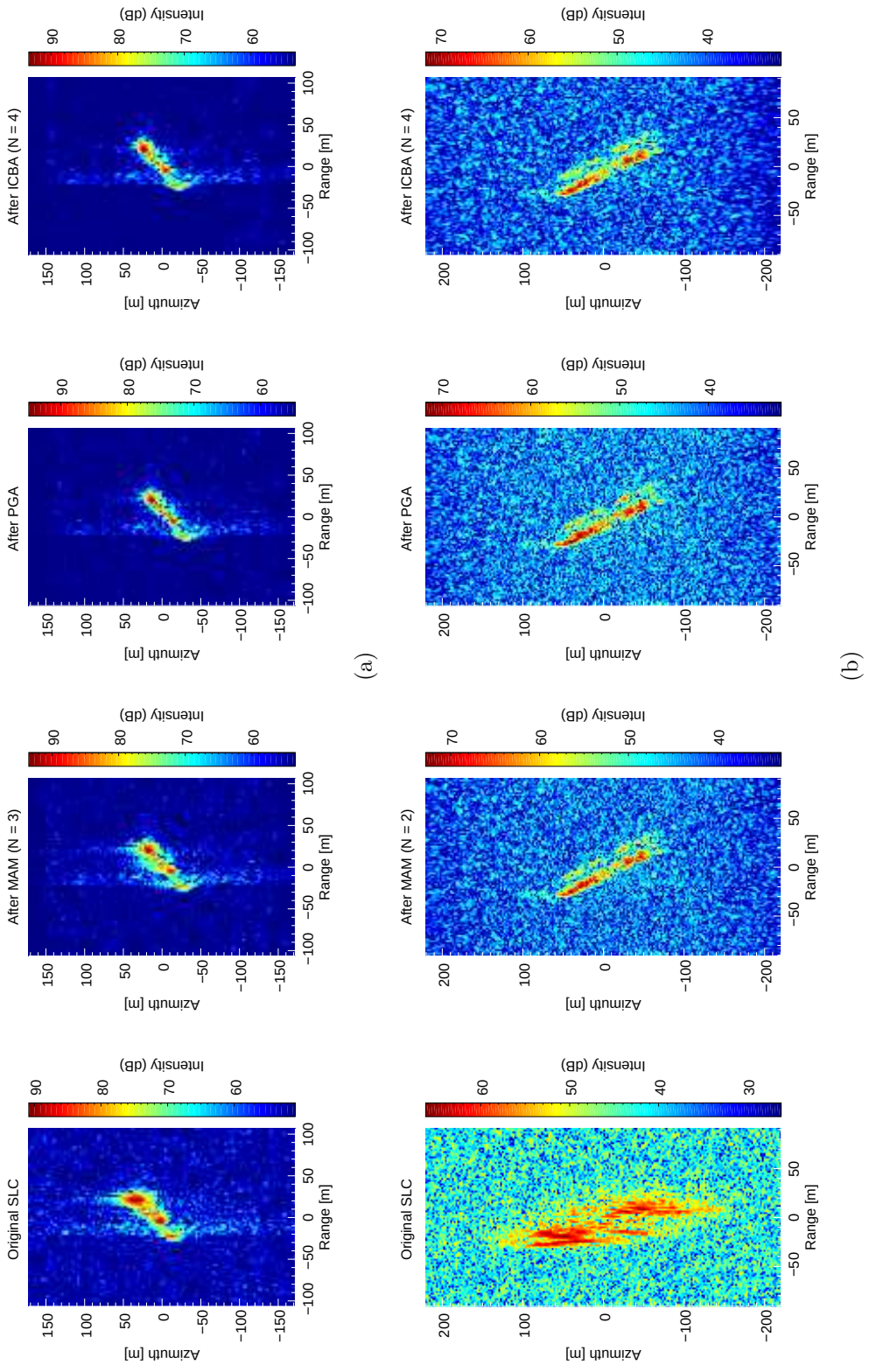

Fig. 4.21 Examples of SLC chips from the test set after the application of autofocus algorithms: (a) SLC Chip 9; (b) SLC Chip 14

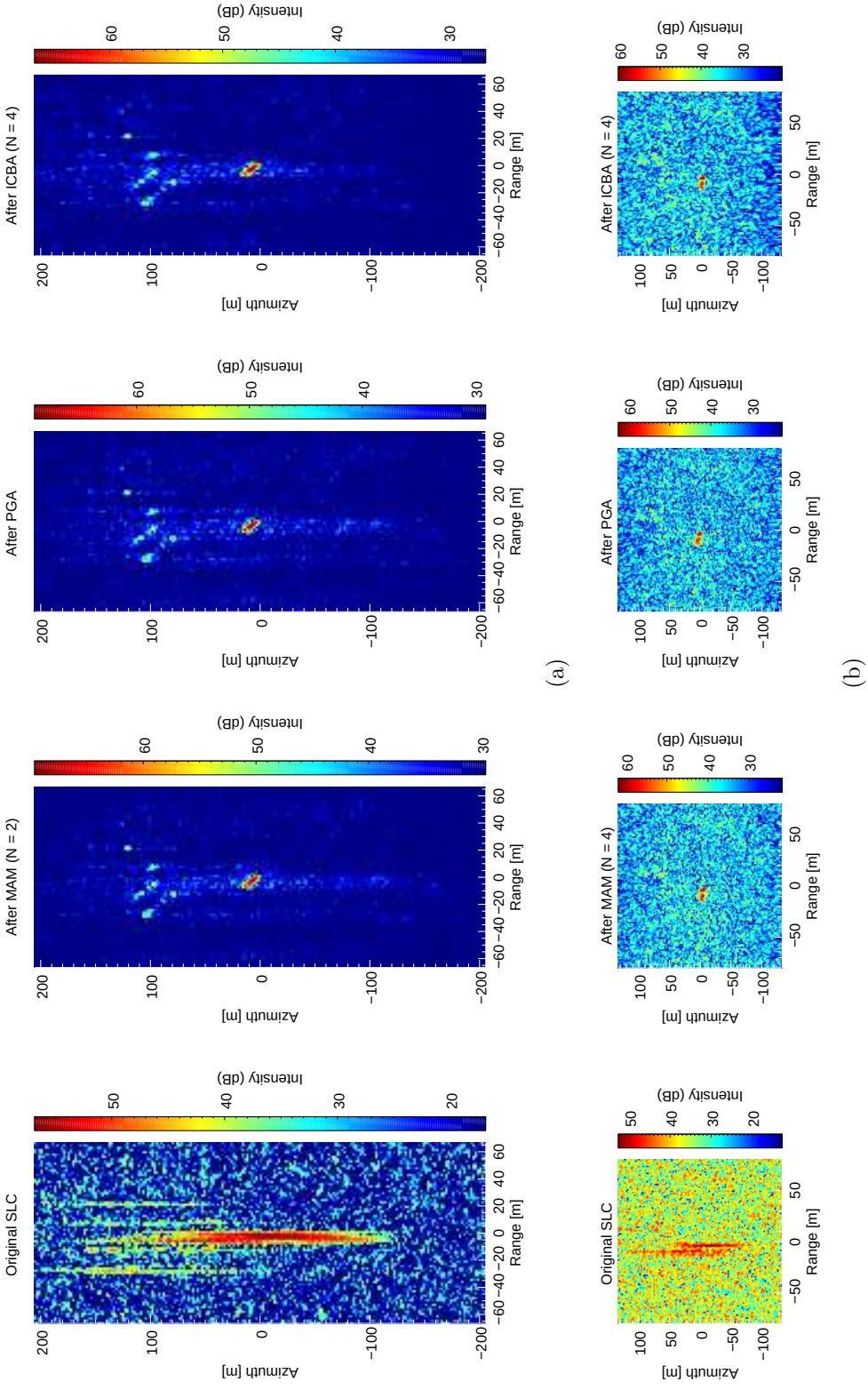

Fig. 4.22 Examples of SLC chips from the test set after the application of autofocus algorithms: (a) SLC Chip 13; (b) SLC Chip 11

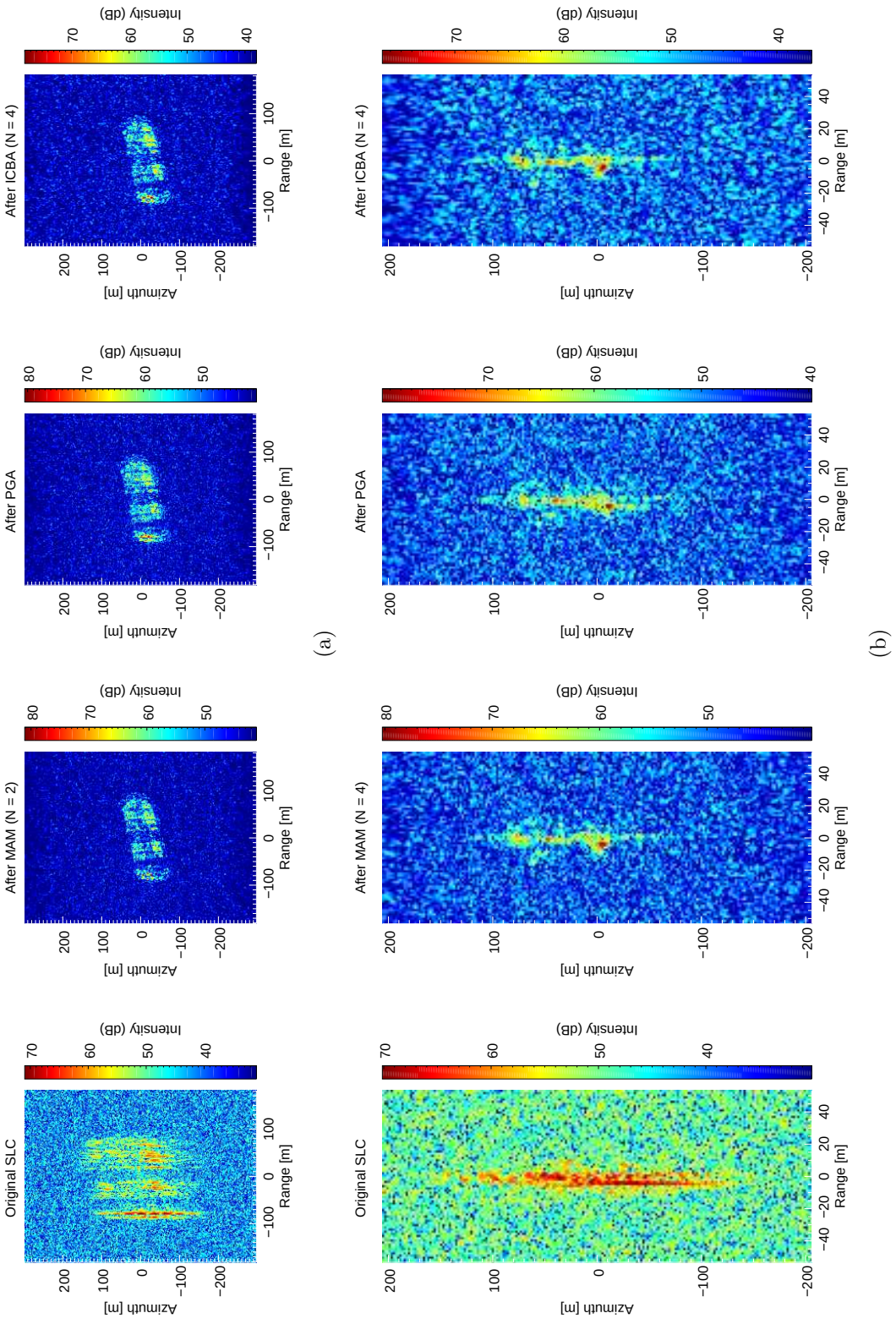

Fig. 4.23 Examples of SLC chips from the test set after the application of autofocus algorithms: (a) SLC Chip 15; (b) SLC Chip 19

Independent range-bin application mode autofocus

In general, by considering the traditional implementation of the autofocus algorithms, which assumes that the same phase error affects the whole signature, the processed images tend to have a better focus than the originals. This is particularly noticeable when the defocus is severe in all of the target signatures as in Figure 4.22a. But in cases where the structure of the vessels is defined, assuming a single phase error for the whole signature may lead to unwanted sectional defocus. Figure 4.24b shows an example of this phenomenon. The shape of a vessel is mostly well defined, but since the classical implementation of the algorithms employs the stronger scatterers, the processed image tends to focus the brighter cluster of pixels while defocusing the right section of the signature. This indicates that the signature does in fact present different degrees of defocus along the range direction, which can be attributed to possible rotational motion of the vessels.

In this thesis, the proposal to overcome the problem of sectional defocus is to apply the autofocus algorithms in an independent range-bin mode. Instead of their classical implementation, the algorithms are applied considering each range bin separately, obtaining a phase error function for each of them. In this way, the vessel signature is processed and focused according to the possible variation of the phase error function along the range direction. Figure 4.24c shows an example of using the MAM algorithm in each range bin independently (similar results are obtained for PGA and ICBA). Note that the final shape of the SAR signature resembles more closely the rectangular shape expected for a vessel.

The performance of this approach is compromised by the content of the SAR signature. It has been observed that the best refocus of the SAR signature occurs when there is a small cluster with very high reflectivity in each range bin as in Figure 4.24. In this case, a quasi-ideal target condition for the three algorithms is fulfilled, and the focus preserves the distribution of the signature along the range direction. In contrast, other conditions affect each of the autofocus algorithms differently. For instance, in the presence of SAR signatures with several clusters along the range bins, the PGA algorithm tends focus only the strongest scatterer in each bin as it is part of the core of the phase error estimation process (Section 4.2.2). For MAM and ICBA, the variation in the SNR of each range bin affect the estimate of the phase error function of consecutive range bins, which may break the continuity of the distribution of the scatterers along the range direction and create a jagged outline of the SAR signature of the vessel. Figure 4.25 illustrates an example of these unwanted effects after the application of the autofocus algorithms in an independent range-bin mode for a typical SAR signature. It is worth noting that the image contrast and the peak-intensity value of the processed image is higher than in original, but the distribution of the scatterers is what ends up deteriorating the quality of the final image.

In summary, for a random SAR signature of a vessel, the best performance is obtained by applying the autofocus algorithms as described in Section 4.2; only after identifying suitable

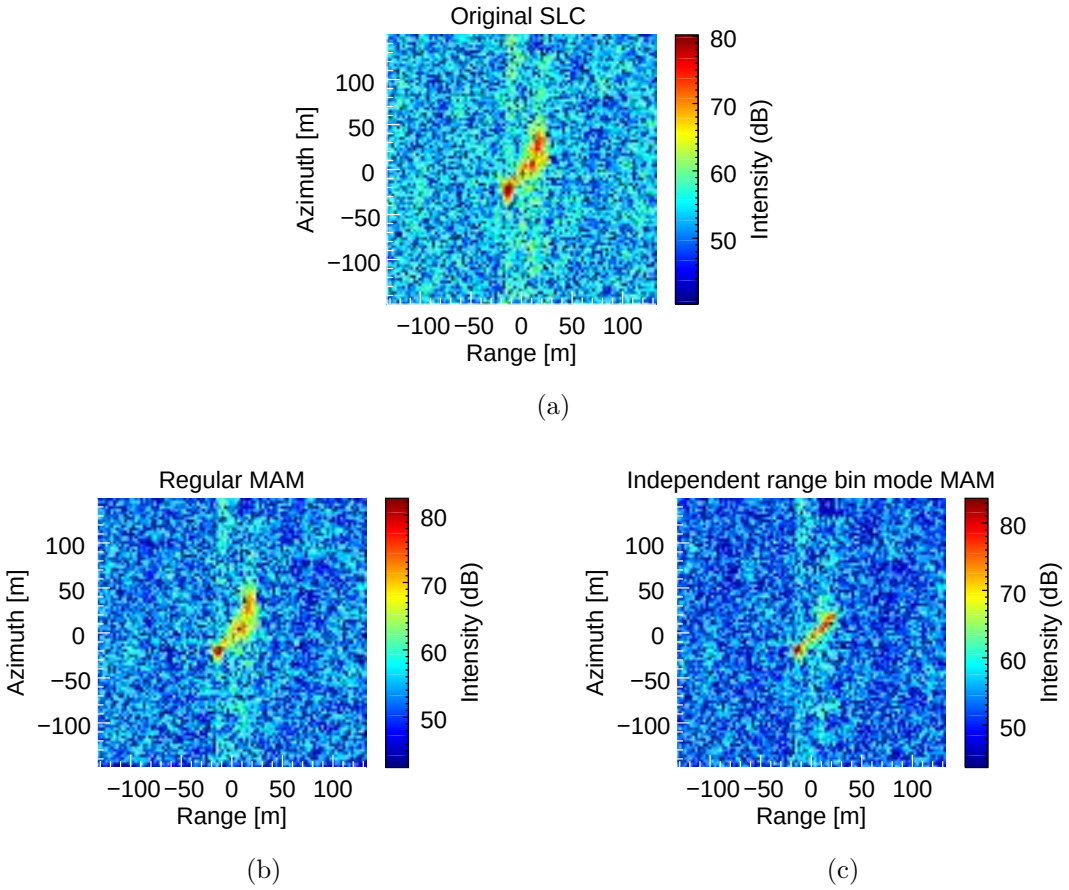

Fig. 4.24 Example of the application of the autofocus algorithms in an independent range-bin (IRB) mode: (a) Original SLC chip; (b) typical application of the autofocus algorithm; (c) independent range-bin mode

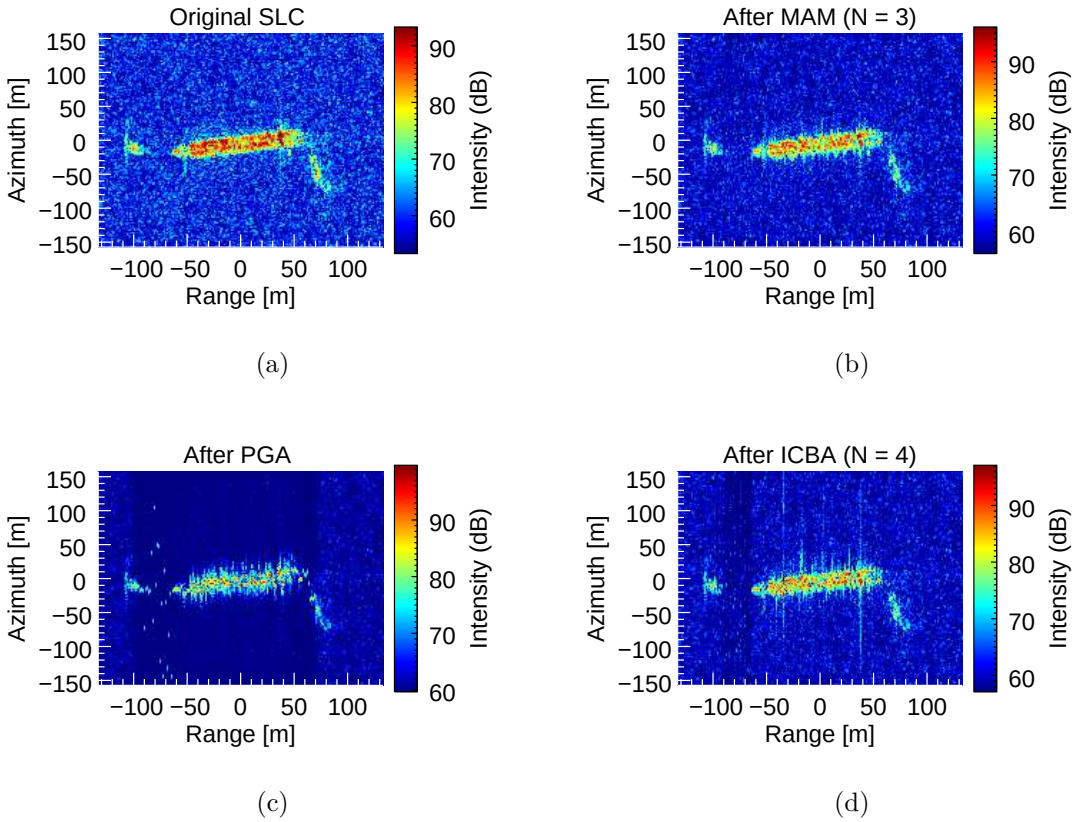

Fig. 4.25 Unwanted effects after applying the autofocus algorithms in an independent range-bin mode: (a) original SAR signature; (b) MAM; (c) PGA; (d)ICBA

SAR signatures, can the independent range-bin mode be applied to further improve their focus.

4.5 Summary

Autofocus techniques allow the improvement of the focus of the final image by automatically estimating the phase errors from the SAR signal. They are commonly applied in the azimuth direction due its sensitivity to the phase errors that result from the differences between the model of the range variation and its actual evolution. Second and higher order phase errors are usually the ones that the autofocus techniques aim to estimate and compensate. In the presence of these type of phase errors, the deterioration of the SAR image appears in the form of blurring artefacts.

In the case of spaceborne SAR sensors, the platform trajectory is virtually stable, so one can assume that, after the proper processing of the image, localized blurring artefacts are mainly produced by targets in motion. These effects are commonly appreciable in the SAR

signatures of vessels in maritime SAR images. The application of the autofocus techniques to the SAR signatures of the vessels can enhance their quality, so they can be used later to extract a more reliable estimation of features such as the length or breadth of the vessel.

Three widely used autofocus techniques were implemented to compensate the defocus in the azimuth direction: phase gradient autofocus (PGA), multiple aperture mapdrift (MAM), and the image contrast based autofocus (ICBA). The first one follows a non-parametric approach; it does not assume an explicit model of the phase error function, which means that, in theory, it could compensate arbitrary high order phase errors. The others follow the model-based approach by assuming an *a priori* polynomial function to model the phase error. A preprocessing step was considered for the chips of stripmap SAR data in the cases of PGA and MAM, so they can be implemented in their normal way. The stripmap range-compressed (with RCMC) data was adapted via a dechirping process. This results in range-compressed SLC chips whose complex image and azimuth phase history are Fourier transform pairs, which is the condition expected in PGA and MAM.

The validation of the implemented autofocus techniques were carried out for different cases of azimuth phase error functions. These phase functions were inserted into the stripmap SAR data of a corner reflector simulated in GRECOSAR. In all of the cases, the three autofocus algorithms were able to refocus the image correctly, except in the case of the high-order phase error function. There, only PGA was able to do it. This was expected since the other algorithms are constrained by the polynomial phase error model that they assume. Additionally, it was observed that PGA may introduce a linear phase component in the obtained phase error function. This linear term is attributed to the result of the integration of the estimated gradient function with a residual constant value.

A set of SLC chips from RADARSAT-2 and Cosmo-SkyMed acquisitions were used to refocus the enclosed SAR signatures of the vessels. In every SLC chip, the algorithms employ only a subset of range bins with the brightest scatterers that belong presumably to the structure of the vessel. Once the azimuth phase error function has been estimated, a single compensation function is applied to all of the range bins of the SLC chip to refocus the SAR signature. In general, both the peak-intensity value and the image contrast of each SLC chip improved after the application of any of the three autofocus techniques. In fact, a gain of up to 10 dB in the peak-intensity value was obtained in some cases. Additionally, it was observed that PGA and MAM achieved slightly higher gain in the final peak-intensity value, which indicates that this algorithms tended to better concentrate the energy in most of the cases of the data set used. However, it has been observed that the performance of the algorithms depends on the content of the image. The presence of scatterers with different phase errors jeopardizes the correct refocus of the images when using a single correction function. Moreover, if the scatterers with different defocus are in the same range bin, the performance of the autofocus algorithms would likely deteriorate since this goes against the

assumptions of their implementations. Examples of the effects of scatterers with different defocus can be seen in the reduction of the intensity peak value of SLC chips 5 and 18.

In this thesis, the application of the autofocus techniques in an independent range-bin (IRB) mode is proposed. The algorithms are applied considering each range bin separately, obtaining and compensating a phase error function for each of them. As a result, the different degrees of defocus in the SAR signature can be partly compensated. Again, the performance of this approach is compromised by the content of the SAR image. In the case of SLC chips of the data set, the best refocus of the SAR signature was obtained in cases where there is a small cluster with very high reflectivity per range bin. Then, using the autofocus algorithms in IRB mode the focus of the SAR signature can be further improved, but user supervision is required to identity the cases where this can be applied.

Chapter 5

Feature extraction: dimensions, heading, and ground-range velocity

5.1 Introduction

For maritime surveillance systems, it is often advantageous to identify the type/category of the detected vessels and to know their likely sailing behaviour. Consequently, getting as much information as possible about specific targets in SAR imaging has been an active area of research, although the development of high-resolution SAR systems for civil applications is relatively new; this makes target feature extraction a still-emerging research area. Nowadays, it is possible to obtain SAR images with finer details from spaceborne SAR systems that could be used to classify the detected vessels into a type or category. In general, the features that are usually considered for classification are the dimensions of the detected targets and their reflectivity distribution [33].

The most straight-forward way of roughly identifying the vessel through its SAR signature is by estimating its length and width (breadth). The idea is to isolate the SAR signature of the vessel from the sea clutter, and then to estimate its dimensions. For the single-channel image case, the method is usually applied to the image domain by exploiting the high reflectivity of the vessel signature and using a combination of techniques such as segmentation, clustering, and morphological operations. Then, the estimated dimension is usually used as part of a feature vector that contains additional information on the reflectivity of the SAR signature [53, 54, 85]. However, getting reliable information about the scattering distribution for the classification of the vessels is still a challenging problem to tackle due to the fluctuation of their reflectivity as a function of the angle of observation [34]; the aim of recent research works is to figure out the best scattering features to use when classifying with high-resolution SAR sensors [52, 55, 57]. For now, the estimated dimensions of the vessel are still fundamental for their classification.

Another parameter of interest for surveillance systems using SAR imaging is the motion of the vessel. By estimating the likely sailing direction of the vessel, changes in the expected routes and anomalous behaviour could be detected. In the case of spaceborne SAR systems and slow-moving targets such as vessels, the radial component of the velocity of the vessel may significantly affect the respective azimuth SAR signal; it induces shifts in the Doppler spectrum of the target which translates to azimuth shifts in the final SAR image [22]. Then, by measuring these shifts in the image, the range velocity component can be retrieved. Classical methods measure the shifts by using the relative distance between the vessel and its wake in the image [86, 87]. However, it is not always possible to detect the wake in the SAR image and other effects in the SAR signal have to be analysed, for instance, modifications in the Doppler spectrum as is done in this work.

This chapter presents the extraction of features using the SAR signature of vessels from stripmap data of single-channel spaceborne SAR sensors. First, Section 5.2 describes a method that uses the statistical modelling of the sea clutter to extract, in an unsupervised manner, the vessel's contour and its real dimensions, which can be used later as a parameter for the identification of the type of vessel. Then, a proposed method for the computation of their heading based on the orientation of the signatures and ground-range velocities is described in Section 5.3. Finally, Section 5.4 reviews the effects of the vessel's velocity components in the SLC SAR image, and discusses the limitations in estimating these components in the single-channel case. It is shown that the along-track velocity of the vessel mainly affects the quadratic phase term of the SAR signal, although its effects are expected to be negligible in the case of typical low speeds of medium/large vessels and spaceborne SAR sensors. Thus, this section is focused mainly on the estimation of the range velocity component by exploiting the spectral information, and analysing the effects of using range-compressed data and SLC data.

5.2 Unsupervised extraction of the dimensions of the vessel

Once a vessel has been detected in the SAR image, it is advantageous to know more about its features (e.g. family type, orientation, motion) and, if possible, to find them out in an automatic way, in order to minimize time spent obtaining them manually for each detection. An algorithm has been developed to work with the detection interface (Section 3.3.2), estimating the length and width of the SAR signature of each target. This algorithm could be summarized as follows:

1. Obtaining the contour of the SAR signature of the vessel.
   (a) Preliminary masking (using a rough model of the statistic of the sea clutter).
   (b) Refined modelling of the statistics of the sea clutter.

(c) Extraction of the contour of the vessel's signature.

2. Computation of the enclosing box for the contour.

3. Geocoding of the vertices of the box to get the dimensions in ground-range of the SAR signature of the vessel.

As implemented, the algorithm assumes that a single SAR signature is present in the processed SLC chip, i.e. it is known *a priori* that there is a vessel in the input image. This is a consequence of its implementation with the detection interface that separates each target into individual chips. In the following sections, further details about the characteristics of the input images and the extraction of the vessel's dimensions are presented.

5.2.1 The statistical model of the sea clutter in SLC SAR images

Statistical distributions such as K, Weibull, and Log-normal are well-known for modelling reflectivity of the sea clutter in SAR images [21, 42]. However, the Weibull distribution was selected because of two attractive characteristics. Firstly, the distribution is able to model the statistics of the sea clutter observed in the vast majority of the SLC chips of high resolution SAR images. Secondly, it is analytically tractable, i.e. its cumulative distribution function (c.d.f.) is expressed in a closed form. Thus, using IDL® in-built routines to fit the theoretical model with the empirical data, the estimation of the parameters of the distribution becomes easier.

The c.d.f. of the Weibull model is defined as [88]

$$F_X(x|a,b) = 1 - e^{-(\frac{x}{a})^b} \tag{5.1}$$

and its probability density function (p.d.f.):

$$f_X(x|a,b) = \left(\frac{b}{a}\right)\left(\frac{x}{a}\right)^{b-1} e^{-(\frac{x}{a})^b} \tag{5.2}$$

a being the scale parameter, b the shape parameter, and X the random variable that represents the amplitude of the reflectivity of the sea clutter. However, it is also useful to work with intensity SAR images in dB for the interpretation of the image. In these cases, a change of variable is required in the distribution model such as

$$Y = 20\log(X); \qquad X > 0 \tag{5.3}$$

Since the logarithm is a monotonically increasing function, the change can be done directly to the c.d.f. Thus, the so called log-Weibull distribution is obtained with its c.d.f as (Appendix A.1)

$$F_L(y|\alpha,\beta) = 1 - e^{-e^{\beta(y-\alpha)}} \tag{5.4}$$

and its p.d.f.:

$$f_L(y|\alpha,\beta) = \beta e^{\beta(y-\alpha)-e^{\beta(y-\alpha)}} \tag{5.5}$$

α and β being the new scale and shape parameters, respectively, and y representing the reflected intensity in dB. This log-Weibull distribution will be used to model the sea clutter in the intensity SAR images in dB.

5.2.2 Contour of the SAR signature of the vessel

Preliminary masking

In order to obtain the contour of the vessel, we need to separate it from the sea clutter. The *a priori* knowledge of the content of the input image can make it easier to get the contour of the vessel's signature automatically. In each of these images, it is expected that there is a single vessel and that most of the pixels belong to the sea clutter. Assuming these conditions, we use the log-Weibull model and roughly estimate a threshold, T_0, that will be the basis for obtaining a preliminary mask. In this way, we would be able to separate the pixels of the sea clutter from those of the vessel and its surroundings. Since we do not know the statistical model of the target, it is not possible to follow the classical Neyman-Pearson approach to obtain the threshold [89]; instead, T_0 is computed by defining a relaxed probability of false alarm (e.g. $PFA = 0.95$) and solving the equation

$$PFA = \int_{T_0}^{\infty} f_L(y)dy \tag{5.6}$$

$f_L(y)$ being the log-Weibull distribution. Alternatively, since its c.d.f. can be inverted, the threshold can be computed via the log-Weibull inverse distribution function derived from equation (5.4) as

$$T_0 = \frac{1}{\beta}\ln\left[\ln\left(\frac{1}{1-P_{fa}}\right)\right] + \alpha \tag{5.7}$$

Figure 5.1 shows an example of a typical input intensity image (in dB) and its empirical p.d.f along with the respective log-Weibull model. Additionally, the threshold for a $PFA = 0.95$ is also depicted in the distribution plots.

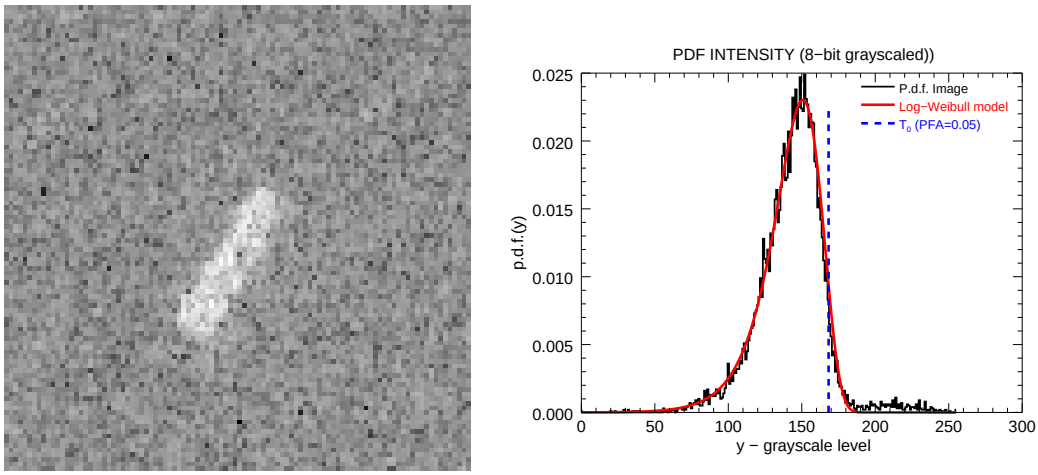

(a) (b)

Fig. 5.1 Input intensity image in dB: (a) gray-scaled intensity image in dB; (b) Empirical p.d.f. and its corresponding log-Weibull model of the whole intensity image.

The threshold T_0 is used to decide whether the pixels belongs to the vessel using the simple decision rule

$$\mathbf{M_0}(i,j) = \begin{cases} 1 & \mathbf{I_{input}}(i,j) \geq T_0 \\ 0 & \mathbf{I_{input}}(i,j) < T_0 \end{cases} \tag{5.8}$$

where $\mathbf{I_{input}}$ is the intensity SAR image with i and j as the indices of its pixels, and M_0 as the direct mask obtained after applying the threshold (Figure 5.2a). The pixels that belong to the vessel are expected to form either a big cluster or a group of about the same size (for cases of more complicated SAR signatures). Then, $\mathbf{M_0}$ still needs to be enhanced.

The mask can be improved using digital image processing techniques for filtering and geometrical analysis. For example, the morphological operations of *Opening* and *Closing* can be applied to $\mathbf{M_0}$ in order to obtain the main cluster(s). These operations are combinations of *dilation* and *erosion*, which in turn are fundamental operations in mathematical morphology [90]. For a given structuring element, Opening consists of the application of the dilation operation followed by the erosion operation; as a result, the pixel arrays that are smaller than the structuring element are deleted. As for Closing, this consists of the application of the erosion operation followed by the dilation operation, resulting in the holes that are smaller than the structuring element being filled.

For the mask $\mathbf{M_0}$, the Opening operation is performed to eliminate very small and thin arrays of pixels, followed by the Closing operation to fill in small holes inside the cluster or gaps between neighbouring clusters. Then, the cluster with the highest number of pixels is selected. In some special cases, more than one cluster is selected if they have similar numbers of pixels, because they can be considered to be a fraction of a main cluster. Figure 5.2b shows the enhanced mask $\mathbf{M_0}$ after applying the morphological operations.

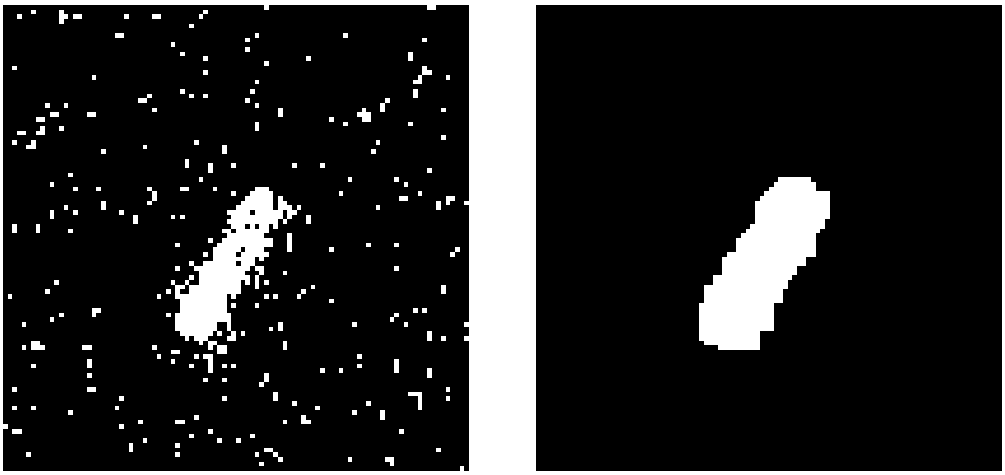

(a) (b)

Fig. 5.2 Preliminary mask: (a) Preliminary mask considering only threshold T_0; (b) Enhanced preliminary mask after morphological operations and clustering.

Final masking

Once we have the preliminary mask, a more precise model of the statistics of the sea clutter can be computed. The $\mathbf{M_0}$ mask is used to isolate the pixels that belong only to the sea clutter; then, the parameters of the statistical model are estimated again. Figure 5.3a shows the empirical p.d.f. and the new log-Weibull model by considering only the sea clutter pixels after applying the $\mathbf{M_0}$ mask to the input image used before. Additionally, a probability-probability plot (P-P plot) is shown in Figure 5.3b as a qualitative way of assessing the agreement of the distribution of the clutter with the log-Weibull model; in an ideal case, this P-P plot should follow a straight line. Similar results have been observed for the different input images.

The refined log-Weibull model is used to get the final mask that traces the contour of the vessel's signature. Now, a similar procedure to that done for the preliminary mask is carried out again. First, a threshold T_1 is computed via equation (5.7), but in this case, a more restrictive PFA is used (e.g. $PFA = 10^{-6}$). Then, the selection of the pixels is based on T_1 to obtain the new mask $\mathbf{M_1}$, and morphological operations and clustering are applied. Figure 5.4 shows the final mask $\mathbf{M_1}$ obtained in an unsupervised way to separate the pixels of the SAR vessel signature and its contour in the input image.

5.2.3 Computation of the bounding box and dimension extraction

Most of the SAR signatures of medium and large vessels present a quasi-rectangular shape in real maritime SAR images. Therefore, the rectangular shape is assumed as a bounding geometry to be found based on the points of the contour, C_v, of the vessel's SAR image.

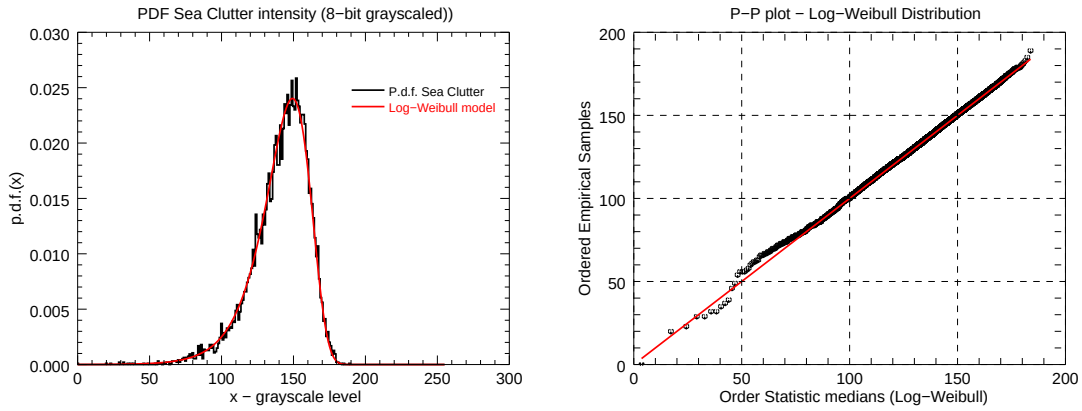

(a) (b)

Fig. 5.3 P.d.f. of the sea clutter pixels after applying the preliminary mask $\mathbf{M_0}$ on the input image. (a) Empirical p.d.f. and the log-Weibull model obtained; (b) Probability-probability plot using the log-Weibull model.

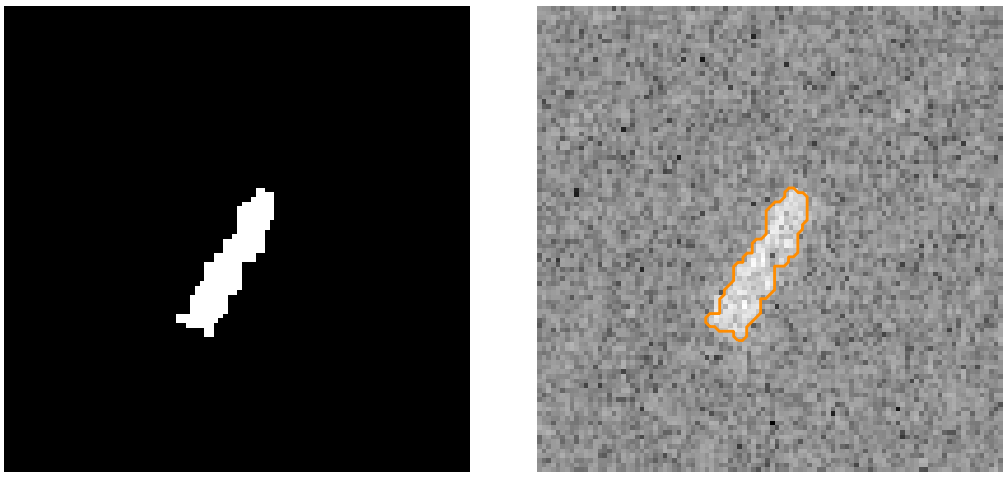

(a) (b)

Fig. 5.4 Contour of the SAR signature of the vessel from the unsupervised algorithm. (a) Final mask $\mathbf{M_1}$ that separate the pixels of the vessel; (b) Intensity input image with the contour computed.

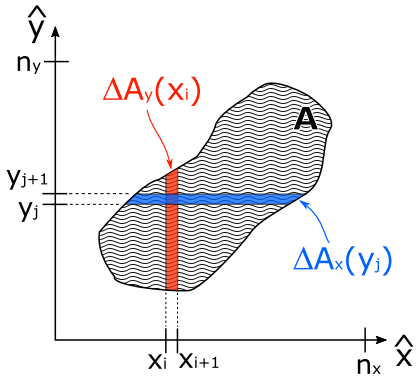

Fig. 5.5 Diagram of the reference system to compute the centre of mass of a vessel SAR signature.

The *centre of mass*, P_{cm}, of the vessel's SAR signature is computed to define the position of the bounding rectangle. By considering the reference system shown in Figure 5.5, the coordinates of $P_{cm} = (x_{cm}, y_{cm})$ are computed as

$$x_{cm} = \frac{1^{st} \text{ Moment about the y-axis}}{\text{Total mass}} = \frac{\sum_{i=0}^{n_x-1} x_i \Delta A_y(x_i)}{A_{total}} \tag{5.9}$$

$$y_{cm} = \frac{1^{st} \text{ Moment about the x-axis}}{\text{Total mass}} = \frac{\sum_{j=0}^{n_y-1} y_j \Delta A_x(y_j)}{A_{total}} \tag{5.10}$$

where x_i and y_j represent the pixel position on the respective axis, n_x and n_y the number of pixels in the x and y direction, respectively; $\Delta A_y(x_i)$ and $\Delta A_x(y_j)$ are the sum of the value of the pixels of the SAR signature along a given position on the x- or y-axis, and A_{total} is the total sum of the values of the pixels of the signature. Notice that it is assumed that the mask $\mathbf{M_1}$ has been applied to the input image and only the pixels within the mask have a non-zero value, i.e. the pixels that belong to the SAR signature of the vessel. Once the centre of mass has been computed, the line of the main axis of the vessel's contour can be defined by knowing its orientation angle, and consequently, its slope m_1. In image processing, one of the most common ways to estimate this direction is by using either the Hough Transform or the Radon Transform; in both cases, the maximum values of the image in the respective transformation domain would give information on the orientation of the SAR signature [91]. Another option is an approach based on the Principal Component Analysis (PCA) [92]. In this case, a mass tensor of the mask $\mathbf{M_1}$ is computed. Since the tensor is proportional to the covariance matrix of the location of the mask's pixels, the eigenvector related to the eigenvalue of largest magnitude indicates the direction of maximum variance of the position of

the pixels. With the assumption of quasi-rectangular shape, that direction would correspond to the one of the main axis.

In general, both approaches are useful for the estimation of the slope m_1 of the main axis. However, it has been observed that the PCA approach presents better alignment of the main axis after visual confirmation; thus, this is the method used in the algorithm. With the centre of mass $P_{cm}(x_{cm}, y_{cm})$ and the slope m_1, the main axis can be expressed as the line

$$y = m_1 x + (y_{cm} - m_1 x_{cm}) = m_1 x + b_1 \tag{5.11}$$

Now, the lines of the bounding rectangle that are parallel to the main axis can be found by using the points of the contour C_v and the parameters of the main axis. Two sets of points are defined, C_{v-A} and C_{v-B}, for the points above and below the main axis, respectively. Since a quasi-rectangular shape is assumed, it is expected that most of the points of these sets are aligned parallel to the main axis and a best-fit line relies on the boundary of the contour at each side. Then, for the sets C_{v-A} and C_{v-B}, the best-fit line is determined through the distance minimization of each set of points to a straight line, which is subjected to the slope constraint of m_1, i.e. the slope of the main axis.

The distance from a point $p_0(x_0, y_0)$ to a line parallel to the main axis is given by [93]:

$$d = \frac{|m_1 x_0 - y_0 + b|}{\sqrt{m_1^2 + 1}} \tag{5.12}$$

Notice that b is the parameter that can vary the distance from the point to the line. For a given set of points $(x_1, y_1), (x_2, y_2), ..., (x_n, y_n)$, the least-squares approach can be used to estimate this parameter for the best-fit line. From equation(5.12) a minimization function can be defined as

$$G(b) = \sum_{i=1}^{n} (m_1 x_i - y_i + b)^2 \tag{5.13}$$

where only the numerator of equation(5.12) is considered because the denominator does not have an impact on minimizing the distance. Setting the gradient of $G(b)$ with respect to b to zero and solving for it:

$$b = \frac{1}{n} \sum_{i=1}^{n} (y_i - m_1 x_i) \tag{5.14}$$

By using equation (5.14) and the set points C_{v-A} and C_{v-B}, their respective parameters b_A and b_B are obtained. In this way, the lines L_A and L_B are defined; both of them are parallel to the main axis and rely on the boundary of the contour of the vessel. This process can be done iteratively, and each time the points furthest from the line can be eliminated for the next iteration. In general, by selecting the points within a distance of one standard deviation from the line-point distances of all the points, it has been observed that 2 or 3 iterations are enough to get a better fitting of the line to the boundary of the vessel.

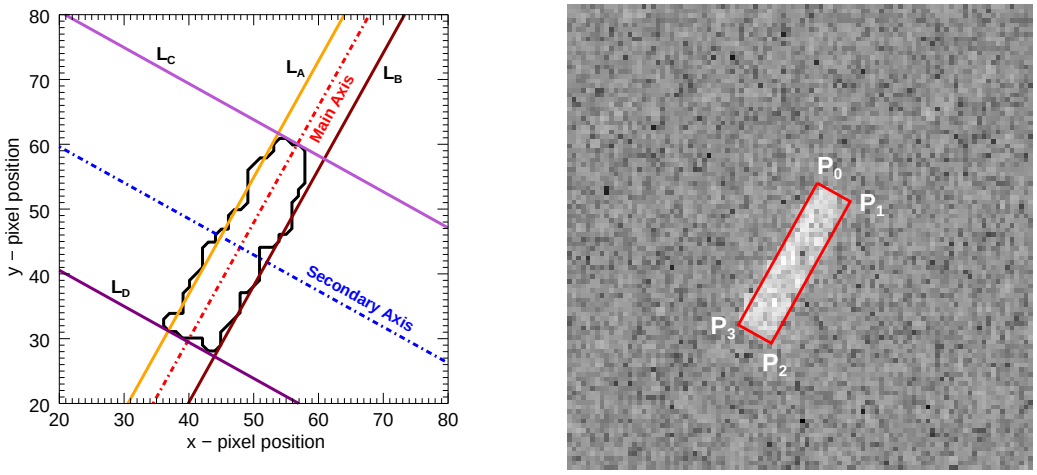

(a) (b)

Fig. 5.6 Boundary lines estimated for the contour of the vessel. (a) Lines estimated for the contour of the vessel; (b) Final boundary rectangle obtained from the algorithm.

The remaining lines, parallel to the secondary axis, are obtained in a simpler way. First, the line of the secondary axis is defined as

$$y = m_2 x + (y_{cm} - m_2 x_{cm}) = m_2 x + b_2 \tag{5.15}$$

where $m_2 = -\frac{1}{m_1}$ for $m_1 > 0$. Again, two sets of points are defined, C_{v-C} and C_{v-D}, but this time for the points that are between lines L_A and L_B, and above and below the secondary axis. Then, for each set the furthest point from the centre of mass is found and taken to define the boundary lines, L_C and L_D, parallel to the secondary axis. Figure 5.6a shows the boundary lines for an example of a vessel SAR signature. The vertex of the bounding rectangle are obtained by finding the intersection of the orthogonal lines (Figure 5.6b).

5.2.4 Computation of the contour dimensions

The ultimate goal is to find the dimensions (length and width) of the SAR signatures of the vessel. Since the input images are in slant-range coordinates, the locations of the vertices of the boundary rectangle have to be mapped to UTM coordinates. In this way, the real dimensions in the ground projection can be computed.

The geocoding of the vertices of the rectangle is performed using the RSLab toolbox[1] and the geolocation grid provided as auxiliary data with the SAR image. In general, it is expected that rectangle turns into a rhomboid after the ground projection. This deformation would

[1]Set of routines developed by the Remote Sensing Lab of the Universitat Politècnica de Catalunya (UPC) for SAR image processing

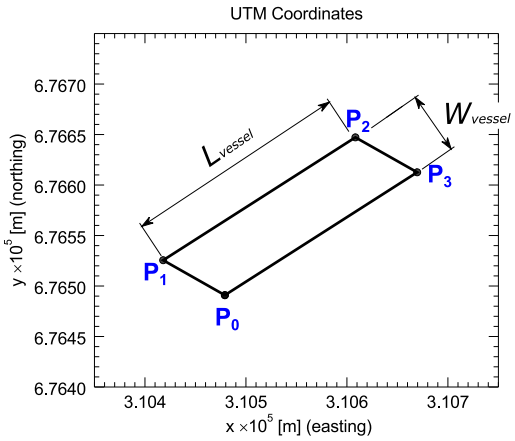

Fig. 5.7 Geometrical distortion of the boundary rectangle to a rhomboid after UTM projection.

only change the way of measuring the width of the SAR signatures. Instead of computing the length of one of the shorter sides, the width is represented by the rhomboid's height. Using the notation of Figure 5.7, the length L_{vessel} and the width W_{vessel} of the SAR signature of the vessel is obtained as

$$L_{vessel} = \|\overrightarrow{P_1P_2}\| \tag{5.16}$$

$$W_{vessel} = \frac{\|\overrightarrow{P_1P_2} \times \overrightarrow{P_0P_1}\|}{\|\overrightarrow{P_1P_2}\|} \tag{5.17}$$

5.3 Heading

The UTM projection of the bounding box, along with an estimate of the ground-range velocity component of the vessel, could be used to obtain the heading. Instead of analysing the reflectivity of the SAR signature to determine the bow and stern of the vessel, a more general approach is employed by using the motion of the vessel, in particular, its ground-range velocity. First, an unitary vector, $\hat{u}$, associated with the main axis of the rhomboid is obtained. To avoid ambiguities, this vector $\hat{u}$ is defined in such a way that its horizontal component is always positive:

$$\hat{u} = \begin{cases} \dfrac{\vec{U}}{\|\vec{U}\|}, & U_E \geq 0 \\ -\dfrac{\vec{U}}{\|\vec{U}\|}, & U_E < 0 \end{cases} \tag{5.18}$$

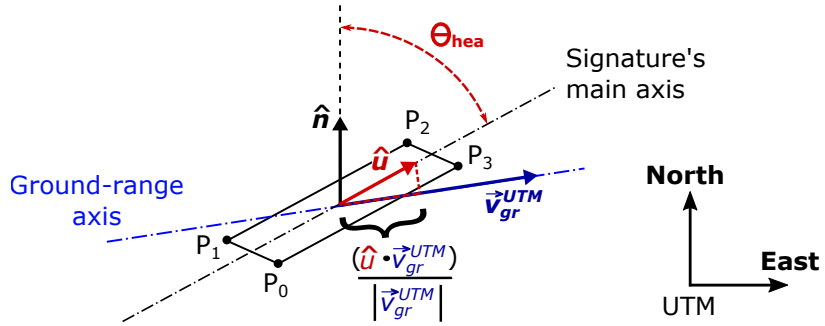

Fig. 5.8 Diagram of the ground projection of the boundary box for the computation of the heading angle.

with $\overrightarrow{U} = (U_E, U_N) = \overrightarrow{P_1P_2}$. Based on the diagram of Figure 5.8, the heading can be obtained by computing the angle of $\hat{u}$ with respect to the North and the sign of the projection of the ground-range velocity component,v_{gr}^{UTM}, to $\hat{u}$:

$$\theta_{hea} = \begin{cases} \arccos\left(\hat{n} \cdot \hat{u}\right), & \left(\overrightarrow{v}_{gr}^{UTM} \cdot \hat{u}\right) \geq 0 \\ \arccos\left(\hat{n} \cdot \hat{u}\right) + 180°, & \left(\overrightarrow{v}_{gr}^{UTM} \cdot \hat{u}\right) < 0 \end{cases} \tag{5.19}$$

where $\hat{n}$ is an unit vector associated with the North axis.

This approach assumes that the vessel is sailing and its translational motion is more significant in the horizontal plane than in the vertical direction (heave axis). Thus, the ground-range velocity component of the vessel can be associated completely with the range velocity component that can be measured from the SAR signal of the vessel (equation (5.33)). Notice that this way of computing the heading is highly dependent on the presence of the ground-range velocity component of the motion of the vessel. This approach can be seen as an alternative method that exploits additional information that can be obtained, as it is explained in detail in Section 5.4, from the SAR signal of the moving vessel.

5.4 Estimation of the ground-range velocity of the vessel

Moving targets introduce aberrations such as defocus and azimuth displacement in their SAR images. As mentioned in the previous chapter, in the case of spaceborne SAR systems the former is usually related to the acceleration of the target, and the latter to its range velocity. In this section, this velocity will be the main parameter of analysis.

The range velocity of a vessel can give information about its likely sailing direction, which is a parameter of interest for maritime surveillance systems such as the one in the NEREIDS project. Moreover, it also can improve the cross-check detection between SAR signatures of vessels and other sources of vessel identification (e.g. AIS, optical images) by compensating the azimuth displacements. For single aperture acquisitions, the estimation of the range

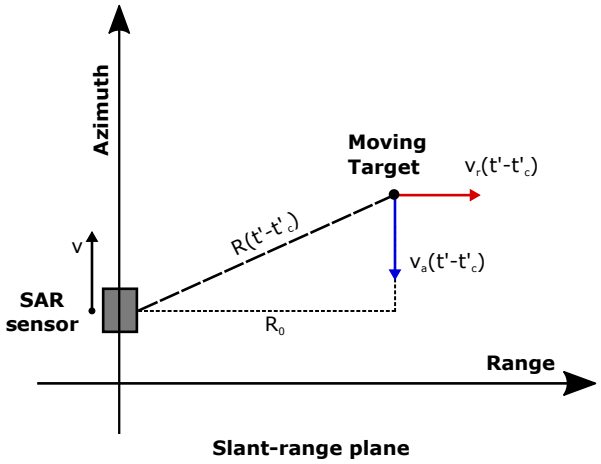

Fig. 5.9 Slant-range projection of the moving target (with only velocity components) for a basic stripmap configuration

velocity of a moving target is focused on the effects on the Doppler centroid of its azimuth signal. In this section, it is shown that a change in the expected Doppler centroid can be used to estimate the range velocity component of the vessel, and later, its corresponding ground-range projection.

5.4.1 Effects of the velocity of the vessel on the SAR signal

In our case, the input SAR signatures of vessels come from stripmap data acquisitions of spaceborne sensors. The model of a slow moving target from Section 2.3 is used:

$$s(\tau, t' - t'_c) \approx A_0 p_r \left(\frac{\tau - 2R_0}{c} \right) w_a \left(t' - t'_c \right) e^{-j \frac{4\pi}{\lambda} R(t' - t'_c)} \tag{5.20}$$

but the accelerated or higher-order motion components are not going to be considered in order to isolate the effects of the velocity on the SAR signal of the target (Figure 5.9). Then, the approximation of the range function $R(t' - t'_c)$ in the case of spaceborne SAR systems (equation 2.16) results in

$$R(t' - t'_c) = R(t) \approx R_0 + v_r(t) + \frac{(v + v_a)^2 t^2}{2R_0} \tag{5.21}$$

with $t = t' - t'_c$, v_r and v_a as the magnitude of the range and along-track velocity components of the moving target, v the nominal speed of the platform, and R_0 the reference distance at

$t' = t'_c \Rightarrow t = 0$. Thus, the baseband model of the range-compressed signal of equation (5.20) is expressed as

$$s(\tau, t) \approx A_0 p_r \left(\frac{\tau - 2R_0}{c} \right) w_a(t)\, e^{-j\frac{4\pi}{\lambda}R_0} e^{-j\frac{4\pi}{\lambda}v_r t} e^{j\pi K_a t^2} e^{-j\frac{4\pi}{\lambda}\left(\frac{2vv_a+v_a^2}{2R_0}\right)t^2} \tag{5.22}$$

where $K_a = -\frac{2v^2}{\lambda R_0}$ is the frequency Doppler Rate used in the azimuth compression of the stripmap signal. The alteration of the instantaneous range by the v_r and v_a components introduces a linear term and a modification of the quadratic term, respectively.

Effect of the along-track velocity component on the Doppler rate

Equation (5.21) shows that the along-track component of the velocity modifies only the quadratic term of $R(t)$. Then, it affects the matching of the Doppler rate of the signal and the one expected for the static case, which would be seen as a defocus effect in the image. In principle, v_a can be estimated by using an autofocus technique. However, for slow moving targets (like the vessels) the variation of the second-order term is more sensitive to the range acceleration in spaceborne SAR sensors. Additionally, the effects of along-track velocity and range acceleration are merged in the same term and they can not be distinguished individually (Section 4.1.1). Only if one considers the specific condition of a non-accelerating target, could the result of the compensation term of the phase from the autofocus technique be associated to v_a. In practice, since the $v \gg v_a$ for typical vessel speed, it is more often assumed that the defocusing effect is only due to range acceleration.

Hereafter, it will be considered that the magnitude of the along-track velocity of the vessel is so small that its effects on the nominal speed of the platform v is negligible in the case of spaceborne SAR systems.

Effect of the radial velocity component over Doppler centroid frequency

Since the platform of the SAR sensor moves much faster than the vessel does in the along-track direction, i.e. $v \gg v_a$, a further simplification can be done in equation (5.21):

$$R(t) \approx R_0 + v_r t + \frac{(v+v_a)^2 t^2}{2R_0} \approx R_0 + v_r t + \frac{v^2}{2R_0} t^2 \qquad \text{with } v \gg v_a \tag{5.23}$$

By using this approximation of $R(t)$ in equation (5.22), it is obtained:

$$s(\tau, t) = A_0 p_r \left(\frac{\tau - 2R_0}{c} \right) w_a(t)\, e^{-j\frac{4\pi}{\lambda}R_0} e^{-j\frac{4\pi}{\lambda}v_r t} e^{j\pi K_a t^2} \tag{5.24}$$

The expression in equation (5.24) is essentially the same as the static point-target, but there is an additional linear term introduced by v_r to the phase history. This linear term has an

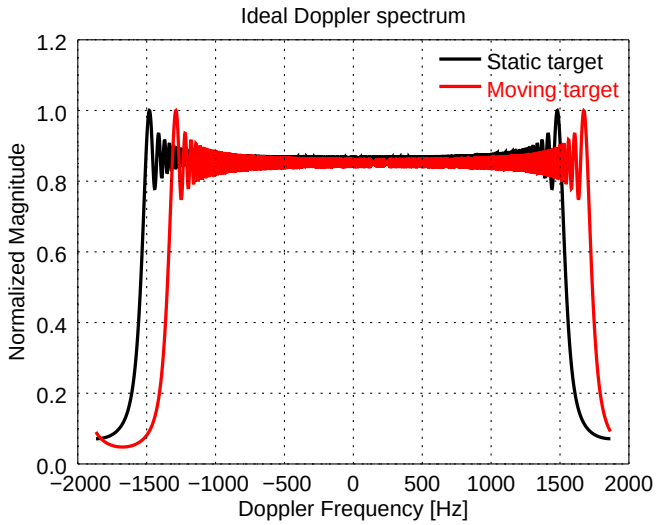

Fig. 5.10 Comparison between the ideal Doppler Spectrum of a static ($v_r = 0$) and moving ($v_r \neq 0$) point target. SAR data simulated for generic spaceborne X-band SAR sensor.

impact on the Doppler domain because it induces a shift of the Doppler spectrum of the signal (Figure 5.10) [22]. Indeed, from the phase of equation (5.24), the Doppler centroid frequency f_{DC} can be obtained at the beam centre crossing time $t' = t'_c \Rightarrow t = 0$; then, the radial velocity component shifts f_{DC} to:

$$f_{DC} = -\frac{2}{\lambda}\frac{\mathrm{d}R(t)}{\mathrm{d}t}\bigg|_{t=0} = -\frac{2v_r}{\lambda} \tag{5.25}$$

Azimuth displacements due to the radial velocity

The radial velocity v_r also has an effect on the azimuth position of the moving target in the SAR image. A straight-forward way to compute this displacement is by comparing the range variation $R_s(t)$ of a static target at time t_a (in the surroundings of $t = 0$) and $R(t)$ of equation (5.21). For the static target:

$$R_s(t) = \sqrt{R_0^2 + (vt - vt_a)^2)} \tag{5.26}$$

and obtaining the second-order Taylor approximation, we have

$$\begin{aligned} R_s(t) &\approx R_0 - \frac{v^2 t_a}{R_0}t + \left[1 - \frac{v^2 t_a^2}{R_0^2}\right]\frac{v^2}{2R_0}t^2 \\ &\approx R_0 - \frac{v^2 t_a}{R_0}t + \frac{v^2 t^2}{2R_0}t^2; \qquad vt_a \ll R_0 \end{aligned} \tag{5.27}$$

By comparing equations (5.21) and (5.27), one can observe that the range variation of a moving target with a given v_r behaves as the one from a static target in a different azimuth time. Thus, for this moving target, its azimuth displacement with respect to its correct location can be computed based on the linear terms of equations (5.21) and (5.27) as

$$\Delta t = [t_a - t]_{t=0} = -\frac{R_0}{v^2} v_r \tag{5.28}$$

or, in terms of the azimuth position $y_a = vt_a$:

$$\Delta y = -\frac{R_0}{v} v_r \tag{5.29}$$

Notice that the ratio in equation (5.28) is similar to the magnitude of Doppler rate ,i.e. $|K_a| = \frac{2v^2}{\lambda R_0}$. Then, the azimuth displacement Δt can be expressed in terms of known parameters of the SAR image such as the Doppler rate K_a, wavelength λ, and PRF, for its practical computation. By using these parameters, equations (5.28) and (5.29) can be written as

$$\Delta t = -\frac{2v_r}{\lambda |K_a|} \tag{5.30}$$

$$\Delta y = -\frac{2v_r PRF}{\lambda |K_a|} \Delta_{APS} \tag{5.31}$$

where Δ_{APS} is the azimuth pixel spacing in meters.

5.4.2 Computation of the ground-range velocity of the target using the estimate of the Doppler centroid frequency

In general, the nominal value of the Doppler centroid frequency, f_{DC_0}, is known *a priori* in order to compress the image. That means that it is possible to infer the radial velocity v_r by comparing the computed Doppler centroid frequency of the SAR signal of the target in equation (5.25) and the nominal value f_{DC_0}:

$$v_r = -\frac{[f_{DC} - f_{DC_0}]\,\lambda}{2} = -\frac{\Delta f_{DC} \lambda}{2} \tag{5.32}$$

Once the radial velocity has been computed, its ground-range projection is obtained by using the incidence angle , θ_{inc}, of the antenna's beam of the SAR sensor,

$$v_{gr} = \frac{v_r}{\sin \theta_{inc}} \tag{5.33}$$

in which it is assumed that the target is moving only in the horizontal plane, i.e. the velocity of the target does not have a vertical component. For many moving targets, this assumption in fulfilled, but in the case of the vessels their motion could be more complicated [67]. The

sea conditions can alter the motion of the vessel due to the oscillation of the waves, adding a vertical component that contributes in some magnitude to its radial velocity. Nevertheless, it could be expected that, in normal conditions, the ground component of the velocity of a sailing vessel would be larger than the component in the vertical direction. Thus, equation (5.33) would represent the motion of the ground-range velocity of the sailing vessel.

5.4.3 Estimation of the Doppler Centroid frequency

The estimation of the Doppler Centroid is usually referred to in fraction and integer parts of the Pulse Rate Frequency (PRF) of the sensor. The fractional PRF part is mainly used in the azimuth compression for the set up of the matched filter and the windowing in azimuth, while the total centroid (fractional plus integer part) is used in the range cell migration correction and in the secondary range compression [24]. In the case of a vessel in motion, it can be assumed that its radial velocity is related only to the fractional part of the Doppler centroid. The PRF used in spaceborne SAR systems for civil application (e.g. RADARSAT-2 and TerraSAR-X) is usually around 2000 [Hz] - 3000 [Hz] for high resolution stripmap-mode [94, 95], and medium to large vessels are typically slowly moving targets with radial velocity components $v_r \leq 10$ [m/s], which shifts their Doppler spectrum only a fraction of the PRF. The estimation of the fractional part of the Doppler centroid could be done by using either the magnitude of the spectrum or the phase of the complex raw data. There are different approaches such as Energy Balancing [96], Maximum-likelihood Estimation (MLE) [97], Matched-correlation Estimation [98], Correlation Doppler Estimator (CDE) [99], or Sign Doppler Estimator [99]. All of these techniques rely on the correlation between the Doppler spectrum and a particular weighting function [98]. However, one can make a distinction between magnitude and phase approaches based on their practical implementation. In this way, the first three techniques would be referred to as magnitude-based, and the last two techniques as phase-based approaches.

In the following sections, the general concepts behind the magnitude- and phase-based approaches are presented as they are commonly applied in the estimation of the fractional PRF part of the Doppler centroid of (static) SAR scenarios.

Magnitude-based approach

In the absence of partially illuminated targets, the magnitude of the Doppler spectrum can be assumed to be symmetrical with respect to the peak value [24, 98]; Figure 5.11a shows an example of the symmetrical shape of the Doppler spectrum of a point target obtained from the simulation of raw data of a X-band SAR sensor. The symmetry allows the Doppler centroid to be estimated by finding the frequency, $\hat{f}_{DC}$, that divides the energy of the spectrum

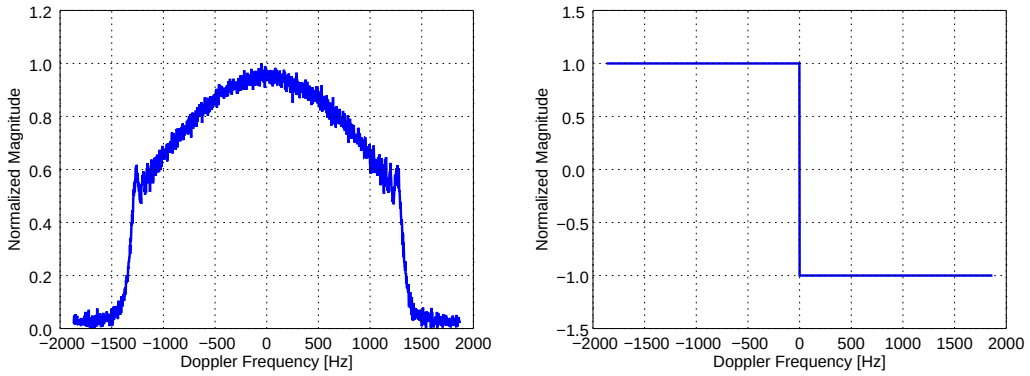

(a) (b)

Fig. 5.11 (a) Doppler spectrum of a point target obtained from the simulation of a X-band SAR sensor($SNR = 10$ dB); (b) Weighting function used for the Doppler centroid estimation.

into two equal parts. An example of a typical function used in this approach is depicted in Figure 5.11b and is described by:

$$B(f) = \begin{cases} 1, & \text{for} \quad -\frac{PRF}{2} < f \leq 0 \\ -1, & \text{for} \quad 0 < f < \frac{PRF}{2} \end{cases} \tag{5.34}$$

Phase-based approach

Instead of using the Doppler spectrum of the data, the phase-based approach employs the complex radar data in the azimuth direction. Common methods that follow this approach are the Correlation Doppler Estimator (CDE) and the Sign Doppler Estimator (SDE). These methods exploit the relationship between phase and frequency, and estimate $\hat{f}_{DC}$ by measuring the average phase increment of the azimuth signal. They take into account that if the beam pattern of the antenna is symmetrical about its beam centre, the expected value of the phase increment equals the value at the time of the centre exposure of the target [24], which is related to the Doppler centroid frequency. In the following section, the explanation is centred on the CDE method since this is the one implemented. The SDE method is similar to the CDE, but it takes into account only the sign of the phase to do the computations. It does not give more weight to bright targets and this makes it less sensitive to strongly varying scenes [99], which could be an interesting option (Section 5.4.5) when the assumption of symmetrical envelope of the data in the azimuth direction it is not quite fulfilled.

To obtain the Doppler centroid frequency $\hat{f}_{DC}$, the phase-based method assumes that the azimuth part of the received signal follows the model of equation (2.13) such that

$$s(t) = w_a(t)e^{j\phi(t)} \quad \text{with } t = t' - t'_c \tag{5.35}$$

where the envelop $w_a(t)$ is a symmetrical function and the signal reaches its maximum at its middle point, $t' = t'_c$, i.e. $t = 0$. Then, the average of the phase increment is computed from the angle of the Average Cross Correlation Coefficient (ACCC) at lag one $\overline{C(t)}$ [24]:

$$\phi_{ACCC} = \angle\overline{C(t)} \tag{5.36}$$

with $\overline{C(t)}$ defined as

$$\overline{C(t)} = \sum_t \Delta s(t) = \sum_t s^*(t)s(t + \Delta t) \tag{5.37}$$

Δt being the azimuth sampling interval, i.e. $\frac{1}{PRF}$, and $s^*(t)$ being the complex conjugate of $s(t)$. The sum of $\Delta s(t)$ can be used instead of the actual average since the analysis is only focused on the phase of $\overline{C(t)}$. Once ϕ_{ACCC} is estimated, it can be related to the phase increment at the centre of the exposure [24]:

$$\phi_{ACCC} \approx \left.\frac{\mathrm{d}\phi(t)}{\mathrm{d}t}\right|_{t=0} \Delta t = 2\pi f_{DC}\Delta t \tag{5.38}$$

then the Doppler centroid frequency is computed as:

$$\hat{f}_{DC} = \frac{1}{2\pi\Delta t}\phi_{ACCC} = \frac{PRF}{2\pi}\phi_{ACCC} \tag{5.39}$$

Considerations for the estimation of the Doppler centroid frequency for vessel SAR signatures

The magnitude- and phase-based approaches are usually applied to different areas of a SAR image and the results are averaged to estimate the fractional part of the Doppler centroid frequency. In this way, biasing due to partial exposure of bright scatterers is mitigated [24]. In our case, a similar methodology can be applied. Assuming that all scatterers of the vessel, on average, have the same radial velocity as the vessel itself, the Doppler centroid frequency of the spectrum of the vessel's SAR signature could be computed using all of its range bins.

Another aspect to take into account is the format of the data. The two approaches usually assume that the input data has not been compressed in azimuth yet. However, in many cases access to raw data is not always possible, making the single-look complex (SLC) format the most available to work with. When using SLC data, one has to consider that the Doppler spectrum has already been affected during the image compression by an azimuth window centred at the nominal Doppler centroid frequency, which changes the shape or suppresses part of the spectrum of the target. Hence, the estimated Doppler centroid that belongs to the target's signal could be biased. Figure 5.12 shows an example of how the shape of the Doppler Spectrum is modified by windowing in the azimuth compression process. In order to overcome this problem, one solution proposed in this study is the computation of

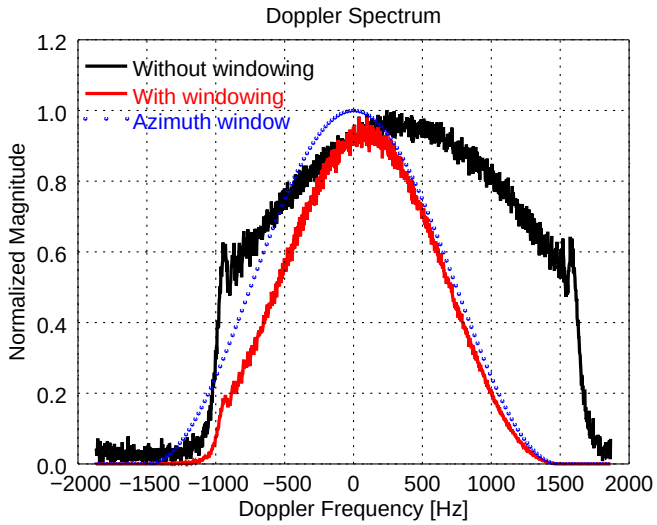

Fig. 5.12 Modification of the shape of the Doppler centroid of a moving point target due to the windowing in the azimuth compression. X-band SAR sensor, $SNR = 30$ [dB], radial velocity $v_r = -5[m/s]$.

a "calibration" curve that takes into account the effects of estimating the Doppler centroid based on the SLC data of a particular SAR system. In this way, the bias of the computed Doppler centroid could be removed, leading to a better estimation of the radial velocity component of the moving target.

5.4.4 Validation with simulated SAR data of ideal point-targets

This section presents the results obtained from applying the magnitude- and phase-based approaches to estimate the Doppler centroid and compute the corresponding radial velocity component of the scatterers, in particular the Energy Balancing (EB) and the Correlation Doppler Estimator (CDE). The estimations of the Doppler centroid are obtained by applying the magnitude- or phase-method to the range bins that contain the brightest targets.

Testing the two approaches to estimate the Doppler centroid frequency of moving targets requires complete control of the dynamics of the target. Therefore, a SAR simulator of ideal point-targets was implemented in IDL ® to generate the stripmap raw data of targets with their own velocity. This simulator employs the parameters of a specific spaceborne SAR sensor (e.g. PRF, antenna length, antenna pattern, carrier frequency, bandwidth, SNR) and simplifies the geometry of the systems by taking into account the flat-Earth approximation and zero squint angle of the antenna. Figure 5.13 shows an example of the Doppler spectrum (averaged over the range bins with higher energy) of the simulated SAR signal of a point-target with and without radial velocity. Note that the Doppler spectrum presents the expected shift of its centroid as in real cases of targets with radial velocity. All of the simulations of the

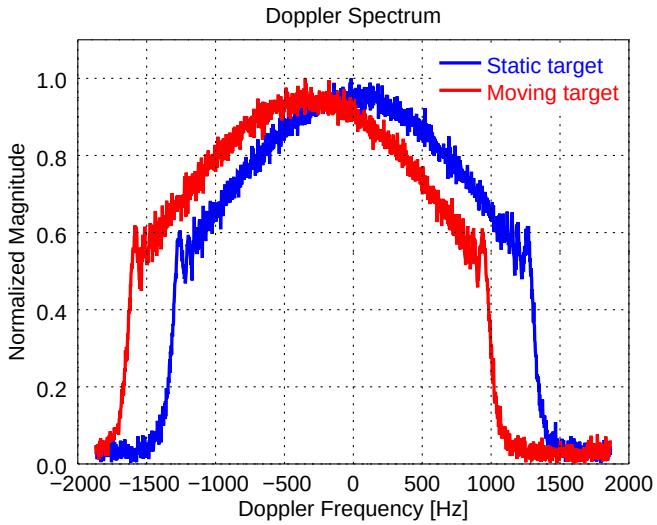

Fig. 5.13 Doppler spectrum (averaged over the range bins) of a single point target without and with radial velocity ($v_r = 5[m/s]$) from the implemented point-target SAR simulator for a generic X-band sensor. $SNR = 30$ dB.

SAR signal were carried out for a X-band sensor with similar parameters to TerraSAR-X, and the Range-Doppler (RD) algorithm is used to process the data. Table 5.1 summarizes the main parameters of the SAR sensor used in all of the simulations.

Using range-compressed data

An array of five independent point-targets is tested. All of the them have the same reflectivity, but each one has different radial velocity (Table 5.2). Additionally, they are located in different range bins in such a way that their range-compresssed signal do not interfere with each other. Figure 5.14 shows the diagram of the array point-targets, the SAR image of the static array, and the SAR image for the point-targets with their own radial velocity.

A sensitive parameter in the estimation of the Doppler centroid (and consequently, of v_r) is the SNR. Different levels of additive white Gaussian noise (AWGN) have been introduced into the radar signal in the simulation setup to compare the results while using the magnitude- and phase-approach. Table 5.3 and Table 5.4 contain the average and the standard deviation, respectively, of the estimated range velocities for each point-target using the magnitude-based approach over 20 simulations for different levels of SNR of the SAR raw data. Similarly, Table 5.5 and Table 5.6 show the respective results by using the phase-based approach. Additionally, Figure 5.15 shows the variation of the standard deviation of the estimation of v_r for each point target as a function of the SNR for both approaches.

Table 5.1 Parameters of the X-band SAR sensor for raw data simulator of point targets

Sensor Parameters	**Value**	
Pulse duration (τ)	28×10^{-6}	[s]
Sampling Frequency	128×10^{6}	[Hz]
Chirp bandwidth	116×10^{6}	[Hz]
Carrier frequency	9.65×10^{9}	[Hz]
PRF	3736	[Hz]
Doppler Rate	−6987.22	[Hz/s]
Reference distance	544293	[m]
Antenna length	5.1	[m]
Nominal speed of the platform	7686	[m/s]
Range resolution	1.3	[m]
Azimuth resolution	2.55	[m]

Table 5.2 Values of the range velocity component v_r used in the set-up of the simulations of the five point-target array

Target 1 $v_{r1}\left[\frac{m}{s}\right]$	**Target 2** $v_{r2}\left[\frac{m}{s}\right]$	**Target 3** $v_{r3}\left[\frac{m}{s}\right]$	**Target 4** $v_{r4}\left[\frac{m}{s}\right]$	**Target 5** $v_{r5}\left[\frac{m}{s}\right]$
−3.000	−1.000	0.000	1.000	2.000

Table 5.3 Average of the estimated range velocity component, $\hat{v}_r$, of each point target using the **magnitude-based approach** to obtain the Doppler centroid from range-compressed data. For each SNR level, 20 simulations were carried out.

SNR* **[dB]**	**Target 1** $\overline{\hat{v}_{r1}}\left[\frac{m}{s}\right]$	**Target 2** $\overline{\hat{v}_{r2}}\left[\frac{m}{s}\right]$	**Target 3** $\overline{\hat{v}_{r3}}\left[\frac{m}{s}\right]$	**Target 4** $\overline{\hat{v}_{r4}}\left[\frac{m}{s}\right]$	**Target 5** $\overline{\hat{v}_{r5}}\left[\frac{m}{s}\right]$
60	−2.985	−0.997	0.017	1.025	2.017
30	−2.985	−0.997	0.017	1.024	2.017
10	−2.984	−0.999	0.015	1.026	2.017
5	−2.988	−0.998	0.015	1.031	2.022
3	−2.987	−0.994	0.017	1.022	2.018
0	−2.968	−0.986	0.008	1.011	2.016
−3	−2.981	−0.981	0.019	1.029	2.016
−5	−3.005	−0.996	0.037	0.964	1.999
−10	−3.014	−1.091	0.051	1.042	1.989

*SNR level of the raw data.

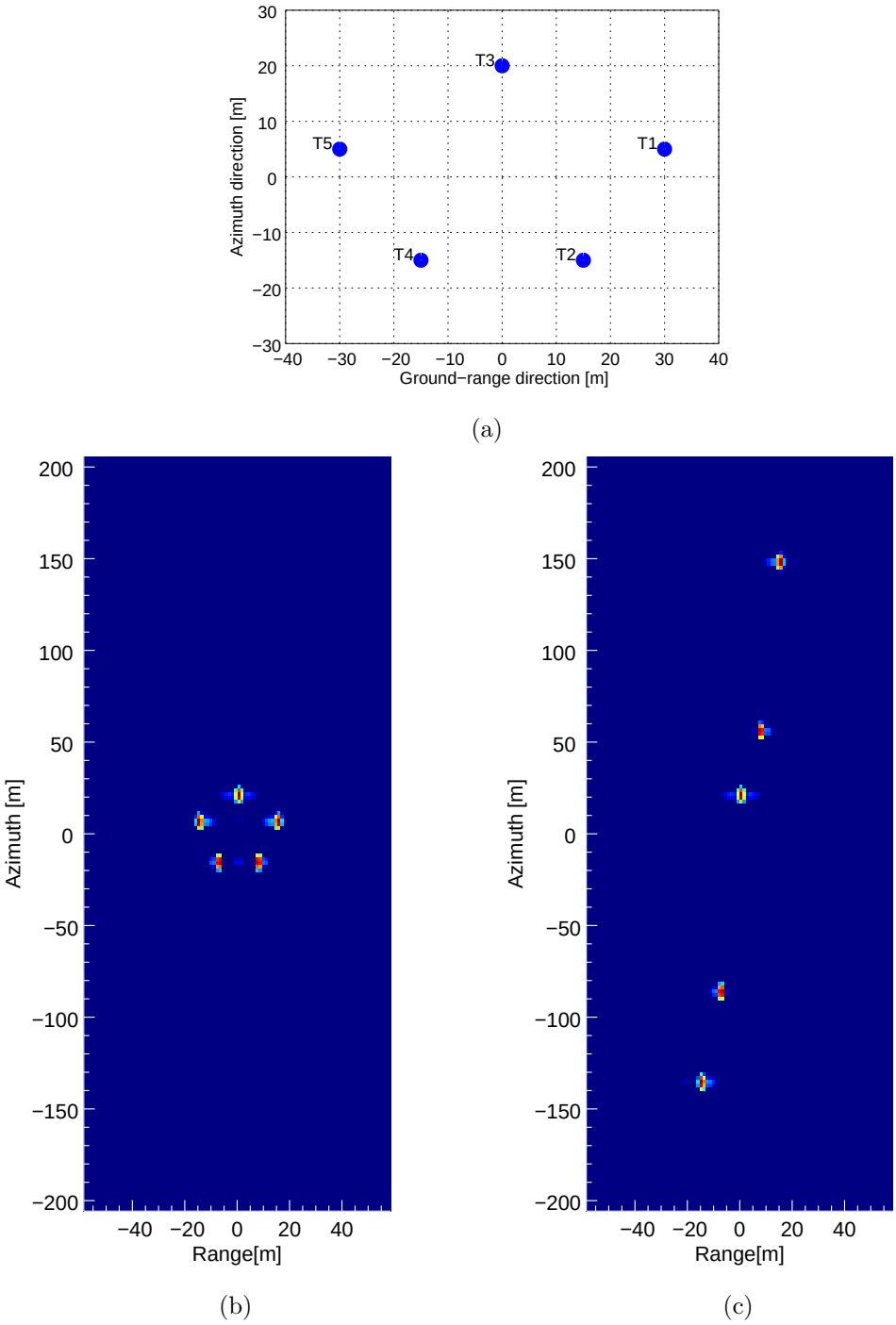

(a)

(b)

(c)

Fig. 5.14 Array of five point targets for validation of frequency centroid estimation; (a) diagram of the point-target array; (b) SAR image of static scenario; c) SAR image of moving point targets. Simulations for generic X-band sensor, resolution $Rg \times Az = [1.3[m] \times 2.4[m]]$. $SNR = 10$ dB (before Azimuth compression).

Table 5.4 Standard deviation σ_M of the estimated range velocity component $\hat{v_r}$ of each point target by using the **magnitude-based approach** in obtaining the Doppler centroid from range-compressed data. For each SNR level, 20 simulations were carried out.

SNR* **[dB]**	**Target 1** $\sigma_{M1}\left[\frac{m}{s}\right]$	**Target 2** $\sigma_{M2}\left[\frac{m}{s}\right]$	**Target 3** $\sigma_{M3}\left[\frac{m}{s}\right]$	**Target 4** $\sigma_{M4}\left[\frac{m}{s}\right]$	**Target 5** $\sigma_{M5}\left[\frac{m}{s}\right]$
60	3.878×10^{-5}	3.843×10^{-5}	2.731×10^{-5}	4.076×10^{-5}	3.692×10^{-5}
30	1.432×10^{-3}	1.475×10^{-3}	0.994×10^{-3}	1.273×10^{-3}	1.004×10^{-3}
10	1.059×10^{-2}	1.483×10^{-2}	0.969×10^{-2}	1.023×10^{-2}	0.749×10^{-2}
5	1.869×10^{-2}	2.036×10^{-2}	1.453×10^{-2}	1.686×10^{-2}	1.532×10^{-2}
3	2.001×10^{-2}	2.032×10^{-2}	2.144×10^{-2}	2.369×10^{-2}	2.749×10^{-2}
0	3.902×10^{-2}	4.167×10^{-2}	2.843×10^{-2}	3.782×10^{-2}	2.582×10^{-2}
-3	4.497×10^{-2}	6.093×10^{-2}	3.740×10^{-2}	4.077×10^{-2}	5.291×10^{-2}
-5	6.559×10^{-2}	6.694×10^{-2}	7.251×10^{-2}	5.945×10^{-2}	6.215×10^{-2}
-10	1.482×10^{-1}	1.051×10^{-1}	0.951×10^{-1}	1.495×10^{-1}	1.731×10^{-1}

*SNR level of the raw data.

Table 5.5 Average of the estimated range velocity component, $\hat{v}_r$, of each point target by using the **phase-based approach** to obtain the Doppler centroid from range-compressed data. For each SNR level, 20 simulations were carried out.

SNR* **[dB]**	**Target 1** $\overline{\hat{v}_{r1}}\left[\frac{m}{s}\right]$	**Target 2** $\overline{\hat{v}_{r2}}\left[\frac{m}{s}\right]$	**Target 3** $\overline{\hat{v}_{r3}}\left[\frac{m}{s}\right]$	**Target 4** $\overline{\hat{v}_{r4}}\left[\frac{m}{s}\right]$	**Target 5** $\overline{\hat{v}_{r5}}\left[\frac{m}{s}\right]$
60	-2.999	-0.998	-0.003	1.000	1.997
30	-2.999	-0.999	-0.004	1.000	1.997
10	-3.005	-0.993	-0.001	0.999	2.001
5	-2.997	-0.997	-0.011	1.002	2.007
3	-3.009	-0.992	0.000	0.999	2.001
0	-2.994	-0.992	0.000	1.000	1.999
-3	-3.004	-1.014	0.000	0.998	1.998
-5	-2.987	-1.011	-0.001	1.008	2.006
-10	-2.981	-1.041	0.058	1.026	1.999

*SNR level of the raw data.

Table 5.6 Standard deviation σ_θ of the estimated range velocity component $\hat{v_r}$ of each point target by using the **phase-based approach** in obtaining the Doppler centroid from range-compressed data. For each SNR level, 20 simulations were carried out.

SNR* [dB]	**Target 1** $\sigma_{\theta 1}\left[\frac{m}{s}\right]$	**Target 2** $\sigma_{\theta 2}\left[\frac{m}{s}\right]$	**Target 3** $\sigma_{\theta 3}\left[\frac{m}{s}\right]$	**Target 4** $\sigma_{\theta 4}\left[\frac{m}{s}\right]$	**Target 5** $\sigma_{\theta 5}\left[\frac{m}{s}\right]$
60	3.679×10^{-5}	4.161×10^{-5}	4.991×10^{-5}	4.655×10^{-5}	3.747×10^{-5}
30	1.799×10^{-3}	1.384×10^{-3}	1.085×10^{-3}	1.619×10^{-3}	1.331×10^{-3}
10	1.377×10^{-2}	1.411×10^{-2}	1.154×10^{-2}	1.677×10^{-2}	1.070×10^{-2}
5	2.556×10^{-2}	2.784×10^{-2}	1.840×10^{-2}	2.539×10^{-2}	2.396×10^{-2}
3	3.003×10^{-2}	4.468×10^{-2}	2.584×10^{-2}	3.546×10^{-2}	3.079×10^{-2}
0	4.682×10^{-2}	4.543×10^{-2}	4.523×10^{-2}	5.297×10^{-2}	4.201×10^{-2}
-3	5.292×10^{-2}	8.712×10^{-2}	5.009×10^{-2}	6.587×10^{-2}	6.275×10^{-2}
-5	5.848×10^{-2}	7.875×10^{-2}	7.316×10^{-2}	9.870×10^{-2}	9.863×10^{-2}
-10	1.199×10^{-1}	1.583×10^{-1}	1.100×10^{-1}	1.892×10^{-1}	1.499×10^{-1}

*SNR level of the raw data.

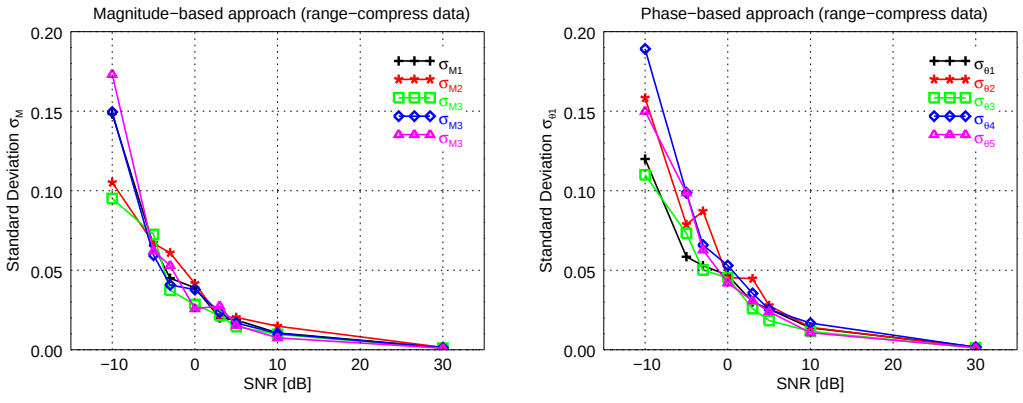

(a) (b)

Fig. 5.15 Standard deviation of the estimated range velocity component as a function of the SNR for each point-target from range-compressed data. (a) magnitude-based approach; (b) phase-based approach. (20 simulations were carried out for each SNR level of the raw data)

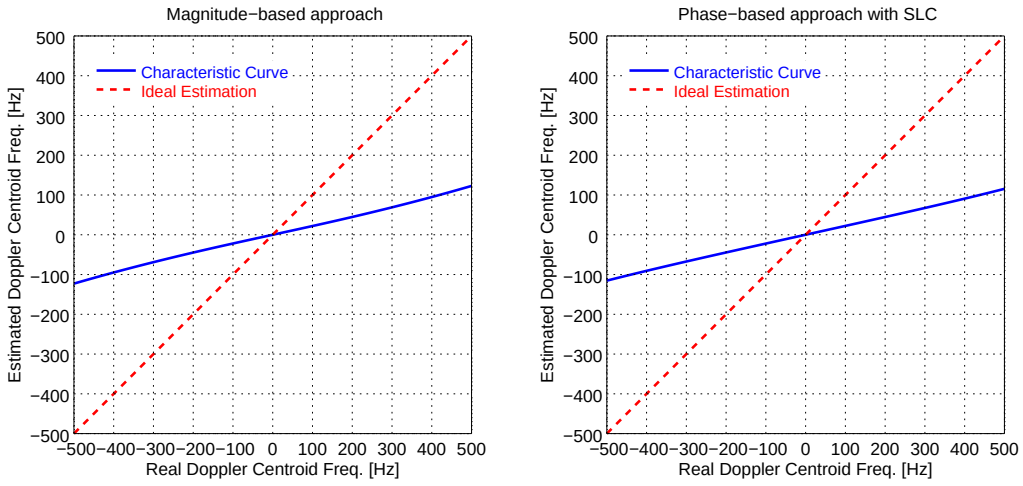

(a) (b)

Fig. 5.16 Characteristic curves for the estimation of the Doppler centroid using SLC images for an X-band sensor: (a) magnitude-based approach; (b) phase-based approach. Range of the radial velocity $v_r = [-7, 7]\,[\frac{m}{s}]$, $PRF = 3762$ [Hz], window: Hanning, window bandwidth: $0.8 \times PRF$.

Using SLC data

In practice, the SLC data from spaceborne SAR sensors is often more accessible than the actual raw data. However, the disadvantage of using SLC data is that: 1) the shape of the Doppler spectrum of the signal has been modified by the windowing of the processor; 2) a portion of the shifted Doppler spectrum may have already been suppressed. Consequently, the estimation of the Doppler centroid and the radial velocity of the scatterers may be inaccurate. Our proposal to overcome this issue is the computation of a characteristic curve which considers the effects of the azimuth windowing when estimating the Doppler centroid in order to compensate for the bias in the estimation.

To compute the characteristic curve, the parameters of the SAR sensor (e.g. antenna pattern, PRF, working frequency) and the parameters of the azimuth processing (e.g. window type, usable bandwidth) have to be known. With this information, the ideal azimuth signal of a point-target can be simulated for different radial velocities, estimating in each case the Doppler centroid. In this way, it is possible to obtain an empirical curve which represents the bias in the estimation of the centroid. Figure 5.16 depicts examples of the characteristic curves of the estimation of the Doppler centroid for the magnitude- and phase-based approaches; the dashed lines indicate the ideal case when the true value and the estimated Doppler centroid are the same. In this case, the SLC data was processed with a Hanning window applied to 80% of the PRF.

Table 5.7 Average of the estimated range velocity component, $\hat{v}_r$, of each point target by using the **magnitude-based approach** to obtain the Doppler centroid from SLC data. For each SNR level, 20 simulations were carried out.

SNR* **[dB]**	**Target 1** $\overline{\hat{v}_{r1}}\left[\frac{m}{s}\right]$	**Target 2** $\overline{\hat{v}_{r2}}\left[\frac{m}{s}\right]$	**Target 3** $\overline{\hat{v}_{r3}}\left[\frac{m}{s}\right]$	**Target 4** $\overline{\hat{v}_{r4}}\left[\frac{m}{s}\right]$	**Target 5** $\overline{\hat{v}_{r5}}\left[\frac{m}{s}\right]$
60	−2.929	−0.880	0.102	1.053	2.077
30	−2.928	−0.882	0.103	1.052	2.075
10	−2.935	−0.887	0.098	1.058	2.077
5	−2.933	−0.871	0.081	1.060	2.078
3	−2.916	−0.893	0.105	1.048	2.048
0	−2.965	−0.886	0.078	1.054	2.109
−3	−2.904	−0.878	0.106	1.059	2.009
−5	−2.981	−0.838	0.168	1.025	2.116
−10	−2.749	−0.820	0.195	0.944	2.046

*SNR level of the raw data.

The raw data of the simulations of the five point-target array (Figure 5.14) with their own radial velocities (Table 5.2) is compressed to obtain the SLC image. Only a region of interest (ROI) that enclosed all of the targets is selected, this being the input SLC chip used for the estimation of their range velocity component.

To start the estimation of the Doppler centroid, the input SLC chips are zero-padded. Then, either the magnitude-based or phase-based approach is applied, as when using range-compressed data. However, this time the estimation must take into account the bias which occurs due to the azimuth windowing during the compression. Thus, once the Doppler centroid frequency is estimated, the corresponding calibration curve is used to remove the expected bias.

Table 5.7 and Table 5.8 show the average and the standard deviation, respectively, of the final estimated range velocities for each point-target in the array using the magnitude-based approach for 20 simulations per level of SNR of the SAR signal. Similarly, Table 5.9 and Table 5.10 show the respective results achieved using the phase-based approach. Additionally, Figure 5.17 shows the variation of the standard deviation of the final estimation of v_r for each point target as a function of the SNR level for both approaches.

Comments on the estimated $\hat{v_r}$ using the Range-Compressed and SLC data input

In general, for each target the average value of the estimate $\hat{v_r}$ tends to be the correct value for the different levels of SNR. The estimation techniques presented similar performance, although the magnitude-based approach had a slightly lower standard deviation than the phase-based one when using range-compressed data. As expected, the decrease of the SNR in the simulated raw data translates to a slight increment in the value of the standard deviation of $\hat{v_r}$ as shown in Figure 5.15 and Figure 5.17. Additionally, it is observed that the average

Table 5.8 Standard deviation σ_M of the estimated range velocity component $\hat{v_r}$ of each point target using the **magnitude-based approach** to obtain the Doppler centroid from SLC data. For each SNR level, 20 simulations were carried out.

SNR* **[dB]**	**Target 1** $\sigma_{M1}\left[\frac{m}{s}\right]$	**Target 2** $\sigma_{M2}\left[\frac{m}{s}\right]$	**Target 3** $\sigma_{M3}\left[\frac{m}{s}\right]$	**Target 4** $\sigma_{M4}\left[\frac{m}{s}\right]$	**Target 5** $\sigma_{M5}\left[\frac{m}{s}\right]$
60	$\sim 0^{**}$	~ 0	~ 0	~ 0	~ 0
30	2.081×10^{-3}	3.44×10^{-3}	2.684×10^{-3}	2.302×10^{-3}	3.183×10^{-3}
10	2.618×10^{-2}	2.526×10^{-2}	2.115×10^{-2}	2.466×10^{-2}	3.169×10^{-2}
5	5.549×10^{-2}	4.933×10^{-2}	3.218×10^{-2}	4.725×10^{-2}	4.809×10^{-2}
3	5.703×10^{-2}	6.834×10^{-2}	6.809×10^{-2}	7.393×10^{-2}	5.888×10^{-2}
0	9.332×10^{-2}	8.864×10^{-2}	6.053×10^{-2}	9.250×10^{-2}	9.327×10^{-2}
−3	1.059×10^{-1}	1.589×10^{-1}	1.357×10^{-1}	1.413×10^{-1}	1.198×10^{-1}
−5	1.326×10^{-1}	1.507×10^{-1}	0.983×10^{-1}	1.663×10^{-1}	1.446×10^{-1}
−10	3.561×10^{-1}	3.624×10^{-1}	3.218×10^{-1}	3.209×10^{-1}	2.407×10^{-1}

*SNR level of the raw data.

$^{**} \sim 0$ indicates a value smaller than 1×10^{-5}

Table 5.9 Average of the estimated range velocity component, $\hat{v}_r$, of each point target by using the **phase-based approach** to obtain the Doppler centroid from SLC data. For each SNR level, 20 simulations were carried out.

SNR* **[dB]**	**Target 1** $\overline{\hat{v}_{r1}}\left[\frac{m}{s}\right]$	**Target 2** $\overline{\hat{v}_{r2}}\left[\frac{m}{s}\right]$	**Target 3** $\overline{\hat{v}_{r3}}\left[\frac{m}{s}\right]$	**Target 4** $\overline{\hat{v}_{r4}}\left[\frac{m}{s}\right]$	**Target 5** $\overline{\hat{v}_{r5}}\left[\frac{m}{s}\right]$
60	−2.993	−0.992	0.006	1.006	2.008
30	−2.994	−0.991	0.007	1.006	2.007
10	−2.984	−0.972	0.007	0.991	2.002
5	−2.994	−0.981	−0.003	0.991	1.997
3	−3.000	−0.961	−0.018	1.015	2.004
0	−2.996	−0.957	0.038	1.026	2.029
−3	−2.944	−0.987	0.035	0.958	2.005
−5	−3.047	−1.012	0.020	1.004	2.029
−10	−3.018	−1.096	−0.006	1.109	1.906

*SNR level of the raw data.

Table 5.10 Standard deviation σ_θ of the estimated range velocity component $\hat{v}_r$ of each point target using the **phased-based approach** to obtain the Doppler centroid from SLC data. For each SNR level, 20 simulations were carried out.

SNR* **[dB]**	**Target 1** $\sigma_{\theta 1}\left[\frac{m}{s}\right]$	**Target 2** $\sigma_{\theta 2}\left[\frac{m}{s}\right]$	**Target 3** $\sigma_{\theta 3}\left[\frac{m}{s}\right]$	**Target 4** $\sigma_{\theta 4}\left[\frac{m}{s}\right]$	**Target 5** $\sigma_{\theta 5}\left[\frac{m}{s}\right]$
60	$\sim 0^{**}$	~ 0	~ 0	~ 0	~ 0
30	2.628×10^{-3}	2.479×10^{-3}	2.302×10^{-3}	3.508×10^{-3}	2.498×10^{-3}
10	3.174×10^{-2}	3.676×10^{-2}	2.855×10^{-2}	2.478×10^{-2}	2.919×10^{-2}
5	4.437×10^{-2}	5.555×10^{-2}	6.444×10^{-2}	3.594×10^{-2}	4.392×10^{-2}
3	7.288×10^{-2}	7.730×10^{-2}	4.864×10^{-2}	8.331×10^{-2}	4.359×10^{-2}
0	8.967×10^{-2}	1.203×10^{-1}	6.848×10^{-2}	1.024×10^{-1}	6.237×10^{-2}
-3	8.856×10^{-2}	1.512×10^{-1}	1.172×10^{-1}	1.334×10^{-1}	1.674×10^{-1}
-5	1.349×10^{-1}	2.018×10^{-1}	1.584×10^{-1}	1.393×10^{-1}	1.620×10^{-1}
-10	2.787×10^{-1}	2.405×10^{-1}	2.301×10^{-1}	2.586×10^{-1}	3.400×10^{-1}

*SNR level of the raw data.

** ~ 0 indicates a value smaller than 1×10^{-5}

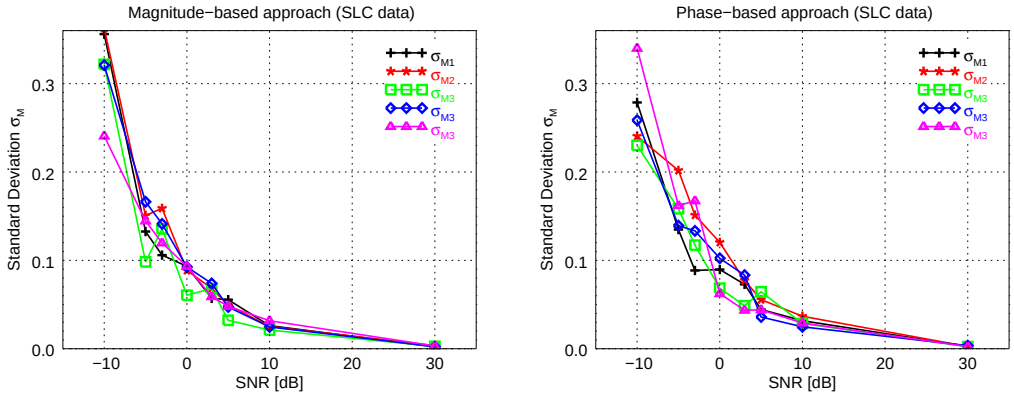

(a) (b)

Fig. 5.17 Standard deviation of the estimated radial velocity as a function of the SNR for each point-target from SLC data. (a) magnitude-based approach; (b) phase-based approach. (20 simulations were carried out for each SNR level of the raw data)

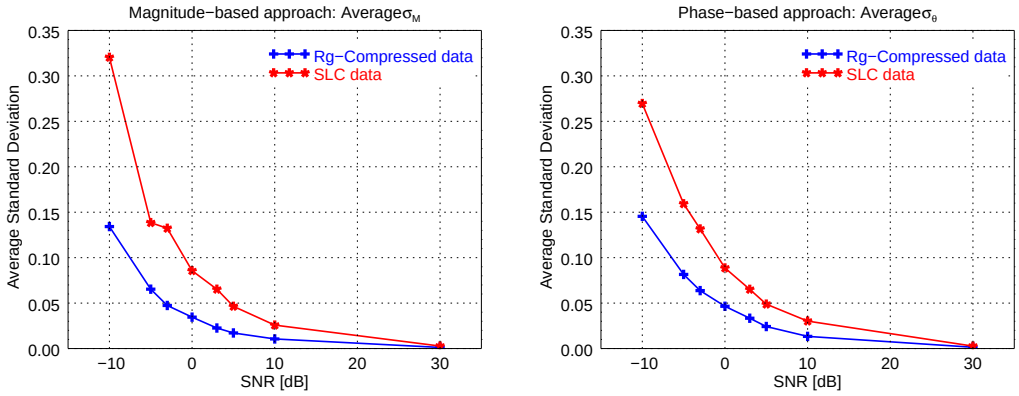

(a) (b)

Fig. 5.18 Average of the standard deviation of $\hat{v_r}$ of all the targets as a function of the SNR using the range-compressed and SLC data: (a) magnitude-based approach; (b) phase-based approach.

standard deviation of $\hat{v_r}$ obtained from all of the targets when using the SLC data is always larger than when using the range-compressed data. Figure 5.18 illustrates this behaviour; the plots are the average standard deviations of $\hat{v_r}$ of all the targets as a function of the SNR (of the raw data) for the range-compressed and SLC data. By comparing the two curves, it can be seen that the average of the standard deviation for the SLC case tends to be double that of the range-compressed data.

5.4.5 Estimation of the ground-range velocity of realistic targets from GRECOSAR simulations

The model of moving point targets from the previous sections allows assessing the performance of the estimation algorithms for the Doppler centroid frequency (and consequently, for the radial velocity) in ideal conditions. Now, the SAR data from the simulator GRECOSAR (Section 3.2) is used to estimate the ground-range velocity of more realistic targets.

First, a trihedral object (i.e. corner reflector) is selected as a the target, which is commonly used for validation and calibration in real SAR systems. Simulations are carried out for a C- and X-band sensor with parameters similar to RADARSAT-2 and to TerraSAR-X systems (Table 5.11), respectively. Figure 5.19 shows the diagram of the positioning of the corner reflector in the simulations and the Doppler spectrum obtained.

The magnitude- and phase-based algorithms were applied to the simulated data of the moving corner reflector with different ground-range velocities (typical for vessels) to estimate the Doppler centroid frequency; then $\hat{v}_r$ and $\hat{v}_{gr}$ were computed through equation (5.25) and (5.33), respectively. Table 5.12 and Table 5.13 show the results of the estimated ground-range

Table 5.11 Parameters of the C- and X-band SAR sensor for the set-up of GRECOSAR simulations

Sensor Parameter	**C-band**		**X-band**	
Pulse duration (τ)	21×10^{-6}	[s]	28×10^{-6}	[s]
Sampling Frequency	31.67×10^{6}	[Hz]	128×10^{6}	[Hz]
Chirp bandwidth	30×10^{6}	[Hz]	116×10^{6}	[Hz]
Carrier frequency	5.405×10^{9}	[Hz]	9.65×10^{9}	[Hz]
PRF	1256	[Hz]	3736	[Hz]
Doppler Rate	-6987.22	[Hz/s]	-5370.18	[Hz/s]
Reference distance	1003717.82	[m]	654174.71	[m]
Antenna length	15	[m]	5.1	[m]
Nominal speed of the platform	7548.87	[m/s]	7686.12	[m/s]
Range resolution	5	[m]	1.3	[m]
Azimuth resolution	6.31	[m]	2.08	[m]

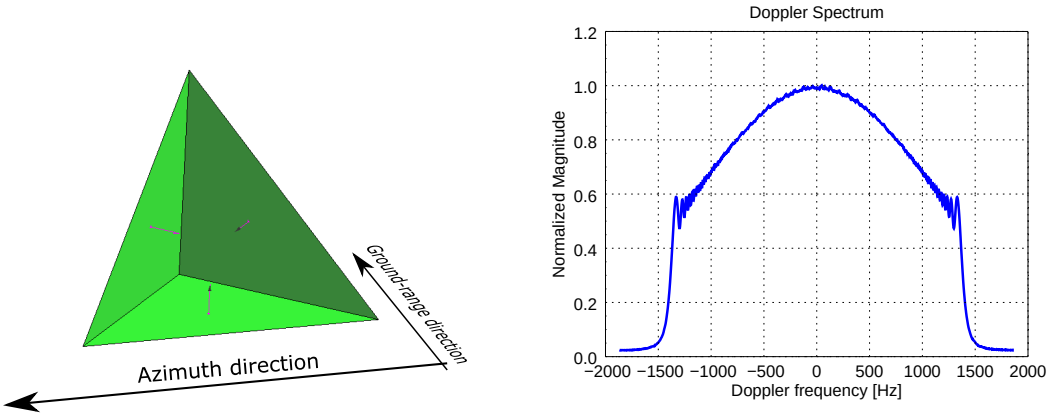

(a) (b)

Fig. 5.19 (a) Diagram of the positioning of the corner reflector in the simulation; (b) average Doppler spectrum of the corner reflector from GRECOSAR's SAR data.

Table 5.12 Estimate of v_{gr} (magnitude- and phase-based approaches) using the Range-Compressed and SLC data from GRECOSAR simulations of the C-Band sensor. SNR = 30 dB (raw data).

$v_{sway}\left[\frac{m}{s}\right]$	$v_{gr}\left[\frac{m}{s}\right]$	**Rg-Comp. data**		**SLC data**	
		$\hat{v}_{gr-M}\left[\frac{m}{s}\right]$	$\hat{v}_{gr-\theta}\left[\frac{m}{s}\right]$	$\hat{v}_{gr-M}\left[\frac{m}{s}\right]$	$\hat{v}_{gr-\theta}\left[\frac{m}{s}\right]$
−5	−4.912	−4.786	−4.927	−4.257	−4.368
−2	−1.969	−1.914	−1.982	−1.615	−1.731
0	−0.007	0.028	−0.018	0.124	−0.004
1	0.974	1.000	0.962	1.000	0.859
7	6.860	6.775	6.843	6.248	6.188

Table 5.13 Estimate of v_{gr} (magnitude- and phase-based approaches) using the Range-Compressed and SLC data from GRECOSAR simulations of the X-Band sensor. SNR = 30 dB (raw data).

$v_{sway}\left[\frac{m}{s}\right]$	$v_{gr}\left[\frac{m}{s}\right]$	**Rg-Comp. data**		**SLC data**	
		$\hat{v}_{gr-M}\left[\frac{m}{s}\right]$	$\hat{v}_{gr-\theta}\left[\frac{m}{s}\right]$	$\hat{v}_{gr-M}\left[\frac{m}{s}\right]$	$\hat{v}_{gr-\theta}\left[\frac{m}{s}\right]$
−5	−4.912	−4.936	−4.750	−4.614	−4.514
−2	−1.969	−2.016	−1.903	−1.800	−1.802
0	−0.007	0.035	0.006	0.093	0.018
1	0.974	1.052	0.958	1.016	0.921
7	6.860	6.954	6.621	6.578	6.353

velocity $\hat{v}_{gr}$ achieved using the range-compressed and SLC data as described in Section 5.4.4 for the C- and X-band sensors, respectively.

In general, the estimated ground-range velocities correspond to their actual values used in their simulations of the moving corner reflector. This behaviour was expected since the reflector was oriented to ensure that its scattering pattern was symmetrical, thus, its Doppler spectrum (Figure 5.19b) was as well. In this way, the target fulfilled the conditions assumed by the estimation techniques of the Doppler centroid frequency.

In the case of more complex targets, such as vessels, the scattering pattern of the whole structure may not always be symmetric. Indeed, the superposition of the scattering patterns of the different parts of the vessel's structures is not likely to present symmetry at each possible angle of observation from the radar. In real scenarios, Doppler centroid estimation algorithms are usually applied to the average of the Doppler spectrum of some hundreds of range bins; and for quasi-homogeneous areas, this averaged spectrum tends to be symmetrical [24]. However, SAR signatures of vessels are contained in fewer range bins and the influence of bright scatterers can distort the spectral shape. Moreover, the Doppler spectrum of the vessel changes with the angle of observation due to the change in the distribution of the radar signal reflected from the structure. Figure 5.20 shows an example of the (average) Doppler power spectrum obtained from GRECOSAR's range-compressed data of the SAR signature

Table 5.14 Estimate of v_{gr} (magnitude- and phase-based approaches) using the Range-Compressed data from GRECOSAR simulations of the X-Band sensor for a static vessel with different bearing angle. SNR = 30 dB (raw data).

Bearing angle [°]	**Rg-Comp. data** $\hat{v}_{gr-M}\left[\frac{m}{s}\right]$	$\hat{v}_{gr-\theta}\left[\frac{m}{s}\right]$
−90.0	−3.344	−3.618
−30.0	1.092	2.264
0.0	−7.547	−7.408
45.0	0.165	0.127
90.0	−9.862	−8.886

of a static vessel with different orientation with respect to the SAR sensor; in these cases, the Doppler spectrum obtained is not symmetric and changes with the orientation of the vessel.

Despite the use of range-compressed data, all of the reflectivity phenomena of the vessels' structure would lead to a bias in the estimate of its $\hat{f}_{DC}$, and consequently in its $\hat{v}_{gr}$, when the magnitude- and phase-based algorithms that assume a symmetric spectrum are used. Table 5.14 contains the estimated $\hat{f}_{DC}$ and $\hat{v}_{gr}$ for a static vessel with different orientations as shown in Figure 5.20 and simulated in GRECOSAR. Similar characteristics can be found in actual SAR acquisitions; Figure 5.21 shows an example of the average Doppler spectrum of a SAR signature of a quasi-static vessel (according to its Automatic Identification System (AIS) information) from a RADARSAT-2 acquisition. These irregularities in the envelope of the spectrum may induce an estimated $\hat{v}_{gr}$ other than zero. In order to compensate this bias, modifications to the estimation algorithms can be made to lessen the effects of the bright scatterers.

Modification of Magnitude-based estimation algorithm

In this thesis, the proposed modification of the magnitude-based estimation relies on the fact that the Doppler spectrum, be it symmetric or not, would shift in proportion to the radial velocity of the target. Then, a threshold process can be applied to obtain a new shape of the Doppler spectrum as:

$$\tilde{S}_s(f) = \begin{cases} \max\{S(f)\}, & S(f) \geq T_S \\ S(f), & S(f) < T_S \end{cases} \tag{5.40}$$

In this way, all the values above a given power threshold T_s are set to the same value, resulting in an ideal spectrum with a rectangular envelope. The selection of the threshold can be based on a fraction of the maximum value of the power spectrum. Figure 5.22 shows an example of the original Doppler spectrum and the modified Doppler spectrum after applying a threshold for a power level 6 dB below the maximum value.

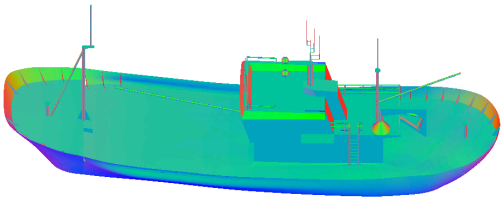

(a) View from the sensor

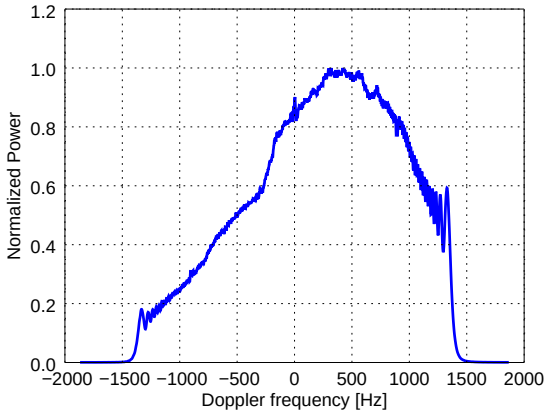

(b) Average Doppler power spectrum

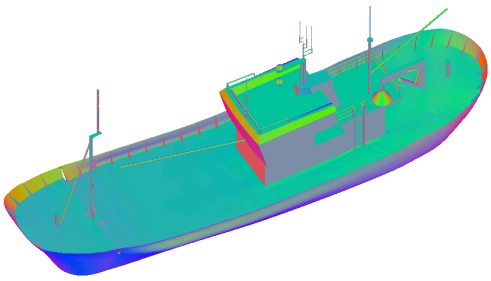

(c) View from the sensor

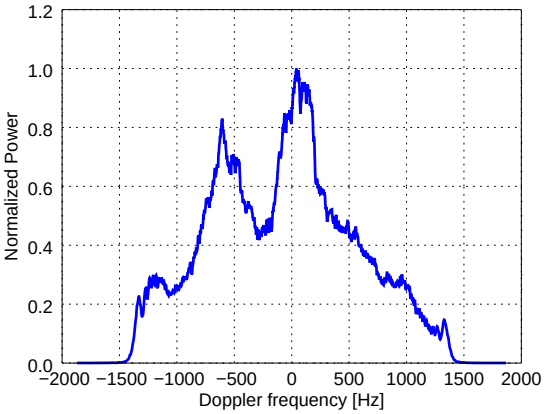

(d) Average Doppler power spectrum

Fig. 5.20 Average Doppler power spectrum of a static vessel for two different orientations with respect to the SAR sensor. Raw data simulated with GRECOSAR for the X-band sensor. SNR = 30 dB (raw data).

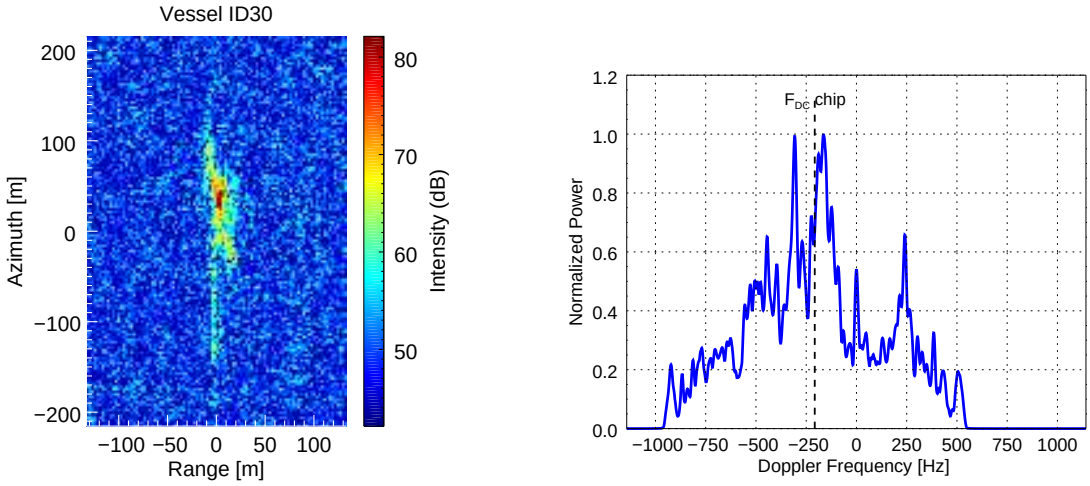

(a) SLC chip

(b) Average Doppler power spectrum

Fig. 5.21 Example of average Doppler power spectrum of a quasi-static vessel from a RADARSAT-2 image: (a) SLC chip Vessel ID 30 (IMO:9209477), 0.4 knots ; (b) average Doppler spectrum.

Table 5.15 Estimate of v_{gr} using the thresholding of the Doppler spectrum and the magnitude-based approach for a static vessel with different orientations.

Bearing angle [°]	**Rg-Comp. data** $\hat{v}_{gr-M}\left[\frac{m}{s}\right]$	**SLC data** $\hat{v}_{gr-M}\left[\frac{m}{s}\right]$
−90.0	0.070	0.072
−30.0	0.094	0.128
0.0	−0.311	−0.321
45.0	−0.024	−0.022
90.0	−0.163	−0.169

When using range-compressed data, the thresholding can be done directly to the Doppler spectrum, but the SLC data requires additional processing since the azimuth window has to be compensated. Additionally, a new calibration curve that considers this modification to the envelope of the spectrum has to be computed. Table 5.15 shows the results of applying this modification to the range-compressed and SLC data to estimate the Doppler centroid frequency for a static vessel with different orientations. Notice that the estimate of the ground-range velocity, $\hat{v}_{gr-M}$, is closer to 0 $\left[\frac{m}{s}\right]$ as expected for the case of a static vessel. Nevertheless, special care has to be taken in the selection of the threshold level when highly bright scatterers are present in the SAR signature of the vessel. If the threshold is not set properly, the modification of the envelope of the spectrum may still lead to a wrong estimate of v_{gr}.

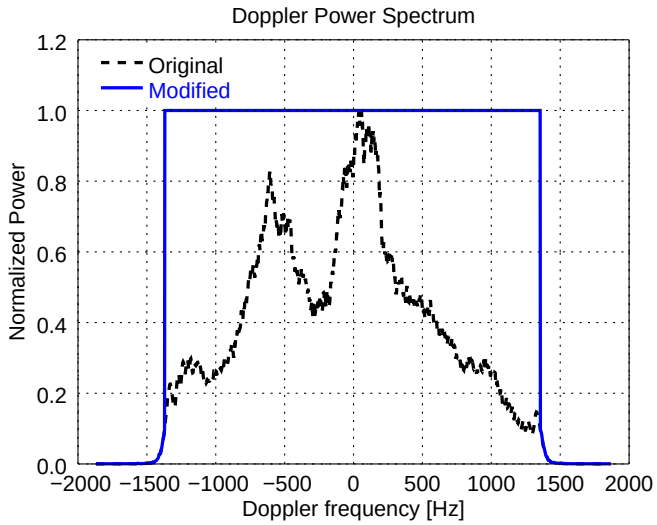

Fig. 5.22 Modification of the Doppler spectrum to avoid biasing of brighter scatterers in the estimation of f_{DC} for the magnitude-based approach.

Modification of Phase-based estimation algorithm

The modification of the phase-based algorithm has been proposed by Madsen [99] to perform a more robust estimation of the Doppler centroid frequency for non-homogeneous scenes. His proposal assumes that the addition of the random phases of the scatterers to a resolution cell is a random walk that can be modelled as a circular symmetric Gaussian process. Then, the autocorrelation function can be derived only from the signs of the Gaussian processes with the "arcsine law" [99]. In this way, the estimation of the Doppler centroid does not take into account the intensity of the targets, which makes it less sensitive to the bias due to bright scatterers.

The procedure first obtains a new function with the signs of the azimuth signal. By writing the complex azimuth signal $s(t)$ as

$$s(t) = I(t) + jQ(t) \tag{5.41}$$

where $I(t)$ and $Q(t)$ are real functions, then the sign function results in

$$g(t) = g_I(t) + jg_Q(t) \tag{5.42}$$

by applying

$$g_X(t) = \begin{cases} 1, & X(t) \geq 0 \\ -1, & X(t) < 0 \end{cases} \qquad X = I, Q \tag{5.43}$$

Table 5.16 Estimate of v_{gr} using the sign Doppler estimation for the phase-based approach for a static vessel with different orientations.

Bearing angle [°]	**Rg-Comp. data** $\hat{\boldsymbol{v}}_{\boldsymbol{gr-\theta}}\left[\frac{\boldsymbol{m}}{\boldsymbol{s}}\right]$	**SLC data** $\hat{\boldsymbol{v}}_{\boldsymbol{gr-\theta}}\left[\frac{\boldsymbol{m}}{\boldsymbol{s}}\right]$
−90.0	−0.179	0.679
−30.0	0.045	0.749
0.0	0.059	−0.739
45.0	0.015	0.679
90.0	0.019	0.679

From the "arcsine law", the normalized correlation coefficients are obtained as [99]:

$$\rho_{XY}\left(\Delta t\right) = \sin\left(\frac{\pi}{2} R_{g_{XY}}\left(\Delta t\right)\right) \qquad X, Y = I, Q \tag{5.44}$$

and the new normalized cross correlation coefficient ρ_s of the azimuth signal $s(t)$ can be computed as

$$\rho_s\left(\Delta t\right) = \frac{1}{2}\left[\rho_{II}(\Delta t) + \rho_{QQ}(\Delta t)\right] + j\frac{1}{2}\left[\rho_{QI}(\Delta t) - \rho_{IQ}(\Delta t)\right] \tag{5.45}$$

Since the arguments of $\rho_s\left(\Delta t\right)$ and the cross correlation of $s(t)$ are the same, a new ACCC angle at lag one, $\widetilde{\phi}_{ACCC}$, can be obtained from the average of $\rho_s\left(\Delta t\right)$, $\Delta t = \frac{1}{PRF}$, over several azimuth lines as in equation 5.37:

$$\widetilde{\phi}_{ACCC} = \angle\overline{\rho_s\left(\Delta t\right)} \tag{5.46}$$

and the estimate of $\hat{f}_{DC}$ can be computed in the same way presented in equation (5.39). Table 5.16 shows the results of the estimation of $\hat{v}_{gr-\theta}$ for the case of a static vessel with different orientations when the modified phase-based approach is used. Notice that the estimate of the ground-range velocity is now close to $0\left[\frac{m}{s}\right]$ as expected. However, the estimated $\hat{v}_{gr-\theta}$ presents a bias when using the SLC data and the modified method due to the shape of the calibration curve around the zero-Doppler, which presents a constant value in the range of −20[Hz] to +20 [Hz]. If the calibration curve is not used for the static case, the estimate $\hat{v}_{gr-\theta}$ results closer to $0\left[\frac{m}{s}\right]$.

5.5 Summary

Current spaceborne SAR sensors are able to provide high-resolution images that can be used to detect man-made objects. For maritime surveillance systems, as well as detecting the vessels, it is often advantageous to extract as much information as possible from their SAR signatures. In this context, the characteristics of the SAR signal of vessels from single-channel stripmap acquisitions have been analysed. In this way, additional features such as the

dimensions of the vessels and their likely sailing direction can be extracted automatically from the SLC images.

Automatic extraction of the dimensions of the vessels requires, first, the isolation of the SAR signatures from the sea clutter, and later, the computation of the corresponding bounding box. Since the input SLC chips come from single-channel images, the high reflectivity of the vessel signature is exploited to differentiate the pixels that belong to the target and those belonging to the clutter. From the intensity image (in dB), the local sea clutter statistics are modelled by a log-Weibull distribution, allowing discrimination between the pixels based on a given probability of false alarm. Clustering and morphological operations are combined to obtain the final mask for the SAR signature of the vessel. Now, by assuming that, in general, the contour of the SAR signature of a vessel present a quasi-rectangular shape, the final mask is then processed to compute a bounding box that follows this signature. The vertex positions of the bounding box are mapped into the UTM plane, and the dimensions of the SAR signature are computed in this ground projection.

With the bounding box projected in the UTM plane, the heading of the vessel can be computed based on the main orientation of this box. But instead of analysing the reflectivity of the SAR signature to determine the bow and stern of the vessel, a more general approach is taken by using the motion of the vessel , and in particular, its ground-range velocity. Thus, by knowing the direction of this velocity, the heading of the vessels is defined. This approach has the limitation of being highly dependent on the presence of the ground-range velocity component, but it can be seen as an alternative for complex SAR signatures where the analysis of the distribution of the scatterers hinders the identification of the bow and stern in the signature.

The computed ground-range velocity is, in fact, a projection of the radial velocity that is extracted from the analysis of the SAR signal of the vessels. As suggested in the model of a slow-moving target for the spaceborne SAR case, the measurements of the shifts of the Doppler centroid frequency of the spectra of the vessels are used to compute their range velocities; and by assuming that the motion of the vessels are more significant in the horizontal plane, their ground-range components are obtained. In addition, these range velocities can also be used to correct the position of the vessels. The presence of these velocities cause variations in the azimuth position of the targets in the final images. Then, the obtained range velocities can be employed to identify the actual position of the vessels in azimuth at instant the SAR image was acquired. In this way, the azimuth positions of the detected vessels can be compensated and therefore more suitable for use in cross-checking with others sources of vessel identification (e.g. AIS, optical images).

The measurement of the shifts in the Doppler spectra of the vessels is done via Doppler centroid frequency estimation methods. They are locally applied to the range-bins that contain the SAR signature of the respective targets. Two techniques have been implemented: Energy balancing and Correlation Doppler Estimator (CDE). The former follows the magnitude-

based approach by using the envelope of the Doppler spectrum, while the latter follows the phase-based approach using the complex radar data in the azimuth direction. Both Doppler centroid frequency estimation techniques exploit the ideal symmetry in the evolution of the SAR signal that has not been compressed in azimuth direction yet. In this sense, when using SLC data (the most available type of data to work with in practice) as the input, the estimated Doppler centroid may be biased due the modification and suppression of the signal during the windowing in the azimuth compression process. Theses effects on the estimation can be reduced with the use of a calibration curve obtained from simulations of ideal moving targets, along with the accurate model of the SAR acquisition for the sensor of interest.

Validations of the estimation techniques for the Doppler centroid were carried out by generating SAR data of ideal point targets with different radial velocities. In general, both techniques presented similar performance and were able to retrieve the expected radial velocity for a given input. Besides the deterioration of the estimate as SNR decreases, the only difference observed in the computed Doppler centroid was when SLC (along with the calibration curve) and azimuth-uncompressed data were used as the input. The average standard deviation of the estimations when using the SLC data was always slightly larger than in the case of uncompressed data. These variations are attributed to the effects of the modification of the signal due to the azimuth compression.

Finally, additional tests with SAR data generated with GRECOSAR were carried out to analyse the response of the estimation techniques when using more realistic targets. In the case of a classical trihedral reflector oriented towards the SAR sensor, the estimation of the ground-range velocities corresponded to the expected ones for both of the estimation techniques. However, for a more complicated target, e.g. a vessel, the complexity of its envelope may bias the estimation, presumably, due to the presence of partially illuminated bright scatterers. Modification of both magnitude- and phase-based approaches were introduced to reduce these effects. For the former, a saturation process of the spectrum is proposed in this thesis in order to obtain to the assumed symmetrical envelope; and for the phase-based approach, the proposed method by Madsen of considering only the signs of the complex data can be used, as in the case of the estimation of the Doppler centroid frequency for non-homogeneos scenes. Despite the results obtained with simulated SAR data, these modified methods may not present the same good performance for actual SAR images of vessels. For instance, for the magnitude-based approach, the saturation of the envelope of the spectrum requires an *a priori* power threshold that may be different for each SAR signature of a vessel. And for the phase-based approach, the use of only the signs makes the estimation more sensible to errors induced from weak reflections (such as the ones from the sea surface) since the power of the signal is no longer a weighting factor.

Chapter 6

Experimental results with real SAR data

6.1 Introduction

The processing techniques described in the previous chapters are employed here in a processing chain of an automatic feature extraction algorithm. It is intended to be applied to chips of the detected vessels from stripmap single-look complex (SLC) images, obtaining information of interest for maritime surveillance systems, namely the dimensions of the vessel and its likely heading. A dataset of stripmap SLC chips with ground-truth is employed to analyse the capabilities of the feature extraction algorithm with real data. This dataset was obtained from the acquisition campaigns and the available AIS records in the frame of the European Project NEREIDS [19, 20], so the SAR signatures of the vessels could be correlated with their AIS information.

In this chapter, Section 6.2 describes the steps of feature extraction algorithm proposed in this thesis; Section 6.3 discusses the assumptions made in the processing chain to extract the features from the vessels' SAR signatures. Then, Section 6.4 is devoted to the results and the discussion of the application of the algorithm to a dataset of real SLC chips with ground-truth. And finally, Section 6.5 gives a summary of this chapter.

6.2 Implementation of the feature extraction algorithm

The implementation of the feature extraction algorithm is shown in Figure 6.1. Briefly, the process can be summarized as follows: 1) a SLC chip containing a single SAR signature of a vessel is selected; 2) a masking process is used to select the range bins containing the SAR signature; 3) employing the parameters of the SAR sensor, the SLC chip is zero-padded in the azimuth direction up to the length of the synthetic aperture; 4) the signal is decompressed in azimuth direction; 5) the ground range-velocity estimation and the autofocus procedure are

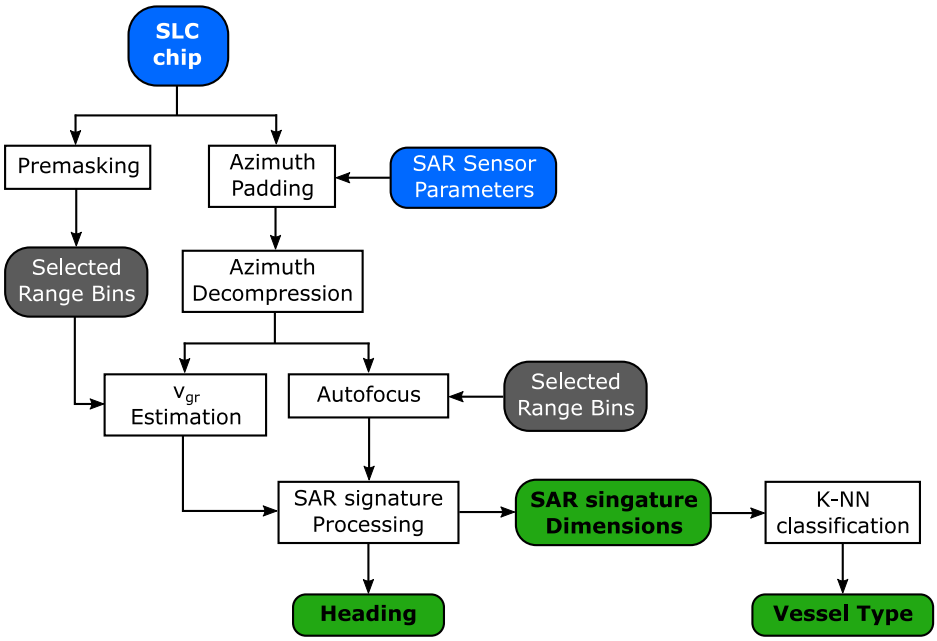

Fig. 6.1 Block diagram of the feature extraction algorithm.

applied using the range bins selected in step 2; 6) the dimensions of the enhanced signature are computed, and the heading is obtained with its orientation and the direction of the ground range-velocity; 7) a distance-weighted K-Nearest Neighbour(K-NN) classification is applied by using the estimated dimension.

In the algorithm, the estimation of the range-velocity and the autofocus procedure are performed independently. In the previous chapters, it has been shown that the autofocus of the signal in fact modifies its phase history, and it may introduce linear terms as in the case of PGA (Section 4.2.2). Recalling that the effect of the range velocity of a target is the introduction of a linear term in its phase history, it is better to employ the original azimuth decompressed signal to avoid compromising its estimation. The independence of the range-velocity estimation and the autofocus procedure gives the algorithm flexibility to either apply both or just one of the two procedures.

6.3 Practical Considerations

Using real SAR data for vessel detection and feature extraction processing is challenging. There are several variables in real maritime scenarios such as the sea state, the variety of vessel types and their dynamics, and the variation of the SAR signature of the vessels as a function of their orientation and interactions with the sea surface. Even though simulation tools like GRECOSAR aim to reflect realistic scenes, all the conditions of a maritime scene have to be in some way simplified in order to get a feasible simulator. In the same sense,

feature extraction processing algorithms for SAR images are often limited by assumptions about the conditions of the scene. This section discusses the assumptions established in order to analyse the results obtained by the feature extraction algorithm proposed in this thesis.

6.3.1 About the ground-range velocity estimation

As explained in the previous chapter, the ground-range velocity component of the vessel was obtained by a projection of the estimated range velocity (section 5.4.2). In real cases of maritime SAR acquisitions, the range velocity component may enclose motions of the vessel that are more complex than just translation. Indeed, for general maritime conditions, the range velocity component of the scatterers of the vessel can be produced by the up/down motion of the structure, as well as by approaching or moving away from the nadir track. Moreover, rotational motion may induce different range velocities for individual scatterers of the vessels. Strictly, the range component of the velocity is the result of both translational and rotational motion of the structure. These kinds of motions are expected to be linked to both the sailing direction and the response of the type of vessel to the sea state during the SAR acquisition. However, for the scope of this thesis that considers medium to large size vessels, a simplification can be made for calm to moderate sea states. Under these conditions, one can loosely assume that the range velocity is caused mainly by the translational motion (i.e. the sailing) of the vessel. Hereinafter, these conditions are assumed for the estimation of the ground-range velocity of the vessels, and consequently their sailing direction.

For the estimation of the range velocity, another assumption has to be made. During the estimation, the shift of the Doppler spectrum of the target (proportional to its range velocity) has to be compared to the Doppler centroid frequency of reference. When using the SLC chips from the real SAR acquisitions, this reference is obtained from the product specifications via a polynomial function in terms of the range. In general, the polynomial function is computed from geometrical models of attitude measurements, but they are later refined with measurements of the received data [24]. As with any curve fitting approach, they have a certain degree of accuracy with respect to the true value. For this reason, it would be advantageous to have an expected error figure of the estimation of the reference Doppler centroid frequency, so the uncertainty of the estimated range velocity could be provided. Unfortunately, almost all of the SCL chips associated to a ground-truth used in this research works comes from RADARSAT-2 acquisitions, in which the product specification is vague with regard to the expected error of the Doppler centroid frequency from the polynomial model. Therefore, a definitive value for the uncertainty of this polynomial model cannot be set.

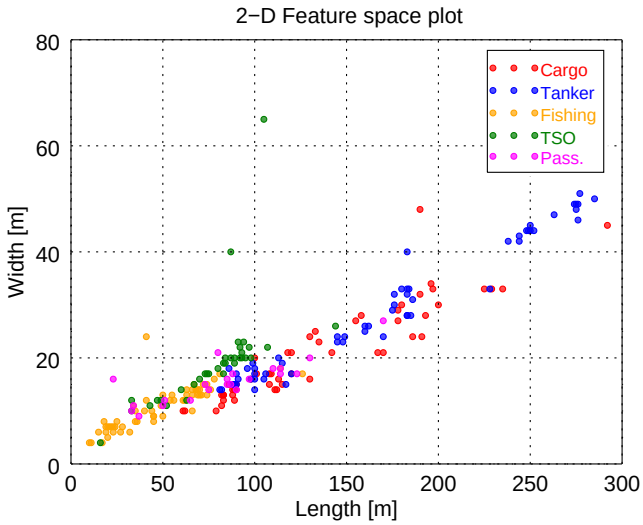

Fig. 6.2 2-D feature space plot of the training samples for the distance-weighted K-NN algorithm.

6.3.2 About the dimension estimation and classification

The scope of the current algorithm is to employ the dimensions of the SAR signature of the vessel to give a classification of the likely type of vessel. As mentioned in earlier chapters, there are inherited distortions of the structures (e.g. foreshortening and layover) due to the nature of the SAR acquisition. Moreover, multiple reflections of the EM pulse or motions of the structures can introduce additional effects besides the expected ones. Even the presence of bright scatters may deteriorate the quality of the image by impeding the detection of details of its surroundings. In this sense, the final SAR signature of a target (in this case the vessel) may result in a complex shape to be analysed. Nevertheless, it has been observed that the basic rectangular shape is preserved in the cases of medium to large vessels. Thus, even though there are slant-range distortions, it will be assumed that, after the autofocus process and UTM projection are applied, the dimensions of the SAR signature of the vessels are related to their real length and breadth.

The estimated dimensions of the SAR signature can be used as a simple feature vector for classification. A distance-weighted K-Nearest Neighbour (K-NN) algorithm [100] is employed, using several samples of the real dimensions of vessels that sail in the area of acquisition of the SAR images employed. For the current algorithm, four types (or classes) of vessels are considered, and the training samples are configured as: Cargo type (52 samples),Tanker type (58 samples), Fishing type (57 samples), Tug/Supply/Other type (35 samples), and Passengers Type (22 samples). Figure 6.2 shows this training set in the 2-D feature space plot. See Appendix B.2 for a detailed description of these samples.

There are specific types of vessels where the assumption of the dimensions of the SAR signature and the actual size of the vessel are related may not apply at all, such as in the case of tug vessels or some types of fishing vessels. Identification using the dimensions of their SAR signatures could be misleading since they could have temporary structures deployed or attached, leading to a large overestimation of the actual size of the vessels. This is one of the limitations to be aware of when applying the current algorithm, which could be a future line of work for improvement.

6.3.3 Ground-truth identification challenges

In the frame of the European Project NEREIDS [19, 20], different SAR acquisition campaigns were carried out in 2013 and 2014. Images from civilian spaceborne SAR sensors (RADARSAT-2, TerraSAR-X, and CosmoSky-MED) were taken over maritime zones near the coasts of Africa and Europe. These SAR images were employed to study the potential of SAR technology in data fusion for maritime traffic surveillance. Hence, it was possible to access complementary AIS data from the date and time of some SAR acquisitions, and in this way, to relate ground-truth with the SAR signature of vessels.

The identification of the likely ground-truth of vessels was done manually by using the geolocation of their SAR signatures. Even though a thorough search was performed, a few misidentifications could occur due to the presence of more vessels in the nearby area. Unfortunately, since access to the historical AIS records employed in NEREIDS was limited in time, it was not possible to cross-check the ground-truth through a second iteration. Although unlikely, misidentification has to be taken into account as a possible source of error in the analysis of the results.

6.4 Application of the Algorithm on experimental data

The algorithm is intended to be applied to single channel SLC SAR data from stripmap mode acquisitions. Practically, the whole experimental dataset with ground-truth comes from RADARSAT-2 acquisitions of the shore of Ålensund, Norway, because of the availability of the corresponding AIS information. Table 6.1 contains the details of the images from which the dataset of SLC chips was extracted.

The experimental dataset is made up of 46 SLC chips containing a single SAR signature of a vessel per chip (see Appendix B.1 for a detailed description). Each SLC chip is processed using to the procedure represented in Figure 6.1. In this way, the dimensions of the vessels and the estimation of their ground-range velocity is obtained using the assumptions mentioned in the previous section. In the case of the ground-range velocity, this component is computed for each SLC chip based on its AIS information (speed and heading) in order to compare it to the estimated ground-range velocity.

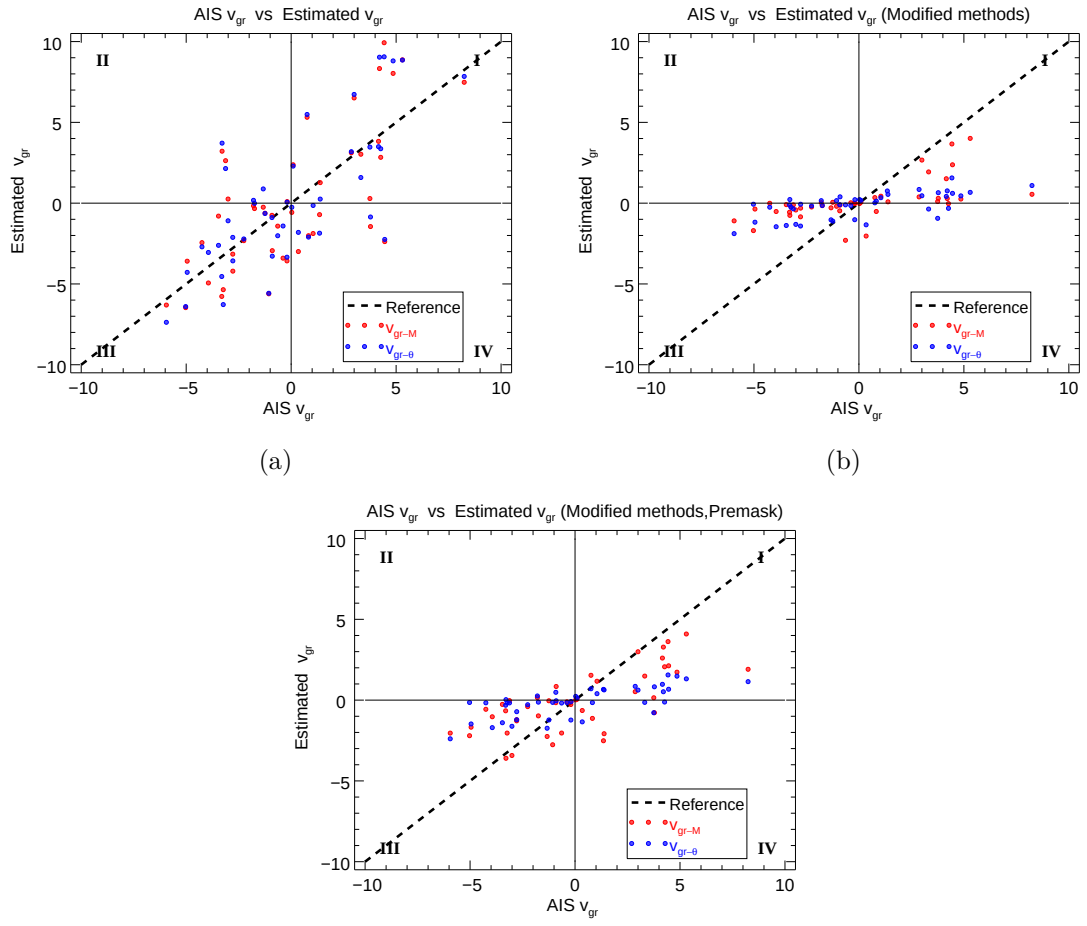

(a) (b)

(c)

Fig. 6.3 Comparison between ground-truth and estimated ground-range component of the velocity. (a) Regular estimation methods. (b) Modified estimation methods. (c) Modified estimation methods with premasking.

6.4.1 Estimated Ground-Range velocity

The estimate of the range velocity component of each vessel of the database is obtained by using the regular magnitude- and phase-based methods described in Section 5.4.3, and their modified versions (Section 5.4.5) with and without premasking. Then, their computed ground projections are compared to the ground-range components of their respective velocities given by the AIS information. These comparisons are depicted in Figure 6.3 for all the vessels in the database.

In each plot of Figure 6.3, the reference line indicates a perfect match between the estimated ground-range velocity component and its respective ground-truth value. Thus, the points on the I and III quadrants indicate that, at least, both ground-range velocities present

the same direction. On the contrary, the points on the II and IV quadrants represent the cases which have ground-range velocities with opposite direction.

Table 6.1 SAR images from which the experimental dataset has been extracted

Image code name (Mode, Date, Hour)	Zone	SLC chips
RS2_OK50548_PK483111_DK430906_FQ15W_20140316_171149_HH_VV_HV_VH_SLC	Ålensund	1
RS2_OK50548_PK483112_DK430907_MF3W_20140319_055431_HH_SLC	Ålensund	9
RS2_OK50548_PK483113_DK430908_MF3W_20140319_055436_HH_SLC	Ålensund	1
RS2_OK50548_PK483114_DK430909_MF4W_20140319_172417_HH_SLC	Ålensund	7
RS2_OK50548_PK483115_DK430910_MF4W_20140319_172422_HH_SLC	Ålensund	5
RS2_OK50548_PK483119_DK430914_MF5W_20140326_055020_HH_SLC	Ålensund	11
RS2_OK50548_PK483120_DK430915_MF5W_20140326_055025_HH_SLC	Ålensund	2
RS2_OK50548_PK483121_DK430916_FQ18W_20140329_060253_HH_VV_HV_VH_SLC	Ålensund	2
RS2_OK50548_PK483124_DK430919_MF6W_20140329_173235_HH_SLC	Ålensund	1
RS2_OK50548_PK483125_DK430920_MF6W_20140329_173240_HH_SLC	Ålensund	5
CS00_SAR_HIM_AB_20130608T050156_20130608T050203_MAT_0_0000	Lampedusa	1
CS00_SAR_HIM_AB_20130608T050159_20130608T050205_MAT_0_0000	Lampedusa	1

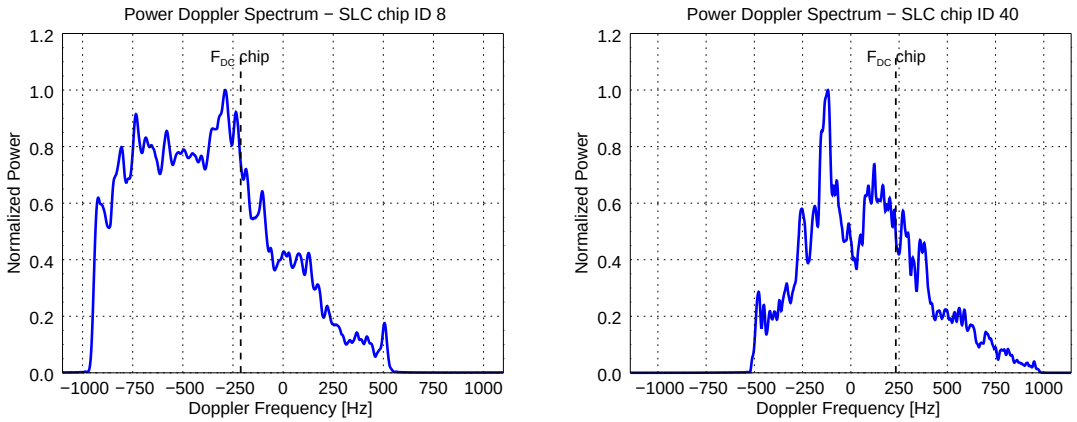

(a) (b)

Fig. 6.4 Examples of the power Doppler spectra of the SAR signatures of vessel. (a) Vessel ID 8. (b) Vessel ID 40.

The results in Figure 6.3 were obtained without using a calibration curve. Recall that regular range velocity estimation methods rely on the assumption of symmetry in the targets' Doppler spectra. From what it is observed in real data, that is not always the case. To illustrate, Figure 6.4 shows two examples of the power Doppler spectra of SLC SAR signatures of vessels. Then, without knowing *a priori* the envelope of the Doppler spectrum of the target, the use of a calibration curve may become a source of additional errors when applying the regular methods of Doppler centroid estimation. In these circumstances, the best option, in general, is to employ the direct estimate of the range velocity.

Now, the modified versions of the range velocity estimation methods would be expected to be more robust against the asymmetry of the envelope of the targets' Doppler spectra, so the use of the calibration curve can be applied. Figure 6.5 again shows the results of Figure 6.3b and Figure 6.3c, but this time using a calibration curve to compensate the expected bias.

Discussion

Despite the different assumptions made in the estimation of v_{gr}, it is observed that the results present the same direction as the ground-range velocity computed from the AIS information for most of the SLC chips processed. Indeed, as depicted in the plots of Figure 6.3, the I and III quadrants contain most of the points, indicating that the estimations of v_{gr} and their ground-truth values have the same sign (i.e. direction) when using either the regular or the modified estimation methods. Nevertheless, the distribution of the points on the plots indicates different performance with regards to the estimated magnitude of v_{gr} in the dataset.

The application of the regular methods for obtaining the Doppler centroid frequency (f_{DC}) gave results that corresponded more closely to the ground-truth information. Qualitatively,

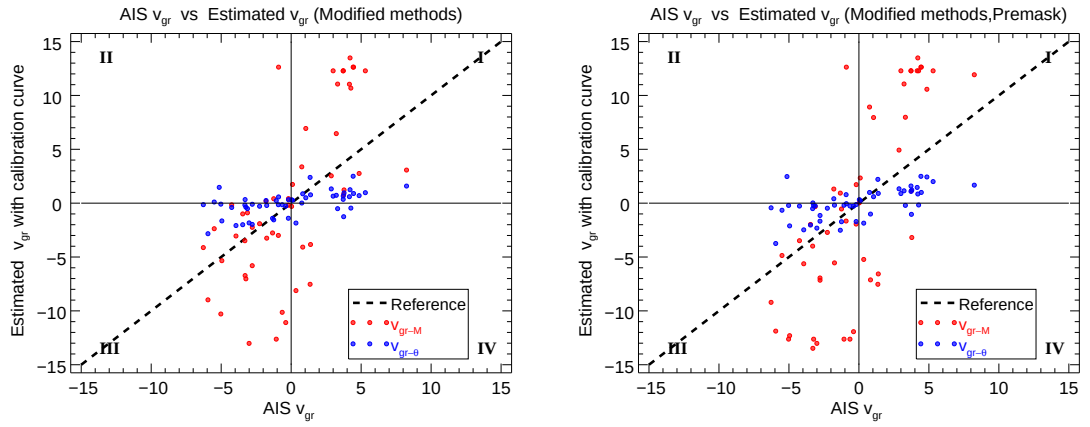

(a) (b)

Fig. 6.5 Comparison between ground-truth and estimated ground-range component of the velocity. (a) Modified estimation methods using calibration curve. (b) Modified estimation methods with premasking using calibration curve.

this can be observed from the plots in Figure 6.3. When using the traditional methods, both the magnitude- and phase-based approaches tend to be aligned with the reference line, which indicates a perfect match. In contrast, the modified methods presented a flatter distribution.

The modified methods were tested as a possible way of reducing the effect of the strong scatters in the estimation of the Doppler centroid frequency (f_{DC}), and consequently, in $\hat{v}_{gr}$. However, the estimated $\hat{v}_{gr}$ presented a flatter distribution. The likely causes of these results are different for each method. In the case of the magnitude-base approach, this kind of behaviour could be expected due to the modification of the envelope of the Doppler spectrum to a constant value based on a given power threshold (see Section 5.4.5); there, for small shifts in the Doppler spectrum, the estimated Δf_{DC} would be smaller than the actual Doppler shift due to the suppression of part of the spectrum by the windowing in the azimuth processing of the SLC image. Additional errors could be attributed to the set-up of the power threshold in the algorithm, which uses the same value to work with when processing all the SLC chips of the dataset. Now, for the phase-based approach, it is observed in Figure 6.3b that there is a tendency to estimate the ground-range velocities towards zero. A very slight improvement can be seen when a premasking process is done to extract the SAR signature from the SLC before the estimation. These results suggest that the clutter and noise may bury the phase history that belongs to the scatterers of the vessels. Recall that this method requires the use of several range bins of SAR data to obtain the estimate of f_{DC} [24], so its application to SAR signatures with few range bins may be not enough to estimate the Doppler centroid of the vessel properly in real SAR data.

The application of the calibration curve in the estimation of f_{DC} was restricted to the modified methods. Due to the assumptions made in the computation of this curve, it could

only be employed with known and symmetric spectra of the targets. Similar to the examples depicted in Figure 6.4, it was observed that, in general, the envelopes of the spectra of SAR signatures from the experimental dataset do not present an evident symmetry. Therefore, the use of the calibration curve was avoided for the traditional methods of centroid Doppler frequency estimation since it could insert additional errors to the output v_{gr}. On the other hand, the modified methods are not expected to be heavily influenced by the presence of bright scatterers and how these could modify the Doppler spectrum envelope. As such, the calibration curve could be used to improve the estimation of v_{gr}; in fact, in the case of the magnitude-base method, it is necessary to compensate the estimate, as it is expected to be an underestimation. Nevertheless, as in shown Figure 6.5, computing and applying this curve following the same methodology in Section 5.4.4 does not result in the same improvement seen in the simulated cases. This suggests that the model of the azimuth signal employed to compute the calibration curves is too simplistic for a complete representation of the phase history in real SAR SLC data.

The results of the estimated magnitude of v_{gr} have to be read with caution. As mentioned in the previous sections, a key factor in the estimation of v_{gr} is the measurement of the shift of the spectrum of the target with respect to the reference value. In this sense, the Doppler centroid frequency employed as the reference for each SLC ship is obtained from the polynomial function specified in the SLC product information datasheet of the respective SAR image. Moreover, since there was no error figure that could be related to the accuracy of this polynomial function, it is difficult to establish the uncertainty of the Doppler centroid of reference since its accuracy depends on factors such as beam mode and scene content. In addition, v_{gr} is obtained as a ground projection of the range component, implying that the most significant motion of the vessel is confined in the horizontal plane in typical conditions. Nevertheless, the motion of the vessels could be more complex, and composed of both vertical and horizontal components, so the estimate v_{gr} would not truly reflect these dynamics.

6.4.2 Estimated dimensions, heading, and classification chain

Dimensions of SAR signature and classification

The length and width of the SAR signatures are computed based on the process described in Section 5.2 that employs the UTM projection of their respective bounding boxes. This is an unsupervised process which is applied independently of the ground-range velocity estimation for each SLC chip of the dataset. Figure 6.6a and Figure 6.6b show the comparison of the estimated dimensions of the SAR signature with their corresponding values from the ground-truth (i.e. the AIS information). Similarly, Figure 6.6d and Figure 6.6c presents the same comparison but after the autofocus process. In this case, the PGA technique applied in independent range-bin (IRB) mode is presented because it showed a better performance in focusing the signatures of the vessels in the dataset.

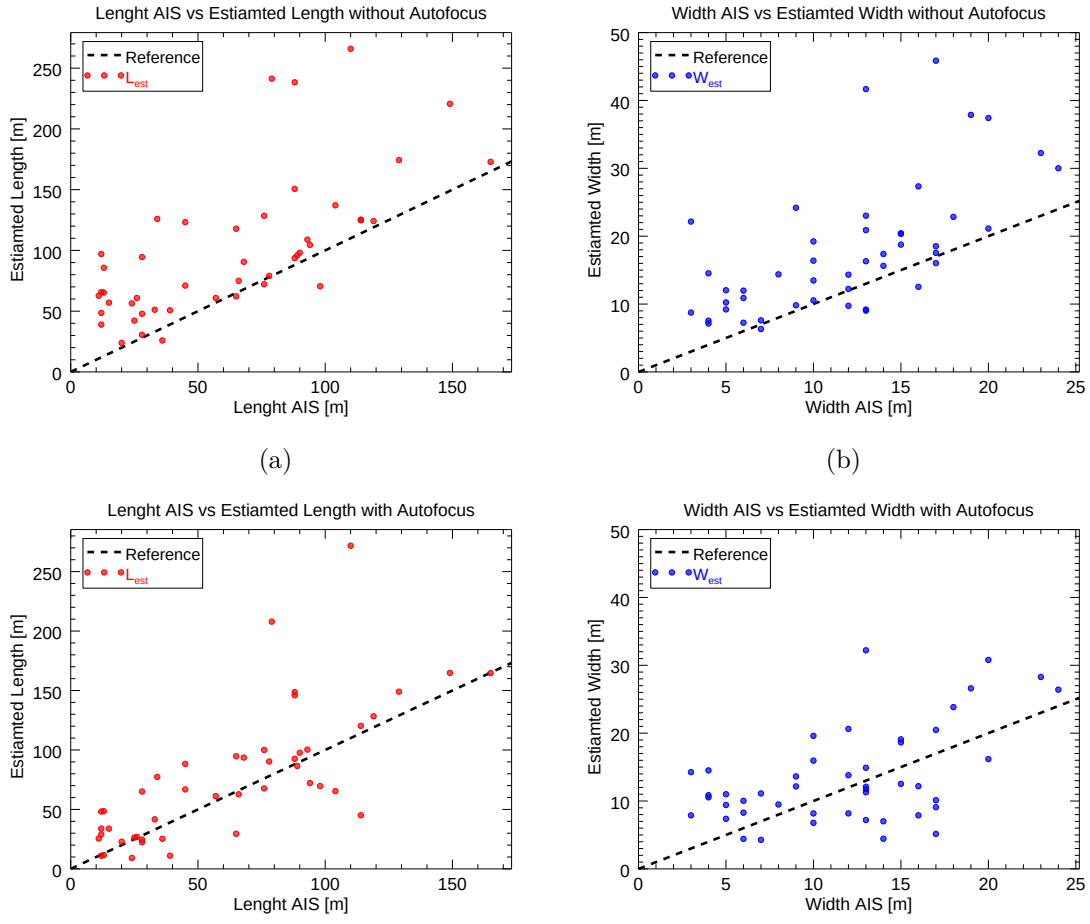

Fig. 6.6 Comparison of the estimated dimensions of SAR signature of the vessels with their corresponding AIS values. (a) Length estimate. (b) Width estimate. (c) Length estimate after PGA technique (IRB mode). (d) Width estimate after PGA technique (IRB mode).

Table 6.2 K-NN classification using direct estimation of the dimensions of the SAR signatures. (K=10)

Ground Truth	Classification Results - No Autofocus					Total by Class
	Cargo	Tanker	Fishing	TSO	Pass.	
Cargo	3	5	0	0	0	8
Tanker	2	2	0	0	0	4
Fishing	5	1	15	3	0	24
TSO*	0	1	2	1	0	4
Pass.**	1	3	1	1	0	6
Total Classified	11	12	18	5	0	46

* Tug/Supply/Other
**Passengers

Table 6.3 K-NN classification using the estimated dimensions of the SAR signatures when applying the PGA technique. (K=10)

Ground Truth	Classification Results - PGA					Total by Class
	Cargo	Tanker	Fishing	TSO	Pass.	
Cargo	2	4	2	0	0	8
Tanker	1	3	0	0	0	4
Fishing	1	1	19	3	0	24
TSO*	0	0	3	1	0	4
Pass.**	2	1	1	2	0	6
Total Classified	6	9	25	6	0	46

* Tug/Supply/Other
**Passengers

Using the estimated dimensions of the vessels as a feature vector, a distance weighted K-NN algorithm [100] is employed to classify each vessel. Table 6.2 and Table 6.3 show the results of the classification using the estimated dimensions from Figure 6.6, i.e. for the case of no autofocus and the case of PGA technique, respectively.

Heading

After estimating the dimensions of the vessel, its heading is computed as described in Section 5.3. The estimate of its ground-range velocity is employed in combination with the orientation of the bounding box defined from its SAR signature. Notice that if it is assumed that this orientation is correct, at least the direction of the estimated ground-range velocity must be correct in order to obtain the right heading angle. Otherwise, one can expect errors of 180° in the heading. Figure 6.7 depicts the angular histograms of the heading error of all the database chips based on their respective AIS information. The first angular histogram corresponds to the case with no autofocus technique applied, while the rest represent the heading angle errors when either the MAM (N=3), PGA, or the ICBA (N=3) technique is

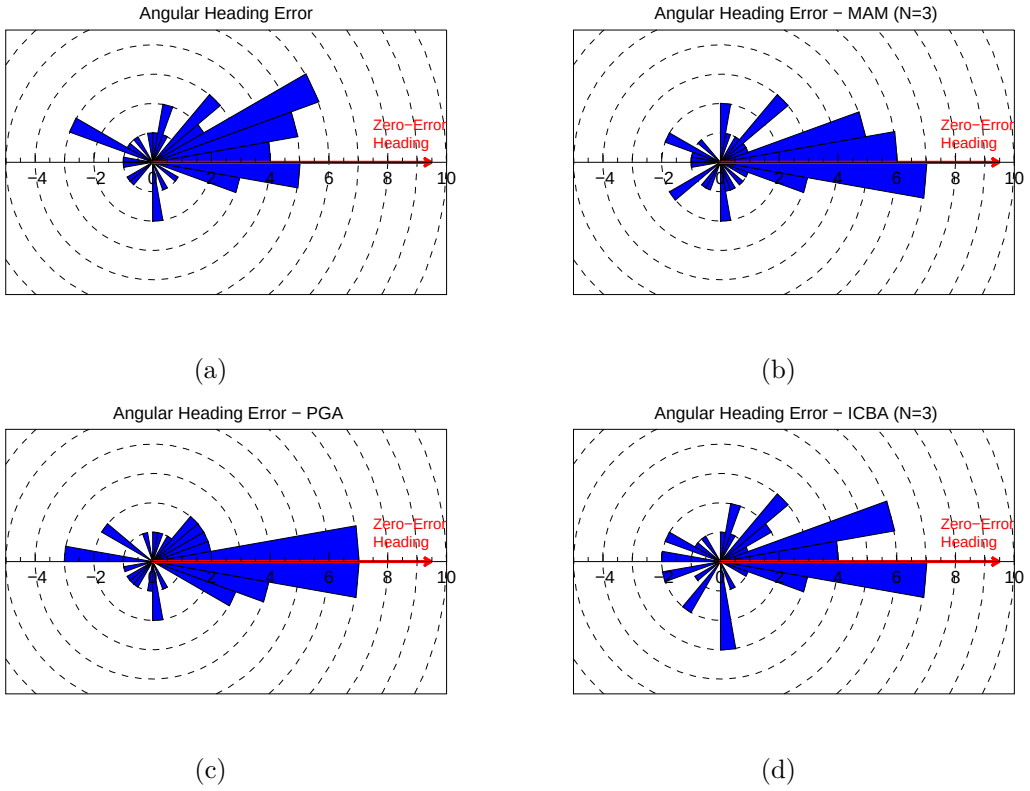

Fig. 6.7 Angular histograms of the heading angle error of the database chips based on their respective ground-truth information. The angular bin size is set to 10°. (a) No autofocus applied. (b) MAM (N=3, IRB mode). (c) PGA (IRB mode). (d) ICBA (N=3, IRB mode).

employed before obtaining the bounding box of the SAR signature. These results correspond to the application of the autofocus algorithms, which are applied in independent range-bin (IRB) mode since this has the best performance for the data set. For all the histograms, the angular bin size is set to 10°, and the zero error heading direction corresponds to the right side of the horizontal axis.

Discussion

For most of the cases of the dataset, the extraction of the SAR signature of the vessel from the sea clutter was done correctly, in the sense that emulates what a user would identify as the SAR signature. The plots of Figure 6.6a and Figure 6.6b depict that, in general, the algorithm overestimates the dimensions of the vessels when it is applied directly to the SLC chip. In some cases, this overestimation is related to defocus effects in the SAR signatures of the dataset. In others, it was observed that the presence of disperse highly reflective scatterers worsened the masking process. In these cases, the algorithm tended to either mask only the area around the highly reflective scatterer or select a broader area due to the presence of secondary lobes.

The application of autofocus techniques aims to enhance the quality of the SAR signature by compensating phase errors in the azimuth signal (presumably related to the motion of the vessel). In this way, the ultimate goal is achieving a better estimation of the dimensions of the SAR signature. The current algorithm has several degrees of freedom regarding the application of the autofocus techniques. First, the MAM, PGA, and ICBA techniques can be chosen as the autofocus method. For MAM and ICBA, the polynomial model has to be chosen from 2^{nd} to 4^{th} order. Second, one can either apply the autofocus algorithm as a single phase compensation for the whole SAR signature or in an independent range-bin (IRB) mode. As mentioned in Section 4.4.2, the decision to apply the algorithms in a single phase function approach or in IRB mode highly depends on the content of the SLC chip. It was observed that if a single phase function is used, the three algorithms produced simialr focused SAR signatures when MAM and ICBA use a 3^{th} order polynomial function. When the algorithms were applied in IRB mode, similar results were obtained with MAM and ICBA, but for the PGA technique, its tendency to focus only the strongest scatterer in the range bin results in a compacted signature that may cause an underestimation of the dimensions of the vessel. In any case, the estimation of the dimensions of the vessels for the cases with severe defocus indeed improved after the autofocus processing, and this tendency can be observed in the distribution of the points around the reference line in Figure 6.6c and Figure 6.6d.

Notice that an improvement in the estimation of the dimensions of the vessels may also have an impact on the computation of the heading. The enhancement of the focus of the SAR signatures would allow a better fit of their respective bounding box to be obtained. In this way, the main axis of this rectangle results closer to the actual orientation of the SAR signature. For the dataset processed, it was observed that slightly better results were obtained in the heading when the PGA technique was applied in IRB mode as shown in Figure 6.7. There, the number of vessels with an estimated heading that falls within the range of $\pm 10^{\circ}$ of its ground-truth value increased the most when applying the PGA technique. The cause could be attributed to the previously mentioned tendency to compact the SAR signature closer to its basic shape, which makes the computation of the orientation of the bounding box easier.

Regarding the classification step, the results suggest that a feature vector based on the dimensions of the vessels is limited to provide only a rough classification. The distribution of the classes in the feature space in Figure 6.2 shows that three main areas could be identified with the training samples used: Cargo/Tanker, Tug/Supply/Other, and Fishing type. This leads to the results shown in Table 6.2 and Table 6.3 where the classifications are well distributed among these types of vessels. For the passenger type class, its samples are spread across this feature space, without populating a defined area. The low amount of training samples used for the Passenger class increases this effect. Nevertheless, one can expect that even using the same training samples for the different classes, there would be overlapping areas.

Therefore, for a better classification, the feature vector must have additional characteristics for each type of vessel besides their dimensions.

Finally, as the algorithm is currently implemented, an additional ambiguity may appear in the classification of the vessel when using only the dimensions. Even in the absence of defocus, for certain types of vessels, such as fishing ships or tugs, their dimensions may be greatly overestimated if they have peripheral structures attached or deployed. In these cases, the length of the SAR signature of the whole structure could be double the expected one, leading to a misclassification of the vessel.

6.4.3 Observed cases

By processing the SLC chips of the dataset, it is observed that the performance of the algorithm is highly dependent on the content of the SLC chip, in particular, the expected shape of the vessels' SAR signatures. Although it can be assumed that the contours of the SAR signatures are quasi-rectangular or elliptical in shape, there are several cases where they are more complex, despite refocusing. Different factors may contribute to this, such as: reflections between the sea surface and the structure of the vessel, an odd distribution of highly reflective scatterers, the sea state at the time of the acquisition, or the dynamics of the vessel that may lead to, not only defocusing, but also geometrical distortions. All these variables can potentially change the content from one SLC chip to another.

Due to the great variety of SAR signatures, this section intends to show examples that represent the main results observed in the dataset. Although the size of this dataset is relatively small, similar features are expected to be found in other SLC chips of SAR signatures of vessels, which would affect the performance of the algorithm in a similar way. Four categories of interest are considered: best cases with little defocus, best cases with defocus, worst cases, and special cases. Briefly, in the first and second cases, the output of the algorithm was similar to the ground-truth information from the AIS, therefore, the algorithm performs as expected. For the other cases, the output was different from the ground-truth due to the complexity of the SAR signature, causing poor performance of the algorithm.

Best cases with no significant defocus

From the dataset, the best cases found belong to SAR signatures of sailing large vessels (e.g. cargos, tankers). They do not present noticeable defocus effects or highly reflective scatterers with significant sidelobes. The outline of the SAR signatures of the vessels resembles their expected shape and can be easily retrieved. Figure 6.8 shows representative examples of these kinds of SAR signatures, while Table 6.4 contains the results of the algorithm and the respective AIS data of each vessel. For the dataset used, these cases represent a minority of the signatures.

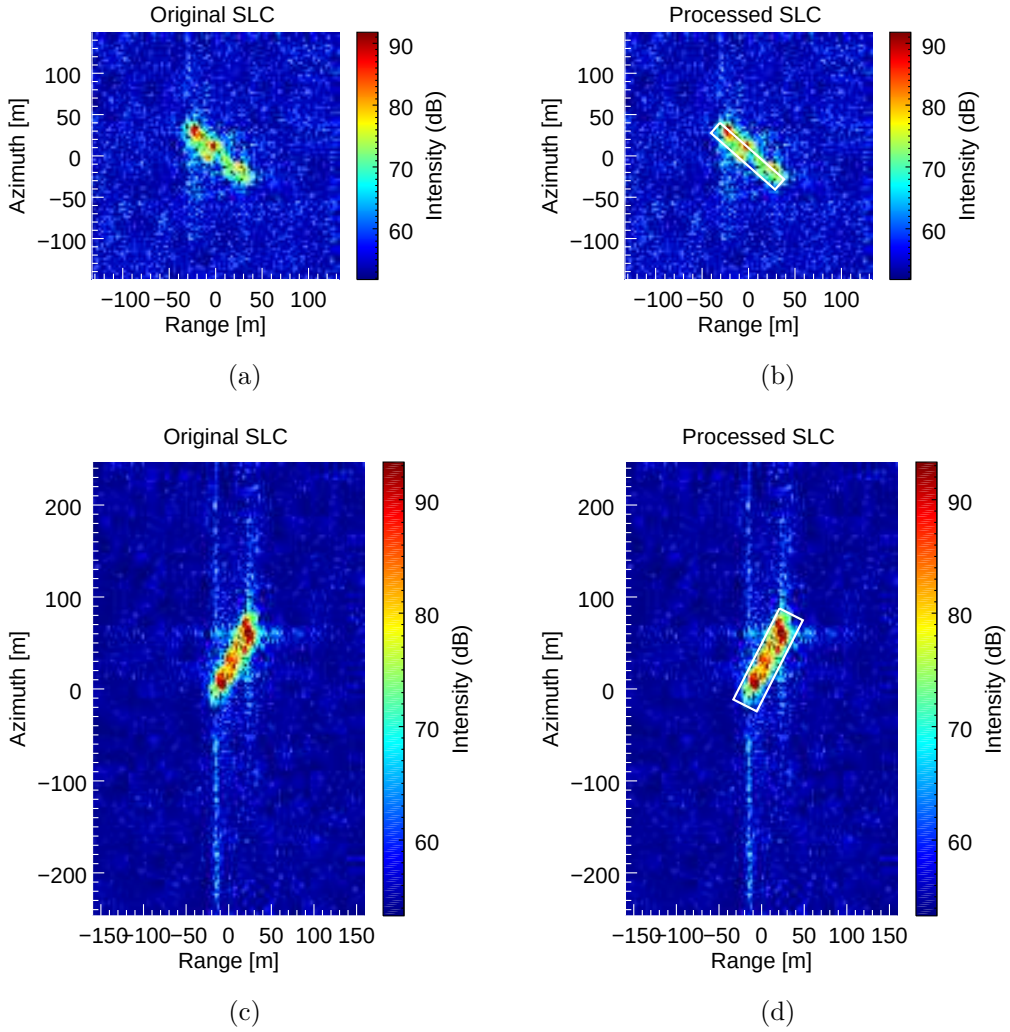

Fig. 6.8 Examples of the best cases of SAR signatures of vessels from the dataset without significant defocus. (a) Original SLC Chip (ID 8). (b) Output of the algorithm (chip ID 8). (c) Original SLC Chip (ID 21). (d) Output of the algorithm (chip ID 21).

Table 6.4 Results and AIS data of the examples of the best cases of SAR signatures of vessels.

SLC chip		**Length [m]**	**Width [m]**	**Heading [°]**
ID 8	**Estimation:**	125.33	18.52	315.24
	AIS data:	114.00	17.00	315.00
ID 21	**Estimation:**	124.15	37.87	210.92
	AIS data:	119.00	19.00	212.00

Table 6.5 Results and AIS data of the examples of the best cases of SAR signatures of vessels with defocus.

SLC chip		Length [m]	Width [m]	Heading [°]
ID 14	**Estimation:**	90.29	20.47	241.19
	AIS data:	78.00	17.00	241.00
ID 38	**Estimation:**	100.32	12.53	39.87
	AIS data:	93.00	15.00	44.00

Best cases with defocus

SAR signatures may present defocusing effects that may have been induced due to the motion of the vessels or, in some instances, a slight error in the parameters of the image formation processor. After the application of an autofocus method, similarly to the previous case, the outline of the SAR signature resembles the expected one and is properly retrieved as shown Figure 6.9. A key factor is whether the autofocus is applied as a single phase error function compensation for the whole signature or in an IRB mode. From what was observed in the dataset, this decision depends on the content as highlighted in Section 4.4.2, and in some cases it leads to a better improvement of the SAR signature, in particular for the heading (see Section 6.4.2). Table 6.5 contains the results of the algorithm and the respective AIS data of each vessel.

Worst cases

SAR signatures of the vessels in the images can appear as more complex clusters than expected. Additionally, recall from Section 4.2 that the autofocus techniques, as they are implemented in the algorithm, assume that scatterers in the same range bin present the same phase error. Therefore, if the vessels happen to be aligned with the azimuth direction, the compensation of the focusing would not be done properly and the refocus of the whole SAR signature is likely to fail. So, even after the application of autofocus, a signature that resembles a typical vessel SAR image may not be retrieved. Figure 6.10 shows two examples of cases where the performance of the algorithm deteriorates. In particular, Figure 6.10b depicts an example where it was possible to detect the vessel as a bright cluster in the SAR image, but with a contour that does not resemble the expected shape of the a vessel's signature, even after applying an autofocus technique. Obtaining its dimension would be equally challenging with an user-supervised approach. Table 6.6 contains the results of the algorithm and the respective AIS data of both of the examples presented.

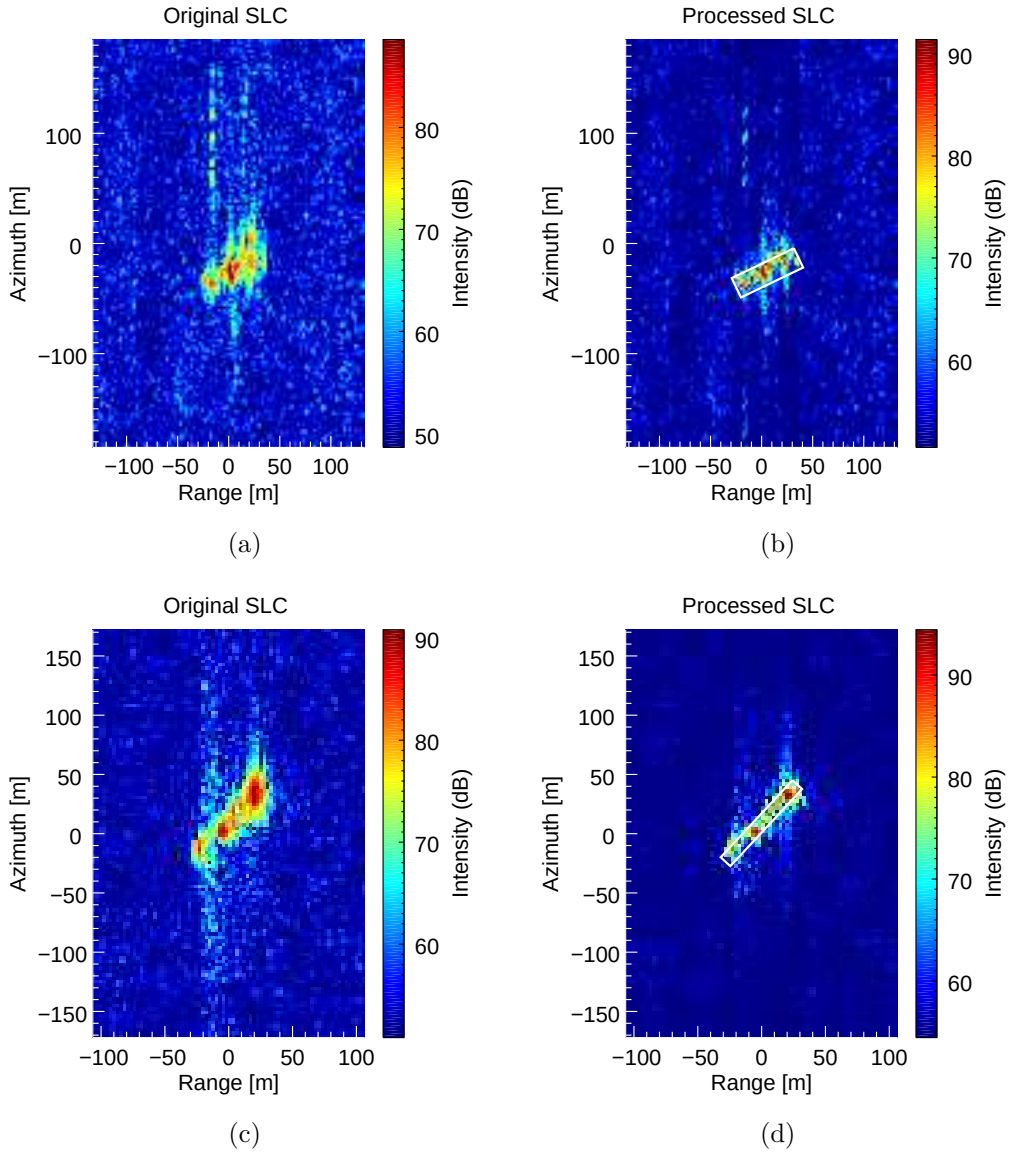

Fig. 6.9 Examples of the best cases of SAR signatures of vessels from the dataset with defocus. (a) Original SLC Chip (ID 14). (b) Output of the algorithm (chip ID 14) using PGA (IRB mode).(c) Original SLC Chip (ID 38). (d) Output of the algorithm (chip ID 38) using PGA (IRB mode).

Table 6.6 Results and AIS data of the examples of the worst cases of SAR signatures of vessels.

SLC chip		**Length [m]**	**Width [m]**	**Heading [°]**
ID 7	**Estimation:**	271.76	23.83	191.29
	AIS data:	110.00	18.00	188.00
ID 18	**Estimation:**	133.99	37.84	197.20
	AIS data:	104.00	16.00	214.00

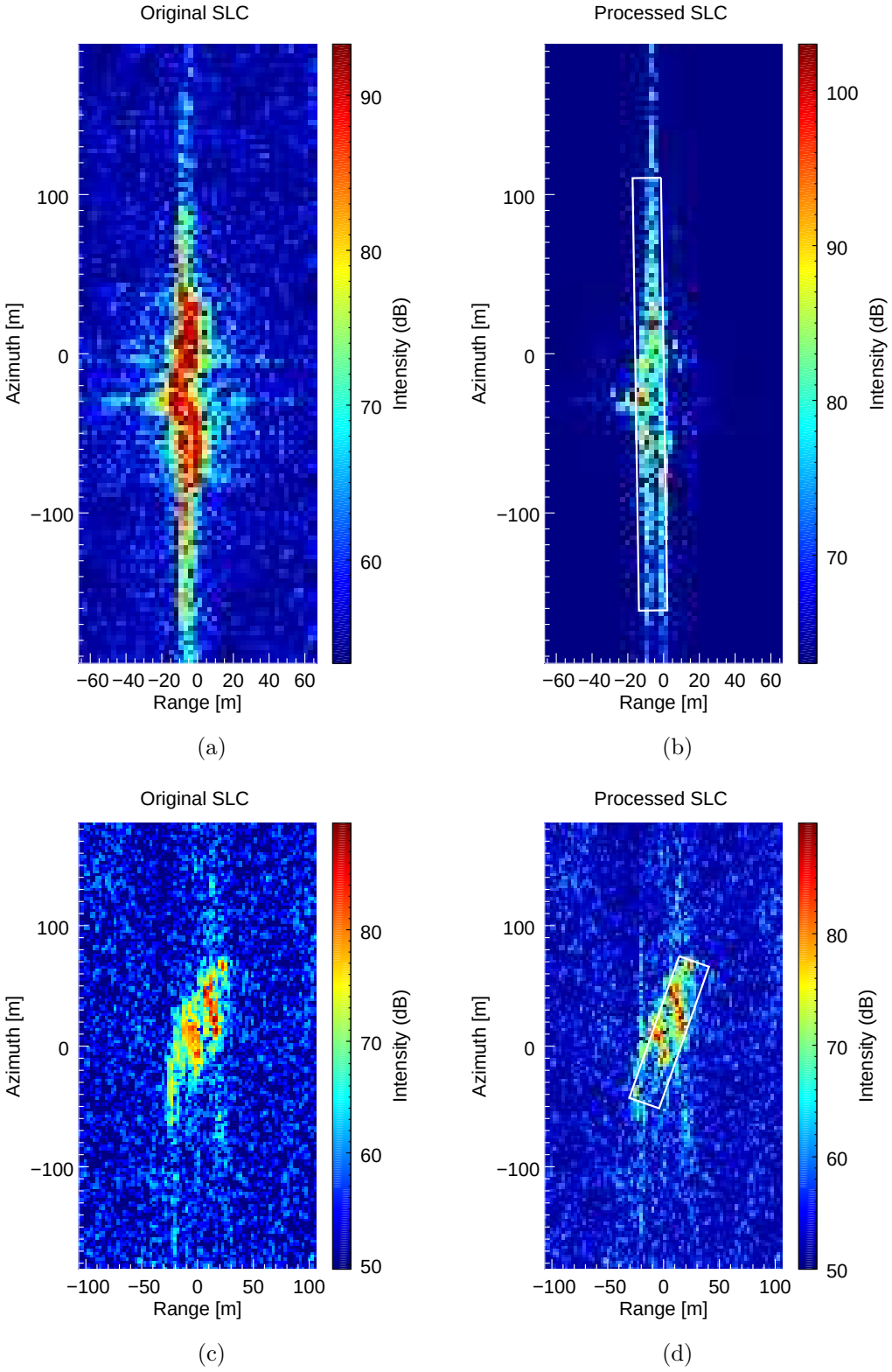

Fig. 6.10 Examples of the worst cases of SAR signatures of vessels from the dataset that deteriorate the performance of the algorithm. (a) Original SLC Chip (ID 7). (b) Output of the algorithm (chip ID 7) using PGA (IRB mode). (c) Original SLC Chip (ID 18). (d) Output of the algorithm (chip ID 18) using MAM (IRB mode).

Table 6.7 Results and AIS data of the examples of the SAR signatures of vessels from the dataset that may mislead the outputs of the algorithm.

SLC chip		Length [m]	Width [m]	Heading [°]
ID 25	**Estimation:**	20.46	13.14	21.54
	AIS data:	20.00	6.00	53.00
ID 12	**Estimation:**	122.02	18.03	203.96
	AIS data:	76.00	14.00	244.00

Special cases

Some of the SLC chips of the dataset presented features that misled the final output of the algorithm despite its good performance. The first case corresponds to SAR signatures of small vessels ($\sim 25[m]$ or less) that appear as a small cluster as shown in Figure 6.11a. With this type of SAR signatures, the estimation of the dimensions and, especially, the heading could be difficult due to the lack of a predominant direction in the distribution of the scatterers. In this example, the estimated dimensions are similar for both the length and the width. Another case is the SAR signature of vessels such as fishing ships or tugs that may have a peripheral structure attached or deployed. To illustrate this, Figure 6.11c shows a SAR signature that, according to the ground-truth, belongs to a tug vessel. Notice that the obtained length of the signature is much larger than the actual length of the vessel, suggesting that it had an external structure attached at the time of the SAR acquisition. Table 6.7 contains the results of the algorithm and the respective AIS data for each of the examples presented.

6.5 Summary

The algorithm proposed in this chapter employs stripmap SLC chips of the detected vessels and processes them to extract features of interest. The algorithm estimates the ground-range velocity of the vessels, its dimensions and heading, and its likely class of vessel based on a distance-weighted k-nearest neighbour classifier.

Due to the complexity of maritime SAR images, different assumptions are made in order to extract the features from the SAR signature of the vessels. For the estimation of the ground-range velocity, first, the expected motion of the vessel is simplified by considering calm/moderate sea state conditions, making the translational motion of the vessel the main contributor to its range velocity. Second, since this range velocity is computed by the shift of the Doppler spectrum of the vessel, the Doppler centroid obtained from the product specifications of the SAR images is assumed as the reference frequency. Then, for the estimation of the dimensions and the classification of the vessels, SAR signatures are expected to present quasi-rectangular shapes, whose dimensions would be quite close to the vessels'

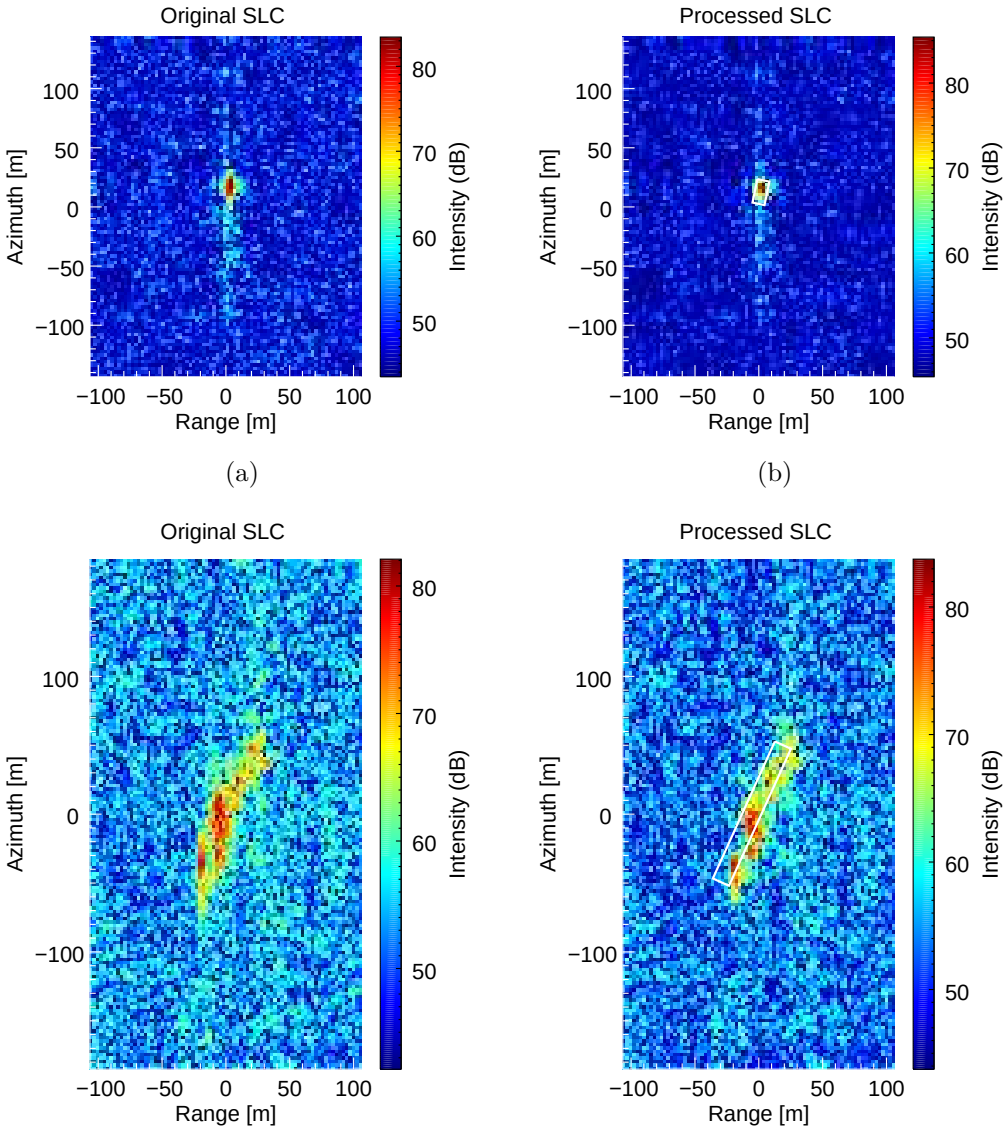

Fig. 6.11 Examples of SAR signatures of vessels of the dataset that may mislead the output dimension of the algorithm. (a) Original SLC Chip (ID 25). (b) Output of the algorithm (chip ID 25) using PGA (regular mode). (c) Original SLC Chip (ID 12). (d) Output of the algorithm (chip ID 12) using PGA (regular mode).

real dimensions despite the inherent distortions of SAR imaging. Thus, a classification based on the signatures' dimensions can be performed, at least to roughly identify the type of vessel.

Regarding the results of v_{gr} from the algorithm, the estimates using the regular Doppler centroid methods presented a better agreement with the ground-truth values than the modified methods. This could be attributed to the fact that the regular methods give more weight to data from strong scatterers when estimating the Doppler centroid of the vessels' in the SLC chip. Both magnitude- and phase-based approaches presented similar results. However, the computed module of v_{gr} has to be taken with caution because of the degree of inaccuracy in the reference Doppler centroid frequency due to its dependence on the content of the SAR image. For this reason, the estimates of v_{gr} in the vicinity of zero may not truly reflect the translational motion of the vessel. In fact, in lack of a concrete uncertainty value given by the product specification of the SLC images in the dataset, an uncertainty range for the Doppler centroid and v_{gr} estimated cannot be established precisely.

Regarding the estimation of the dimensions of the vessel, three key factors were identified: the correct extraction of the contour of the SAR signature, its quality, and its complexity. For the first factor, the performance of the algorithm in obtaining the contour of most of the SAR signatures of the dataset was similar to what would be achieved with a user-supervised approach. This supports the usa of the log-Weibull distribution as a suitable model for the intensity (in dB) of the sea clutter. As for the quality of the SAR signature, the application of autofocus techniques indeed improved its quality when defocus aberrations were present. In these cases, the estimated dimensions improved, along with the estimate heading. For the dataset, using MAM, PGA, and ICBA presented similar results, but the most significant change was observed in their application as a single phase function compensation or in an independent range-bin (IRB) mode. Which approach to use depends highly on each SAR signature and final supervision is required to distinguish the best one in each case. Nevertheless, in some cases, even after using the autofocus processing, improvement in the estimation of the dimensions was not possible due to the complexity of the SAR signature: the unexpected shape of its contour, an odd distribution of highly reflective scatterers, and the presence of noticeable secondary lobes.

In the algorithm, the classification of the vessels took into account only their dimensions in the application of a distance-weighted K-NN classifier. This simple approach showed significant limitations as the processed SAR signatures could only be categorized into three groups (of the AIS types): Cargo/Tanker, Tug/Supply/Other, and Fishing type. Although the K-NN classifier may require a lot more samples to improve its performance, the results suggest that a feature vector based only on the dimensions of the vessels is not enough to classify them into several categories. Additional features suggested in the literature, like the analysis of the distributions of the scatterers and the reflectivity variations along the SAR signature, could be considered to achieve a more precise classification; but these approaches

bring about the challenge of constructing an extensive ground-truth database of vessels' SAR signatures.

Finally, it has been observed that vessel feature extraction depends highly on the content of the SLC chip. Even with the relatively small dataset employed, tendencies were observe in the performance of the algorithm. The best agreement of the extracted features with the ground-truth data was observed in cases of large vessels such as cargo or tankers. In most of them, the shape of their signature was similar to the one assumed; even with the presence of defocus artefacts, the quasi-rectangular shape can be retrieved. The worst cases were the complex SAR signatures that appear as bright structures, but do not resemble an expected signature of a vessel at all. Ambiguous results were observed for medium/small vessels ($\sim 25[m]$ or less) and for some types of fishing ship and tugs. With the former, their SAR signatures appear as small round clusters, whose main dimensions and heading cannot be well established. With the latter, the presence of a peripheral structure attached at the time of the acquisition may lead to an overestimation of its dimensions and to misidentification.

Chapter 7

Conclusions and Future lines of Research

7.1 Main Contributions

The ultimate objective of this study has been to explore the application of the basic single-channel acquisitions from spaceborne SAR sensors to automatic vessel monitoring. The surveillance of human activity in the ocean is crucial to safeguard the marine environment, the sustainability of the industrial sector, and the security of navigation. Nowadays, the robustness of existing cooperative vessel monitoring systems can be increased by combining them with other sources of information such as spaceborne remote sensing systems. Among these, the synthetic aperture radar (SAR) imaging technique stands out due to its monitoring advantages: high-resolution images that allow the identification of man-made objects, image acquisitions at a global scale, and non-dependence on natural illumination and weather conditions over the area of interest. Despite the different configuration and capabilities of current civilian spaceborne SAR sensors, all of them are able to provide basic single-channel images. Thus, using these basic acquisitions, the constellation of all these SAR satellites constitutes a family of sensors that can potentially support the continuous monitoring of vessels in any area of the ocean. The presented research work has shown both the feasibility and the limitations of using vessels' signatures from single-channel SAR images for their detection and feature extraction. The main contributions of this research are:

- *Improvement of SAR simulation tools.* In this thesis, the GRECOSAR simulator was the main tool used to generate raw data. It is a powerful and suitable tool for simulating vessels in maritime environments because of its capabilities in emulating rotations and translations of complex targets. Three key improvements were made to GRECOSAR, namely: 1) the adoption of the sinc interpolation to reduce the simulated aperture positions and, in this way, the processing time; 2) the application of the antenna

pointing in time domain rather than in Doppler domain (as originally implemented) for an accurate representation of the effects of the target's motion in the simulated SAR raw data; and 3) the addition of a multi-harmonic and dynamic model of the surface of the sea, presenting a closer reflectivity response in amplitude to probability distributions of real sea clutter from high-resolution SAR images. These modifications improved GRECOSAR's performance and provided a more realistic approach to simulate the vessels.

- *Adaptation and assessment of classical autofocus in SAR signatures of vessels.* The deterioration of the images due to defocus hinders the extraction of features related to the distribution of the scatterers or the shape of the SAR signatures. To address this, this thesis proposes the local application of autofocus techniques to improve the focus quality of the signatures. Three widely used autofocus techniques were considered in this study: the phase gradient autofocus (PGA), the multiple aperture mapdrift (MAM), and the image contrast based autofocus (ICBA). They were adapted, implemented, and evaluated using real SAR images of vessels from stripmap SAR data. In addition, the application of the autofocus in an independent range-bin (IRB) mode was explored as a way to lessen the effects of different defocus along the range direction.

- *Methodology for feature extraction based on the analysis of the SAR signatures in the image and Doppler domain.* The application of SAR images to vessel monitoring requires, when possible, the extraction of features or relevant information about the targets in addition to simply detecting them. In this framework, the analysis of single-channel stripmap acquisitions led to the development of an automatic algorithm that is proposed in this thesis for estimating the length, width, and heading of the vessels. These features are obtained by exploiting the intensity characteristics of the SAR images and the effects of the motion of the targets in their Doppler spectra.

- *Development and evaluation of a post-processing strategy of vessels' SAR signature for maritime surveillance.* A processing chain integrating autofocusing and feature extraction techniques has been developed to be applied to vessels' SAR signatures from single-channel stripmap SAR images. As a large amount of vessels are often detected in a single image, automation of this post-processing has been contemplated for its practical implementation. In addition, the basic performance characterization of this algorithm has been carried out using real vessels' SAR signatures and their respective ground-truth data.

7.2 Main Conclusions

The main conclusions of this research can be summarized as follows:

- *Framework of SAR imaging in vessel monitoring.* The post-processing of SAR images provides a non-cooperative approach in the surveillance of maritime traffic; in this sense, it represents an independent source of information that can be used for cross-checking with the data of vessel surveillance systems like AIS and VSM. In general, the extraction of relevant information about the vessels from SAR images involves steps of detection and classification of the candidates. Today, these steps present a different level of development. State-of-the-art techniques for vessel detection report great refinement and robustness, achieving low false-alarm rates. On the other hand, classification techniques have shown more modest development. The complexity of the SAR signatures of the vessels, the lack of ground-truth for the analysis, and the distortions in the SAR image due to the dynamics of the vessels are obstacles that hinder the development of these vessel classification algorithms.

- *Simulation tools for vessels in maritime environments.* In the case of spaceborne SAR imaging, the operational complexity of controlled acquisition campaigns makes the simulation tools a cost-effective alternative for studies of vessel monitoring. Simulation tools can offer flexibility in the selection of the parameters of the SAR sensor, and more importantly, in the control of the content of the scene. In this research, the raw data simulator GRECOSAR was used as it has the advantage of combining the reflectivity of complex targets with their motions; and the additional improvements implemented aimed to make GRECOSAR an even more effective simulator for the analysis of vessel SAR signatures.

- *Effects of the motion of medium/large vessels on the received SAR signal.* The dynamics of the vessels are crucial to understand their SAR signal and the artefacts that appear in their respective images due to the induced phase errors. In the case of stripmap acquisition of spaceborne SAR sensors, these phase errors can be entirely associated to the vessel's motion since the satellite trajectory is practically stable during the aperture time. As medium/large vessels can be considered slow-moving targets, the analysis of their typical motion can be reduced to the phase errors in the azimuth direction, highlighting the range component as the main contributor to these errors. The effects of the motion of the vessels are commonly appreciable along the azimuth direction in the SAR images from stripmap acquisitions: relocation of the vessels are induced by their range velocity, and defocusing appears due to the range acceleration and higher order components that modify the expected Doppler rate.

- *Refocus of the vessels' SAR signatures.* The non-parametric(PGA) and the model-based (MAM and ICBA) autofocus techniques proved to enhance the focus quality of vessels' SAR signatures. As implemented, the three algorithms presented similar results for the test set of real SAR signatures used, which suggests that the expected phase errors

of a medium/large vessel can be approximated to polynomial functions for the case of stripmap images from spaceborne SAR sensors. Moreover, in the case of defocused SAR signatures, the application of autofocus techniques improved the extraction of their dimensions and heading.

Heterogeneity of the defocus of the scatterers was a problem observed while applying autofocus. Scatterers with different phase errors jeopardized the correct refocusing of the images as the autofocus techniques compute a single phase correction function. In particular, if the scatterers with different defocus are in the same range bin, the performance of the autofocus algorithms would likely deteriorate since this condition goes against their built-in assumptions. The application of the autofocus in an independent-range bin (IRB) mode aimed to deal with the diversity of the defocusing, but only in the range direction. However, whether to use the single-function or the IRB approach for the best refocus depended highly on each SAR signature and its respective variation of defocus, and final supervision is required to ensure the best focusing results.

- *Feature extraction of the vessels' SAR signatures.* The estimated dimensions and heading of the vessels agree with the corresponding ground-truth values for most of the cases in the data set, although over- and underestimations occurred. In general, the results from the automatic extraction of the contour of the SAR signatures were similar to what would be achieved with a supervised approach. These results indicate that the masking method used is suitable for real single-channel SLC data.

  For the computation of the heading, the approach used has the advantage of not depending on additional assumptions in the reflectivity of the SAR signature in order to determine the bow and stern of the vessel, as long as it is sailing. Moreover, since the range velocity is extracted as part of the process, it can be used for the correction of the vessels' positions at the time of the image acquisition.

- *Complexity of vessels' SAR signatures.* Despite the application of an autofocus technique, the complexity of the SAR signatures and additional reflective artefacts (e.g. high side-lobes) can cause the retrieval of shapes that do not resemble the classical quasi-rectangular or ellipsoidal vessel's SAR signature. In addition, certain types of fishing and tug vessels may be challenging cases. The presence of peripheral structures attached to these types of vessels at the time of the SAR acquisition would likely lead to the overestimation of their dimensions and a potential misidentification.

- *Feature extraction algorithm using real SAR data.* The automatic feature extraction algorithm proposed in this thesis has shown a potential applicability for vessel monitoring using stripmap images from spaceborne SAR sensors. The results indicate that the algorithm presents better performance with medium/large vessels with high reflectivity. However, the complexity of the vessels' SAR signature can compromise its performance.

As implemented, it is ready to be applied as an extension to any vessels detection system working with stripmap SAR images.

7.3 Future lines of research

Future lines of research have been identified during the development of this thesis:

- *Extensive validation of the feature extraction algorithm.* The analysis of the results with a broader data set would provide a more detailed characterization of the algorithm and allow refining the assumptions made for the extraction of the vessels' features. As can be expected, a crucial factor is the compilation of SAR images of vessels along with their corresponding ground-truth, which is a challenge in itself due to the scarcity of this cross-information for spaceborne SAR acquisitions.

- *Side-lobe reduction of strong scatterers.* During the masking process of the vessel's SAR signature, side-lobes of strong reflectors can affect the obtaining of the final contour as they appear as part of the vessel's structure; consequently, they may compromise the extraction of the dimensions and heading of the vessel. In this sense, a side-lobe suppression step could be included in the algorithm to extract the contour of the SAR signature that belongs only to the vessel. Potential techniques to be analysed for application on vessels' SAR signatures are the spatially variant apodization (SVA) and an image-based approach based on a combination of morphological operations.

- *Analysis of different defocus in the same range-bin.* Extensions of the autofocus techniques implemented could be developed in order to compensate different defocus mechanisms within the same range-bin. As seen in the application of the autofocus techniques in the IRB mode, heterogeneous defocus may appear along the SAR signatures of the vessels. A potential approach could be the independent application of the autofocus to sectors of the SAR signatures along the azimuth direction, superimposing the individual segments later to get the final result. Nevertheless, further analysis of these special cases is required since they are generally out of the scope of the assumptions of regular autofocus techniques for SAR imaging.

- *Error figure for the nominal Doppler centroid frequency.* A critical part in the estimation of the range velocity is the comparison of the induced Doppler centroid shift with respect to the nominal Doppler centroid frequency of the SLC chip processed. An error figure of this nominal value would allow a formal analysis of the uncertainty of the estimation of the vessels' range velocity. Since the product information does not provide a direct value for the uncertainty in the Doppler centroid, a methodology could be developed for analysing the error of the provided Doppler function and the Doppler spectra of the SLC data.

- *Analysis of the characteristic reflectivity of the different groups of vessels.* For the single-channel case, a deep study of the reflectivity of the different types of vessels is required to identify particular profiles. The results suggested that using the signatures' dimensions alone would only allow a rough identification of the type of vessel. Sectional reflectivity or the relative distribution of the scatterers along the SAR signature could become part of the feature vector in order to refine the classification of the vessels. Clearly, the construction of an extensive database that contemplates different types of vessels and the variety of their orientation is a key requirement that has to be accomplished first. In this sense, the use of SAR simulators like GRECOSAR is likely to be essential as they are the most cost-effective approach for this endeavour.

- *Extension of the feature extraction algorithm to other SAR modes.* The scope of this research was focused on the analysis of single-channel SLC SAR data from stripmap mode acquisitions. Similar analysis can be done to consider different types of data like polarimetric SAR, spotlight acquisitions, or multi-look products. In this way, the algorithm would be more flexible, since it could use any of the SAR data available and, at the same time, it could take advantage of their characteristics for the extraction of specific features of the vessels.

Finally, this research work highlights the idea of combining SAR processing techniques with image processing for the extraction of features of vessels in maritime SAR images. The results obtained demonstrates both the feasibility and the limitations of using basic single-channel SAR acquisitions in vessel monitoring; and the processing chain presented in this research can be seen as a first iteration for the development of a fully automatic algorithm to support the current vessel detection systems in operation.

Appendix A

A.1 Log-Weibull distribution

The p.d.f. of the intensity (in dB) of the sea clutter on a SAR image can be modelled with a log-Weibull distribution. If X is a random variable that represents the reflectivity (amplitude) of the sea clutter with a Weibull distribution, its c.d.f is given by

$$F_X(x|a,b) = \text{prob}(X \leq x) = 1 - e^{-(\frac{x}{a})^b} \tag{A.1}$$

with a and b as the scale and shape parameters, respectively. Then, for the intensity image a change of variable is required such as

$$Y = 20\log(X) = \frac{20}{\ln(10)}\ln(X) = \frac{1}{k}\ln(X); \qquad X > 0 \tag{A.2}$$

Then, by applying the change of variable in equation (A.1), the log-Weibull model is obtained [88]:

$$\begin{aligned} prob(Y \leq y) &= prob\left[\frac{1}{k}\ln(X) \leq y\right] \\ &= prob\left[X \leq e^{ky}\right] \\ &= 1 - e^{-(\frac{e^{ky}}{a})^b} \\ &= 1 - e^{-(e^{ky-\ln(a)})^b} \\ &= 1 - e^{-e^{bk(y-k^{-1}\ln(a))})} \\ F_L(y|\alpha,\beta) = prob(Y \leq y) &= 1 - e^{-e^{\beta(y-\alpha)})} \end{aligned} \tag{A.3}$$

with $\alpha =$ and β the new scale and shape parameters, respectively, and y representing the sea clutter intensity in dB. The p.d.f. of the log-Weibull distribution is computed by taken the derivative of equation (A.3) respect to y

$$f_L(y|\alpha,\beta) = \frac{\mathrm{d}}{\mathrm{d}y}F_L(y|\alpha,\beta) = \beta e^{\beta(y-\alpha)-e^{\beta(y-\alpha)}} \tag{A.4}$$

Appendix B

B.1 Ground-truth Dataset

This section gives the information of the experimental dataset formed by 46 SLC chips. In the following, a list of the original SAR images are provided. Additionally, Table B.1 contains the information about the location of central pixel of each SLC chip in its respective SAR image. Finally, the AIS information associated to each SLC chip is given in Table B.3.

SAR Image 1:
RS2_OK50548_PK483111_DK430906_FQ15W_20140316_171149_HH_VV_HV_VH_SLC

- **Area:** Ålensund
- **Resolution (range x Azimuth):** 4.73 [m] × 5.11 [m]
- **Range of SLC chips:** ID 0

SAR Image 2:
RS2_OK50548_PK483112_DK430907_MF3W_20140319_055431_HH_SLC

- **Area:** Ålensund
- **Resolution (range x Azimuth):** 2.66 [m] × 2.99 [m]
- **Range of SLC chips:** ID 1 to ID 9

SAR Image 3:
RS2_OK50548_PK483113_DK430908_MF3W_20140319_055436_HH_SLC

- **Area:** Ålensund
- **Resolution (range x Azimuth):** 2.66 [m] × 2.99 [m]
- **Range of SLC chips:** ID 10

SAR Image 4:
RS2_OK50548_PK483114_DK430909_MF4W_20140319_172417_HH_SLC

- **Area:** Ålensund
- **Resolution (range x Azimuth):** 2.66 [m] × 2.47 [m]
- **Range of SLC chips:** ID 11 to ID 17

SAR Image 5:
RS2_OK50548_PK483115_DK430910_MF4W_20140319_172422_HH_SLC

- **Area:** Ålensund
- **Resolution (range x Azimuth):** 2.66 [m] × 2.47 [m]
- **Range of SLC chips:** ID 18 to ID 22

SAR Image 6:
RS2_OK50548_PK483119_DK430914_MF5W_20140326_055020_HH_SLC

- **Area:** Ålensund
- **Resolution (range x Azimuth):** 2.66 [m] × 2.87 [m]
- **Range of SLC chips:** ID 23 to ID 33

SAR Image 7:
RS2_OK50548_PK483120_DK430915_MF5W_20140326_055025_HH_SLC

- **Area:** Ålensund
- **Resolution (range x Azimuth):** 2.66 [m] × 2.87 [m]
- **Range of SLC chips:** ID 34 to ID 35

SAR Image 8:
RS2_OK50548_PK483121_DK430916_FQ18W_20140329_060253_HH_VV_HV_VH_SLC

- **Area:** Ålensund
- **Resolution (range x Azimuth):** 4.73 [m] × 4.97 [m]
- **Range of SLC chips:** ID 36 to ID 37

SAR Image 9:
RS2_OK50548_PK483124_DK430919_MF6W_20140329_173235_HH_SLC

- **Area:** Ålensund
- **Resolution (range x Azimuth):** 2.66 [m] × 2.87 [m]
- **Range of SLC chips:** ID 38

SAR Image 10:
RS2_OK50548_PK483125_DK430920_MF6W_20140329_173240_HH_SLC

- **Area:** Ålensund
- **Resolution (range x Azimuth):** 2.66 [m] × 2.87 [m]
- **Range of SLC chips:** ID 39 to ID 43

SAR Image 11:

CS00_SAR_HIM_AB_20130608T050156_20130608T050203_MAT_0_0000

- **Area:** Lampedusa
- **Resolution (range x Azimuth):** 3.00 [m] × 3.00 [m]
- **Range of SLC chips:** ID 44

SAR Image 12:

CS00_SAR_HIM_AB_20130608T050159_20130608T050205_MAT_0_0000

- **Area:** Lampedusa
- **Resolution (range x Azimuth):** 3.00 [m] × 3.00 [m]
- **Range of SLC chips:** ID 45

Table B.1 Location of the central pixel of each SLC chip in the respective SAR image. Part I.

SLC chip ID	SAR Image #	Image coordinates	
		Sample	Line
0	1	2393	3612
1	2	12419	8141
2	2	14220	13169
3	2	18369	3252
4	2	20886	10328
5	2	12539	14251
6	2	15693	3092
7	2	4773	16888
8	2	2235	15714
9	2	2573	15810
10	3	21740	12253
11	4	2256	13842
12	4	4518	16696
13	4	6336	13368
14	4	12774	4283
15	4	16323	8715
16	4	16188	9385
17	4	20363	11165
18	5	7730	5227
19	5	8402	2123
20	5	8939	8958
21	5	20749	1159
22	5	22692	4216

Table B.2 Location of the central pixel of each SLC chip in the respective SAR image. Part II.

SLC chip ID	SAR Image #	Image coordinates	
		Sample	Line
23	6	13478	1299
24	6	7547	12115
25	6	9728	12659
26	6	4768	15634
27	6	9031	15323
28	6	9226	18566
29	6	12627	17885
30	6	18594	14790
31	6	9500	13213
32	6	1262	15163
33	6	1451	15735
34	7	10502	9512
35	7	18185	16118
36	8	3477	3412
37	8	3439	6034
38	9	8312	10377
39	10	3063	8177
40	10	3492	12320
41	10	6898	13697
42	10	7198	7816
43	10	19449	11876
44	11	3508	12014
45	12	158	9887

Table B.3 AIS information associated to each SLC chip. Part I.

SLC chip ID	**IMO**	**MMSI**	**Length [m]**	**Width [m]**	**Speed [knot]**	**Heading [°]**	**Type**
0	9568330	258526000	28	9	1.8	247	Trawler
1	9145140	311117000	89	12	9.4	50	General Cargo
2	9321380	244140000	114	15	11.1	217	General Cargo
3	9432646	257736000	94	17	5.4	97	Patrol Vessel
4	6920111	258360000	76	14	5.5	134	Trawler
5	-	257053240	13	5	8.2	281	Fishing
6	9200160	257554600	45	10	3.5	92	Trawler
7	9528471	259097000	110	18	9.3	188	Ro-Ro/Passenger
8	9521722	259677000	114	17	12.0	315	Ro-Ro/Passenger
9	9254898	258505000	88	17	10.8	137	Ro-Ro/Passenger
10	9416575	305940000	39	13	9.2	51	Tug
11	9582867	305639000	88	13	7.1	224	General Cargo
12	6920111	258360000	76	14	0.4	244	Trawler
13	-	259536000	24	7	2.6	265	Fishing
14	9617973	257913000	78	17	10.1	241	Fishing Vessel
15	7604398	257296400	65	12	11.3	181	Ro-Ro/Passenger
16	7432290	258318000	28	9	9.1	226	Tug
17	9337884	258408000	68	15	12.0	243	Ro-Ro/Passenger
18	7419200	248131000	104	16	7.6	214	Bulk Carrier
19	-	257057040	15	5	1.6	144	Unspecified
20	8901432	273841710	65	13	11.5	28	Factory Trawler
21	9272735	538002583	119	19	9.8	212	Chem. Tanker
22	-	257557600	25	6	9.4	32	Fishing

Table B.4 AIS information associated to each SLC chip. Part II.

SLC chip ID	IMO	MMSI	Length [m]	Width [m]	Speed [knot]	Heading [°]	Type
23	9175030	259421000	34	10	3.7	40	Trawler
24	9145542	314218000	79	10	10.2	44	General Cargo
25	-	257587600	20	6	1.7	53	Fishing
26	-	257337920	12	4	7.4	269	Fishing
27	-	257053240	13	5	8.8	286	Fishing
28	-	257180440	11	4	6.9	343	Fishing
29	9150494	249772000	88	13	10.4	25	General Cargo
30	9209477	259647000	45	12	0.4	75	Fishing Vessel
31	-	257034440	12	3	7.2	20	Fishing
32	9481829	258416000	33	10	32.1	336	High Speed Craft
33	9406726	259894000	165	24	0.1	223	Chem. Tanker
34	9126596	259374000	66	13	12.4	58	Fishing Vessel
35	9391000	258858000	129	20	12.4	230	Oil/Chem. Tanker
36	-	257034440	12	3	1.2	150	Fishing
37	-	257308140	12	4	8.0	354	Fishing
38	9334404	220447000	93	15	12.8	44	Oil/Chem. Tanker
39	9404259	259690000	98	20	11.6	202	Tug/Supply Vessel
40	9084255	636016339	149	23	12.6	18	Bulk Carrier
41	9219771	257560600	57	13	4.2	11	Trawler
42	6929985	259109000	36	8	8.3	78	Fishing Vessel
43	9017379	314208000	90	16	9.2	52	General Cargo
44	-	247081890	26	7	2.8	102	Fishing
45	-	247143620	28	6	2.8	137	Fishing

B.2 Ground-truth Dataset

This section contain the IMO and/or MMSI number of the vessels employed as the training samples in the K-NN algorithm along with its dimensions (source [101]).

Table B.5 AIS information of the training samples. Type: Cargo. Part I.

Sample #	IMO	MMSI	Length [m]	Width [m]	Type
1	6721113		61	10	General Cargo
2	7002318	258392000	62	10	Self Discharging Bulk Carrier
3	9145554	-	79	10	General Cargo
4	9142526	304905000	82	11	General Cargo
5	9137208	235008290	82	13	General Cargo
6	9000833	314206000	83	13	General Cargo
7	8505549	-	83	12	General Cargo
8	8876572	-	83	13	General Cargo
9	8904434	273118000	86	15	General Cargo
10	8707783	304323000	88	14	General Cargo
11	8915756	245219000	88	13	General Cargo
12	9356529	-	89	12	General Cargo
13	8908806	-	89	14	General Cargo
14	9063885	308542000	90	14	General Cargo
15	9612533	-	90	15	General Cargo
16	9140932	257962000	98	16	Reefer
17	9179995	-	100	20	Ro-Ro Cargo
18	9114787	-	101	17	General Cargo
19	8604606	341353000	108	17	Reefer
20	8904379	273115700	108	15	General Cargo
21	9005326	-	109	17	General Cargo
22	9341732	246512000	111	14	Cargo/Containership
23	9268849	-	112	14	General Cargo
24	8918459	314420000	113	16	General Cargo
25	9534250	-	115	15	General Cargo
26	8008450	-	118	21	Bulk Carrier

Table B.6 AIS information of the training samples. Type: Cargo. Part II.

Sample #	IMO	MMSI	Length [m]	Width [m]	Type
27	9721645	244860255	120	17	General Cargo
28	9642564	-	120	21	Ro-Ro Cargo
29	9235488	304183000	130	16	General Cargo
30	9512587	-	130	24	Cement Carrier
31	9100231	219655000	133	25	Container Ship
32	9234989	-	135	23	Container Ship
33	9349227	210248000	142	21	Container Ship
34	9119074	-	155	27	Bulk Carrier
35	9427574	-	158	28	Bulk Carrier
36	9101730	304219000	167	21	Bulk Carrier
37	9592575	-	170	21	Cargo/Containership
38	9606003	-	178	29	Bulk Carrier
39	9594444	-	178	27	Bulk Carrier
40	9625451	-	180	30	Bulk Carrier
41	9283538	-	186	24	General Cargo
42	9557123	-	190	32	Bulk Carrier
43	9567958	-	190	48	Bulk Carrier
44	9218404	538004244	191	24	Bulk Carrier
45	9292022	-	193	28	General Cargo
46	9609952	-	196	34	Ro-Ro Cargo
47	9552343	-	197	33	Bulk Carrier
48	9259501	-	200	30	Ro-Ro Cargo
49	9642382	-	225	33	Bulk Carrier
50	9624110	-	229	33	Bulk Carrier
51	9275361	-	235	33	Container Ship
52	9538402	-	292	45	Bulk Carrier

Table B.7 AIS information of the training samples. Type: Tanker. Part I.

Sample #	**IMO**	**MMSI**	**Length [m]**	**Width [m]**	**Type**
1	7814254	-	81	14	Oil/Chemical Tanker
2	7431698	-	82	14	Lpg Tanker
3	9320489	-	86	18	Tanker
4	9008512	-	88	15	Lpg Tanker
5	9008469	-	89	15	Lpg Tanker
6	9321603	-	90	17	Oil Products Tanker
7	9020417	-	90	15	Chemical Tanker
8	9566758	-	91	16	Oil/Chemical Tanker
9	9285196	-	96	18	Chemical Tanker
10	9129380	-	98	16	Lpg Tanker
11	9133707	-	99	19	Lpg Tanker
12	9507740	-	100	18	Lpg Tanker
13	9130808	-	100	16	Oil/Chemical Tanker
14	9507582	-	100	14	Lpg Tanker
15	9140827	-	100	17	Chemical Tanker
16	9265249	-	105	16	Chemical Tanker
17	9268239	-	106	17	Oil/Chemical Tanker
18	9623984	-	113	20	Lpg Tanker
19	9342396	-	115	19	Lpg Tanker
20	9283459	-	117	15	Oil Products Tanker
21	9232840	-	120	17	Oil/Chemical Tanker
22	9483516	-	145	24	Oil/Chemical Tanker
23	9156498	-	145	23	Tanker
24	9246152	-	148	23	Oil/Chemical Tanker
25	9460239	-	149	24	Oil/Chemical Tanker
26	9661558	-	160	25	Lpg Tanker
27	9482586	-	160	26	Lpg Tanker
28	9486245	-	162	26	Oil/Chemical Tanker

Table B.8 AIS information of the training samples. Type: Tanker. Part II.

Sample #	IMO	MMSI	Length [m]	Width [m]	Type
29	9255270	-	170	24	Oil/Chemical Tanker
30	9340594	-	175	29	Oil/Chemical Tanker
31	9299434	-	176	30	Oil/Chemical Tanker
32	9239654	-	176	32	Oil/Chemical Tanker
33	9573672	-	180	33	Tanker
34	9379325	-	183	32	Chemical Tanker
35	9261401	-	183	28	Oil/Chemical Tanker
36	9387920	-	183	33	Tanker
37	9240706	-	183	28	Oil/Chemical Tanker
38	9391476	-	183	40	Oil Products Tanker
39	9543548	-	184	33	Oil/Chemical Tanker
40	9377652	-	185	28	Oil/Chemical Tanker
41	9274666	-	186	31	Oil/Chemical Tanker
42	9289776	-	228	33	Oil Products Tanker
43	9209130	-	238	42	Oil Products Tanker
44	9343352	-	244	43	Tanker
45	9229350	-	244	42	Crude Oil Tanker
46	9235725	-	248	44	Oil Products Tanker
47	9255880	-	249	44	Oil Products Tanker
48	9381732	-	250	44	Crude Oil Tanker
49	9413547	-	250	45	Oil Products Tanker
50	9297357	-	252	44	Tanker
51	9152507	-	263	47	Oil Products Tanker
52	9325049	-	274	49	Crude Oil Tanker
53	9296377	-	275	49	Crude Oil Tanker
54	9248423	-	275	48	Tanker
55	9676137	-	276	46	Shuttle Tanker
56	9630030	-	276	49	Oil Products Tanker
57	9304617	-	277	51	Crude Oil Tanker
58	9472529	-	285	50	Oil Products Tanker

Table B.9 AIS information of the training samples. Type: Fishing. Part I

Sample #	**IMO**	**MMSI**	**Length [m]**	**Width [m]**	**Type**
1	-	257910500	10	4	Fishing
2	-	257645500	11	4	Fishing
3	-	235004290	15	6	Fishing
4	-	235002470	17	4	Fishing
5	-	219010989	18	8	Fishing
6	9564475	-	19	7	Trawler
7	-	220182000	19	6	Fishing
8	-	235009220	20	7	Fishing
9	-	235069008	20	5	Fishing
10	-	235068242	21	7	Fishing
11	-	235004730	22	7	Fishing
12	9658745	-	23	7	Trawler
13	-	220043000	23	6	Fishing
14	-	233345000	24	7	Fishing
15	-	235064434	25	8	Fishing
16	-	219751000	27	6	Fishing
17	-	219633000	28	7	Fishing
18	-	219481000	32	6	Fishing
19	9175030	-	34	11	Trawler
20	9605889	-	35	10	Fishing Vessel
21	-	219765000	35	8	Fishing
22	5128572	-	36	8	Fishing Vessel
23	7404803	-	40	10	Trawler
24	-	233308000	41	24	Fishing
25	9211808	-	41	12	Trawler
26	-	228165600	44	10	Fishing
27	8701416	-	45	9	Trawler

Table B.10 AIS information of the training samples. Type: Fishing. Part II.

Sample #	IMO	MMSI	Length [m]	Width [m]	Type
28	-	219125000	45	8	Fishing
29	-	219140000	45	9	Fishing
30	9160322	-	49	11	Fishing Vessel
31	9565429	-	50	13	Fishing Vessel
32	7618820	-	50	9	Fishing Vessel
33	8612794	-	54	12	Trawler
34	9657193	-	55	13	Fishing Vessel
35	9113422	-	56	12	Trawler
36	9191539	-	61	12	Fishing Vessel
37	9223148	-	62	12	Fishing Vessel
38	9621948	-	63	14	Fishing Vessel
39	-	258381000	63	13	Fishing
40	9048902	-	66	13	Trawler
41	7719985	-	66	14	Factory Trawler
42	5359652	-	66	10	Fishing Vessel
43	9669756	-	67	15	Fishing Vessel
44	9605542	-	68	14	Fishing Vessel
45	8705008	-	69	13	Fishing Vessel
46	9281645	-	69	14	Fishing Vessel
47	8131453	-	70	13	Fishing Vessel
48	9125633	-	70	14	Fishing Vessel
49	8506828	-	71	13	Trawler
50	9378840	-	72	15	Trawler
51	9717084	-	74	15	Fishing
52	9151591	-	74	13	Fishing Vessel
53	6920111	-	76	14	Trawler
54	9710919	-	78	16	Fishing Vessel
55	9554573	-	81	17	Fishing Vessel
56	8707537	-	114	18	Trawler
57	9175834	-	126	17	Factory Trawler

Table B.11 AIS information of the training samples. Type: Tug/supply/Other.

Sample #	**IMO**	**MMSI**	**Length [m]**	**Width [m]**	**Type**
1	9141455	311781000	87	40	Research/Survey Vessel
2	8820327	232003524	16	4	Tug
3	9381794	235059525	33	10	Tug
4	9510773	235089032	43	11	Offshore Supply Ship
5	9418042	257461000	52	11	Tug/Supply Vessel
6	8206961	249560000	33	12	Tug/Supply Vessel
7	9407897	-	47	12	Tug/Supply Vessel
8	9419125	-	49	12	Diving Support Vessel
9	9263514	-	63	12	Offshore Supply Ship
10	9319246	-	60	14	Standby Safety Vessel
11	9643867	-	67	15	Offshore Supply Ship
12	9521667	-	70	16	Multi Purpose Offshore Vessel
13	9229477	-	73	17	Tug/Supply Vessel
14	-	257910900	74	17	Medical Trans
15	9139763	-	75	17	Patrol Vessel
16	8769418	-	83	17	Platform
17	9372901	-	80	18	Supply Vessel
18	8506854	-	83	19	Supply Vessel
19	9361421	-	84	19	Offshore Supply Ship
20	7611470	-	89	19	Multi Purpose Offshore Vessel
21	8019394	-	84	20	Standby Safety Vessel
22	8211887	-	87	20	Standby Safety Vessel
23	9482354	-	89	20	Offshore Supply Ship
24	9442433	-	92	20	Tug/Supply Vessel
25	9386691	-	93	20	Offshore Supply Ship
26	9393852	-	95	20	Multi Purpose Offshore Vessel
27	9503483	-	98	20	Standby Safety Vessel
28	9383871	259239000	93	21	Tug/Supply Vessel
29	9364021	235050073	92	22	Offshore Supply Ship
30	9475181	259795000	97	22	Offshore Supply Ship
31	9127320	259412000	107	22	Offshore Supply Ship
32	9666546	257597000	91	23	Multi Purpose Offshore Vessel
33	9329928	319641000	94	23	Offshore Supply Ship
34	9546605	257608000	144	26	Supply Vessel
35	9388950	259332000	105	65	Offshore Supply Ship

Table B.12 AIS information of the training samples. Type: Passengers.

Sample #	IMO	MMSI	Length [m]	Width [m]	Type
1	9375472	-	23	16	Passengers Ship
2	9481829	-	33	10	High Speed Craft
3	9544580	-	34	11	High Speed Craft
4	9684885	-	37	9	High Speed Craft
5	6820919	-	50	11	Ro-Ro/Passenger Ship
6	7618832	-	51	12	Ro-Ro/Passenger Ship
7	7700403	-	65	12	Ro-Ro/Passenger Ship
8	9251949	-	73	15	Ro-Ro/Passenger Ship
9	7805203	-	75	14	Ro-Ro/Passenger Ship
10	9263758	-	80	21	Ro-Ro/Passenger Ship
11	9055759	-	85	15	Ro-Ro/Passenger Ship
12	9172090	-	85	16	Ro-Ro/Passenger Ship
13	8714360	-	87	15	Ro-Ro/Passenger Ship
14	9254898	-	88	17	Ro-Ro/Passenger Ship
15	8304775	-	90	14	Ro-Ro/Passenger Ship
16	9018634	-	97	16	Ro-Ro/Passenger Ship
17	9528469	-	110	18	Ro-Ro/Passenger Ship
18	9419204	-	114	17	Ro-Ro/Passenger Ship
19	9553335	-	114	18	Ro-Ro/Passenger Ship
20	9477139	-	123	17	Ro-Ro/Passenger Ship
21	9344758	-	130	20	Ro-Ro/Passenger Ship
22	9586605	-	170	27	Ro-Ro/Passenger Ship

References

[1] Hoegh-Guldberg, O. et al., *Reviving the Ocean Economy: the case for action - 2015.* WWF International, Gland, Switzerland, 2015.

[2] Food and Agriculture Organization (FAO), *The State of World Fisheries and Aquaculture.* Food and Agriculture Organization of the United Nations, Rome, Italy, 2014.

[3] European Commission (EC), "EuroStats: Statistics Explained," Feb 2016. [online] http://ec.europa.eu/eurostat/statistics-explained/index.php/Main_Page.

[4] United Nations Conference on Trade And Development (UNCTAD, *Review of Maritime Transport - 2015.* United Nations Publications, 2015.

[5] International Chamber of Shipping (ICS), "Environmental Performance," Feb 2015. [online] http://www.ics-shipping.org/shipping-facts/environmental-performance.

[6] C. Mora, D. P. Tittensor, S. Adl, A. G. B. Simpson, and B. Worm, "How Many Species Are There on Earth and in the Ocean?," *PLoS Biology*, vol. 9, pp. 1–8, 08 2011.

[7] Nellemann, C., Corcoran, E., Duarte, C. M., Valdés, L., De Young, C., Fonseca, L., Grimsditch, G. (Editors), *Blue Carbon: The role of healthy oceans in binding carbon - A Rapid Response Assessment.* United Nations Environment Programme,GRID-Arendal, 2009.

[8] J. Tanzer (Editor-in-Chief) et al., *Living Blue Planet Report: Species, habitats and human well-being - 2015.* WWF International, Gland, Switzerland, 2015.

[9] J. Tournadre, "Anthropogenic pressure on the open ocean: The growth of ship traffic revealed by altimeter data analysis," *Geophysical Research Letters*, vol. 41, no. 22, pp. 7924–7932, 2014.

[10] International Maritime Organization (IMO), "Automatic Identification Systems (AIS)," 2015. [online] http://www.imo.org/en/OurWork/Safety/Navigation/Pages/AIS.aspx.

[11] European Commission, "Vessel monitoring system (VMS)," May 2015. [online] http://ec.europa.eu/fisheries/cfp/control/technologies/vms/index_en.htm.

[12] Satellite Imaging Corporation, "Satellite Sensors," 2015. [online] http://www.satimagingcorp.com/satellite-sensors/.

[13] P. Martimort, V. Fernandez, V. Kirschner, C. Isola, and A. Meygret, "Sentinel-2 MultiSpectral imager (MSI) and calibration/validation," in *Geoscience and Remote Sensing Symposium (IGARSS), 2012 IEEE International*, pp. 6999–7002, July 2012.

[14] D. M. Winker, J. R. Pelon, and M. P. McCormick, "CALIPSO mission: spaceborne lidar for observation of aerosols and clouds," in *SPIE 4893, Lidar Remote Sensing for Industry and Environment Monitoring III*, p. 11, March 2003.

[15] Canadian Space Agency, "RADARSAT Constellation," November 2015. [online] http://www.asc-csa.gc.ca/eng/satellites/radarsat/default.asp.

[16] R. Werninghaus and S. Buckreuss, "The TerraSAR-X Mission and System Design," *IEEE Transactions on Geoscience and Remote Sensing*, vol. 48, pp. 606–614, Feb 2010.

[17] D. Geudtner, R. Torres, P. Snoeij, A. Ostergaard, and I. Navas-Traver, "Sentinel-1 mission capabilities and SAR system calibration," in *Radar Conference (RADAR), 2013 IEEE*, pp. 1–4, April 2013.

[18] D. Lame, G. Born, J. Dunne, A. Spear, and C. Yamarone, "SeaSat performance evaluation: The first two steps," *IEEE Journal of Oceanic Engineering*, vol. 5, pp. 72–73, Apr 1980.

[19] Community Reseach and Development Information Service (CORDIS) - EC, "NEREIDS," 2015. [online] http://cordis.europa.eu/project/rcn/99070_en.html.

[20] G. Margarit, "Integrated maritime picture for surveillance and monitoring applications," in *Geoscience and Remote Sensing Symposium (IGARSS), 2013 IEEE International*, pp. 1517–1520, July 2013.

[21] D. Crisp, "The state-of-the-art in ship detection in synthetic aperture radar imagery," Tech. Rep. DSTO-RR-0272, Chief, Intelligence, Surveillance and Reconnaissance Division, May 2004.

[22] R. Raney, "Synthetic Aperture Imaging Radar and Moving Targets," *Aerospace and Electronic Systems, IEEE Transactions on*, vol. AES-7, pp. 499–505, May 1971.

[23] J. C. Curlander and R. N. McDonough, *Synthetic Aperture Radar: Systems and Signal Processing*. Wiley, 1991.

[24] I. G. Cumming and F. H. Wong, *Digital Processing of Synthetic Aperture Radar Data: Algorithms and Implementation*. Artech House Remote Sensing Library, 2005.

[25] C. Oliver and S. Quegan, *Understanding Synthetic Aperture Radar Images*. SciTech Publishing, Inc, 2004.

[26] A. Moreira, P. Prats-Iraola, M. Younis, G. Krieger, I. Hajnsek, and K. Papathanassiou, "A tutorial on synthetic aperture radar," *Geoscience and Remote Sensing Magazine, IEEE*, vol. 1, pp. 6–43, March 2013.

[27] A. Hein, *Processing of SAR Data: Fundamentals, Signal Processing, Interferometry*. Springer, 2004.

[28] G. Margarit, *Marine applications of SAR polarimetry*. Ph.D. Dissertation, Universitat Politècnica de Catalunya, April 2007.

[29] G. Turin, "An introduction to matched filters," *Information Theory, IRE Transactions on*, vol. 6, pp. 311–329, June 1960.

[30] W. Carrara, R. Majewski, and R. Goodman, *Spotlight Synthetic Aperture Radar: Signal Processing*. Artech House Remote Sensing Library, 1995.

[31] K. Tomiyasu, "Conceptual Performance of a Satellite Borne, Wide Swath Synthetic Aperture Radar," *Geoscience and Remote Sensing, IEEE Transactions on*, vol. GE-19, pp. 108–116, April 1981.

[32] R. Moore, J. Claassen, and Y. Lin, "Scanning spaceborne synthetic aperture radar with integrated radiometer," *Aerospace and Electronic Systems, IEEE Transactions on*, vol. AES-17, pp. 410–421, May 1981.

[33] D. Blacknell and H. Griffiths, *Radar Automatic Target Recognition (ATR) and Non-Cooperative Target Recognition (NCTR)*. IET radar, sonar and navigation series, Institution of Engineering and Technology, 2013.

[34] G. Margarit, J. Mallorqui, J. Rius, and J. Sanz-Marcos, "On the Usage of GRECOSAR, an Orbital Polarimetric SAR Simulator of Complex Targets, to Vessel Classification Studies," *Geoscience and Remote Sensing, IEEE Transactions on*, vol. 44, pp. 3517–3526, Dec 2006.

[35] European Space Agency (ESA), "Scientific Background," July 2014. [online] https://earth.esa.int/handbooks/asar/CNTR1-1-2.html.

[36] V. Kerbaol and F. Collard, "SAR-Derived coastal and marine applications: from research to operational products," *Oceanic Engineering, IEEE Journal of*, vol. 30, pp. 472–486, July 2005.

[37] European Commission (EC), "Copernicus:Europe's eyes on Earth," Feb 2016. [online] http://www.copernicus.eu/.

[38] European Space Agency (ESA), "Copernicus: Observing the earth," 2015. [online] http://www.esa.int/Our_Activities/Observing_the_Earth/Copernicus/Overview3.

[39] S. Brusch, S. Lehner, T. Fritz, M. Soccorsi, A. Soloviev, and B. van Schie, "Ship Surveillance With TerraSAR-X," *Geoscience and Remote Sensing, IEEE Transactions on*, vol. 49, pp. 1092–1103, March 2011.

[40] G. Saur, S. Estable, K. Zielinski, S. Knabe, M. Teutsch, and M. Gabel, "Detection and classification of man-made offshore objects in terrasar-x and rapideye imagery: Selected results of the demarine-deko project," in *OCEANS, 2011 IEEE - Spain*, pp. 1–10, June 2011.

[41] M. Martorella, F. Berizzi, D. Pastina, and P. Lombardo, "Exploitation of cosmo skymed sar images for maritime traffic surveillance," in *Radar Conference (RADAR), 2011 IEEE*, pp. 113–117, May 2011.

[42] K. Ward, R. Tough, and S. Watts, *Sea clutter: scattering, the K-distribution and radar performance*. The Institution of Engineering and Technology, 2006.

[43] G. Gao, "A Parzen-Window-Kernel-Based CFAR Algorithm for Ship Detection in SAR Images," *Geoscience and Remote Sensing Letters, IEEE*, vol. 8, pp. 557–561, May 2011.

[44] A. Gambardella, F. Nunziata, and M. Migliaccio, "A Physical Full-Resolution SAR Ship Detection Filter," *Geoscience and Remote Sensing Letters, IEEE*, vol. 5, pp. 760–763, Oct 2008.

[45] M. Migliaccio, A. Gambardella, and F. Nunziata, "Ship detection over single-look complex SAR images," in *US/EU-Baltic International Symposium, 2008 IEEE/OES*, pp. 1–4, May 2008.

[46] M. Tello, C. Lopez-Martinez, and J. Mallorqui, "A novel algorithm for ship detection in SAR imagery based on the wavelet transform," *Geoscience and Remote Sensing Letters, IEEE*, vol. 2, pp. 201–205, April 2005.

[47] M. Tello, C. Lopez-Martinez, J. Mallorqui, and R. Bonastre, "Automatic Detection of Spots and Extraction of Frontiers in SAR Images by Means of the Wavelet Transform: Application to Ship and Coastline Detection," in *Geoscience and Remote Sensing Symposium, 2006. IGARSS 2006. IEEE International Conference on*, pp. 383–386, July 2006.

[48] G. Ferrara, M. Migliaccio, F. Nunziata, and A. Sorrentino, "Generalized-K (GK)-Based Observation of Metallic Objects at Sea in Full-Resolution Synthetic Aperture Radar (SAR) Data: A Multipolarization Study," *Oceanic Engineering, IEEE Journal of*, vol. 36, pp. 195–204, April 2011.

[49] R. Touzi, J. Hurley, and P. Vachon, "Optimization of the degree of polarization for enhanced ship detection using polarimetric radarsat-2," *Geoscience and Remote Sensing, IEEE Transactions on*, vol. 53, no. 10, pp. 5403–5424, 2015.

[50] C. Liu, P. Vachon, and G. Geling, "Improved ship detection using polarimetric SAR data," in *Geoscience and Remote Sensing Symposium, 2004. IGARSS '04. Proceedings. 2004 IEEE International*, vol. 3, pp. 1800–1803 vol.3, Sept 2004.

[51] S. Suchandt, H. Runge, and U. Steinbrecher, "Ship detection and measurement using the TerraSAR-X dual-receive antenna mode," in *Geoscience and Remote Sensing Symposium (IGARSS), 2010 IEEE International*, pp. 2860–2863, July 2010.

[52] R. Touzi, R. Raney, and F. Charbonneau, "On the use of permanent symmetric scatterers for ship characterization," *Geoscience and Remote Sensing, IEEE Transactions on*, vol. 42, pp. 2039–2045, Oct 2004.

[53] G. Margarit and A. Tabasco, "Ship Classification in Single-Pol SAR Images Based on Fuzzy Logic," *Geoscience and Remote Sensing, IEEE Transactions on*, vol. 49, pp. 3129–3138, Aug 2011.

[54] H. Zhang, X. Tian, C. Wang, F. Wu, and B. Zhang, "Merchant vessel classification based on scattering component analysis for COSMO-SkyMed SAR images," *Geoscience and Remote Sensing Letters, IEEE*, vol. 10, pp. 1275–1279, Nov 2013.

[55] G. Margarit and J. J. Mallorqui, "Scattering-based model of the SAR signatures of complex targets for classification applications," *International Journal of Navigation and Observation*, vol. 2008, Aug 2008.

[56] G. Margarit, J. Mallorqui, J. Fortuny-Guasch, and C. Lopez-Martinez, "Exploitation of Ship Scattering in Polarimetric SAR for an Improved Classification Under High Clutter Conditions," *Geoscience and Remote Sensing, IEEE Transactions on*, vol. 47, pp. 1224–1235, April 2009.

[57] R. Paladini, M. Martorella, and F. Berizzi, "Classification of man-made targets via invariant coherency-matrix eigenvector decomposition of polarimetric SAR/ISAR images," *Geoscience and Remote Sensing, IEEE Transactions on*, vol. 49, pp. 3022–3034, Aug 2011.

[58] C. Cochin, P. Pouliguen, B. DelahayeE, D. Hellard, P. Gosselin, and F. Aubineau, "MOCEM - An 'all in one' tool to simulate SAR image," in *Synthetic Aperture Radar (EUSAR), 2008 7th European Conference on*, pp. 1–4, June 2008.

[59] M. Vandewal, R. Speck, and H. Suess, "Efficient sar raw data generation including low squint angles and platform instabilities," *Geoscience and Remote Sensing Letters, IEEE*, vol. 5, pp. 26–30, Jan 2008.

[60] A. Khwaja, L. Ferro-Famil, and E. Pottier, "Efficient sar raw data generation for anisotropic urban scenes based on inverse processing," *Geoscience and Remote Sensing Letters, IEEE*, vol. 6, pp. 757–761, Oct 2009.

[61] H. Yue, B. Hu, and R. Yang, "Research on spaceborne sar raw data simulation," in *Radar, 2006. CIE '06. International Conference on*, pp. 1–4, Oct 2006.

[62] O. Dogan and M. Kartal, "Time domain sar raw data simulation of distributed targets," *EURASIP J. Adv. Signal Process*, vol. 2010, pp. 100:1–100:11, 2010.

[63] J. Rius, M. Ferrando, and L. Jofre, "GRECO: graphical electromagnetic computing for RCS prediction in real time," *Antennas and Propagation Magazine, IEEE*, vol. 35, pp. 7–17, April 1993.

[64] J. Sanz, P. Prats, and J. Mallorqui, "Platform and mode independent SAR data processor based on the extended chirp scaling algorithm," in *Geoscience and Remote Sensing Symposium, 2003. IGARSS '03. Proceedings. 2003 IEEE International*, vol. 6, pp. 4086–4088 vol.6, July 2003.

[65] G. Margarit and J. J. Mallorqui, "Study of Sea Clutter Influence in Ship Classification Algorithms based on Polarimetric SAR Inteferometry," in *Synthetic Aperture Radar (EUSAR), 2008 7th European Conference on*, pp. 1–4, June 2008.

[66] E. Omerdic and D. Toal, "Modelling of waves and ocean currents for real-time simulation of ocean dynamics," in *OCEANS 2007 - Europe*, pp. 1–6, June 2007.

[67] T. Perez, *Ship motion control : Course Keeping and Roll Stabilisation Using Rudder and Fins*. Springer, 2005.

[68] L. Yam, J. Mallorqui, and J. Rius, "Validation of a sea surface model for simulations of dynamic maritime SAR images," in *Geoscience and Remote Sensing Symposium (IGARSS), 2012 IEEE International*, pp. 2813–2816, July 2012.

[69] L. Xiaowei, C. Jinsong, and Z. Minhui, "A ship detection method for dual polarization SAR data based on whitening filtering," in *Geoscience and Remote Sensing Symposium, 2007. IGARSS 2007. IEEE International*, pp. 4171–4174, July 2007.

[70] E. Makhoul, A. Broquetas, and J. Ruiz Rodon, "Ground moving target indication using multi-channel SAR with non-uniform displaced phase centers," in *Geoscience and Remote Sensing Symposium (IGARSS), 2012 IEEE International*, pp. 1610–1613, July 2012.

[71] S. Mallat, *A Wavelet Tour of Signal Processing: The Sparse Way*. Academic Press, 3rd ed., 2008.

[72] S. Mallat, "A theory for multiresolution signal decomposition: the wavelet representation," *Pattern Analysis and Machine Intelligence, IEEE Transactions on*, vol. 11, pp. 674–693, Jul 1989.

[73] A. Hambaba, "Nonstationary statistical tests in time-scale space," in *Aerospace Conference Proceedings, 2000 IEEE*, vol. 6, pp. 373–379 vol.6, 2000.

[74] G. Nason and B. Silverman, "The Stationary Wavelet Transform and some Statistical Applications," *Lecture Notes in Statistics*, vol. 103, p. 281–299, 1995.

[75] M. Tello, J. Mallorqui, and C. Lopez-Martinez, "Application of multiresolution and multispectral polarimetric techniques for reliable vessel monitoring and control," in *Geoscience and Remote Sensing Symposium, 2005. IGARSS '05. Proceedings. 2005 IEEE International*, vol. 1, pp. 4 pp.–, July 2005.

[76] M. Tello Alonso, C. Lopez-Martinez, J. Mallorqui, and P. Salembier, "Edge enhancement algorithm based on the wavelet transform for automatic edge detection in sar images," *Geoscience and Remote Sensing, IEEE Transactions on*, vol. 49, pp. 222–235, Jan 2011.

[77] NOAA - National Centers for Environmental Information, "GSHHG - A Global Self-consistent, Hierarchical, High-resolution Geography Database," July 2015. [online] https://www.ngdc.noaa.gov/mgg/shorelines/gshhs.html.

[78] M. Martorella, F. Berizzi, and B. Haywood, "Contrast maximisation based technique for 2-d ISAR autofocusing," *Radar, Sonar and Navigation, IEE Proceedings* -, vol. 152, pp. 253–262, Aug 2005.

[79] Y. G. Niho, "Phase difference auto focusing for synthetic aperture radar imaging," Mar. 12 1991. US Patent 4,999,635.

[80] P. H. Eichel, D. C. Ghiglia, and J. Jakowatz, C. V., "Speckle processing method for synthetic-aperture-radar phase correction," *Optics Letters*, vol. 14, pp. 1–3, Jan 1989.

[81] D. Wahl, P. Eichel, D. Ghiglia, and J. Jakowatz, C.V., "Phase gradient autofocus - a robust tool for high resolution SAR phase correction," *Aerospace and Electronic Systems, IEEE Transactions on*, vol. 30, pp. 827–835, Jul 1994.

[82] J. S. Bates, "The phase gradient autofocus algorithm with range dependent stripmap SAR," Master's thesis, Brigham Young University, Provo, UT, December 1998.

[83] L. E. Yam, J. J. Mallorqui, and J. M. Rius, "Constraints in azimuth resolution by refocusing slowly moving targets from single-look complex SAR vignettes," in *EUSAR 2014; 10th European Conference on Synthetic Aperture Radar; Proceedings of*, pp. 1–4, June 2014.

[84] C. Santamaria, J. Cicuendez Perez, H. Greidanus, and J. Broussolle, "Improvement of maritime target signatures in satellite sar images," in *EUSAR 2014; 10th European Conference on Synthetic Aperture Radar; Proceedings of*, pp. 1–4, June 2014.

[85] S. Estable, F. Teufel, L. Petersen, S. Knabe, G. Saur, and T. Ullmann, "Detection and classification of offshore artificial objects in TerraSAR-X images: First outcomes of the DeMarine-DEKO project," in *OCEANS 2009 - EUROPE*, pp. 1–8, May 2009.

[86] K. Eldhuset, "An automatic ship and ship wake detection system for spaceborne SAR images in coastal regions," *Geoscience and Remote Sensing, IEEE Transactions on*, vol. 34, pp. 1010–1019, Jul 1996.

[87] I.-I. Lin, L. K. Kwoh, Y.-C. Lin, and V. Khoo, "Ship and ship wake detection in the ERS SAR imagery using computer-based algorithm," in *Geoscience and Remote Sensing, 1997. IGARSS '97. Remote Sensing - A Scientific Vision for Sustainable Development., 1997 IEEE International*, vol. 1, pp. 151–153 vol.1, Aug 1997.

[88] H. Rinne, *The Weibull Distribution: A Handbook*. Chapman and Hall/CRC, 2009.

[89] S. M. Kay, *Fundamentals of Statistical Signal Processing, Volume II: Detection Theory*. Prentice Hall, 1998.

[90] G. X. Ritter and J. N. Wilson, *Handbook of Computer Vision Algorithms in Image Algebra*. CRC Press, 2nd ed., 2000.

[91] M. van Ginkel, C. L. Hendriks, and L. van Vliet, "A short introduction to the radon and hough transforms and how they relate to each other," Technical Report QI-2004-01, Quantitative Imaging Group, Delft University of Technology, 2004.

[92] I. Jollifre, *Principal Component Analysis*. Springer, 2nd ed., 2002.

[93] K. Riley, M. Hobson, and S. Bence, *Mathematical methods for physics and engineering: A comprehensive guide*. Cambridge University Press, 2nd ed., 2002.

[94] MDA, "RADARSAT-2 Product Description," Tech. Rep. Issue 1/6, November 2013.

[95] DLR Cluster Applied Remote Sensing, "TerraSAR-X Ground Segment Basic Product Specification," Tech. Rep. Issue 1.9, October 2013.

[96] F.-K. Li, D. Held, J. Curlander, and C. Wu, "Doppler Parameter Estimation for Spaceborne Synthetic-Aperture Radars," *Geoscience and Remote Sensing, IEEE Transactions on*, vol. GE-23, pp. 47–56, Jan 1985.

[97] M. Jin, "Optimal Doppler Centroid Estimation for SAR Data from a Quasi-Homogeneous Source," *Geoscience and Remote Sensing, IEEE Transactions on*, vol. GE-24, pp. 1022–1025, Nov 1986.

[98] R. Bamler, "Doppler frequency estimation and the Cramer-Rao bound," *Geoscience and Remote Sensing, IEEE Transactions on*, vol. 29, pp. 385–390, May 1991.

[99] S. Madsen, "Estimating the Doppler centroid of SAR data," *Aerospace and Electronic Systems, IEEE Transactions on*, vol. 25, pp. 134–140, Mar 1989.

[100] S. A. Dudani, "The distance-weighted k-nearest-neighbor rule," *Systems, Man and Cybernetics, IEEE Transactions on*, vol. SMC-6, pp. 325–327, April 1976.

[101] Marine Traffic, November 2015. [online] http://www.marinetraffic.com/es/.